A Thesis Submitted for the Degree of PhD at the University of Warwick

Permanent WRAP URL:

http://wrap.warwick.ac.uk/166110

Copyright and reuse:
This thesis is made available online and is protected by original copyright.
Please scroll down to view the document itself.
Please refer to the repository record for this item for information to help you to cite it.
Our policy information is available from the repository home page.

For more information, please contact the WRAP Team at: wrap@warwick.ac.uk

warwick.ac.uk/lib-publications

Numerical and experimental investigations of self-piercing riveting (SPR) and Riv-Bonding joints

by

Yunpeng Liu

Thesis

Submitted in partial fulfilment of the requirements

for the degree of

Doctor of Philosophy

School of Engineering, University of Warwick
September 2021

Table of Contents

Table of Contents i

List of Figures iv

List of Tables xii

Acknowledgements xiii

List of Publications xiv

Declarations xv

Abstract xvi

Nomenclature xvii

Abbreviation xix

1. Introduction 1

- 1.1. Research Background 1
  - 1.1.1. Self-piercing riveting technique 1
  - 1.1.2. Riv(et)-Bonding technique 3
- 1.2. Research Gaps 4
- 1.3. Outline of the Thesis 5

2. Literature Review 7

- 2.1. Self-Piercing Riveting Technique 7
  - 2.1.1. Self-piercing riveting system 8
  - 2.1.2. Evaluation of joint quality 10
  - 2.1.3. Sheets, rivet and die 12
  - 2.1.4. Mechanical strength of SPR joint 18
- 2.2. Adhesive Bonding Technique 19
- 2.3. Riv(et)-Bonding Technique 22

3. Influences of Specimen Cutting Position on SPR Joint Quality Measurement 30

- 3.1. Introduction 30
- 3.2. Improper Specimen Cutting 32
  - 3.2.1. Types of improper cutting positions 32
  - 3.2.2. Influences on the joint cross-sectional profile 33
- 3.3. Evaluation of Cutting Position’s Effects on the Joint Quality Indicators 35
  - 3.3.1. Error estimation of the rivet head height 35

3.3.2. Error estimation of the interlock 35
3.3.3. Error estimation of the remaining bottom sheet thickness 43
3.3.4. Correction of cutting position’s effects on the joint quality indicators 48
3.4. Assessment of the Proposed Estimation and Correction Methods 50
3.4.1. Development of graphical user interface (GUI) 51
3.4.2. Experiment design 51
3.4.3. Results and discussion 55
3.5. Conclusions 60

4. Finite Element Modelling of Self-Piercing Riveting Process 62

4.1. Introduction 62
4.2. FE Model Development 63
4.2.1. Model simplification 63
4.2.2. Material properties of rivet and sheets 65
4.2.3. Fracture of the sheets and rivet 67
4.2.4. Element meshing of the sheets and rivet 68
4.2.5. Friction coefficients 69
4.3. Sensitivity Studies 69
4.3.1. Mesh size of the bottom sheet 71
4.3.2. Mesh size of the top sheet 73
4.3.3. Mesh size of the rivet 75
4.3.4. Threshold thickness for the top sheet separation 77
4.4. Validation of the FE Model 79
4.4.1. Experiment design 79
4.4.2. Results and discussion 82
4.5. Conclusions 86

5. Influences of Different Die Parameters on the SPR Process 88

5.1. Introduction 88
5.2. Simulation Design 89
5.3. Results and Discussion 91
5.3.1. Effect of the die type 91
5.3.2. Effect of the die diameter 96
5.3.3. Effect of the die depth 100
5.3.4. Effect of the die pip height 102
5.3.5. Interaction effects among different die parameters 105
5.4. Conclusions 107

6. Finite Element Modelling of Riv-Bonding Process 108

6.1. Introduction 108
6.2. Experiment Tests 109

6.2.1. Sample preparation 109
6.2.2. Geometrical characterization of the Riv-Bonding joints 112
6.3. FE Model Development 113
6.3.1. Model description 113
6.3.2. Material properties 116
6.3.3. Validation of the FE model 118
6.4. Conclusions 123

7. Influences of the Adhesive Layer on the Riv-Bonding Process and Joint Quality 125

7.1. Introduction 125
7.2. Experimental Procedures 127
7.2.1. Experiment plan 127
7.2.2. Sample preparation 129
7.2.3. Geometrical characterization of the SPR and Riv-Bonding joints 130
7.3. Results and Discussion 131
7.3.1. Influence of the adhesive layer on the joining process 131
7.3.2. Effects of the top sheet thickness on the Riv-Bonding joints 140
7.4. Conclusions 147

8. Conclusions and Future Work 149

8.1. Conclusions 149
8.2. Future Work 151

References 154

List of Figures

Figure 1.1: Schematic of the four major steps in a self-piercing riveting process 1

Figure 1.2: Relationships between the joint cross-sectional profile and the joint mechanical performance 3

Figure 1.3: Schematic of the major steps in a Riv-bonding process 3

Figure 2.1: Annual publications during the last three decades on the SPR (Data from Web of Science) 7

Figure 2.2: Research structure and hotspots of the SPR technique 8

Figure 2.3: Schematic of the three quality indicators measured on the joint cross-sectional profile... 11

Figure 2.4: Possible defects formed in a SPR joint: (a) fracture of the rivet shank [42], (b) gap between the rivet and top sheet, (c) gap between sheets and (d) fracture of the bottom sheet [41], ... 11

Figure 2.5: Characteristic curves for SPR joints of carbon steel sheets with rivets of 555 HV hardness [38] 12

Figure 2.6: Schematic of the (a) two-layer and (b) three-layer SPR joints... 13

Figure 2.7: Schematic of the (a) sheet thickness ratio and (b) sheet sequence 14

Figure 2.8: Schematic of (a) the flat die, (b) the pip die, (c) the SPR joints with flat dies [66, 68–70] and (d) the SPR joints with pip dies [24, 33, 71, 72] 17

Figure 2.9: Schematic of different specimen shapes used in the (a) cross-tensile test [68, 79], (b) lap-shear test [80] and (c) coach-peel test [81] to evaluate the SPR joint mechanical strengths 19

Figure 2.10: Testing fixtures developed to alter the loading direction of SPR joint [68, 86] 19

Figure 2.11: Schematic of the three steps for an adhesive bonding process....................................... 20

Figure 2.12: Schematic of the three failure modes of the adhesive bonded region and failures of the adherend 20

Figure 2.13: Factors affecting the mechanical performance of the adhesive bonded joint.................. 21

Figure 2.14: Schematic of the four approaches for the modelling of adhesive bonded joints 22

Figure 2.15: Cross-sectional profiles of different types of hybrid joints: (a) Riv-Bonding, (b) traditional rivet-bonding [132], (c) Clinch-bonding [134], (d) Bolt-bonding [135], (e) SSRR-bonding [136] and (f) Weld-bonding [137] 23

Figure 2.16: Schematic of the two strategies for the simulation of Riv-Bonding process................... 26

Figure 2.17: Schematic of the two possible approaches for the modelling of adhesive bonded connection in Riv-Bonding joints 28

Figure 3.1: Three joint quality indicators measured on the cross-sectional profile of a SPR joint...... 31

Figure 3.2: Quality evaluation procedures for SPR joints 31

Figure 3.3: SPR joints in the car Body-in-White (BIW) structure 31

Figure 3.4: The ideal specimen cutting position and three improper cutting positions: (a) correct position, (b) pure offset, (c) pure rotation and (d) offset+rotation.. 32

Figure 3.5: Procedures to get the joint cross-sectional profiles virtually at different cutting positions33

Figure 3.6: Joint appearances and cross-sectional profiles at different pure offset distances (Δh) 34

Figure 3.7: Joint appearances and cross-sectional profiles at different pure rotation angles (θ_1)........ 34

Figure 3.8: Locations of the two boundaries for the rivet head height (H) and the two boundaries for the interlock (I).. 35

Figure 3.9: Projections of the two interlock boundaries on the cutting plane with an offset distance (Δh)... 36

Figure 3.10: Schematic of the interlock values on the joint central plane and on the cutting plane with an offset distance (Δh)... 36

Figure 3.11: Absolute error ($e$offset) of the interlock with different offset distances (Δh) 38

Figure 3.12: Relative error (δoffset) of the interlock with different offset distances (Δh) 38

Figure 3.13: Projections of the two interlock boundaries from the joint central plane to the cutting plane with a rotation angle (θ_1).. 39

Figure 3.14: Schematic of the interlock values on the joint central plane and the cutting plane with a rotation angle (θ_1) 39

Figure 3.15: Absolute error ($e$rotation) of the interlock with different rotation angles (θ_1) 40

Figure 3.16: Relative error (δrotation) of the interlock with different rotation angles (θ_1) 41

Figure 3.17: Projections of the two interlock boundaries from the joint central plane to the cutting plane with a offset distance (Δh) and a rotation angle (θ_1): (a) $\theta_1>0$ and (b) $\theta_1<0$ 41

Figure 3.18: Schematics of the interlock on the joint central plane and on the measurement plane with an offset distance (Δh) and a rotation angle (θ_1).. 42

Figure 3.19: Schematics of (a) points located on the upper and lower surfaces of the bottom sheet and (b) projection of the boundary points A and B from the joint central plane to the cutting plane . 43

Figure 3.20: Schematic of the (a) ideal and actual cutting positions, (b) the bottom sheet profile on the joint central plane and (c) the bottom sheet profile on the cutting plane with an offset distance (Δh)... 44

Figure 3.21: Projection trajectories of the boundary points from the joint central plane to the cutting plane with an offset distance (Δh) 44

Figure 3.22: Virtually captured bottom sheet profiles on the cutting plane with different offset distances (Δh): (a) 0.0mm and 0.5mm, and (b) 0.0mm, 1.0mm and 1.5mm 45

Figure 3.23: Schematic of the (a) ideal and actual cutting positions, (b) the bottom sheet profile on the joint central plane and (c) the bottom sheet profile on the cutting plane with a rotation angle (θ_1) 46

Figure 3.24: Projection trajectories of the boundary points from the joint central plane to the cutting plane with a rotation angle (θ_1).. 46

Figure 3.25: Virtually captured bottom sheet profiles on the cutting plane with different rotation angles (θ_1): (a) 0°, 5°, and (b) 0°, 10°, 15°, 20°.. 46

Figure 3.26: Schematic of the bottom sheet profiles on the joint central plane and on the cutting plane with an offset distance (Δh) and a rotation angle (θ_1)... 47

Figure 3.27: Flow chart for the interlock error correction in practical applications 49

Figure 3.28: Strategies to obtain the six parameters (Δh, θ_1, S_1, S_2, R_{in} and I_{m}) for the interlock error correction.. 50

Figure 3.29: Developed graphical user interfaces (GUI) for (a) interlock error estimation and (b) interlock error correction 51

Figure 3.30: Specimen dimensions of the SPR joint (in mm) 52

Figure 3.31: Dimensions of the (a) semi-tubular rivets and (b) dies (in mm) 53

Figure 3.32: Structure of the Tucker SPR system 53

Figure 3.33: Joint cross-sectional profiles from experimental SPR tests 54

Figure 3.34: Procedures to virtually cut the SPR joint at different cutting positions and capture the corresponding cross-sectional profiles 55

Figure 3.35: Estimation of the interlock errors caused by the offset distance (Δh) under the (a) ideal condition and (b) practical condition.. 56

Figure 3.36: Estimated (a) absolute error e_{offset} and (b) relative error δ_{offset} of the tested SPR joints with different offset distances (Δh) 56

Figure 3.37: Estimation of the interlock errors caused by the rotation angle (θ_1) under the (a) ideal condition and (b) practical condition.. 57

Figure 3.38: Estimated (a) absolute error $e_{rotation}$ and (b) relative error $\delta_{rotation}$ of the 15 SPR joints with different rotation angles (θ_1).. 57

Figure 3.39: Relative error ($\delta_{off+rot}$) of the interlock in the 15 SPR joints with varying offset distances (Δh) and rotation angles (θ_1)... 59

Figure 3.40: Cross-sectional profiles of the dummy joint 3-10 at the ten different cutting positions . 60

Figure 3.41: Comparison of the (a) interlock and (b) relative error at the ten cutting positions of the dummy joint 3-10 60

Figure 4.1: Structure of the Tucker self-piercing riveting system 64

Figure 4.2: Schematic of the C-frame deflection under a high joining force 64

Figure 4.3: Schematic of the 2D axisymmetric simulation model of SPR process 65

Figure 4.4: Plastic stress-strain curves of the AA5754 at different temperatures (strain rate=1.0 s^{-1}) [170] 66

Figure 4.5: Plastic stress-strain curve of the boron steel (strain rate=0.01 s^{-1}).................................. 67

Figure 4.6: The critical thickness for the separation of the top sheet 68

Figure 4.7: Dimensions of the employed pip die (Pip die-A) in the sensitivity studies 70

Figure 4.8: Four indicators measured on the joint cross-sectional profile... 71

Figure 4.9: Simulated joint cross-sectional profiles with different bottom sheet mesh sizes: (a) 0.06mm, (b) 0.08mm, (c) 0.10mm, (d) 0.12mm, (e) 0.15mm, (f) 0.20mm and (g) 0.25mm....... 72

Figure 4.10: The predicted four indicators with varying bottom sheet mesh sizes: (a) interlock I, (b) deformed rivet shank radius R_2, (c) remaining bottom sheet thickness under the rivet tip t_{tip} and (d) remaining bottom sheet thickness around the joint centre t_{c}.. 72

Figure 4.11: Influences of the bottom sheet mesh size on (a) the bottom sheet element number and (b) the simulation time 73

Figure 4.12: The simulated joint cross-sectional profiles with different top sheet mesh sizes: (a) 0.06mm, (b) 0.08mm, (c) 0.10mm, (d) 0.12mm, (e) 0.15mm, (f) 0.20mm and (g) 0.25mm....... 74

Figure 4.13: The predicted four indicators with different top sheet mesh sizes: (a) interlock I, (b) deformed rivet shank radius R_2, (c) remaining bottom sheet thickness under the rivet tip t_{tip} and (d) remaining bottom sheet thickness around the joint centre t_{c}.. 74

Figure 4.14: The simulated joint cross-sectional profiles when the rivet penetrated the top sheet (rivet displacement=3.29mm) with different top sheet mesh sizes: (a) 0.06mm, (b) 0.08mm, (c) 0.10mm, (d) 0.12mm, (e) 0.15mm, (f) 0.20mm and (g) 0.25mm 75

Figure 4.15: Influences of the top sheet mesh size on (a) the top sheet element number and (b) the simulation time 75

Figure 4.16: The simulated joint cross-sectional profiles with different rivet mesh sizes: (a) 0.04mm, (b) 0.06mm, (c) 0.08mm, (d) 0.10mm, (e) 0.12mm, (f) 0.15mm and (g) 0.20mm...................... 76

Figure 4.17: The predicted four indicators with different rivet mesh sizes: (a) interlock I, (b) deformed rivet shank radius R_2, (c) remaining bottom sheet thickness under the rivet tip t_{tip} and (d) remaining bottom sheet thickness around the joint centre t_{c}.. 76

Figure 4.18: Influences of the rivet mesh size on (a) the rivet element number and (b) the simulation time.. 77

Figure 4.19: The simulated joint cross-sectional profiles with different threshold thicknesses: (a) 0.02mm, (b) 0.04mm, (c) 0.08mm, (d) 0.12mm, (e) 0.15mm and (f) 0.20mm 78

Figure 4.20: Fracture/separation of the top sheet with different threshold thicknesses: (a) 0.02mm, (b) 0.04mm, (c) 0.08mm, (d) 0.12mm, (e) 0.15mm and (f) 0.20mm 78

Figure 4.21: The predicted four indicators with different threshold thicknesses: (a) interlock I, (b) deformed rivet shank radius R_2, (c) remaining bottom sheet thickness under the rivet tip t_{tip} and (d) remaining bottom sheet thickness around the joint centre t_{c}.. 79

Figure 4.22: Specimen dimensions of the SPR joint (in mm) 81

Figure 4.23 The experimentally recorded force-displacement curve and the corresponding true curves with different C-frame stiffnesses 82

Figure 4.24 Comparisons of force-displacement curves: (a) between the experimentally recorded and simulated and (b) between the modified experimentally measured and simulated 82

Figure 4.25: Comparison between joint cross-sectional profiles during the SPR process from (a) interrupted laboratory tests and (b) simulations 83

Figure 4.26:Comparison of the joint cross-sectional profiles from the simulations and experimental tests: (a) joint 4-33, (b) joint 4-34, (c) joint 4-35, (d) joint 4-36, (e) joint 4-37, (f) joint 4-39, (g) joint 4-40, (h) joint 4-41 and (i) joint 4-42 83

Figure 4.27: Comparisons between the experimentally tested and numerically predicted interlock (I) in SPR joints with varying configurations... 84

Figure 4.28: Comparisons between the experimentally tested and numerically predicted minimum remaining thickness on the bottom sheet (T_{min}) in SPR joints with varying configurations........ 84

Figure 4.29: Comparisons between the simulated and experimentally tested true force-displacement curves of the SPR joint 4-32.. 85

Figure 4.30: Comparisons of the true force-displacement curves from experimental SPR tests and simulations: (a) joint 4-33, (b) joint 4-34, (c) joint 4-35, (d) joint 4-36, (e) joint 4-37, (f) joint 4-39, (g) joint 4-40, (h) joint 4-41 and (i) joint 4-42 86

Figure 5.1: Cross-sectional profiles of the referenced dies: (a) pip die-A and (b) flat die-A 90

Figure 5.2: Cross-sectional profiles of the pip dies with different pip heights................................... 90

Figure 5.3: Schematic of the three critical rivet and die cavities.. 91

Figure 5.4: Schematic of the remaining bottom sheet thickness at the joint centre (t_c) and the flared rivet shank radius (R_1) measured on the joint cross-sectional profile... 91

Figure 5.5: Force-displacement curves in the joint 5-1 with pip die-A and the joint 5-2 with flat die-A 92

Figure 5.6: Joint cross-sectional profiles at different rivet displacements during the riveting processes of the (a) joint 5-1 with pip die-A and (b) joint 5-2 with flat die-A 93

Figure 5.7: Equivalent stress distributions on the top and bottom sheets in (a) the joint 5-1 with pip die-A and (b) the joint 5-2 with flat die-A (rivet displacement=0.52mm) 93

Figure 5.8: Variation curve of the flared rivet shank radius (R_1) in the joint 5-1 with pip die-A........ 94

Figure 5.9: Variation curve of the flared rivet shank radius (R_1) in the joint 5-2 with flat die-A........ 94

Figure 5.10: Materials flowing behaviour of the rivet and sheets in the joint 5-2: (a) before and (b) after the cavity 3 was fully filled... 95

Figure 5.11: Equivalent stress distributions before and after the point B in the joint 5-2 with flat die-A 96

Figure 5.12: Force-displacement curves in the SPR joints with different die diameters..................... 96

Figure 5.13: Joint cross-sectional profiles during SPR processes with different die diameters (D_1): (a) 7.5 mm (flat die-B) and (b) 10.0 mm (flat die-C)... 97

Figure 5.14: Variation curves of the remaining bottom sheet thickness at the joint centre (t_c) in SPR processes with different die diameters (D_1) 98

Figure 5.15: Equivalent stress distribution in the joint 5-3 at different phases (D_1=7.5 mm): (a) phase Ⅰ, (b) phase II and (c) phase III 99

Figure 5.16: The flared rivet shank radius (R_1) in SPR processes with different die diameters (D_1) .. 99

Figure 5.17: Force-displacement curves in the SPR joints with different die depths 100

Figure 5.18: Joint cross-sectional profiles during SPR processes with different die depths: (a) H_1=1.8 mm (flat die-E) and (b) H_1=2.4 mm (flat die-F) 101

Figure 5.19: Variation curves of the remaining bottom sheet thickness at the joint centre (t_c) during the SPR processes with different die depths (H_1) 102

Figure 5.20: Equivalent stress distribution on the sheets after the bottom sheet contacted with the bottom of the die cavity: (a) H_1=1.8 mm (flat die-E) and (b) H_1=2.4 mm (flat die-F) 102

Figure 5.21: The flared rivet shank radius during SPR processes with different die depths (H_1) 102

Figure 5.22: Force-displacement curves in the SPR joints with different die pip heights 103

Figure 5.23: Joint cross-sectional profiles during SPR processes with different die pip heights: (a) 0.0mm (pip die-A), (b) −0.4mm (pip die-B) and (c) −0.8mm (pip die-C) 104

Figure 5.24: Variation curves of the remaining bottom sheet thickness at the joint centre (t_c) in SPR processes with different die pip heights 105

Figure 5.25: The flared rivet shank radius (R_1) during SPR processes with different die pip heights105

Figure 6.1: Schematic of the Riv-Bonding process 108

Figure 6.2: Schematic of the semi-tubular rivet and dies (in mm) 111

Figure 6.3: Dynamic viscosity-temperature curve of the adhesive SikaPower 498 [181] 112

Figure 6.4: Schematic of applying the uncured adhesive on the bottom sheet 112

Figure 6.5: Schematic of the cutting position on the specimen 113

Figure 6.6: Geometrical dimensions measured on the cross-sectional profile of the Riv-Bonding joint 113

Figure 6.7: 2D axisymmetric simulation model of the Riv-Bonding process 114

Figure 6.8: Deformed top sheets at the rivet head height H=4.0mm: (a) the SPR joint 6-1 and (b) the Riv-Bonding joint 6-6 115

Figure 6.9: Two stages of the adhesive flow during the clamping process 115

Figure 6.10: Simulation procedures of the Riv-Bonding process: (a) clamping process and (b) riveting process 115

Figure 6.11: Shear stress-viscosity curves of the adhesive SikaPower 498 at different temperatures [182] 117

Figure 6.12: Shear strain rate-viscosity curves of the adhesive SikaPower 498 at different temperatures 117

Figure 6.13: Equivalent stress-strain rate curve of the adhesive SikaPower 498 (50°C)................... 118

Figure 6.14: Comparison between the joint cross-sectional profiles during the Riv-Bonding process from (a) the interrupted laboratory tests and simulations, (b) considering or (c) without considering the blank-holder strike 119

Figure 6.15: Shapes of the Riv-Bonding joint 6-9 (*H*=1.0mm): (a) tested, (b) simulated with or (c) without considering the blank-holder strike 120

Figure 6.16: Comparison of the Riv-Bonding joint 6-10 quality indicators between the laboratory tests and the simulation 121

Figure 6.17: Simulated and tested cross-sectional profiles of the Riv-Bonding joint 6-10 (Effective plastic strain) 121

Figure 6.18: Simulated and tested true load-displacement curves of the Riv-Bonding joint 6-10 121

Figure 6.19: Simulated and tested joint cross-sectional profiles for model validation...................... 122

Figure 6.20: Comparison of the critical quality indicators between the experimentally tested and simulated joints.. 122

Figure 6.21: Simulated and experimentally tested true load-displacement curves for FE model validation 123

Figure 7.1: Schematic of the (a) self-piercing riveting process and (b) Riv-Bonding process.......... 126

Figure 7.2: Schematic of the semi-tubular rivet (in mm) 128

Figure 7.3: Schematic of the (a) flat die-A and (b) pip die-A (in mm).. 128

Figure 7.4: Schematic of applying the uncured adhesive on the bottom sheet................................. 130

Figure 7.5: Dynamic viscosity-temperature curve of the adhesive SikaPower 498 [181]................. 130

Figure 7.6: Dimensions measured on the cross-sectional profiles of the (a) SPR joint and (b) Riv-Bonding joint... 131

Figure 7.7: Comparison of the joint cross-sectional profiles during the (a) SPR process and (b) Riv-Bonding process with the pip die-A 131

Figure 7.8: Comparison of the joint cross-sectional profiles during the (a) SPR process and (b) Riv-Bonding process with the flat die-A 132

Figure 7.9: Schematics of the adhesive distribution after the clamping process with (a) a low blank-holder speed and (b) a high blank-holder speed 133

Figure 7.10: Remaining adhesive around the clamping region between the blank-holder and the die (joint 7-F6) 133

Figure 7.11: A loosely connected SPR joint with a gap formed between the rivet head and the top sheet [183] 134

Figure 7.12: Schematic of the top sheet penetration processes in Riv-Bonding joints with (a) the pip die and (b) the flat die.. 135

Figure 7.13: Joint cross-sectional profiles with (a) premature failure of top sheet [19] and (b) top sheet fragment [184] 136

Figure 7.14: Variation curves of the deformed rivet shank diameter (D_r) with or without the adhesive layer: (a) pip die-A and (b) flat die-A........ 138

Figure 7.15: Threshold filling conditions of the die cavity for rapid rivet shank flare with the pip die and flat die 139

Figure 7.16: Force-displacement curves during the joining processes with or without the adhesive layer: (a) pip die and (b) flat die 140

Figure 7.17: Cross-sectional profiles of (a) the SPR joints 7-P11~7-P13 and (b) the Riv-Bonding joints 7-P14~7-P16 with different top sheet thicknesses T_t (pip die) 141

Figure 7.18: Cross-sectional profiles of (a) the SPR joints 7-F11~7-F13 and (b) the Riv-Bonding joints 7-F14~7-F16 with different top sheet thicknesses T_t (flat die) 141

Figure 7.19: Schematics of the initially trapped adhesive around the joining region after the clamping processes with (a) a thin top sheet and (b) a thick top sheet........ 143

Figure 7.20: Changing trends of the (a) interlock and (b) radius of the interlock boundaries in the SPR and Riv-Bonding joints with the pip die........ 144

Figure 7.21: Changing trends of the (a) interlock and (b) radius of the interlock boundaries in the SPR and Riv-Bonding joints with the flat die........ 144

Figure 7.22: Influences of the top sheet thickness T_t on the remaining bottom sheet thickness in the SPR and Riv-Bonding joints with (a) the pip die and (b) the flat die 145

Figure 7.23: Schematic of the (a) the SPR joint and (b) the Riv-Bonding joint under the lap-shear loading condition........ 147

Figure 8.1: Texture modification of the die bottom surface 151

Figure 8.2: Schematic of the three rivet geometric parameters 152

Figure 8.3: Cross-sectional profiles of the two-layer and three-layer SPR joints........ 152

Figure 8.4: Schematic of the joining parameters that may affect the final quality of Riv-Bonding joints 153

Figure 8.5: Schematics of the (a) local sheet deformation induced by the adhesive pocket, (b) joining sequence of multiple Riv-Bonding joints and (c) ways of applying uncured adhesive 153

List of Tables

Table 3.1: Joint configurations and experiment results 52

Table 3.2: Ten cutting positions of the dummy joint 3-10 55

Table 4.1: Material properties of the rivet and sheets........ 66

Table 4.2: Simulation design for the sensitivity studies 70

Table 4.3: Design of the interrupted experimental SPR tests 80

Table 4.4: Design of the SPR joints with varing sheet thickness and rivet length........ 80

Table 5.1: Joint configurations with different die geometric parameters 90

Table 6.1: Properties of the adhesive SikaPower 498 [181] 111

Table 6.2: Experiment design of the interrupted laboratory tests for the SPR and the Riv-Bonding processes........ 111

Table 6.3: Experiment design of the SPR and Riv-Bonding joints for FE model verification 111

Table 7.1: Interruption tests of SPR process and Riv-Bonding process with different types of dies 128

Table 7.2: SPR and Riv-Bonding joints with different top sheet thicknesses (T_t) 129

Acknowledgements

I would like to express my appreciations to supervisor Professor Xianping Liu and industrial supervisor Dr Li Han. They have provided strong support and guidance during the PhD study, and also spent a lot of time and efforts in improving my journal paper writing. It would be not possible to complete this thesis without their patience and commitment. I would also like to thank Dr Yanling Tian, who gave me a lot of encouragements these years.

Many thanks to Dr Matthias Wissling, Paul Bartig and their team members from Tucker GmbH. They generously shared their SPR equipment and helped me to conduct all the experimental tests presented in this thesis. I learned a lot of practical knowledge from them. It would be impossible to complete this research without their supports. I would like to thank my progress panel of Professor David Towers and Professor Ken Mao for their general support and advice. I am also grateful for the opportunity of interacting with industrial people from Jaguar Land Rover (JLR), and this has offered me many useful experiences during the project.

I would like to thank my friends Zhen Yang, Yumeng Song, Yue Yang, Wuweikai Xiang, Lijin Deng, Xianlei Shan, Yiwei Ma and Jiajing Zhu. They brought a lot of happiness to my PhD study, and also gave me many kind suggestions in the study and daily life.

Special appreciations are given to my parents Yanrong Li and Huichuan Liu for their encouragements and understandings. Many thanks to my father-in-law Xinfeng Zhao and mother-in-law Xiang Feng for their full supports. Many thanks to my aunt Yanhui Liu and uncle Jingkao Li for their helpful advice and supports. Many thanks to my brother Yunlong Liu for his contributions and sacrifices for our family. I would also like to thank my wife Huan Zhao for her company and understandings during these years. She is the sunshine in my life.

Finally, many thanks for the financial supports from China Scholarship Council (CSC), School of Engineering, University of Warwick, and Jaguar Land Rover (JLR) UK.

List of Publications

Journal papers:

[1] **Yunpeng Liu**, Li Han, Huan Zhao, and Xianping Liu. "Evaluation and correction of cutting position's effects on quality indicator measurement of self-piercing riveted joint." *Materials & Design* 202 (2021): 109583. [**Q1**, **IF = 7.991**]

[2] **Yunpeng Liu**, Li Han, Huan Zhao, and Xianping Liu. "Numerical modelling and experimental investigation of the Riv-Bonding process." *Journal of Materials Processing Technology* 288 (2021): 116914. [**Q2**, **IF = 5.551**]

[3] **Yunpeng Liu**, Li Han, Huan Zhao, and Xianping Liu. " Experimental investigation of the adhesive layer's impact on the Riv-Bonding process and joint quality." *Thin-Walled Structures* 167 (2021): 108255. [**Q1**, **IF = 4.442**]

[4] **Yunpeng Liu**, Li Han, Huan Zhao, and Xianping Liu. "Effects of the die parameters on the self-piercing riveting process." *The International Journal of Advanced Manufacturing Technology* 105, no. 7 (2019): 3353-3368. [**Q2**, **IF = 3.226**]

Conference paper:

[1] **Yunpeng Liu**, Li Han and Xianping Liu. "Finite element analysis of force-displacement curves with different self-piercing riveting joint configurations." *19th International Conference and Exhibition*, EUSPEN (2019), Pages 414-415.

Others:

[1] Huan Zhao, Li Han, **Yunpeng Liu**, and Xianping Liu. "Modelling and interaction analysis of the self-pierce riveting process using regression analysis and FEA." *The International Journal of Advanced Manufacturing Technology* 113.1 (2021): 159-176. [**Q2**, **IF = 3.226**]

[2] Huan Zhao, Li Han, **Yunpeng Liu**, and Xianping Liu. "Quality prediction and rivet/die selection for SPR joints with artificial neural network and genetic algorithm." *Journal of Manufacturing Processes* 66 (2021): 574-594. [**Q2**, **IF = 5.010**]

Declarations

This thesis is submitted to the University of Warwick in partial fulfilment of the requirements for the Doctor of Philosophy. The work presented here was conducted by the candidate Yunpeng Liu under the supervision of Professor Xianping Liu and Dr Li Han at the University of Warwick. Any part of it has not been submitted for any degree at other institutions.

Abstract

Self-piercing riveting (SPR) and Riv(et)-Bonding techniques have been widely employed for the assembly of vehicle Body-in-White (BIW) structures in the automotive industry. To deepen understanding of the two fastening methods and to facilitate their practical applications, numerical and experimental investigations of the SPR/Riv-Bonding processes were carried out in this thesis. Four problems encountered during practical applications of the SPR and Riv-Bonding were systematically studied, and the main contents are summarised below:

(1) Quality of the SPR joint is usually assessed by analysing the joint cross-sectional profile captured from the sectioned specimen. However, it is still not clear how much impact the specimen cutting position may impose on the captured shape of this joint profile, and on the joint quality evaluation result. Therefore, the influences of improper specimen cutting positions on the joint cross-sectional profile and on the measurement accuracy of joint quality indicators were systematically investigated. A strategy was also proposed accordingly to correct the measurement error of interlock, and was proved to be effective to reduce the relative interlock error to 1%~3%.

(2) It has been widely acknowledged that the die geometry can significantly influence the SPR joint quality by altering the deformation behaviours of rivet and sheets during the joining process. However, due to the limitations of experimental SPR tests, there is still not clear understanding of how different die parameters affect the events happened during the SPR process. Therefore, a two-dimensional (2D) simulation model of SPR process was firstly developed, and then employed to numerically investigate the effects of die type, die depth, die diameter and die pip height on the flare behaviour of rivet shank, the deformation behaviours of sheets and the variation trend of riveting force.

(3) Strong fluid-structure interaction (FSI) happens between the solid parts (i.e., rivet and sheets) and uncured adhesive layer during the Riv-Bonding process. Until now, it is still a challenge to numerically simulate this phenomenon. In this thesis, a 2D simulation model of Riv-Bonding process was successfully developed. The uncured adhesive (i.e., SikaPower 498) was meshed with Lagrangian elements, and its flow behaviour was approximately represented with the Ostwald-de Waele power law. Experimental Riv-Bonding tests with different configurations were conducted, and a good agreement between the simulation and experimental results was obtained. The developed simulation model was proved capable of predicting the adhesive flow behaviour, rivet and sheets deformation behaviours and riveting force during the joining process.

(4) During the Riv-Bonding process, how the adhesive layer affects the events happened in the riveting process and the final quality of riveted connection is still not clearly understood. Therefore, interrupted experimental tests with flat die and pip die were carried out in this thesis to figure out the differences between the SPR process and the corresponding Riv-Bonding process. SPR/Riv-Bonding joints with different top sheet thicknesses were also tested to study the effects of adhesive layer in joints with varying configurations. The experimental results revealed that, regardless of the die type and top sheet thickness, adhesive pockets were always formed around the joining region and thus affected the deformations of rivet and sheets. The adhesive layer imposed negative influences on the interlock formation, whilst its effects on the remaining bottom sheet thickness varied under different joint configurations.

Nomenclature

l_1	Remaining rivet head thickness perpendicular to the sectioned surface, mm
l_2	Height of the captured joint cross-sectional profile from direction A, mm
l_3	Height of the captured joint cross-sectional profile from direction B, mm
r	Pearson’s correlation coefficient
t_{tip}	Remaining bottom sheet thickness under the rivet tip, mm
t_{cen}	Remaining bottom sheet thickness at the joint centre, mm
t_{c}	Remaining bottom sheet thickness at the joint centre, mm
v_1	Punch speed, mm/s
D_1	Die diameter, mm
D_{h}	Diameter of the rivet head on the specimen, mm
$D_{\mathrm{h\text{-}m}}$	Width of the rivet head on the captured joint cross-sectional profile, mm
D_{in}	Diameter of the inner interlock boundary, mm
D_{out}	Diameter of the outer interlock boundary, mm
F	Joining force, kN
F_{r}	Riveting force, kN
F_{clamping}	Clamping force, kN
F_{max}	Maximum riveting force, kN
H	Rivet head height, mm
H_1	Die depth, mm
I	Interlock, mm
I_{m}	Measured interlock, mm
I_{true}	True interlock, mm
K	Stiffness of the C-frame, kN/mm
L_1	Rivet length, mm
L_2	Die displacement along the vertical direction, mm
L_3	Length of the cantilever, mm

R_1	Flared rivet shank radius, mm
R_2	Deformed rivet shank radius, mm
R_{in}	Radius of the inner interlock boundary, mm
$R_{\mathrm{in\text{-}true}}$	True radius of the inner interlock boundary, mm
R_{out}	Radius of the outer interlock boundary, mm
S_1	Vertical distance between inner interlock boundary and the top surface of rivet, mm
S_2	Vertical distance between the two interlock boundaries, mm
T_{t}	Top sheet thickness, mm
T_{b}	Bottom sheet thickness, mm
T_{min}	Minimum remaining bottom sheet thickness, mm
Δh	Offset distance, mm
α_1	Deflection angle, °
θ_1	Rotation angle, °
δ_{offset}	Relative error of interlock with only the Δh, %
$\delta_{off+rot}$	Relative error of interlock with Δh as well as θ_1, %
$\delta_{rotation}$	Relative error of interlock with only the θ_1, %
e_{offset}	Absolute error of interlock with only the Δh, mm
$e_{off+rot}$	Absolute error of interlock with Δh as well as θ_1, mm
$e_{rotation}$	Absolute error of interlock with only the θ_1, mm

Abbreviation

2D	Two-dimensional
3D	Three-dimensional
ALE	Arbitrary Lagrangian Eulerian
BIW	Body-in-White
CEL	Coupled Euler Lagrangian
CFD	Computational Fluid Dynamics
CFRP	Carbon fibre reinforced polymer
E-SPR	Electromagnetic self-piercing riveting
EP-SPR	Electroplastic self-piercing riveting
FE	Finite element
FEM	Finite element modelling
FSI	Fluid-structure interaction
GUI	Graphical user interface
HSS	High strength steel
JLR	Jaguar Land Rover
NVH	Noise, vibration and harshness
RSW	Resistance spot welding
SPG	Smoothed Particle Galerkin
SPR	Self-piercing riveting
SSPR	Single-sided piercing riveting
TA-SPR	Thermally assisted self-piercing riveting
UHSS	Ultra-high strength steel

1. Introduction

1.1. Research Background

1.1.1. Self-piercing riveting technique

Over recent years, lightweight construction strategies have become increasing important due to economic reasons and environmental protection [1]. In the automotive industry, more and more lightweight materials, such as aluminium alloys, magnesium alloys and composites, have been widely utilized on the car Body-in-White (BIW) structures to reduce fuel consumption and greenhouse gas emissions [2, 3]. The resistance spot welding (RSW) is the most widely used technique to join steel car body panels, but encounters many challenges when joining aluminium alloy parts due to the high thermal conductivity, low melting point and natural surface oxide layer [4]. To deal with this issue, self-piercing riveting (SPR) achieved a rapid development during the last few decades. It has been reported that the SPR joint can achieve similar or even higher shear strength and T-peel strength compared to the RSW joint [5]. Meanwhile, it can also achieve a similar or even better fatigue strength than the RSW joint [6]. Until now, the SPR technique has been widely adopted by many motor companies, such as Audi, JLR and BMW [7], as one of the major fastening approaches for the assembly of car BIW structures. In addition, this joining technique has also been widely used in the packing industry [8] and civil engineering field [9] to connect thin-walled structures.

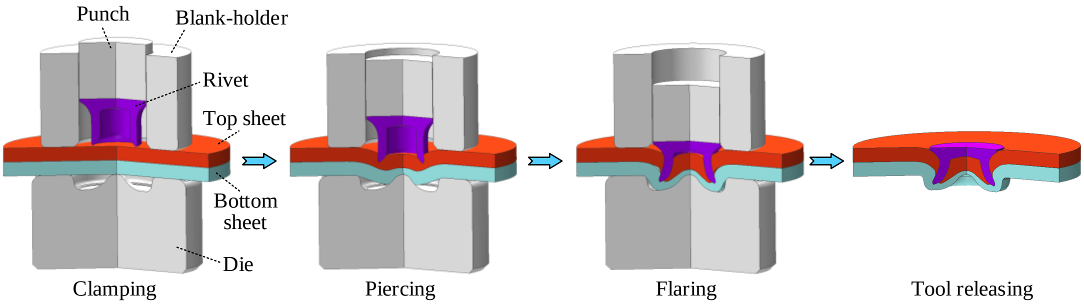

Figure 1.1: Schematic of the four major steps in a self-piercing riveting process

As a mechanical joining technique, the SPR is effective to connect two or more similar/dissimilar sheets. **Figure 1.1** illustrates the four steps during a SPR process: (1) Clamping; (2) Piercing; (3) Flaring; (4) Releasing the joining tools. First of all, the top and bottom sheets are clamped together by the blank-holder and the die. Then, under high pressure from the punch, a semi-tubular rivet pierces through the top sheet and flares into the bottom sheet. Finally, all the joining tools are released, and the two sheets are successfully connected together by a mechanical interlock formed between the rivet shank and the bottom sheet. The advantages and disadvantages of the SPR technique are summarised below.

Advantages of the SPR technique:

1. No pre-drilled hole is required [10] and thus each SPR joint can be manufactured in one operation. This effectively simplifies the assembly procedures compared with conventional mechanical fastening approaches, such as bolting [11] and traditional riveting [12].
2. Suitable for joining structures made of similar or dissimilar materials [13], such as high strength steels, aluminium alloys and composites.
3. Not sensitive to surface conditions of the connected structures and therefore suitable for coated and painted parts [14].
4. Environmentally friendly: low energy requirement, no fume and low-noise emission.
5. No heating is required, and thus can eliminate the possible thermal deformation of connected structures.
6. Higher fatigue strength than the RSW joint [15].
7. Easy to be integrated into the automatic production line.

Disadvantages of the SPR technique:

1. Two-sided accessibility of the connected structures is required.
2. Large riveting force is required.
3. Inflexibility of changing the die during the SPR operation
4. Poor performance for brittle materials [16].

The mechanical performance of SPR joints, such as tensile strengths [9], fatigue life [6] and corrosion resistance [17], is highly important for the performance of connected structures. Therefore, the main objective of SPR joint design is to ensure the joint strengths. As a mechanical connection, the performance of a SPR joint is directly linked with the joint cross-sectional profile as shown in **Figure 1.2**. Three quality indicators are usually measured from the joint cross-sectional profile to assess the SPR joint quality, including the interlock (I), the minimum remaining bottom sheet thickness ($T_{\min}$) and the rivet head height (H) [18]. The SPR joint quality is significantly affected by the joint configuration, including the rivet material, rivet profile, die profile, die-to-rivet volume ratio, sheet material, sheet thickness and sheet sequence [19]. In addition, the setting parameters of the SPR system, such as the riveting speed, the clamping force and the C-frame stiffness will also influence the final joint quality. Therefore, to achieve a high quality SPR joint and to improve the joint strengths, it is necessary to have comprehensive understanding of the above-mentioned factors' impact on the joining process as well as the final joint quality.

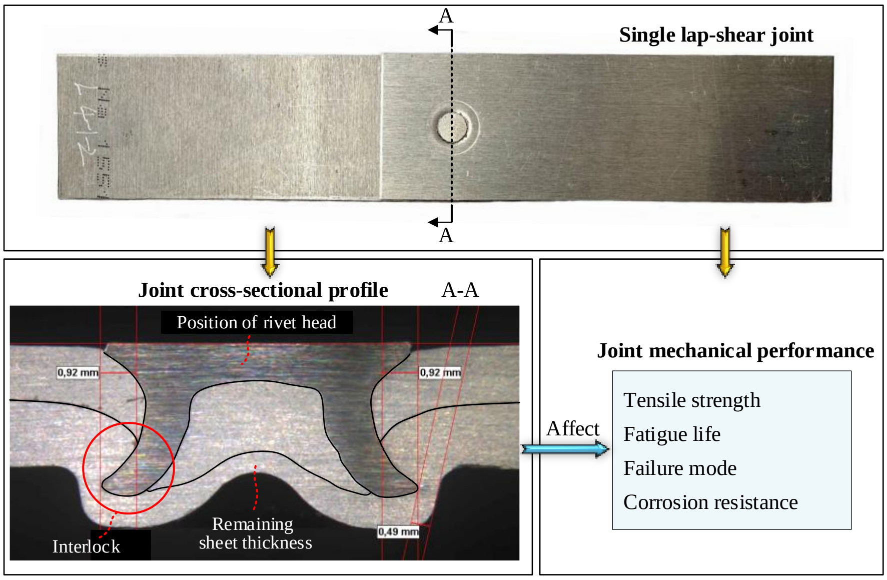
A
Single lap-shear joint
A
Joint cross-sectional profile
A-A
Position of rivet head
0,92 mm
0,92 mm
Interlock
Remaining
sheet thickness
0,49 mm
Affect
Joint mechanical performance
Tensile strength
Fatigue life
Failure mode
Corrosion resistance

Figure 1.2: Relationships between the joint cross-sectional profile and the joint mechanical performance

1.1.2. Riv(et)-Bonding technique

In order to enhance the strengths and to improve the noise, vibration and harshness (NVH) performance of the self-piercing riveted structures, a thin adhesive layer is normally involved at the interface between connected sheets. This hybrid joining technique is called Riv(et)-Bonding, and has also been widely used in the automotive industry. **Figure 1.3** shows the major steps during a Riv-bonding process: (1) Applying the uncured adhesive; (2) Clamping; (3) Riveting; (4) Tools releasing and (5) Adhesive curing. Compared with the SPR process, the main differences are the added thin adhesive layer before the riveting process and the adhesive curing operation after the riveting process.

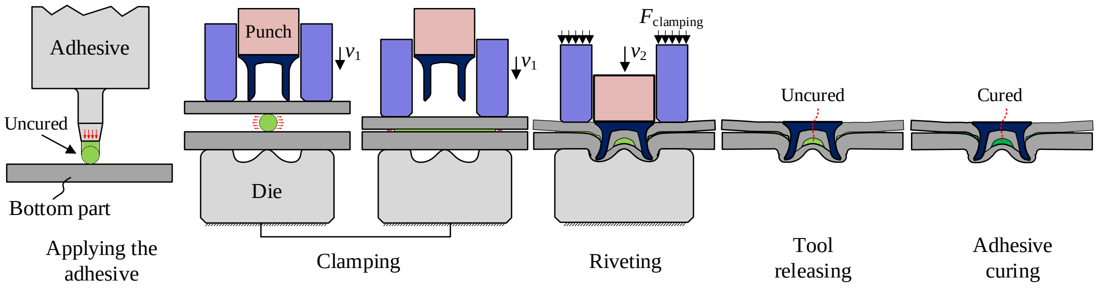
Adhesive
Uncured
Bottom part
Applying the
adhesive
Punch
v_1
Die
v_1
Clamping
F_{clamping}
v_2
Riveting
Uncured
Tool
releasing
Cured
Adhesive
curing

Figure 1.3: Schematic of the major steps in a Riv-bonding process

The SPR system designed for SPR joints still works well for Riv-Bonding joints. The Riv-bonding technique can effectively overcome the individual drawbacks of the SPR joint and the adhesive bonded joint. For example, the adhesive layer in the Riv-Bonding joint can effectively reduce the stress concentration around the riveted region, and avoid the galvanic corrosion caused by direct contacts between dissimilar metals [6]. The riveted connection in the Riv-Bonding joint is less sensitive to the service environments, and thus can effectively overcome the mechanical strength decay of the adhesive bonded connection when exposing in the environments with a high moisture, a high temperature or corrosive agents [20].

The mechanical performance of Riv-Bonding joints is determined together by the riveted connection and the adhesive bonded connection. The above-mentioned factors that affect the SPR joint quality (e.g., rivet material, sheet sequence and die profile) will also influence the final Riv-Bonding joint quality. In addition, the joint parameters that affect the adhesive bonded joint quality, such as the adhesive type, adhesive thickness and structure surface conditions, will also influence the performance of Riv-Bonding joints. Different from the adhesive bonded joints, the adhesive usually distributes non-uniformly between the connected sheets in the Riv-Bonding joints. This is because the adhesive around the riveting zone will be squeezed outward due to the high riveting force during the forming process of the riveted connection. As a result, the riveting process will unavoidably influence the mechanical performance of the adhesive bonded connection. In turn, the adhesive layer will also impose effects on the riveting process, especially when a large amount of adhesive is trapped around the riveting zone. The trapped adhesive will directly alter the deformation behaviours of rivet and sheets, and therefore affect the quality of riveted connection. Therefore, to achieve a high quality Riv-Bonding joint, it is very important to have clear understanding of the events happened during the joining process and how different joint parameters affect this joining process.

1.2. Research Gaps

During the last few decades, a considerable number of studies have been conducted by researchers to extend application ranges and to deepen understanding of the SPR and Riv-Bonding techniques. However, due to the complex joining parameters affecting the final joining results, the two fastening techniques still have many unsolved theoretical and practical problems. More efforts are required to extend the applications of the two joining techniques. Some existing research gaps are summarised below:

(1) Research gap 01:

As mentioned above, the SPR joint quality is usually assessed by measuring the three quality indicators from the joint cross-sectional profile. It is widely acknowledged that the joint cutting position has a critical influence on the captured joint cross-sectional profile and on the three quality indicators. However, there is still not clear understanding of how much influence the improper joint cutting position may bring to the captured joint cross-sectional profile and to the magnitudes of three quality indicators.

(2) Research gap 02:

The die profile has critical influences on the joint formation and the final joint quality. However, due to the intrinsic property of the SPR joint, it is difficult to directly observe the joint formation during the SPR process. Until now, there is still not clear understanding of how the different die geometrical parameters (e.g., die diameter and die depth) affect the rivet and sheets deformation behaviours. This is not only meaningful for the selection of rivet/die during new joint design, but also benefit for the development of new type dies.

(3) Research gap 03:

The Riv-Bonding technique has been widely used in the industry field. However, because of the difficulties to model the fluid-structure interaction (FSI) between the solid parts and the uncured adhesive, there is still not a simulation model of Riv-Bonding process suitable for industry applications in the public domain. This significantly affects the development of Riv-Bonding technique, and limits the development of simulation models for strength prediction of Riv-Bonding joints.

(4) Research gap 04:

Compared with the SPR joints, the better mechanical performance of the Riv-Bonding joints has been widely reported. However, the impact of the adhesive layer on the events happened during the riveting process is rarely studied. The flow behaviour of the uncured adhesive during the riveting processes with different die types is still not clear. The influence of the adhesive layer on the quality of riveted connection has not been comprehensively studied.

1.3. Outline of the Thesis

Experimental and numerical studies were conducted in this thesis to fill up the above-mentioned research gaps. The whole thesis is divided into eight chapters, and the contents of each chapter are summarised below:

(1) Chapter 1 briefly introduces the SPR and Riv-Bonding techniques, and summarises the existing challenges as well as the main objectives of this thesis.

(2) Chapter 2 systematically reviews the literatures relevant to the SPR, adhesive bonding and Riv-bonding techniques.

(3) Chapter 3 investigates the influences of improper cutting position on the measurement accuracy of the joint quality indicators (i.e., H, I and $T_{\min}$). The improper cutting position induced distortion of the joint cross-sectional profile was qualitatively compared and

discussed. A mathematic model was developed to estimate the interlock errors under different improper cutting conditions. The impact of the cutting position on the remaining bottom sheet thickness was also analysed and discussed in detail. A correction approach was proposed to compensate the interlock error caused by the improper cutting position. Two graphical user interfaces (GUI) for the interlock error estimation and correction were also developed to facilitate the practical applications.

(4) Chapter 4 describes the development procedures of the FE model for the SPR process. The determinations of critical model input information were discussed in detail, including the rivet and sheet material properties, the mesh size, the material damage model and the friction coefficients. The FE model developed in this chapter lays a foundation for the FE model development of the Riv-bonding process.

(5) Chapter 5 numerically explores the influences of critical die geometric parameters, including the die type, die diameter (D_1), die depth (H_1) and die pip height, on the SPR process using the developed FE model of SPR process in Chapter 4. The variation trends of the flared rivet shank radius (R_1) and the remaining bottom sheet thickness at the joint centre (t_c) during the SPR process were numerically monitored. The relationships between the material deformations and the SPR joint quality were also discussed. Compared with the experimental SPR test, the FE model of SPR process demonstrated huge advantages in efficiency to extend the understanding of the SPR technique.

(6) Based on the developed FE model of SPR process in Chapter 4, a 2D axisymmetric FE model of Riv-Bonding process was successfully developed in Chapter 6 to meet the strong demands from the automotive industry. The Ostwald-de Waele power law was adopted to approximately represent the properties of the adhesive SikaPower 498. Interrupted laboratory tests of the Riv-Bonding process, and experimental tests of Riv-Bonding joints with varying configurations were carried out to validate the prediction accuracy of the FE model. The work conducted in this chapter lays a foundation for further quality prediction and mechanical strengths modelling of Riv-Bonding joints.

(7) Using the interrupted experimental tests, Chapter 7 explores the impact of adhesive layer on the riveting process, including the deformation behaviours of the rivet and sheets, variation trend of the riveting force and distribution of the adhesive. The potential defects and benefits induced by the adhesive layer on the riveted connection with different dies were also identified and analysed. Single factor experiments were also carried out to investigate the influences of top sheet thickness (T_t) on the final quality of the riveted connection and on the adhesive distribution.

(8) Chapter 8 summarises the major conclusions from this thesis, and discusses the potential research topics that might be benefit for further developments of the SPR and Riv-Bonding techniques.

2. Literature Review

A comprehensive literature review was conducted in this chapter to better understand the up-to-date research status of the self-piercing riveting (SPR), the adhesive bonding and the Riv(et)-Bonding techniques. The research hotspots and strategies of each fastening approach were reviewed from the aspects of finite element (FE) simulation and experimental test.

2.1. Self-Piercing Riveting Technique

The SPR technique was initially proposed in the 1960s but did not attract enough attentions during the following three decades. Due to the strong demands from the automotive industry to find out a suitable joining approach for aluminium alloys and mixed-material structures, it achieved a rapid growth and development since 1990s [19]. After 30 years development, the SPR has become one of the major joining approaches in the automotive industry. A considerable number of studies have been carried out to explore and to extend the application ranges of the SPR technique [19, 21–23]. **Figure 2.1** shows the changing trend of annual publications about the SPR during the past 25 years. It can be seen that increasing attentions are being paid on this topic.

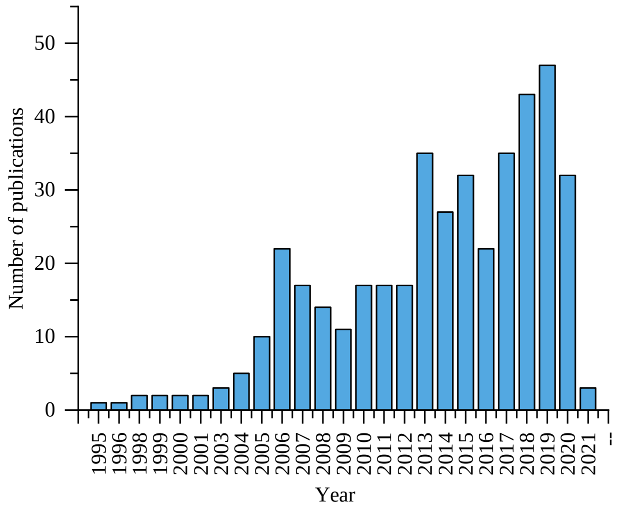

Figure 2.1: Annual publications during the last three decades on the SPR (Data from Web of Science)

The major objectives of SPR joint design are to improve the SPR joint quality and to enhance the corresponding joint mechanical performance. **Figure 2.2** summaries the research hotspots relevant to the SPR technique, including the setting parameters of SPR system, the sheet configurations, the rivet parameters and the die profiles. Impact of the SPR system on the joint quality has been widely studied from the aspects of driving system, joining speed, clamping force, C-frame structure and other assistant technologies. The sheet configuration is the basis of a SPR joint, and its critical factors include the sheet material, sheet thickness, sheet thickness ratio, number of layers and sheet sequence. These parameters will significantly affect the joint quality and thus the final joint mechanical performance. For a specific sheet combination, improvement of joint quality is mainly achieved by optimizing the parameters of rivet and die. The most important rivet parameters are the rivet material, rivet hardness, rivet type, rivet shank diameter, rivet length and rivet surface coating. The most important die parameters include the die type, die diameter, die depth and other geometric parameters. In addition, the die-to-rivet volume ratio is also very critical for the final joint quality [24–26]. The experimental SPR test, finite element (FE) modelling and mathematic modelling are the three most frequently used research approaches for the SPR technique.

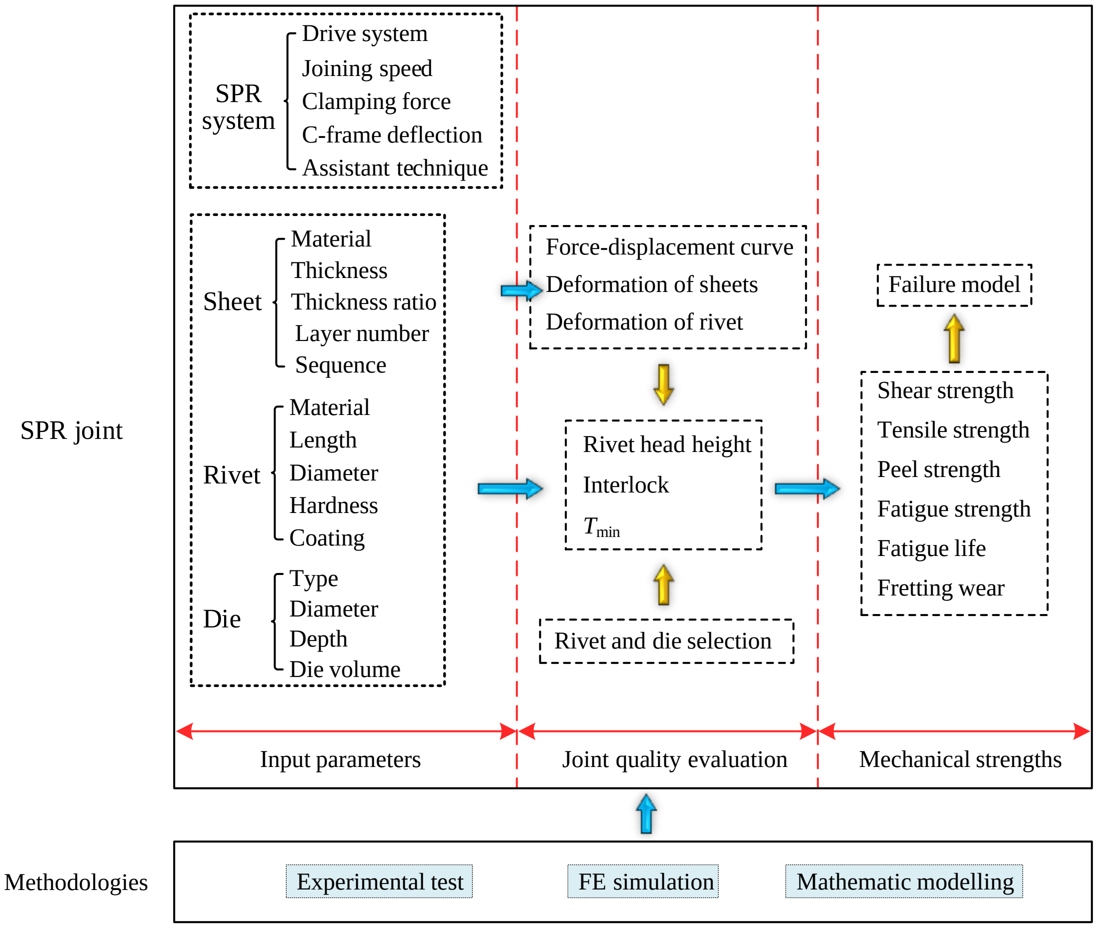
SPR system
Drive system
Joining speed
Clamping force
C-frame deflection
Assistant technique
Sheet
Material
Thickness
Thickness ratio
Layer number
Sequence
Rivet
Material
Length
Diameter
Hardness
Coating
Die
Type
Diameter
Depth
Die volume
Force-displacement curve
Deformation of sheets
Deformation of rivet
Rivet head height
Interlock
T_{min}
Rivet and die selection
Failure model
Shear strength
Tensile strength
Peel strength
Fatigue strength
Fatigue life
Fretting wear
SPR joint
Input parameters
Joint quality evaluation
Mechanical strengths
Methodologies
Experimental test
FE simulation
Mathematic modelling

Figure 2.2: Research structure and hotspots of the SPR technique

2.1.1. Self-piercing riveting system

The SPR system plays a very important role in the joining results. The Böllhoff, Henrob and Tucker are the three largest SPR system suppliers in the industrial sector. Their SPR systems are also widely applied in the academic sector. Different driving units and control strategies are adopted in these SPR systems.

Böllhoff GmbH develops the SPR riveting system driven by a hydraulic system, and the joining process is controlled by the hydraulic pressure and the rivet displacement. The riveting process will be terminated once the pre-set pressure or the specified distance of rivet penetration is reached [27]. Henrob Ltd develops the servo-driven SPR system. During the joining process, the punch is first speeded up to a specified speed and then drives the rivet into the sheets by its inertia. Different initial speeds of the punch are usually selected for different joint configurations to achieve a flush rivet head and to ensure a desired joint quality [24, 28]. The rivet coatings [29] and sheet coatings [30] will affect the optimal setting parameters of the above two types of SPR systems. Tucker GmbH also develops the servo-driven SPR system, but the joining process is controlled by the rivet displacement. The punch moves downward at a constant speed and presses the rivet into the sheets. The joining process is terminated when the pre-set rivet head height is reached. Different from the Henrob and the Böllhoff SPR systems, it is no need to frequently adjust the system setting parameters to achieve a uniform rivet head height in every SPR joint.

In addition to the abovementioned three types of SPR systems, some other new SPR systems have also been developed by researchers from academia. An electromagnetic self-piercing riveting (E-SPR) system was developed by Liang et al. [31], in which the punch is accelerated by the electromagnetic force and then drives the rivet into the sheets. The changing trend of the punch speed is very similar to that in the Henrob SPR system: the punch speed first increases to the maximum value and then decreases to zero. The maximum punch velocity of this E-SPR system reached up to 7.2m/s, and thus this SPR system has the ability to achieve high speed riveting. However, to get a sound SPR joint, the discharge energy of the riveting system should be optimized for each joint configuration. A gunpowder driving SPR system was proposed by Wang et al. [15], and the maximum punch speed could reach up to 54 m/s. This system is especially designed for repairing failed SPR joints. Electroplastic self-piercing riveting (EP-SPR) was proposed by Lou et al. [32], in which a direct current was applied on the sheet to improve its plasticity (Electroplastic effect). It was found that the EP-SPR method could effectively increase the plasticity of the metal sheet and lead to a higher SPR joint quality. Meanwhile, the riveting force was relatively lower than the SPR process. A thermally assisted self-piercing riveting (TA-SPR) process was proposed by Deng et al. [33], and successfully utilized to connect the 2.0mm AA6061-T6 top sheet and 1.2mm DP980 bottom sheet by improving the ductility of the DP980 using the induction heating method. Similarly, a laser assisted self-piercing riveting approach was developed by Durandet et al. [34] to connect low ductility materials without cracking of the bottom sheet.

The influences of riveting speed on the joint quality have been investigated in some studies. For example, the quality of SPR joints made with high and low riveting speeds was examined by Liang et al. [31]. The high riveting speed (7.2m/s) was achieved using an electromagnetic self-piercing riveting (E-SPR) system, while the lower riveting speed (2.0mm/s) was achieved using a universal testing machine. The results indicated that a higher riveting speed could contribute to a greater interlock and therefore a higher maximum shear strength. Wang et al. [15] further improved the riveting speed to around 54m/s using an impact SPR system driven by the gunpowder. A conventional hydraulic press-based SPR system was also utilized to manufacture SPR joints under a lower speed. It was found that a higher riveting speed could reduce the plastic deformations of the top sheet and rivet shank, and improve the joint tensile-shear strength. In contrast, a study carried out by Hahn et al. [35] reported that the riveting speed showed very limited influences on the final SPR joint quality. Experiment results from Li et al. [36] revealed that the riveting speed had significant effects on the SPR joint quality when the Henrob SPR system was employed. This is mainly attributed to the special driving unit used in the SPR system, which first accelerates the punch to predefine speed and then strokes on the rivet to form the SPR joint.

Due to the large riveting force during the SPR process, the C-frame of the SPR system will be deflected. The deflection of different structure C-frames under high loading forces was numerically analysed by Markowski et al. [37], and the strategies to reduce the C-frame mass without compromising the structure rigidity were also discussed. A approach was proposed by Haque et al. [38] to deduce the C-frame displacement from the recorded force-displacement curve to get the true force-displacement curve. By adding a high stiffness spring underneath the die, Hönsch et al. [39] considered the C-frame deflection in the developed 2D simulation model of SPR process.

2.1.2. Evaluation of joint quality

The quality standard of SPR joint is usually designed according to the application requirements and may vary at different industrial sectors. As shown in **Figure 2.3**, three most important characteristic values measured on the joint cross-sectional profile are usually employed to preliminarily evaluate the SPR joint quality: (1) the interlock (I), which is the horizontal distance that the rivet shank flares into the bottom sheet and directly determines the joint mechanical performance. Too small interlock might lead to failures of the rivet shank pull-out from the bottom sheet [40]; (2) the minimum remaining bottom sheet thickness (T_{min}), which is the minimum thickness on the deformed bottom sheet. It can appear at any position of the deformed bottom sheet, and its magnitude directly affects the joint corrosion performance (e.g. resistance to liquids and gases) [22]. Fatigue failure may occur on the bottom sheet if the T_{min} is too small [41]; (3) the rivet head height (H), which is the vertical distance between the upper surfaces of the top sheet and the rivet, and directly influences the surface flatness of the connected structures. According to the study of [36], the *H* also determines the final position of the rivet inserted into the sheets and therefore will affect the final magnitudes of the *I* and $T_{\min}$. The assessment criteria for the three indicators varies from company to company. For example, according to the quality standard of a world-leading car manufacturer [19], the *H* should be between 0.3mm and −0.5mm. The *I* should be greater than 0.4mm for SPR joints with an aluminium alloy bottom sheet and greater than 0.2mm with a steel bottom sheet. The $T_{\min}$ should be always greater than 0.2mm and fracture of the bottom sheet should be avoided [36].

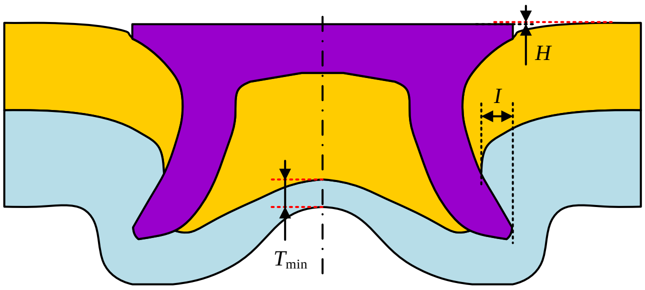

Figure 2.3: Schematic of the three quality indicators measured on the joint cross-sectional profile

In addition to satisfying the joint quality standard, a high quality SPR joint should also avoid any other type of defect. **Figure 2.4** shows the potential defects that might be formed during the SPR process, including: (1) fracture of the rivet shank in **Figure 2.4**(a); (2) large gap between the rivet and the top sheet in **Figure 2.4**(b); (3) large gap between the sheets in **Figure 2.4**(c) and (4) fracture of the bottom sheet in **Figure 2.4**(d). These defects will impose significant influences on the joint mechanical performance, and thus should be eliminated during new joint design, for example by selecting suitable rivet and die combinations.

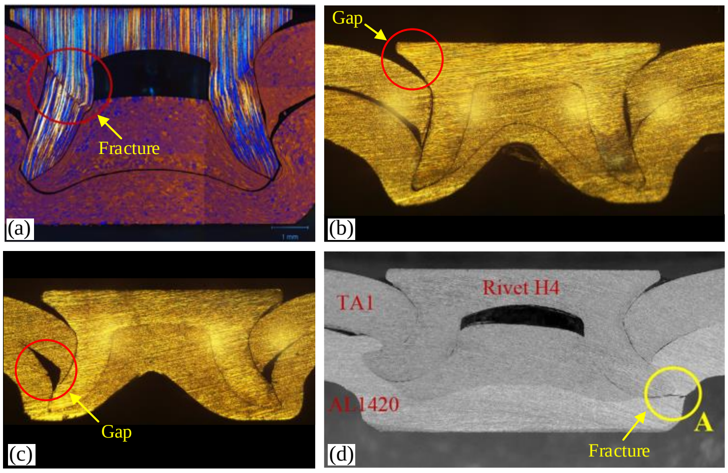

Figure 2.4: Possible defects formed in a SPR joint: (a) fracture of the rivet shank [42], (b) gap between the rivet and top sheet, (c) gap between sheets and (d) fracture of the bottom sheet [41],

In practical applications, the force-displacement curve is still the most effective indicator to monitor the joining process and the final joint quality [43]. Changes of the joint quality or incorrect usage of rivets (e.g., rivet length or hardness level) can be easily detected from this curve. With interrupted experimental tests, the force-displacement curve of the SPR process with carbon steel sheets and steel rivets was systematically studied by Haque et al. [38]. **Figure 2.5** shows the characteristic curves for joints with carbon steel sheets. It was proved that that the critical events (e.g., the sheet bending, piercing of the top sheet, blanking of the top sheet, die filling and rivet flaring) are directly linked with the force-displacement curve and can be recognized from the variation trends of the riveting force.

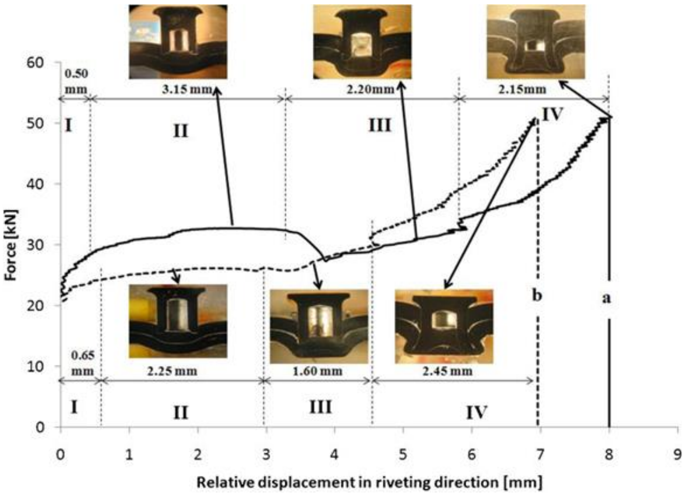

Figure 2.5: Characteristic curves for SPR joints of carbon steel sheets with rivets of 555 HV hardness [38]

2.1.3. Sheets, rivet and die

Sheets:

As a mechanical fastening approach, the SPR technique can be used to join sheets made of similar or dissimilar materials. It is very suitable for ductile materials and can also be extended to join low ductile materials with the help of other assistant technologies, such as the induction heating method [33] and the laser heating method [34]. A huge number of studies have been conducted to investigate the suitability of the SPR technique on different types of sheet materials. For instance, the joinability of the magnesium alloy and aluminium alloy sheets was explored by Luo et al. [16], including the combinations between AA6063-T6 and AM50, and between AA5754-0 and AZ31B-0. The joinability of high tensile strength steel and aluminium alloy AA5052-H34 with conventional rivet and die was experimentally and numerically studied by Abe et al. [44]. The quality of SPR joints with dissimilar sheet materials (i.e., PA6-matrix thermoplastic composite, PA6 with reinforcing fibres (glass fibre and carbon fibre), AA5754 aluminium alloy) was investigated by Zhang et al. [45]. To date, it has be proved that the SPR technique has a very wide application range, including aluminium alloys [18], magnesium alloys [46], fiberglass composites [47], high strength steels [44], titanium [48] and copper alloys [49].

In addition to two-layer stacks, the SPR can also be utilized to connect stacks with three or more layers. So far, SPR joints with three layers have been widely used in the automotive industry. However, most of the existing studies focused on two-layer joints and only a few studies paid attention to the three-layer joints. Kato et al. [50] numerically investigated the joinability of SPR joints with three aluminium alloy sheets. Abe et al. [51] experimentally and numerically studied the joinability of SPR joints with three high strength steel and aluminium alloy sheets. By redesigning the shapes of rivet and die, the quality of three-layer joints with the 5000 series aluminium alloy top sheet and ultra-high strength steel middle and bottom sheets successfully optimized by Abe et al. [52]. The influences of joint configuration on the mechanical strengths and failure mode of three-layer SPR joints were experimentally studied by Han et al. [53]. Therefore, more efforts are still required to gain clear understanding of the formation mechanism of three-layer joints, and the differences between the two-layer and three-layer SPR joints.

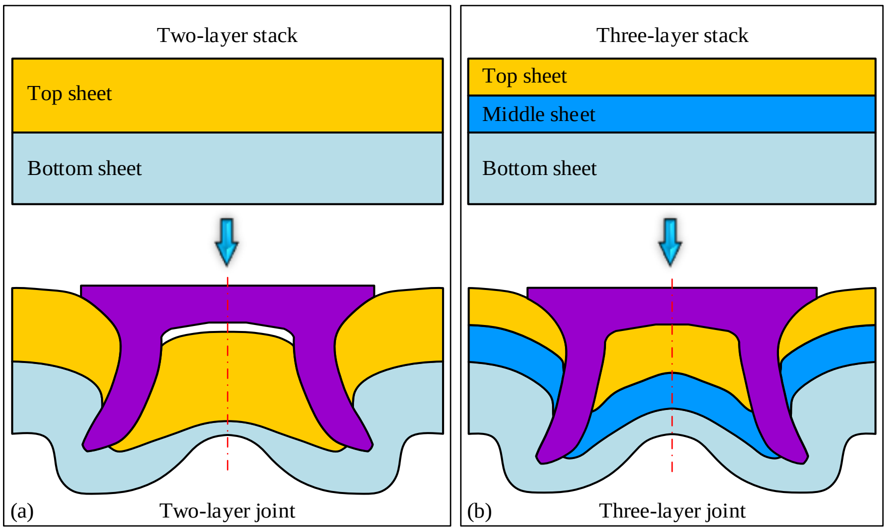

Figure 2.6: Schematic of the (a) two-layer and (b) three-layer SPR joints

As shown in **Figure 2.7**(a), the thickness ratio between the top sheet and bottom sheet (i.e., T_t/T_b) is also a very important factor for the final joint quality. The effects of sheet thickness ratio on the SPR joint quality with a 2D FE model were numerically investigated by Mucha [54]. The results revealed that the interlock (I) decreased with the increment of the sheet thickness ratio, while the remaining bottom sheet thickness under the rivet shank tip (t_{tip}) showed an increasing trend. The significant influence of the sheet thickness ratio on the SPR joint failure model was reported in the study of Yuan et al. [55]. The rivet tail was pulled out from the bottom sheet if the bottom sheet was thinner than the top sheet, while the rivet head was pulled out from the top sheet if the bottom sheet was apparently thicker than the top sheet. In general, stacks with a small thickness ratio are much easier to be connected with the SPR technique than stacks with a large thickness ratio. This is because the contact area between the rivet shank and the top sheet increases with the increment of the top sheet thickness, which will prevent the deformation of the rivet shank along the radial direction and leave a shorter rivet length to form a sufficient mechanical interlock in the bottom sheet. The thin bottom sheet usually has a relatively low stiffness [56] and is more likely to be pressed backward rather than pierced by the rivet shank. In addition, there is not enough space for the rivet shank to form a sufficient interlock without penetrating the thin bottom sheet.

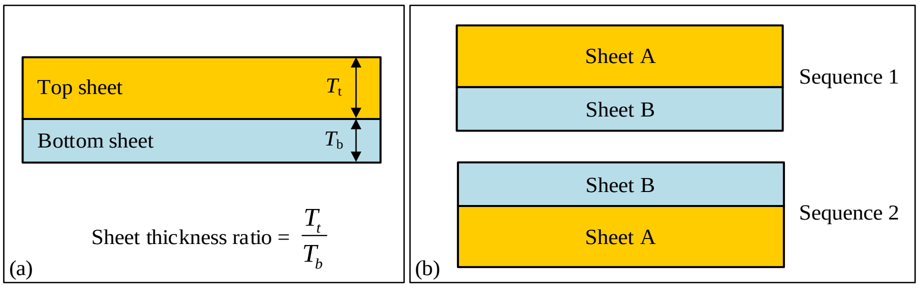

Figure 2.7: Schematic of the (a) sheet thickness ratio and (b) sheet sequence

The sheet sequence also has critical influences on the SPR joint quality, as shown in **Figure 2.7**(b). It will not only change the sheet thickness ratio but also alter the bottom sheet material if dissimilar sheet materials are employed. In general, to achieve a higher joint quality, it is recommended to place the thinner sheet on the punch side (i.e., top sheet) and the thicker one on the die side (i.e., bottom sheet). For sheets with different materials, there is still not a uniform conclusion about the sheet sequence. Some researchers believe that the sheet with a higher strength should be used as the top sheet, while the sheet made of a greater ductility material should be used as the bottom sheet [57]. This is because the bottom sheet usually undergoes a larger deformation than that of the top sheet during the SPR process. The ductile material on the die-side is much easier to be deformed to form a sufficient mechanical interlock, and is more likely to prevent the appearance of bottom sheet cracks [16]. However, the rivet shank might be severely compressed when piercing through the high strength top sheet due to the large riveting force, or even cannot pierce through the top sheet. In contrast, some researchers think that the sheet with a higher strength should be placed on the die side, while the sheet with a more ductile material should be placed on the punch side. The effect of sheet sequence on the quality of SPR joints with vibration-damping steel and Al5052-H32 sheets was studied by Kam et al. [40]. The results indicated that larger interlock and $T_{\min}$ were achieved when the vibration-damping steel was employed as the bottom sheet. However, the problem is that the harder bottom sheet is more difficult to be deformed and thus may impose negative influences on the formation of interlock.

Rivet:

During the SPR process, the rivet firstly pierces through the top sheet and then flares into the bottom sheet to mechanically connect the sheets together. The rivet material, rivet geometry and rivet surface condition are the three research hotspots. Steel rivets at different hardness levels demonstrate very good performances, and have been widely employed to connect stacks made of aluminium alloys, high strength steels and other types of materials. Aluminium alloy rivets usually undergo severe deformation during the SPR process, and thus have limited applications in practice [27]. However, the steel rivet will increase the difficulty and costs for recycling of aluminium alloy structures. Therefore, some researchers made efforts to improve the performance of aluminium alloy rivets for aluminium alloy structures. For example, to reduce the severe compression of aluminium alloy rivets, Abe et al. [58] numerically optimised the shapes of die and aluminium alloy rivet with the developed FE model. The experimental results revealed that the aluminium alloy rivet can be used to connect aluminium alloy stacks, but the joining range was very narrow. The possibility of joining aluminium alloy 6060 sheets with rivets made of three different aluminium alloys, including the 6082-T6, 7108-T5 and 7287-T6, was investigated by Hoang et al. [27]. The results indicated that it was possible to join aluminium alloy sheets if a proper aluminium alloy for the rivet was chosen. Meanwhile, it was also found that the rivet material had no influence on the initial stiffness of the SPR joint when the tensile displacement was small, but a crucial effect on the maximum force and maximum displacement of the tested joints. The fracture mechanism of AA7278-T6 rivets during the SPR process was also experimentally and numerically studied by the same authors [42]. The tensile strength, grain structure and the particle distribution along three directions (0°, 45°, 90°) with respect to the extrusion direction were comprehensively investigated. In addition to the rivet materials, surface decarburization technique was also employed by Van Hall et al. [59] to improve the rivet performance. The experiment results revealed that the intentional surface decarburization of the rivet can prevent the formation of fractures along the rivet leg periphery, while maintain sufficient column strength to pierce through the sheet without rivet shank buckling.

The rivet geometry has significant influences on the SPR joint quality, and also attracts a lot of attentions from the industry and academia. For example, Jiang et al. [60] investigated the effects of rivet geometry on the quality and mechanical properties of the electromagnetic self-piercing riveting (E-SPR) with CFRP/Al and steel/Al stacks. Nine rivets with different blade angle, inner diameter and leg length were employed. Ma et al. [16] studied the influences of rivet length on the joint quality, and found that the interlock increased but the remaining bottom sheet thickness decreased with the rivet length changing from 5.0mm to 6.0mm. Karathanasopoulos et al. [61] numerically explored the influences of inner radius of rivet leg on the SPR joint quality. The rivet geometry was numerically optimized by Uhe et al. [62] to successfully connect the sheets with two different material combinations initially requiring two rivet geometries. The influences of rivet tip geometry on the SPR joint quality and mechanical strengths were experimentally studied by Li et al. [63]. The results indicated that the rivets with a sharper tip could lead to a greater interlock and a higher lap-shear strength. Fu and Mallick [64] investigated the influences of rivet diameter, rivet length and rivet hardness on the static and fatigue performances of AA5754 SPR joints.

In addition to the rivet geometry, the rivet surface condition will also affect the SPR joint quality. Because it can directly influence the friction forces between the rivet and sheets, and therefore changes the deformation behaviour of rivet. The frequently used surface modification methods include coatings [30], impression [65], polishing, grit blasting [66] and lubricants [67]. Some efforts have been made to understand the influences of rivet surface conditions on the joining process and the final joint quality. For example, Karim et al. [29] compared the influences of the mechanically plated Zn-Sn-Al (Almac®) and the electroplated Zn–Ni rivet coatings on the SPR joint quality indicators and mechanical strengths. The experiment results indicated that the Zn-Ni rivet coating contributed to a greater interlock compared to the Almac® rivet coating. With a 2D model of SPR process in MSC Marc, Mucha [54] found that the friction coefficient between the rivet and sheets (0.05~0.25) had limited effects on the maximum riveting force, but imposed apparent influences on the deformation behaviours of the rivet shank and top sheet. Similarly, it was reported by Hoang et al. [42] that the friction coefficient between the rivet and sheets had less effects on the force-displacement curve, but significantly influenced the plastic strain localisation on the rivet shank.

Die:

The major function of die is to properly guide the deformation behaviours of rivet and sheets to form a desired SPR joint. Any change of the die geometry will inevitably alter the joining results. Dies with different geometries have been reported in the existing studies, and can be roughly classified into the flat die and the pip die, as shown in **Figure 2.8**(a)(b). The main difference between the two types of dies is whether there is a die pip around the centre of die cavity or not. The die pip can effectively increase the rivet shank flare, and reduce the accumulation of bottom sheet material around the central area. **Figure 2.8**(c)(d) show the cross-sectional profiles of SPR joints made with flat dies and pip dies respectively. The die depth, die diameter and die pip height are the three most important die parameters. A considerable number of studies have been performed to uncover the die parameters' influences on the joining results, and to improve the SPR joint quality. For example, Ma et al. [24] studied the influences of the die diameter and pip height on the rivetability of the self-piercing riveted AA6061-T6 and mild steel CR4 sheets. It was found that the changes of the die diameter and pip height could affect the joint quality by altering the deformation behaviours of the sheets. The possibility to make SPR joints with a flat anvil rather than contour dies was experimentally proved by Hahn et al. [35]. This was achieved using a high punch velocity (greater than 10m/s).

The effects of five different dies on the quality of SPR joints with vibration-damping steel and Al5052-H32 sheets were studied by Kam et al. [40]. It was found that the flat die had a better performance than the pip die. With the increment of the die taper angle and the die diameter, the interlock showed a decreasing trend, but the $T_{\min}$ showed an increasing trend. Using a FE simulation model, Abe et al. [51] numerically optimized the die profile for three-layer SPR joints with high strength steel and aluminium alloys sheets, and assessed the effect of the optimized die on the joining range of three-layer joints. The experimental results showed that a die with larger depth and diameter could effectively extend the joining range of the three-layer joints.

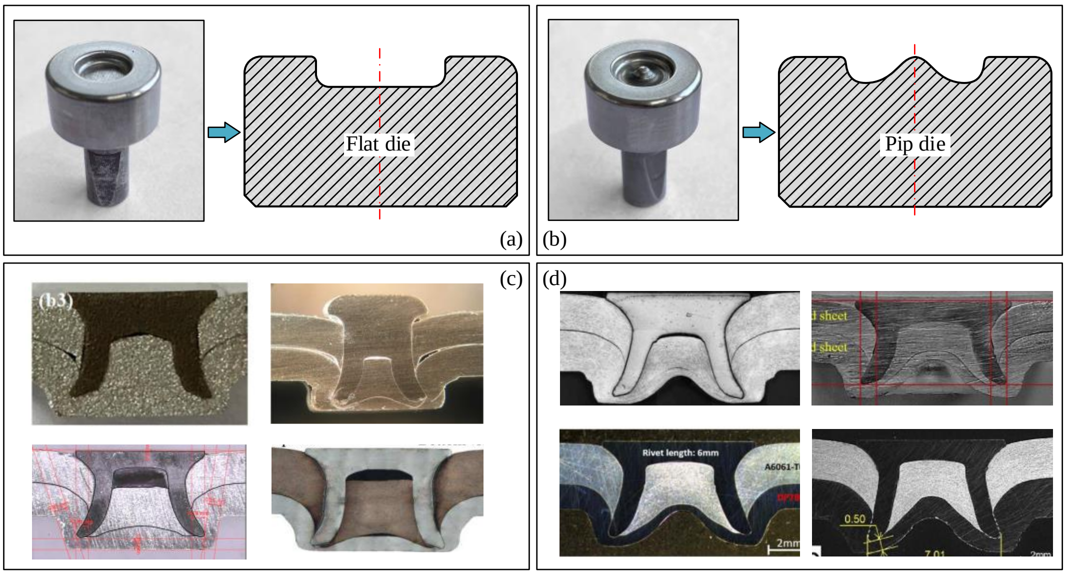

Figure 2.8: Schematic of (a) the flat die, (b) the pip die, (c) the SPR joints with flat dies [66, 68–70] and (d) the SPR joints with pip dies [24, 33, 71, 72]

Compared with the experimental test, the FE simulation approach is more convenient to be employed for the die parameter analysis. For instance, with a 2D simulation model in LS-DYNA, the die diameter and die depth were numerically optimized by Mori et al. [4] according to the sheet sequence, and successfully utilized to connect the ultra-high strength steel and aluminium alloy sheets with the SPR technique. Mori et al. [73] also numerically analysed the deformation behaviours of rivet and sheets with different die profiles, and found that the severe compression of the rivet leg when piercing the upper high strength steel sheet could be eliminated by optimizing the die diameter and depth. The effects of the die profile on the rivet shank deformation and SPR joint quality were studied by Mucha [54] using a 2D model in MSC Marc Mentat. It was found that the die profile had significant influences on the force-displacement curve and the final joint quality. Jäckel et al. [74] established a 2D axisymmetric simulation model in DEFORM V11 and then sensitivity studies were carried out to investigate the effects of die geometry on the SPR joint quality. A new die conception with a force-controlled moveable bottom was proposed by Drossel and Jäckel [75] to improve the joinability of materials with limited ductility by SPR technique. The simulation and experimental results showed that the stacks with top sheet made of EN AW-6016-T4 and bottom sheet made of AlSi9MnF could be joined successfully without cracks on the bottom sheet. The damages of the carbon fibre reinforced plastic sheet during the SPR process was studied by Landgrebe et al. [76], in which the effects of the traditional die and a new die with a moveable bottom proposed in [75] on the damage situation of the CFRP sheet were also compared.

Rivet and die selection:

In addition to individual parameters of the rivet and die, during the SPR joint design process, the rivet and die should also match with each other. The die-to-rivet volume ratio, which is the ratio between the die cavity volume and the rivet volume, is a critical factor during the selection of rivet and die for new stacks. A die-to-rivet volume ratio smaller than one means that the die cavity is smaller than the rivet volume. This may lead to large compressive forces between rivet and sheets, and result in a relatively large riveting force. A die-to-rivet volume ratio greater than one means that the die cavity is greater than the rivet volume, and there is enough space in the die cavity to accommodate the rivet and sheet materials during the SPR process. Lou et al. [77] reported that the die-to-rivet volume ratio slightly larger than 1.0 could lead to a greater interlock for Al-to-steel or steel-to-Al sheet combinations, and was also benefit for the tightness of SPR joints. The influences of the die-to-rivet volume ratio on the SPR joint were studied by Ma et al. [24]. The experiment results indicated that a fully filled die cavity can provide a greater resistance to speed up the rivet leg flare, while an incompletely filled die cavity could make the deformation of the bottom sheet easier and result in a smaller interlock. The interaction effects of rivet and die parameters on the SPR joint quality were investigated by Zhao et al. [25, 78]. The results emphasized the critical influences of the die-to-rivet volume ratio on the interlock. In practical applications, this volume ratio can be adjusted by controlling the rivet head height (H) within the range defined in the quality criterion. Under some conditions, the die-to-rivet volume ratio cannot correctly reflect the real fill condition of the die cavity if the rivet cavity is not fully filled, especially with a flat die. More efforts are still required to get clear understanding of the die-to-rivet volume ratio’s impact on the SPR process and on the joint quality.

2.1.4. Mechanical strength of SPR joint

Tensile tests under different static or dynamic loading conditions are usually conducted to evaluate the mechanical performance of a SPR joint. To date, a large number of studies have been carried out to assess the joint performance. Figure 2.9 shows the frequently used specimen shapes during the cross-tensile test [68, 79], lap-shear test [80] and coach-peel test

[81]. To assess the joint strength under different loading directions, testing fixtures shown in **Figure 2.10** were employed during the cross-tensile tests in [68, 79]. The joint mechanical strength, energy absorption [82], fretting wear [72, 83], fatigue life [28, 71] and failure mode [84, 85] are the research hotspots.

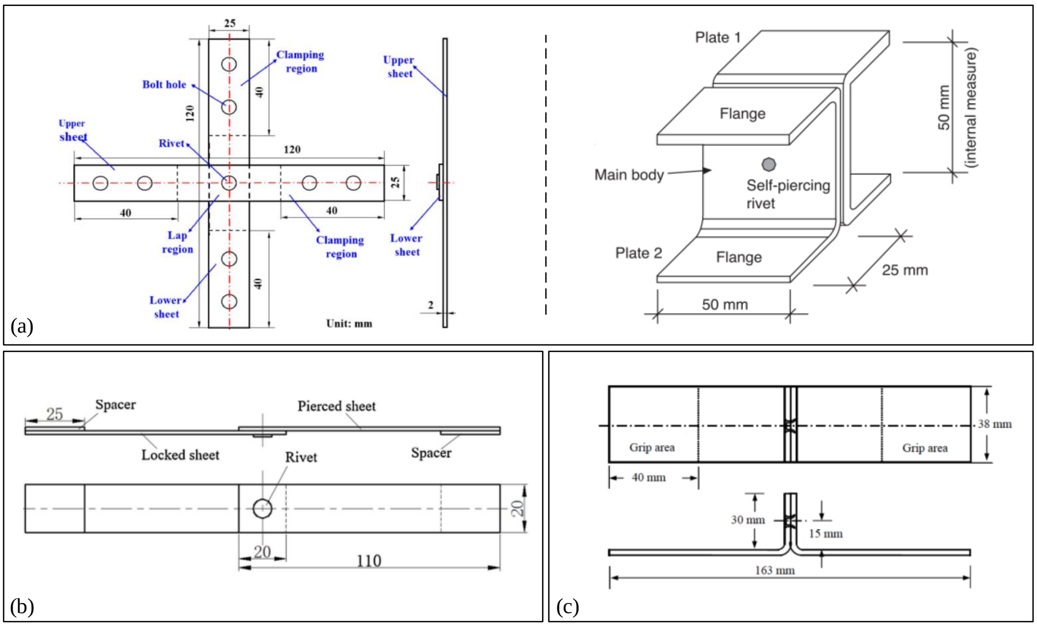
25
Clamping region
Upper sheet
Bolt hole
40
120
Upper sheet
Rivet
120
25
40
40
Lap region
Clamping region
Lower sheet
40
Lower sheet
2
Unit: mm
(a)
Plate 1
Flange
50 mm
(internal measure)
Main body
Self-piercing rivet
Plate 2
Flange
25 mm
50 mm
25
Spacer
Pierced sheet
Locked sheet
Rivet
Spacer
20
20
110
(b)
38 mm
Grip area
Grip area
40 mm
30 mm
15 mm
163 mm
(c)

Figure 2.9: Schematic of different specimen shapes used in the (a) cross-tensile test [68, 79], (b) lap-shear test [80] and (c) coach-peel test [81] to evaluate the SPR joint mechanical strengths

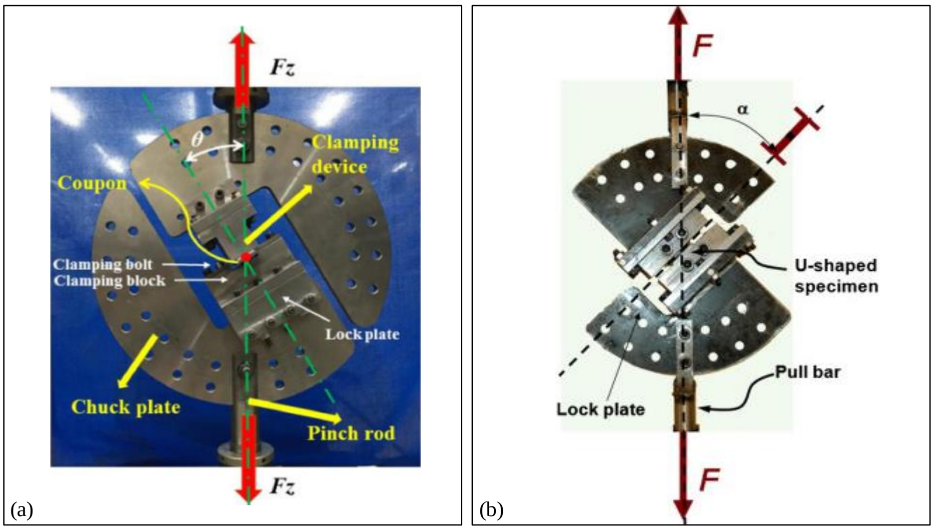
Fz
θ
Clamping device
Coupon
Clamping bolt
Clamping block
Lock plate
Chuck plate
Pinch rod
Fz
(a)
F
α
U-shaped specimen
Pull bar
Lock plate
F
(b)

Figure 2.10: Testing fixtures developed to alter the loading direction of SPR joint [68, 86]

2.2. Adhesive Bonding Technique

Adhesive bonding is a widely employed fastening approach in the modern industry field due to the potentials of reducing joint weight and manufacturing cost [87]. **Figure 2.11** shows the three steps in an adhesive bonding process: (1) Applying the adhesive; (2) Pressing the top sheet to make the adhesive uniformly distributed between the connected sheets; (3) Curing the adhesive. In practice, the adhesive thickness is usually controlled by adding glass balls with a specific diameter into the adhesive [88] or using spacers [89]. Different from the SPR technique, the adhesive bonding process is quite simple and thus the vast majority of existing studies focus on the mechanical strength evaluation of adhesive bonded joints. With a high strength adhesive, the bonded joint usually can achieve a very good mechanical performance.

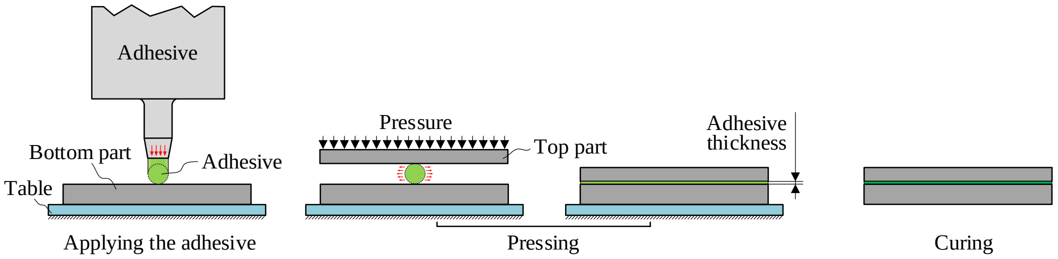

Figure 2.11: Schematic of the three steps for an adhesive bonding process

In general, there are three macro-mechanical failure types of adhesive bonded joints: (1) adhesive failure shown in **Figure 2.12**(a), in which the crack initiation and subsequent propagation occur at the interface between the adherend and the adhesive; (2) cohesive failure shown in **Figure 2.12**(b), in which the crack occurs in the middle of the bondline due to existing voids or high strength bi-material interfaces; (3) hybrid failure shown in **Figure 2.12**(c), in which cracks partially occur at the interface between the adherend and the adhesive, and partially happen in the middle of the bondline. Compared with the cohesive failure, the adhesive failure is more likely to happen because of the high stress concentration at the bi-material interface. In many failure cases, it can be found that the cracks initiate in the adhesive layer, but propagate to the bi-material interface [90]. In addition to the failure of adhesive bonded region, failure of the adherend will also happen if the strength of the adherend is obvious lower than that of the adhesive bonded zone [91], as shown in **Figure 2.12**(d)(e).

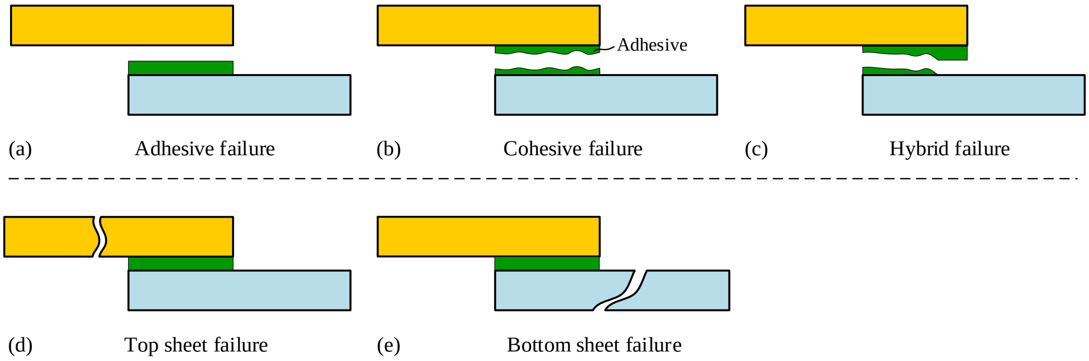

Figure 2.12: Schematic of the three failure modes of the adhesive bonded region and failures of the adherend

Many factors will affect the mechanical performance of the adhesive bonded joints, including the adhesive thickness [92, 93], adhesive type [94, 95], defects in the adhesive layer [96, 97], surface conditions of the adherends [98, 99], adhesive curing conditions [100, 101], operating temperature [102, 103], scarf angle [104, 105], overlap length [106, 107] and adherend properties [108, 109], as shown in **Figure 2.13**. So far, a huge number of experimental studies have been conducted to investigate the influences of above-mentioned factors on the joint tensile strengths under different loading conditions [110, 111], the fatigue strength [112, 113], the failure mode and corrosion resistance [114, 115]. In addition to the experimental method, the finite element modelling approach has also been widely employed by researchers. A considerable number of FE models have been developed to predict the mechanical performance of the adhesive bonded joints. ABAQUS [90, 116–118], ANSYS [118–122], LS-DYNA [123] and MSC Marc [124] are the most popular commercial FE software used in this research area. During the simulation of adhesive bonded joints, the biggest challenge is how to model the behaviours of the adhesive bonded zone. Until now, there are four major approaches frequently used for the modelling of the adhesive bonded connection.

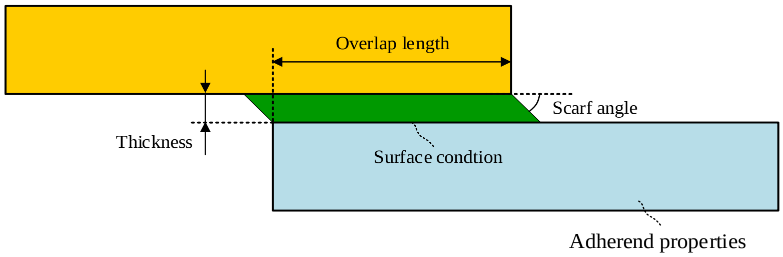

Figure 2.13: Factors affecting the mechanical performance of the adhesive bonded joint

Figure 2.14(a) schematically shows the first approach: the adhesive layer is modelled with continuum elements, and the adjacent elements at the interface between the adhesive layer and the adherends share same nodes (i.e., assuming the perfect bonding condition). To simulate the failure behaviour and evaluate the mechanical strengths of adhesive bonded joints, material failure criteria should be selected carefully according to the adhesive type. For brittle adhesives, maximum principal stress criterion, yield criterion, and maximum shear stress criterion can be used to numerically analyse the failure process. For ductile adhesives, maximum principal strain criterion, maximum shear strain and strain energy can be used [125]. This simulation method is capable of investigating the deformation behaviour of the adhesive layer, the effects of the adhesive thickness and the stress distribution around the bonded zone. However, it neglects the effect of the bi-material interface in terms of its stiffness and strength, and cannot be used to model the adhesive failure of bonded joints. It is also highly dependent on the mesh refinement because stress concentration usually appears around the areas near the edges of the adhesive layer [127, 128]. **Figure 2.14**(b) shows the second approach: continuum elements are used to model the behaviour of bulk adhesive and zero-thickness interface elements are inserted at the adhesive-adherend interface to model the adhesive failure of bonded joints. In the third and fourth approaches, the adhesive layer is totally represented by interface or cohesive elements. A single or several layers of finite thickness cohesive elements are utilized in the third approach and damage criteria are used to describe the failure behaviour of adhesive layer, as shown in **Figure 2.14**(c). A layer of zero-thickness cohesive elements is used in the fourth approach and the failure behaviour of adhesive layer is governed by different kinds of traction-separation laws, as shown in **Figure 2.14**(d).

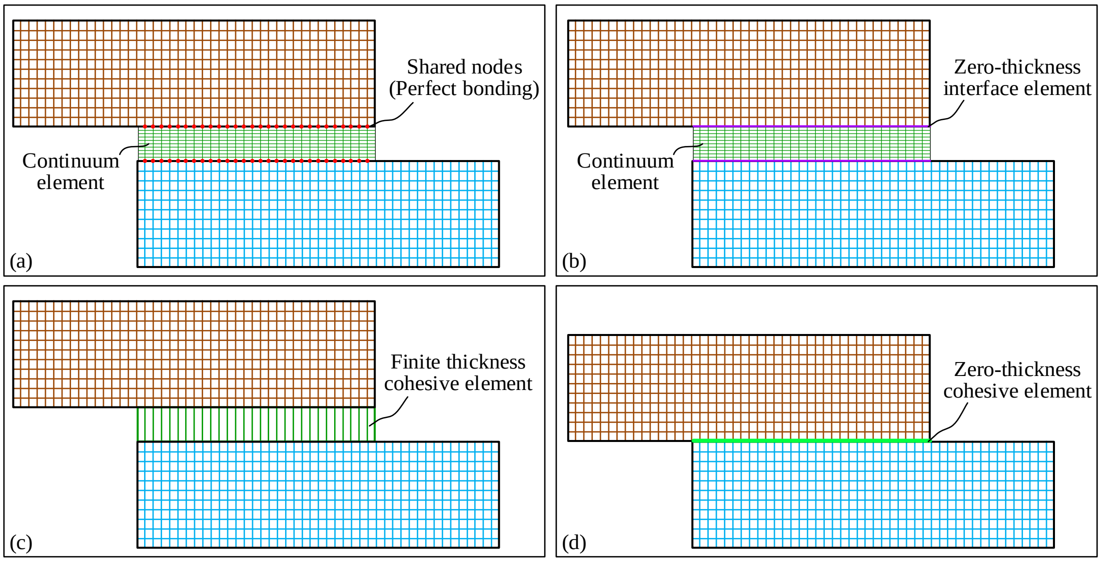
Shared nodes
(Perfect bonding)
Continuum element
(a)
Zero-thickness interface element
Continuum element
(b)
Finite thickness cohesive element
(c)
Zero-thickness cohesive element
(d)

Figure 2.14: Schematic of the four approaches for the modelling of adhesive bonded joints

2.3. Riv(et)-Bonding Technique

The Riv-Bonding technique, which is developed based on the SPR technique and the adhesive bonding technique, integrates the benefits of the two joining approaches and overcomes their individual limitations [128]. **Figure 2.15**(a) shows the cross-sectional profile of a Riv-Bonding joint. The adhesive layer in the Riv-Bonding joint can effectively eliminate the stress concentration problem of the solo SPR joint. Meanwhile, a significant increment of static strength, fatigue strength, energy absorption and corrosion resistance can also be achieved in the Riv-Bonding joints [129]. Due to the great performance of the Riv-Bonding joint, it has been widely utilized in many industrial sectors, especially the automotive industry [130]. The main drawback of the Riv-Bonding joint is that adhesive pockets might be formed between the multiple SPR joints, and lead to global deformations of the connected structures [131]. In addition to the Riv-Bonding, there are also other types of hybrid joining techniques widely used in the industry field, such as the traditional rivet-bonding [133, 134], Clinch-bonding [134], Bolt-bonding [135], the single-sided piercing riveting (SSPR)-bonding [136] and Weld-bonding [137]. **Figure 2.15**(b)~(f) show the cross-sectional profiles of joints manufactured with these hybrid joining methods.

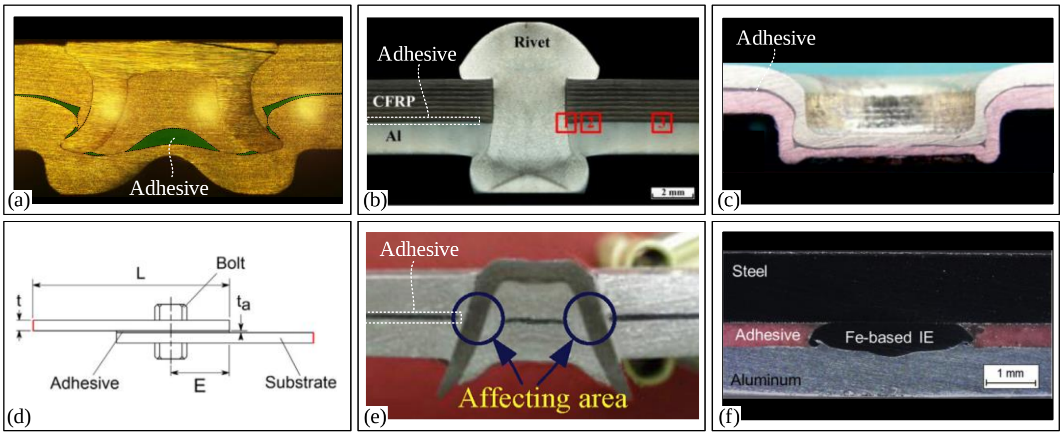

Figure 2.15: Cross-sectional profiles of different types of hybrid joints: (a) Riv-Bonding, (b) traditional rivet-bonding [132], (c) Clinch-bonding [134], (d) Bolt-bonding [135], (e) SSRR-bonding [136] and (f) Weld-bonding [137]

According to the sequence of riveting process and bonding process, there are three different ways to manufacture a Riv-Bonding joint: (1) the sequential method, the SPR process is conducted after the adhesive layer is cured, and initial micro-damages might be introduced into the adhesive layer and reduce the mechanical strength of the bonded connection [134]; (2) the fixing method, the SPR process is performed before the adhesive layer is cured; (3) the injection method, the rivet is installed and then the adhesive is injected into the gap between the sheets [139, 140]. Among the three approaches, the second method is the most frequently utilized way in the industry sector. Many parameters can affect the quality of Riv-Bonding joints, such as the adhesive viscosity, the amount of the adhesive, the adhesive application method (e.g., continuous beads or intermittent beads) and the magnitude of clamping force [140]. The rivet and die parameters will also impose influences on the quality of Riv-Bonding joints. To date, many experimental studies have been carried out by researchers to extend the application range of the Riv-Bonding technique, and to better understand the differences between the SPR process and the Riv-Bonding process.

According to the research direction, the existing studies can be divided into two groups. The first group focuses on exploring the impact of the adhesive layer on the events happened during the joining process, such as the distribution of adhesive, deformation behaviours of rivet and sheets and the final quality of Riv-Bonding joints. However, only a limited number of studies classified to this group were reported in the public domain. Moroni [141] reported that no adhesive was found around the joining region of the Riv-Bonding joint, and the adhesive layer demonstrated little influence on the deformations of rivet and sheets. The influences of adhesive layer on the interlock formation in the Riv-Bonding joint with DC04 sheets and 3.0mm diameter rivets were evaluated by Hahn and Wibbeke [140]. It was found that the adhesive pocket formed during the joining process imposed negative effects on the interlock formation. The influences of die diameter, die depth and rivet length on the quality of three-layer SPR joints with or without the adhesive layer were studied by Abe et al. [52]. Hahn and Wibbeke [140] reported that joints with thin sheets or low yield strength sheets would be more possibly affected by the adhesive layer. To better understand the Riv-Bonding process and facilitate the design of Riv-Bonding joints, more studies are still required to find out how the adhesive layer affects the joining process and the final quality of riveted connections. Meanwhile, influences of the rivet, die and SPR system parameters on the Riv-Bonding process and the final joint quality are also worth investigating.

The second group pays more attention to the performance evaluation of Riv-Bonding joints, such as the tensile strengths under different loading conditions, energy absorption and fatigue life. So far, most of the existing studies belong to this group. For example, the shear strengths of SPR joints and Riv-Bonding joints with a hot-melt adhesive layer were experimentally compared by Baurova et al. [138]. The results revealed that the joint shear strength apparently increased after adding the adhesive. He et al. [142] experimentally investigated the shear strength and energy absorption of Riv-Bonding joints with AA5754 sheets. The results indicated that the maximum shear load of the Riv-Bonding joint is 14% higher than that of the corresponding SPR joint, whereas the energy absorption is much lower than that of the SPR joint. Liu and Zhuang [143] experimentally studied the mechanical strengths and failure mechanisms of Riv-Bonding joints with the carbon fibre reinforced polymer (CFRP) top sheet and the AA5754-H22 bottom sheet. It was found that the ply angle of the CFRP and the sheet thickness had significant influences on the joint shear strength and the failure mode. Sun et al. [6] found that the application of the adhesive Dow Betamate 4601 significantly enhanced the fatigue strength of SPR joints under lap-shear loading condition, but a smaller improvement was observed under cross-tension loading condition. The shear strength and fatigue strength of adhesive aided SPR joints with AM50 magnesium alloy sheets were studied by Miyashita et al. [144]. The results showed that the adhesive layer could not eliminate the cracks on the bottom sheet, but effectively improved the joint shear strength and fatigue strength. It was also found that the adhesive properties had significant influences on the shear strength of the Riv-Bonding joint. Di Franco et al. [145] studied the lap-shear strength of Riv-Bonding joints with CFRP top sheet and aluminium alloy AA2024-T6 bottom sheet. The influences of the distance between rivets on the shear strength and fatigue life of Riv-Bonding joints with 1.5mm CFRP top sheet and 2.7mm aluminium 2024-T6 bottom sheet were also investigated by Di Franco et al. [146]. It was found that both of the maximum shear strength and the fatigue life at different load levels increased when the rivet distance changed from 30mm to 60mm, while a same failure mode was observed for all joints with different rivet distances. Hahn and Wibbeke [140] evaluated the influences of adhesive layer on the shear strength and energy absorption of the Riv-Bonding joints with DC04 sheets and 3.0mm diameter rivets. It was found that the mechanical strength of the Riv-Bonding joints could be optimized by increasing the rivet hardness and punching velocity, and by decreasing the clamping force and the adhesive viscosity. Lee et al. [147] reported the greater lap-shear strengths of the Riv-Bonding joints with high strength steel (HSS) sheets or ultra-high strength steel (UHSS) sheets compared with solo SPR joints. Jiang et al. [148] experimentally investigated the lap-shear strength and the failure process of Riv-Bonding joints. The results revealed that the Riv-Bonding joint endured a greater peak load than the solo SPR joint. The failure process of bonded connection in the Riv-Bonding joint was divided into two stages rather than the instantaneous failure of the solo bonded joint. Song et al. [149] reported that the lap-shear strength of the Riv-Bonding joints with composite/steel sheets was 45.3% greater than that of the pure SPR joints, but the energy absorption decreased after adding the adhesive layer (9.1%). Zvorykina et al. [137] experimentally compared the lap-shear strength and cross-tension strength of SPR joints and Riv-Bonding joints. The lap-shear strength and fatigue performance of the Riv-Bonding joints with aluminium alloy AA5754-H32 sheets were evaluated Moroni [141]. Guo and El-Tawil [150] studied the influences of adhesive layer on the lap-shear strength, T-peel strength and fatigue life of the SPR joints with steel and aluminium sheets. Fiore et al. [151] studied the effects of adhesive curing time on the performance of Riv-Bonding joints with GFRP top sheet and aluminium alloy 6082 T6 bottom sheet. Presse et al. [152] proposed a stress-based approach to calculate the fatigue life of multi-material connections by SPR and adhesive. The fatigue lives of the SPR joint and adhesive bonded joint were calculated individually, and then simply superposed together to get the fatigue life of the Riv-Bonding joint. The fatigue life of Riv-Bonding joints and SPR joints under different loading directions and different load levels was experimentally compared by Wu et al. [153]. A mechanism-based fatigue life evaluation method was also proposed based on the failure analysis to predict the fatigue life of Riv-Bonding joints. Actually, the mechanical strength of a Riv-Bonding joint depends on both of the bonded connection and the riveted connection. In addition to the performance evaluation of the entire Riv-Bonding joints, attentions should also be paid to the quality of the riveted connections in the Riv-Bonding joints. Because adhesives with different functions are usually utilized according to the application requirements. For example, in the automotive industry, some types of adhesives are employed to improve the structure crash resistance, while other types are just used for sealing purpose or a long-term corrosion resistance.

In addition to the experimental test, the finite element modelling is also an effectively way to study the Riv-Bonding joints. The existing FE models can be classified into two groups: (1) FE model of Riv-Bonding process, which can be utilized to predict the joint quality and to visually inspect the joint formation process; (2) FE model for strength prediction of Riv-Bonding joint, which is mainly designed to assess the joint mechanical strengths. As for FE models of Riv-Bonding process, the biggest challenge is how to model the fluid-structure interaction (FSI) between the solid parts (i.e., rivet and sheets) and the liquid-like uncured adhesive during the joining process. Due to the different natures of solids and fluids, the metal rivet and sheets show elastic-plastic behaviours but the uncured adhesive demonstrates a viscous flow behaviour. Solid structures can be conveniently simulated with the finite element (FE) method. As for the uncured adhesive, the Computational Fluid Dynamics (CFD) method, Arbitrary Lagrangian Eulerian (ALE) method and the Coupled Euler Lagrangian (CEL) method are the promising simulation approaches. For the FE model of Riv-Bonding joint strength prediction, the biggest challenge is how to obtain the joint cross-sectional profile, including the deformed rivet, deformed sheets and the adhesive distribution between the connected sheets. Experimental approach can be used to get the joint cross-sectional profile, and then the joint geometries are extracted to establish the FE model. However, this method is time consuming and makes the model development process very complicated. The ideal method is to directly use the joint model from the simulated Riv-Bonding joint. The stress and strain distributions of the joint can also be transferred and considered into the FE model of Riv-Bonding joint strength prediction. But this needs a mature FE model of Riv-Bonding process.

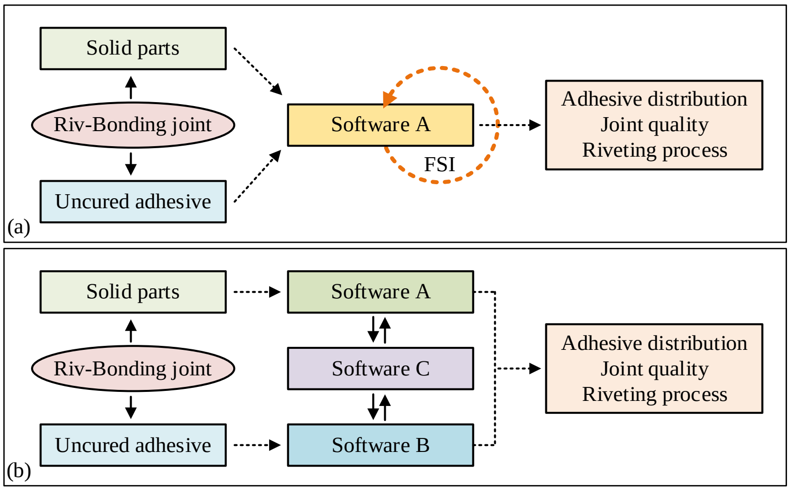
Solid parts
Riv-Bonding joint
Uncured adhesive
Software A
FSI
Adhesive distribution
Joint quality
Riveting process
(a)
Solid parts
Riv-Bonding joint
Uncured adhesive
Software A
Software C
Software B
Adhesive distribution
Joint quality
Riveting process
(b)

Figure 2.16: Schematic of the two strategies for the simulation of Riv-Bonding process

There are generally two strategies to simulate the Riv-Bonding process [154]. The first one is simulating all the solid parts and uncured adhesive with only one software, as shown in **Figure 2.16**(a). Many commercial FE software have already integrated the modules for solid simulation and fluid simulation, such as ABAQUS, ANYSIS and Ls-Dyna. The second strategy is simulating the solid parts with one software and simulating the liquid adhesive with another software. Then, the interaction between the solid parts and the adhesive is achieved by exchanging data using a coupling software (e.g., MpCCI), as shown in **Figure 2.16**(b). Due to the function limitations of the accessible simulation software, modelling of the top sheet penetration during the Riv-Bonding process is still a challenge. Until now, there are only a limited number of studies focusing on the simulation model development of Riv-Bonding process. Neugebauer et al. [155] firstly developed the simulation model of Riv-Bonding process using the second strategy mentioned above. The simulation result showed a reasonable agreement with that from the experimental test. Three types of software were employed, including the ABAQUS, FLUENT and MpCCI. Landgrebe et al. [156] experimentally inspected the formation of adhesive pockets between two Riv-Bonding joints, and studied the influences of the distance between two joints on the deformations of the top and bottom sheets. A surrogate model was proposed based on the developed FE model of Riv-Bonding process in [155], and was utilized to analyse the adhesive distribution in the structure assembled with multiple Riv-Bonding joints. Then, Fricke et al. [132, 155] from the same research group also demonstrated the capability of surrogate model of Riv-Bonding process simulation model on the simulation of complex industrial structures. The surrogate model was developed by extracting the time-dependent adhesive flow rate and the sheets' displacements on a cylindrical boundary using the FE simulation model of Riv-Bonding process. With the proposed surrogate model, the impact of the adhesive flow on a complex structure with multiple joints was successfully predicted. Potgorschek et al. [157] successfully developed a 2D simulation model of the Riv-Bonding process in software Simufact.Forming 15. The material property of the uncured epoxy-based adhesive was modelling using the stress-strain rate curves at different temperatures. A good agreement between the simulated and the experimentally tested joint cross-sectional profiles was observed.

Compared with the FE model of Riv-Bonding process, the simulation model development for joint mechanical strength prediction is relatively easier because the adhesive layer has already cured in the Riv-Bonding joints. The methods for modelling of adhesive bonded joints (see **Figure 2.14**) can also be employed to model the Riv-Bonding joint. So far, to the author's knowledge, there are few FE models of Riv-Bonding joint strength prediction. This might be limited by the slow progress of the FE model for the Riv-Bonding process. There are two possible strategies to simulate the adhesive bonded connection during the strength prediction of Riv-Bonding joint, as shown in **Figure 2.17**. The first one is using continuum elements to model the behaviour of cured adhesive layer. The second one is using finite thickness cohesive elements to represent the cured adhesive layer. More work is still needed in order to better understand the mechanical performances of Riv-Bonding joints using the FE technique.

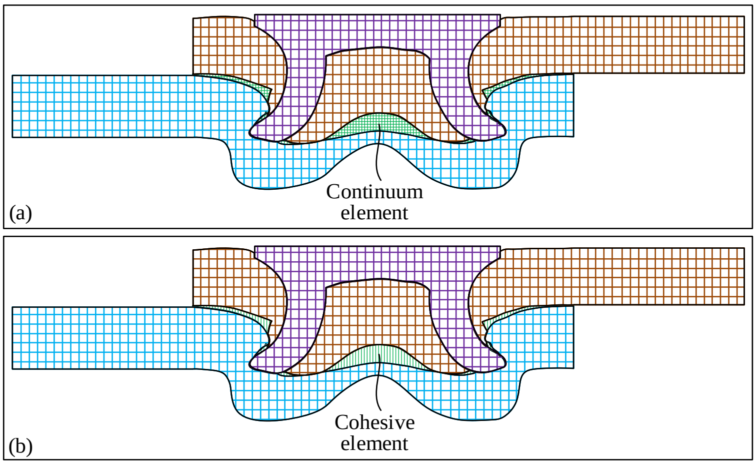

Figure 2.17: Schematic of the two possible approaches for the modelling of adhesive bonded connection in Riv-Bonding joints

2.4. Summary

In this chapter, the up-to-date literatures relevant to the SPR, adhesive bonding and Riv-bonding techniques are systematically reviewed, including the joint quality assessment and mechanical performance evaluation. Limitations of the current research and the solutions proposed in this thesis are summarized below:

(1) In the existing studies, the SPR joint quality was usually evaluated by quality indicators measured from the joint cross-sectional profile. Although it is widely acknowledged that the joint cutting position has critical influences on the joint profile and on the quality indicators, there are few studies focusing on the influence of the improper joint cutting position on the joint quality evaluation. Therefore, a systematic investigation was carried out in this thesis to uncover the impact of the joint cutting position.

(2) The relationships between the die parameters and the joint quality have been widely studied in the literature. However, due to the difficulties to directly observe the joint formation during the SPR process, there is still no clear understanding of how die parameters (e.g., die diameter and die depth) affect the joint formation. Therefore, the impact of different die geometrical parameters on the joint formation was numerically investigated in this thesis.

(3) Because of the difficulties to model the fluid-structure interaction (FSI) between the solid parts and the uncured adhesive, there is still not a simulation model of Riv-Bonding process suitable for industry applications in the existing literature. Therefore, a finite element (FE) model of Riv-Bonding process was developed in this thesis to meet the fast response requirement from the industry sector.

(4) The better mechanical performance of Riv-Bonding joints compare to SPR joints has been widely reported. However, the impact of the adhesive layer on the events happened during

the riveting process is rarely studied. The flow behaviour of the uncured adhesive during the riveting processes with different die types is still not clear. The influence of the adhesive layer on the quality of riveted connection has not been comprehensively studied. Therefore, experimental investigation was carried out in this thesis to explore the impact of the adhesive layer.

3. Influences of Specimen Cutting Position on SPR Joint Quality Measurement

It is widely acknowledged that the joint cutting position plays an important role in the joint quality evaluation. However, there is still no clear understanding of how much impact the improper cutting position has on the measurement accuracy of the three quality indicators (i.e., the rivet head height (H), interlock (I) and minimum remaining bottom sheet thickness (T_{min})). Therefore, this chapter systematically investigated the influences of joint cutting positions on the measurement accuracy of these quality indicators. Firstly, the improper cutting position induced distortion of joint cross-sectional profile was qualitatively compared and discussed. Then, the influences of the cutting position on the H and the I were analysed. A mathematic model was developed to estimate the interlock errors under different cutting conditions. The impact of the improper cutting position on the remaining bottom sheet thickness was also analysed and discussed in detail. To compensate the interlock error caused by the improper cutting position, a correction/compensation approach was proposed by measuring the offset distance (Δh) and the rotation angle (θ_1) between the cutting plane and the joint central plane. To facilitate the practical applications, two graphical user interfaces (GUI) for the interlock error estimation and correction were also developed. Finally, experimental SPR tests were carried out to estimate the interlock error levels for physical SPR joints and to verify the performance of the proposed interlock error correction method.

3.1. Introduction

The SPR joint quality is usually evaluated by three quality indicators measured on the joint cross-sectional profile as shown in **Figure 3.1**: the rivet head height (H), the interlock (I), and the minimum remaining bottom sheet thickness (T_{min}). Therefore, the accuracy of the captured joint cross-sectional profile is very important for the joint quality evaluation. **Figure 3.2** illustrates the procedures to experimentally get the cross-sectional profile of a SPR joint, including the specimen manufacturing, specimen cutting, sectioned surface polishing and cross-sectional profile inspection. Under the ideal conditions, the specimen is cut along the joint central plane, and the true values of the three quality indicators are measured on the captured cross-sectional profile. However, during the experimental tests, many factors will affect the specimen cutting position, such as the specimen shape, the specimen clamping position and the wear of grinding wheel. Therefore, it is very difficult to experimentally cut the specimen through the joint central plane. The misalignment between the cutting plane and the joint central plane will inevitably affect the accuracy of the captured joint cross-sectional profile, and bring measurement errors to the three quality indicators. By standardizing the specimen size and using specially designed fixtures during the riveting and cutting processes, this misalignment could be effectively reduced and the influences on the joint quality indicators could also be minimised. However, these special fixtures may become not workable under some situations. For example, the SPR joints cut from a vehicle Body-in-White (BIW) (as shown in **Figure 3.3**) usually have a nonstandard size/shape, and thus can only be sectioned roughly based on the operator's experience. Moreover, improper polishing operation for the sectioned surface may further aggravate such misalignment. Consequently, the specimen preparation, especially the improper cutting operation, will cause errors to the captured joint cross-sectional profile and the measured three quality indicators.

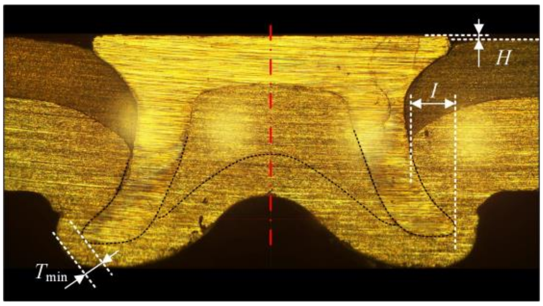

Figure 3.1: Three joint quality indicators measured on the cross-sectional profile of a SPR joint

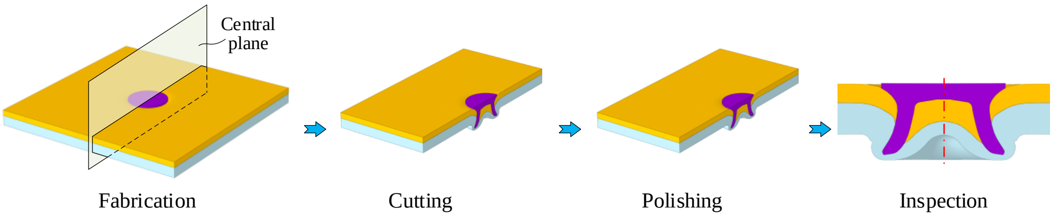

Figure 3.2: Quality evaluation procedures for SPR joints

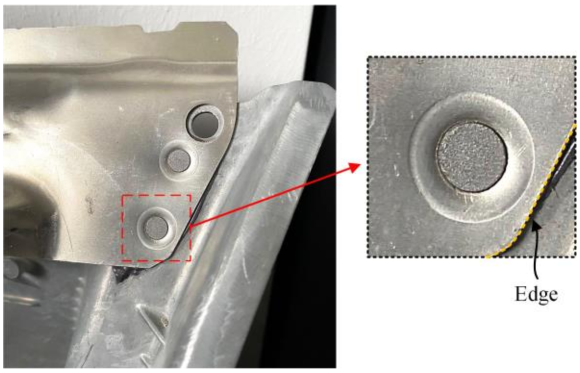

Figure 3.3: SPR joints in the car Body-in-White (BIW) structure

Recent years, FE models of SPR process have been successfully developed to predict the joint quality [159, 160]. Different from experimental SPR tests, the cutting operation carried out in the FE software will not affect the measurement accuracy of the three quality indicators, because the simulated specimens can be exactly cut along the joint central plane. However, experimental SPR tests are still required for the calibration and validation of FE models [2, 161]. The errors from the specimen preparation stage during the experimental SPR tests will therefore indirectly affect the prediction accuracy of the developed SPR simulation model. Although the specimen preparation (especially the specimen cutting) is so important for the SPR joint quality evaluation and for the FE model development, there are still few reports devoting to this issue in the public domain.

3.2. Improper Specimen Cutting

During the specimen preparation process, the improper polishing operation for the sectioned surface may also affect the captured joint cross-sectional profile and the measured joint quality indicators. For clarity, the error induced by the improper specimen polishing is also regarded as the error caused by the specimen cutting.

3.2.1. Types of improper cutting positions

Under the ideal conditions, as shown in **Figure 3.4**(a), the SPR joint is exactly cut along the joint central plane (Red line). The joint central plane and the cutting plane (Blue line) coincide with each other. However, a misalignment always exists between these two planes in any experimental SPR test. According to the relative positions, the improper specimen cutting positions can be divided into three types: (1) Pure offset in **Figure 3.4**(b), the two planes are parallel but with a offset distance (Δh); (2) Pure rotation in **Figure 3.4**(c), the cutting plane passes through the central line of the rivet head but had a rotation angle (θ_1) against the joint central plane; (3) Offset+Rotation in **Figure 3.4**(d), there is an offset distance (Δh) as well as a rotation angle (θ_1) between the two planes.

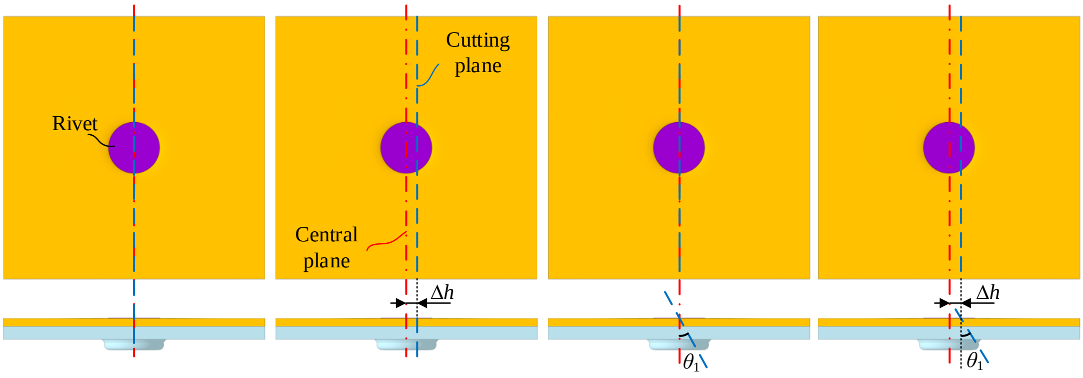

(a) Correct (b) Pure offset (c) Pure rotation (d) Offset+Rotation

Figure 3.4: The ideal specimen cutting position and three improper cutting positions: (a) correct position, (b) pure offset, (c) pure rotation and (d) offset+rotation

3.2.2. Influences on the joint cross-sectional profile

Taking the SPR joint with the 1.2mm+2.0mm AA5754 sheets and the 6.0mm long boron steel rivet as an example, the joint cross-sectional profiles at different cutting positions were captured using software SolidWorks 2018. As shown in **Figure 3.5**, a 3D joint model was first created based on the experimentally observed joint cross-sectional profile (left half or right half). Then, this 3D model was virtually sectioned at different cutting positions, and all the corresponding joint cross-sectional profiles were recorded. The tested SPR joint was not exactly axisymmetric, but was assumed to be axisymmetric in the created 3D joint model. This will not affect the following discussions because the left half and right half of the SPR joint can be evaluated individually in practice. In addition, the accuracy of the tested joint profile would not affect the reliability of the conclusions made in this section. Because all the analyses were carried out based on the 3D joint model rather than the experimentally tested joint. The joint appearances and cross-sectional profiles with the pure offset distances (Δh) and pure rotation angles (θ_1) are given in **Figure 3.6** and **Figure 3.7** respectively.

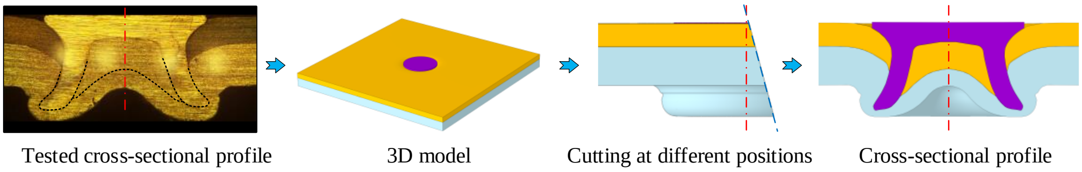
Tested cross-sectional profile
3D model
Cutting at different positions
Cross-sectional profile

Figure 3.5: Procedures to get the joint cross-sectional profiles virtually at different cutting positions

As shown in **Figure 3.6**, when the Δh is smaller than 1.0mm, it is not easy to identify the occurrence of cutting offset by visually observing the joint appearance and the cross-sectional profile. The rivet profile (Purple region) kept almost the same when the Δh increased from 0.0mm to 1.0mm. In contrast, when the Δh becomes greater than 1.0mm, the rivet profile changed a lot compared to that without the cutting offset (Δh=0mm). The severe distortion of rivet profile and the captured outside surface of bottom sheet (Zone 1) clearly indicated the occurrence of cutting offset. For the joint quality, the Δh showed no influence on the rivet head height (H) because the relative positions between the upper surfaces of the rivet and top sheet were not affected, but imposed significant influences on the remaining bottom sheet thickness. The Δh also showed some impacts on the interlock (I) and this will be discussed later.

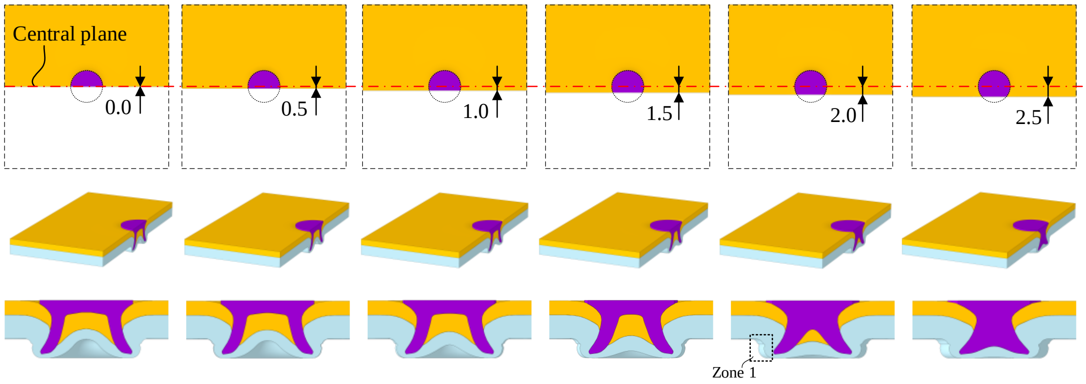

Δh=0.0mm Δh=0.5mm Δh=1.0mm Δh=1.5mm Δh=2.0mm Δh=2.5mm

Figure 3.6: Joint appearances and cross-sectional profiles at different pure offset distances (Δh)

Compared with the cutting offset distance, the occurrence of cutting rotation angle is easier to be visually identified from the joint appearance but still difficult to be discovered from the joint cross-sectional profile as shown in **Figure 3.7**. When the θ_1 is less than 10°, the joint cross-sectional profiles kept almost the same. When the θ_1 becomes larger than 10°, obvious changes of the remaining bottom sheet thickness were noticed. The changes of rivet profile become evident when the θ_1 increases to 20° and 25°. It was also discovered that the θ_1 imposed a larger influence on the bottom half than on the upper half of the joint cross-sectional profile. This is because the cutting plane passes through the central line of the rivet head, and the points on the cutting plane have different distances to the joint central plane. A larger distance resulted in a greater distortion between the joint profiles captured on the joint central plane and on the cutting plane. For the joint quality, the θ_1 also showed no influence on the rivet head height (H) but imposed obvious influences on the interlock (I) and on the remaining bottom sheet thickness.

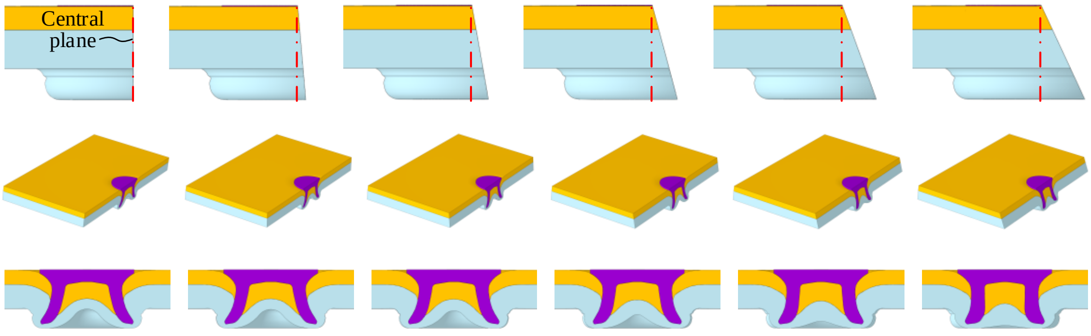

θ_1=0° θ_1=5° θ_1=10° θ_1=15° θ_1=20° θ_1=25°

Figure 3.7: Joint appearances and cross-sectional profiles at different pure rotation angles (θ_1)

When the cutting offset and cutting rotation happen at the same time, a superimposed effect would be imposed on the joint cross-sectional profile. The joint appearances and cross-sectional profiles at such type of cutting position would be a combination of **Figure 3.6** and **Figure 3.7**, and are not presented here to avoid repetition.

3.3. Evaluation of Cutting Position's Effects on the Joint Quality Indicators

To better understand the relationships between the cutting position and the measurement errors of the joint quality indicators, influences of the three types of improper cutting positions on the rivet head height (*H*), the interlock (*I*) and the remaining bottom sheet thickness were analysed and discussed.

3.3.1. Error estimation of the rivet head height

As shown in **Figure 3.8**, the rivet head height (*H*) is the vertical distance between the top surface of the rivet (Surface A) and the upper surface of the top sheet (Surface B). During the experimental tests, the locations of these two surfaces are not affected by the cutting position. Therefore, the *H* observed on the cutting plane equals exactly to the true *H* on the joint central plane, and will not be influenced by the Δh and θ_1.

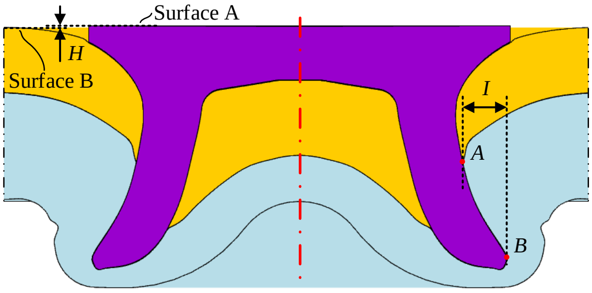

Figure 3.8: Locations of the two boundaries for the rivet head height (*H*) and the two boundaries for the interlock (*I*)

3.3.2. Error estimation of the interlock

According to the definition, the magnitude of interlock (*I*) is directly determined by the locations of the inner interlock boundary (Point *A*) and the outer interlock boundary (Point *B*), as shown in **Figure 3.8**. The appearance of the Δh and θ_1 would affect the measured value of *I* by altering the locations of the two interlock boundaries. Therefore, the influences of the three types of improper cutting positions on the *I* were analysed, and the corresponding relative and absolute errors of interlock were estimated.

3.3.2.1. With only the offset distance (Δh)

As shown in **Figure 3.9**, the inner and outer interlock boundaries are two circles in the three-dimensional space (Circle A for the inner boundary and Circle B for the outer boundary). The intersection points (i.e., Points *A* and *B*) between the two circles and the joint central plane are the true positions of the two interlock boundaries. When there is a Δh between the joint central plane and the cutting plane, the observed positions of the two interlock boundaries become the intersection points between the two circles and the cutting plane (Point A_1 and B_1). The true interlock boundaries on the central plane are projected onto the cutting plane along the trajectories of the Circles A and B.

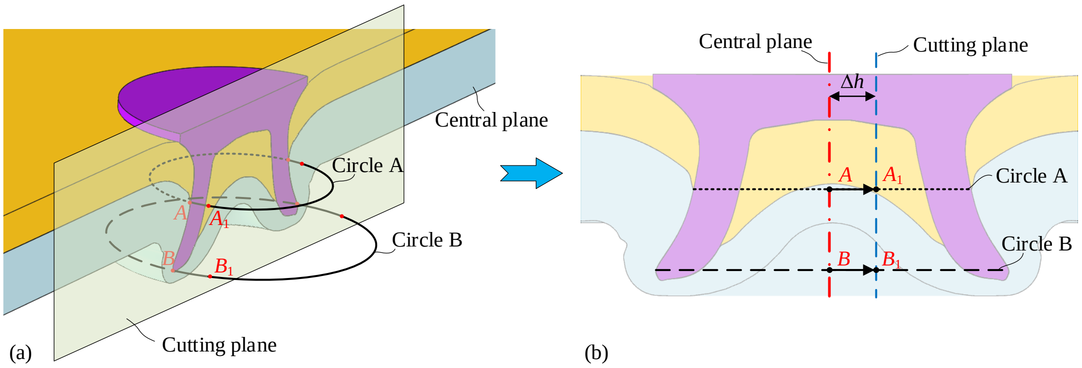
Central plane
Circle A
Circle B
A
A_1
B
B_1
Cutting plane
(a)
Central plane
Cutting plane
Δh
A
A_1
Circle A
Circle B
B
B_1
(b)

Figure 3.9: Projections of the two interlock boundaries on the cutting plane with an offset distance (Δ*h*)

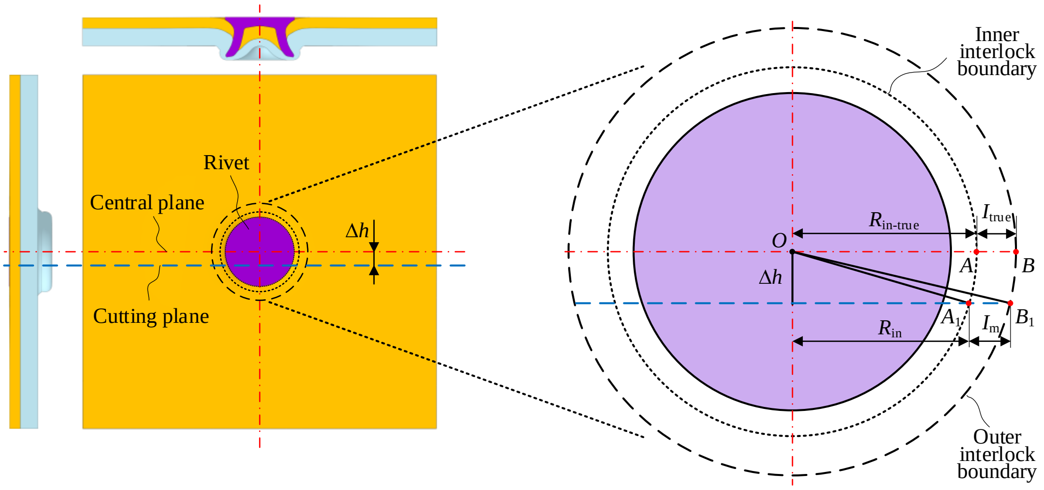
Rivet
Central plane
Δh
Cutting plane
Inner interlock boundary
$R_{\text{in-true}}$
I_{true}
O
A
B
Δh
A_1
I_m
B_1
R_{in}
Outer interlock boundary

Figure 3.10: Schematic of the interlock values on the joint central plane and on the cutting plane with an offset distance (Δ*h*)

To evaluate the interlock error induced by the improper cutting position, as shown in **Figure 3.10**, the measured interlock (I_{m}) on the cutting plane was firstly derived using the dimensions on the joint central plane and the cutting plane. The $R_{\text{in-true}}$ and I_{true} denote the true radius of the inner interlock boundary and the true interlock on the joint central plane. The magnitude of $R_{\text{in-true}}$ is determined by the initial radius of rivet shank and its degree of deformation during the riveting process. According to the geomatical relationships, the I_{m} can be expressed as a function of the I_{true}, $R_{\text{in-true}}$ and Δh:

$$I_m = \sqrt{\left(R_{in-true} + I_{true}\right)^2 - \Delta h^2} - \sqrt{R_{in-true}{}^2 - \Delta h^2} \qquad (3.1)$$

The relative error (δ_{offset}) and absolute error (e_{offset}) of interlock with only the Δh can be calculated using Eq.(3.2) and Eq.(3.3) respectively. Substituting Eq.(3.1) into Eq.(3.2) and

Eq.(3.3) yields Eq.(3.4) and Eq.(3.5). By observing the structures of the Eq.(3.4) and Eq.(3.5), it can be found that the δ_{offset} and e_{offset} are always equal to (Δh =0) or greater than zero (Δh >0). This means the I_{m} would be always greater than the I_{true} due to the existence of Δh. Meanwhile, it was found that the magnitudes of δ_{offset} and e_{offset} are not only affected by the Δh but also by the $R_{\text{in-true}}$ and I_{true}.

$$\delta_{offset} = \frac{I_m - I_{true}}{I_{true}} \times 100\% \tag{3.2}$$

$$e_{offset} = I_m - I_{true} \tag{3.3}$$

$$\delta_{offset} = \left(\frac{I_{true} + 2R_{in-true}}{\sqrt{\left(R_{in-true} + I_{true}\right)^2 - \Delta h^2} + \sqrt{R_{in-true}^2 - \Delta h^2}} - 1 \right) \times 100\% \tag{3.4}$$

$$e_{offset} = \sqrt{R_{in-true}^2 + I_{true}^2 - \Delta h^2 + 2 \cdot I_{true} \cdot R_{in-true}} - \sqrt{R_{in-true}^2 + I_{true}^2 - \Delta h^2 + 2 \cdot I_{true} \cdot \sqrt{R_{in-ture}^2 - \Delta h^2}} \tag{3.5}$$

Taking the SPR joints with Ø5.3mm boron steel rivet and AA5754 sheets as an example, the influences of the Δh on the interlock were demonstrated. For this type of SPR joints, the $R_{\text{in-true}}$ usually locates in the range of 2.65mm~4.0mm and the I_{true} generally belongs to the range of 0.0mm~2.0mm. Using Eq.(3.4) and Eq.(3.5), surface diagrams of the e_{offset} and δ_{offset} at the offset distances 0.5mm, 1.0mm, 1.5mm, 2.0mm and 2.5mm are presented **Figure 3.11** and **Figure 3.12** respectively. It can be seen that both of the e_{offset} and δ_{offset} showed an increasing tendency with the increment of Δh. For a fixed Δh, the e_{offset} showed an increasing trend with the increment of I_{true}. In contrast, the δ_{offset} demonstrated an opposite trend and decreased with the increment of I_{true}. Moreover, both of the e_{offset} and δ_{offset} showed a decreasing tendency with the increment of $R_{\text{in-true}}$. This means that the Δh would impose a smaller influence on the measurement accuracy of interlock if the interlock was formed at a position far from the joint axis. As shown in **Figure 3.11**, the $R_{\text{in-true}}$ showed very limited influence on the e_{offset} when the interlock was relatively small (I_{true}<0.5mm), but an obvious impact when the interlock had a large value (I_{true} >1.0mm). As shown in **Figure 3.12**, the $R_{\text{in-true}}$ always had a significant influence on the δ_{offset}, and imposed a greater influence with a small interlock than with a large one. In addition, it can also be found that both of the e_{offset} and δ_{offset} could still maintain at a low level when the Δh increased to 1.0mm as shown in **Figure 3.11** (b) and **Figure 3.12** (b). However, further increment of Δh resulted in unacceptable measurement errors as presented in **Figure 3.11** (c)(d) and **Figure 3.12** (c)(d).

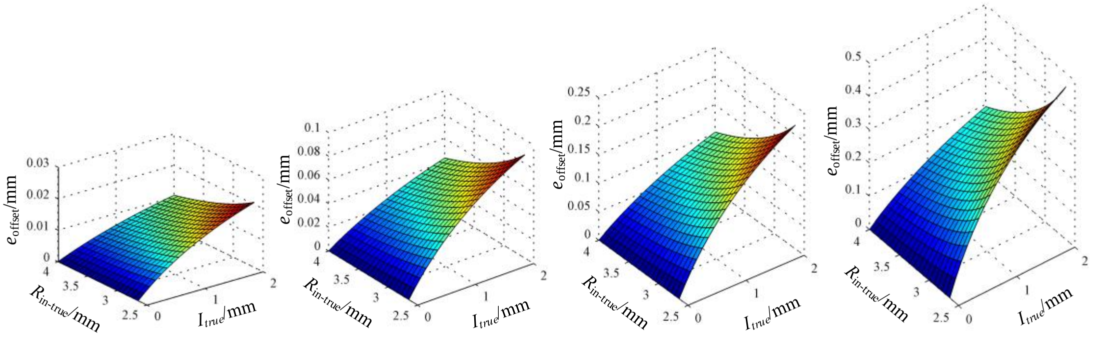

(a) Δ*h*=0.5mm (b) Δ*h*=1.0mm (c) Δ*h*=1.5mm (d) Δ*h*=2.0mm

Figure 3.11: Absolute error (e_{offset}) of the interlock with different offset distances (Δ*h*)

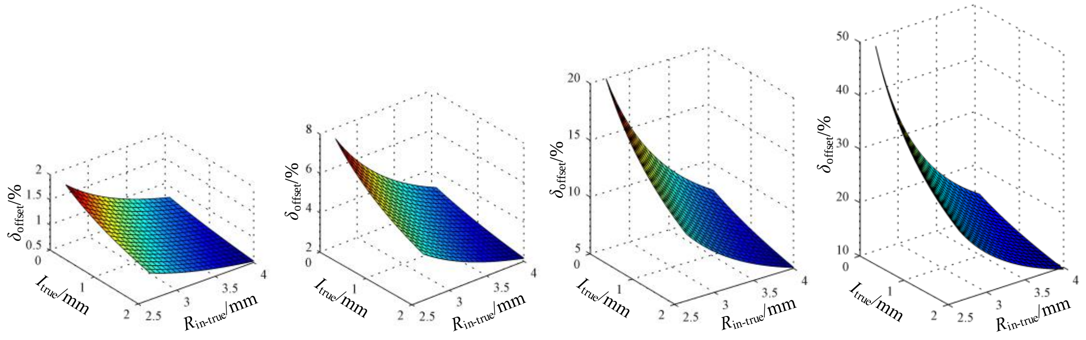

(a) Δ*h*=0.5mm (b) Δ*h*=1.0mm (c) Δ*h*=1.5mm (d) Δ*h*=2.0mm

Figure 3.12: Relative error (δ_{offset}) of the interlock with different offset distances (Δ*h*)

3.3.2.2. With only the rotation angle (θ_1)

As shown in **Figure 3.13**, the joint central plane and the cutting plane become not parallel when there is a rotation angle (θ_1). The two interlock boundaries on the joint central plane (Points *A* and *B*) are projected along the trajectories of Circle A and B onto two different planes (Plane A and Plane B) paralleling to the central plane. The Δh_1 denotes the offset distance from the Plane A to the central plane, and can be expressed as a function of the θ_1 and the vertical distance (S_1) between the inner interlock boundary (Point *A*) and the top surface of the rivet, as shown in Eq.(3.6). The Δh_2 denotes the offset distance between the plane A and plane B. It can be expressed as a function of the θ_1 and the vertical distance (S_2) between the two interlock boundaries (Points *A* and *B*), as shown in Eq.(3.7).

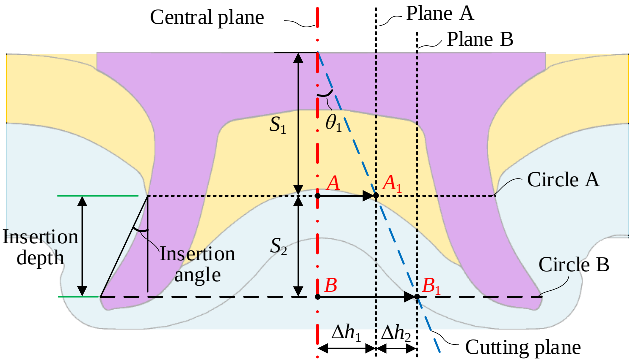
Central plane
Plane A
Plane B
S_1
θ_1
A
A_1
Circle A
Insertion depth
Insertion angle
S_2
Circle B
B
B_1
Δh_1
Δh_2
Cutting plane

Figure 3.13: Projections of the two interlock boundaries from the joint central plane to the cutting plane with a rotation angle (θ_1)

$$\Delta h_1 = S_1 \cdot \tan\theta_1 \tag{3.6}$$

$$\Delta h_2 = S_2 \cdot \tan\theta_1 \tag{3.7}$$

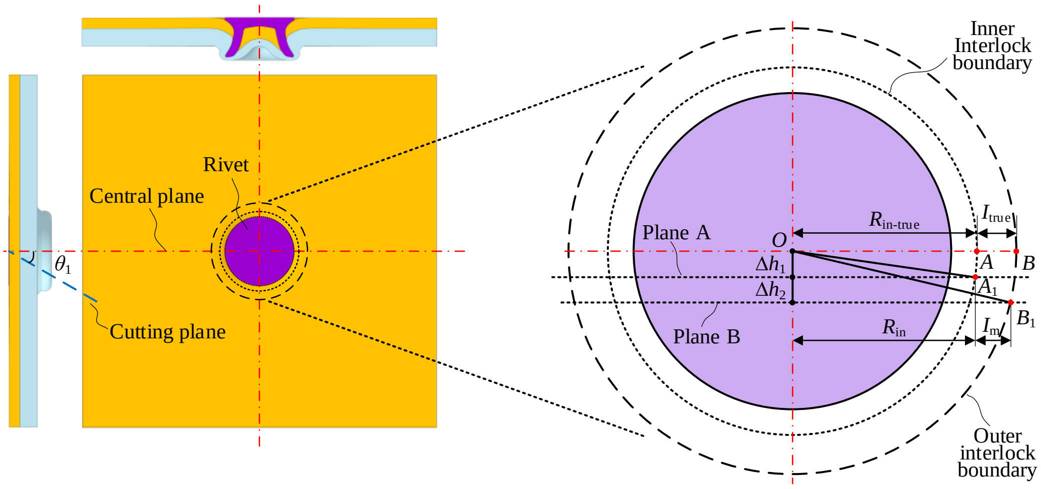

Figure 3.14: Schematic of the interlock values on the joint central plane and the cutting plane with a rotation angle (θ_1)

Figure 3.14 shows the dimensions on the joint central plane and on the cutting plane. According to the geometrical relationships, the I_{m} can be expressed as a function of the $R_{\text{in-true}}$, I_{true}, Δh_1 and Δh_2, as shown in Eq.(3.8). Substituting the Eq.(3.6) and Eq.(3.7) into the (3.8) gives the Eq.(3.9). It can be seen that the I_{m} is not only affected by the horizontal distance from the interlock formation zone to the joint axis (i.e., $R_{\text{in-true}}$), but also influenced by the vertical distance from the interlock formation zone to the rivet head (i.e., S_1 and S_2). To evaluate the effects of the θ_1 on the interlock measurement accuracy, the relative error ($\delta_{rotation}$) and absolute error ($e_{rotation}$) of the interlock with only the θ_1 are calculated using the Eq.(3.10) and Eq.(3.11) respectively. Substituting the Eq.(3.9) into Eq.(3.10) and Eq.(3.11) yields Eq.(3.12) and Eq.(3.13). However, different from the δ_{offset} and e_{offset}, the sign of the $\delta_{rotation}$ and $e_{rotation}$ cannot be determined by simply comparing the structures of Eq.(3.12) and Eq.(3.13).

$$I_m = \sqrt{\left(R_{in-true} + I_{true}\right)^2 - \left(\Delta h_1 + \Delta h_2\right)^2} - \sqrt{R_{in-ture}^2 - \Delta h_1^2} \tag{3.8}$$

$$I_m = \sqrt{\left(R_{in-true} + I_{true}\right)^2 - \left(S_1 + S_2\right)^2 \cdot \tan\theta_1^2} - \sqrt{R_{in-true}{}^2 - S_1^2 \cdot \tan\theta_1^2} \tag{3.9}$$

$$\delta_{rotation} = \frac{I_m - I_{true}}{I_{true}} \times 100\% \tag{3.10}$$

$$e_{rotation} = I_m - I_{true} \tag{3.11}$$

$$\delta_{rotation} = \left(\frac{I_{true} \cdot \left(2R_{in-true} + I_{true}\right) - S_2^{\,2} \cdot \tan\theta_1^2}{I_{true} \cdot \left(\sqrt{\left(R_{in-true} + I_{true}\right)^2 - \left(S_1 + S_2\right)^2 \cdot \tan\theta_1^2} + \sqrt{R_{in-true}^{\;\;2} - S_1^2 \cdot \tan\theta_1^2} \right)} - 1 \right) \times 100\% \quad (3.12)$$

$$e_{rotation} = \frac{I_{true} \cdot \left(2R_{in-true} + I_{true}\right) - S_2^{\,2} \cdot \tan\theta_1^2}{\sqrt{\left(R_{in-true} + I_{true}\right)^2 - \left(S_1 + S_2\right)^2 \cdot \tan\theta_1^2} + \sqrt{R_{in-true}^{\;\;2} - S_1^2 \cdot \tan\theta_1^2}} - I_{true} \quad (3.13)$$

To find out the effects of the θ_1 on the interlock, the $e_{rotation}$ and $\delta_{rotation}$ at different rotation angles (5°, 10°, 15° and 20°) of SPR joints with the Ø5.3mm boron steel rivet and AA5754 sheets were plotted in **Figure 3.15** and **Figure 3.16**. The $R_{\text{in-true}}$ and S_1 were assumed to be fixed at 2.65mm and 3.0mm respectively. This would not affect the changing trend of interlock with varying rotation angles. The I_{true} and the S_2 changed within the ranges of 0.0mm~2.0mm and 0.0mm~4.0mm. It can be seen from **Figure 3.15** that the $e_{rotation}$ was negative in most cases and only had a positive value when the S_2 was very close to zero. This indicates that the I_{m} is more likely smaller than the I_{true} if only the θ_1 existed between the joint central plane and the cutting plane. For a fixed I_{true}, the absolute value of $e_{rotation}$ always demonstrated an increasing trend with the increment of S_2. This means the interlock formed by a larger insertion angle would be less affected by the θ_1 compared with that formed by a larger insertion depth (**Figure 3.13**). For a fixed S_2, the absolute value of $e_{rotation}$ always showed a decreasing trend with the increment of I_{true}. A faster changing speed of $e_{rotation}$ was found with a larger S_2. As shown in **Figure 3.16**, similar changing trends of $\delta_{rotation}$ were observed with the variations of S_2 and I_{true}. It is worth noting that the largest absolute value of $\delta_{rotation}$ was found at a small I_{true} but a large S_2.

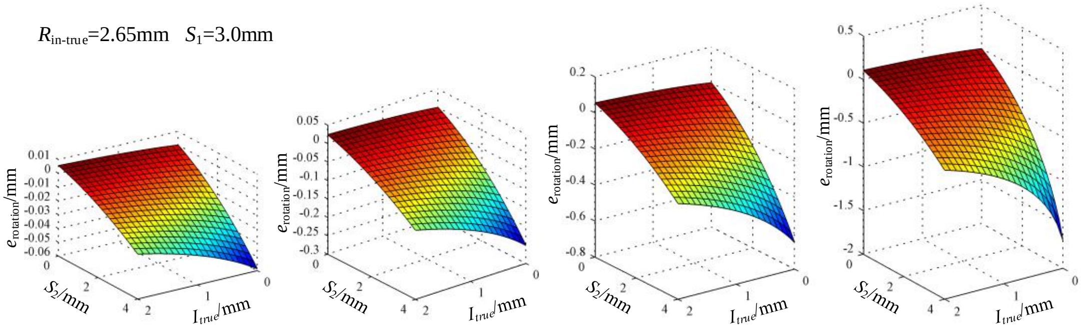

(a) θ_1=5° (b) θ_1=10° (c) θ_1=15° (d) θ_1=20°

Figure 3.15: Absolute error (e_{rotation}) of the interlock with different rotation angles (θ_1)

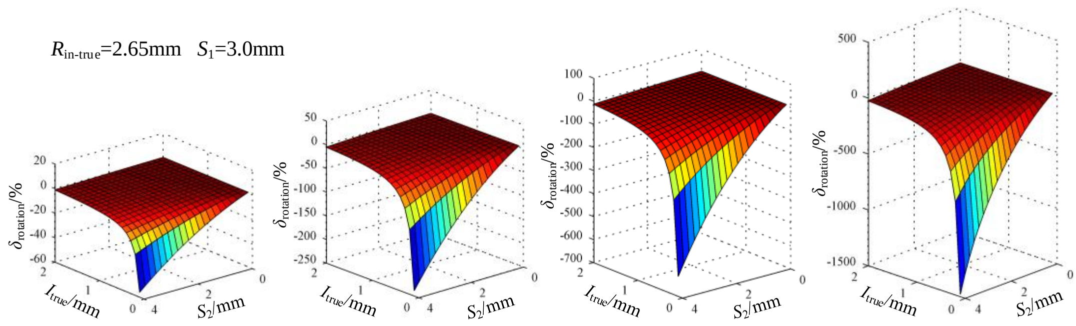

(a) θ_1=5° (b) θ_1=10° (c) θ_1=15° (d) θ_1=20°

Figure 3.16: Relative error ($\delta_{rotation}$) of the interlock with different rotation angles (θ_1)

3.3.2.3. With the offset distance (Δ*h*) and rotation angle (θ_1)

In practical applications, the cutting offset and the cutting rotation more likely occur at the same time. According to the rotation directions of the cutting plane, there are two possible situations as shown in **Figure 3.17**(a) with a positive rotation angle ($\theta_1>0$) and in **Figure 3.17** (b) with a negative rotation angle ($\theta_1<0$). The projected two interlock boundaries (Points A_1 and B_1) move far away from the joint central plane when the θ_1 is positive, while move close to the joint central plane with a negative θ_1. **Figure 3.18** shows the relationships between the I_{true} and the I_m at the two situations. According to the geometrical relationships, the I_m can be calculated using Eq.(3.14) for the $\theta_1>0$ and Eq.(3.15) for the $\theta_1<0$. The Δh_1 and Δh_2 can be calculated with Eq.(3.16). Substituting the Eq.(3.16) into the Eq.(3.14) and Eq.(3.15) yield a same equation Eq.(3.17). So the I_m under the two situations can be calculated using a uniform equation. The relative error ($\delta_{off+rot}$) and absolute error ($e_{off+rot}$) of interlock with Δh as well as θ_1 can be calculated using the Eq.(3.18) and Eq.(3.19) respectively. The sign of $\delta_{off+rot}$ and $e_{off+rot}$ will be positive if the Δh had a dominating effect and be negative if the θ_1 had a greater influence. Due to the multiple variables involved in Eq.(3.17), it is difficult to discuss the changing trends of the $\delta_{off+rot}$ and $e_{off+rot}$. Instead, the interaction effects of Δh and θ_1 on the measurement accuracy of interlock were discussed in the following sections using experimental SPR joint data.

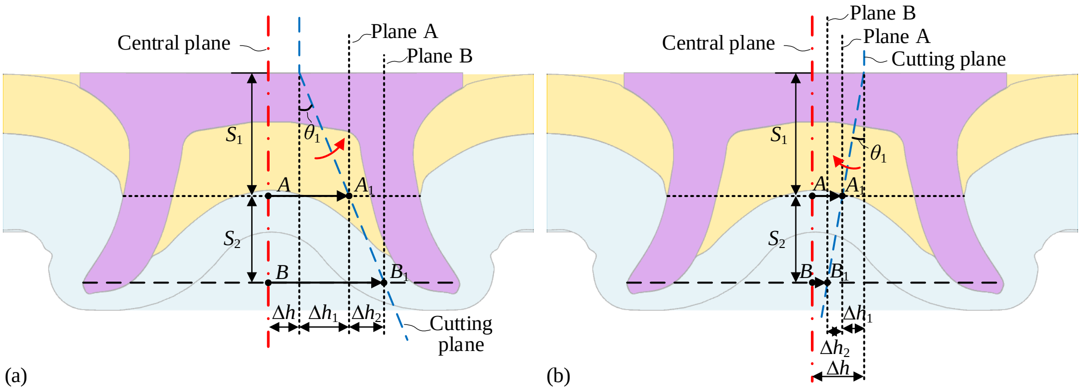

Figure 3.17: Projections of the two interlock boundaries from the joint central plane to the cutting plane with a offset distance (Δh) and a rotation angle (θ_1): (a) $\theta_1>0$ and (b) $\theta_1<0$

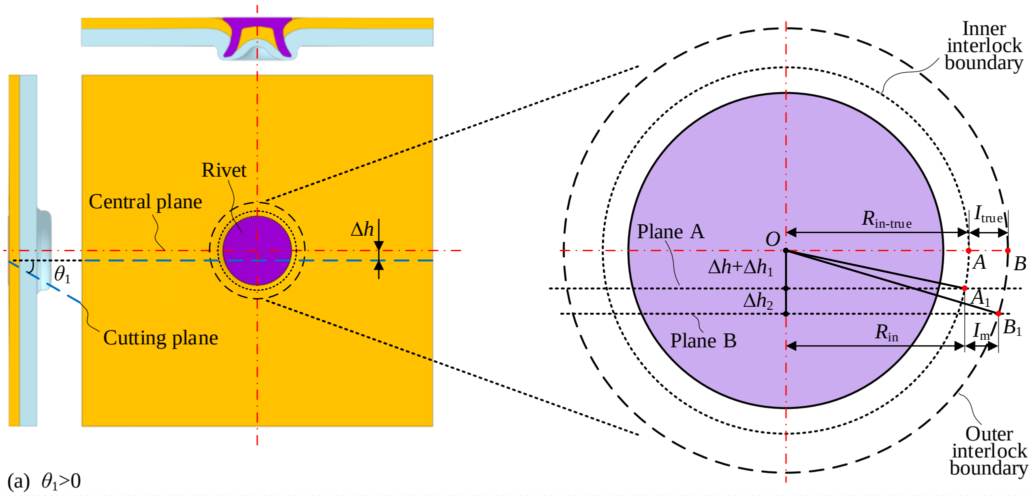
Rivet
Central plane
Δh
θ_1
Cutting plane
Inner interlock boundary
Plane A
O
$R_{\text{in-true}}$
I_{true}
A
B
$\Delta h+\Delta h_1$
Δh_2
A_1
Plane B
R_{in}
I_{m}
B_1
Outer interlock boundary

(a) $\theta_1>0$

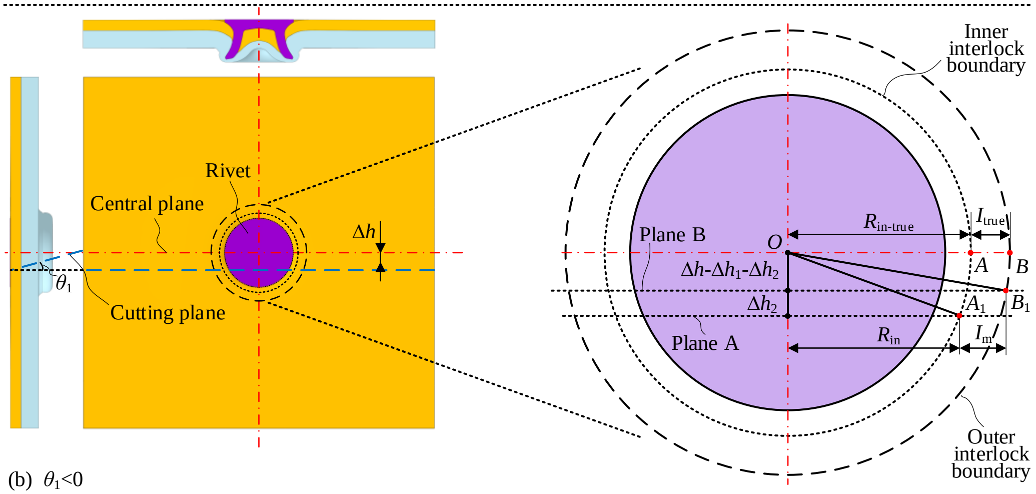
Rivet
Central plane
Δh
θ_1
Cutting plane
Inner interlock boundary
Plane B
O
$R_{\text{in-true}}$
I_{true}
A
B
$\Delta h\text{-}\Delta h_1\text{-}\Delta h_2$
Δh_2
A_1
B_1
Plane A
R_{in}
I_{m}
Outer interlock boundary

(b) $\theta_1<0$

Figure 3.18: Schematics of the interlock on the joint central plane and on the measurement plane with an offset distance (Δh) and a rotation angle (θ_1)

$$I_m=\sqrt{\left(R_{in-true}+I_{true}\right)^2-\left(\Delta h+\Delta h_1+\Delta h_2\right)^2}-\sqrt{R_{in-true}{}^2-\left(\Delta h+\Delta h_1\right)^2} \tag{3.14}$$

$$I_m=\sqrt{\left(R_{in-true}+I_{true}\right)^2-\left(\Delta h-\Delta h_1-\Delta h_2\right)^2}-\sqrt{R_{in-true}{}^2-\left(\Delta h-\Delta h_1\right)^2} \tag{3.15}$$

$$\begin{aligned}&\begin{cases}\Delta h_1=S_1\cdot\tan\theta_1\\ \Delta h_2=S_2\cdot\tan\theta_1\end{cases}\qquad(\theta_1>0)\\ &\begin{cases}\Delta h_1=-S_1\cdot\tan\theta_1\\ \Delta h_2=-S_2\cdot\tan\theta_1\end{cases}\qquad(\theta_1<0)\end{aligned} \tag{3.16}$$

$$I_m=\sqrt{\left(R_{in-true}+I_{true}\right)^2-\left(\Delta h+S_1\cdot\tan\theta_1+S_2\cdot\tan\theta_1\right)^2}-\sqrt{R_{in-true}{}^2-\left(\Delta h+S_1\cdot\tan\theta_1\right)^2} \tag{3.17}$$

$$\delta_{off+rot}=\frac{I_m-I_{true}}{I_{true}}\times 100\% \tag{3.18}$$

$$e_{off+rot}=I_m-I_{true} \tag{3.19}$$

3.3.3. Error estimation of the remaining bottom sheet thickness

As shown in **Figure 3.19**(a), the remaining bottom sheet thickness on the joint cross-sectional profile is directly determined by the infinite points on the upper surface (Red) and lower surface (Black) of the bottom sheet. The projection of these points from the joint central plane to the cutting plane is very similar to that of the two interlock boundary points in **Figure 3.8**. Taking the points *A* and *B* in **Figure 3.19**(a) as an example, the projection trajectories (Circles A and B) of the two points are shown in **Figure 3.19** (b). When with the Δh or θ_1, only part of these points can be projected from the joint central plane to the cutting plane. Meanwhile, the relative positions of these points would be affected during the projection process, and become different from the original ones on the joint central plane. This would lead to an unrealistic bottom sheet thickness distribution. Therefore, the influences of the three types of improper cutting positions on the captured bottom sheet profile were analysed and discussed qualitatively.

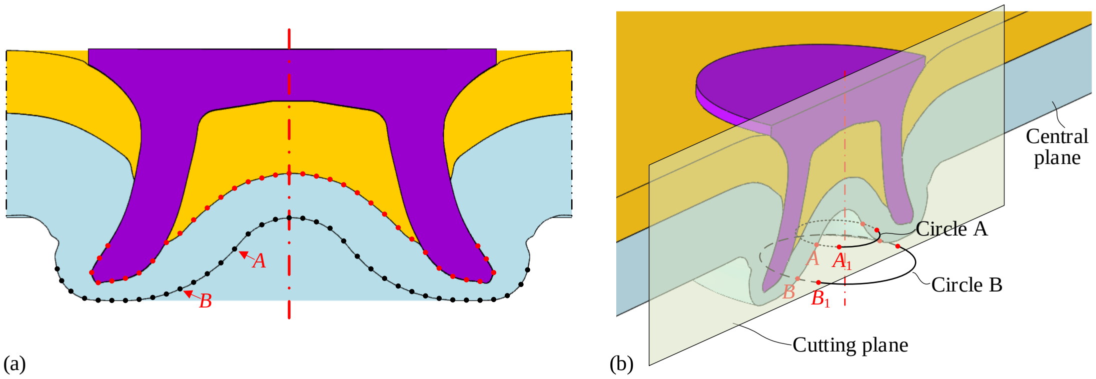

(a)

(b)

Figure 3.19: Schematics of (a) points located on the upper and lower surfaces of the bottom sheet and (b) projection of the boundary points *A* and *B* from the joint central plane to the cutting plane

3.3.3.1. With only the offset distance (Δ*h*)

Figure 3.20 shows the true bottom sheet profile on the joint central plane and the captured one on the cutting plane with the Δh. It can be seen that only the bottom sheet profile in the green region of **Figure 3.20** (b) was projected onto the cutting plane as shown in **Figure 3.20** (c). The bottom sheet profile in the yellow region of **Figure 3.20** (b) could not be projected onto the cutting plane and thus the thickness data in this region was not accessible on the cutting plane. The width of the yellow region is two times of the Δh, which means the amount of missing thickness data increase with the increment of the Δh.

It can also be found that the shape of the green region in **Figure 3.20** (b) is quite different from that of the blue region in **Figure 3.20** (c). During the projection process, the green region was stretched along the horizontal direction in order to cover the larger blue region. **Figure 3.21** shows the projection trajectories of these boundary points from the green region to the blue region. The radius of the projection trajectory is different for each point and equals to the distance from the projected point to the original point O. Due to the different trajectory radiuses, a large distortion occurred around the joint central region while a limited distortion was found around the rivet tip. For example, the green region between points A_1 and B_1 was stretched to a wider blue region between the points A_3 and B_3. While the green region between points D_1 and E_1 was stretched to an almost same width blue region between the points D_3 and E_3.

According to the projection pattern, the bottom sheet thickness along the vertical direction in the green region of **Figure 3.20** (b) can be exactly measured on the cutting plane but with a position shift ($\leq \Delta h$). While the measured thickness along the direction perpendicular to the bottom sheet surface would be greater than the true values in the green region. Because of the different distortion levels on the blue region, the bottom sheet thickness measured around the joint central area would have a higher measurement error than that measured around the rivet tip. In other words, the measurement error of bottom sheet thickness demonstrates a decreasing trend from the joint centre to the rivet tip, as presented in **Figure 3.20** (c).

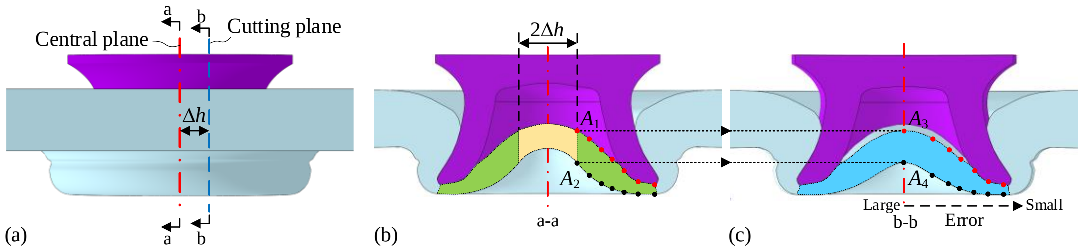

Figure 3.20: Schematic of the (a) ideal and actual cutting positions, (b) the bottom sheet profile on the joint central plane and (c) the bottom sheet profile on the cutting plane with an offset distance (Δh)

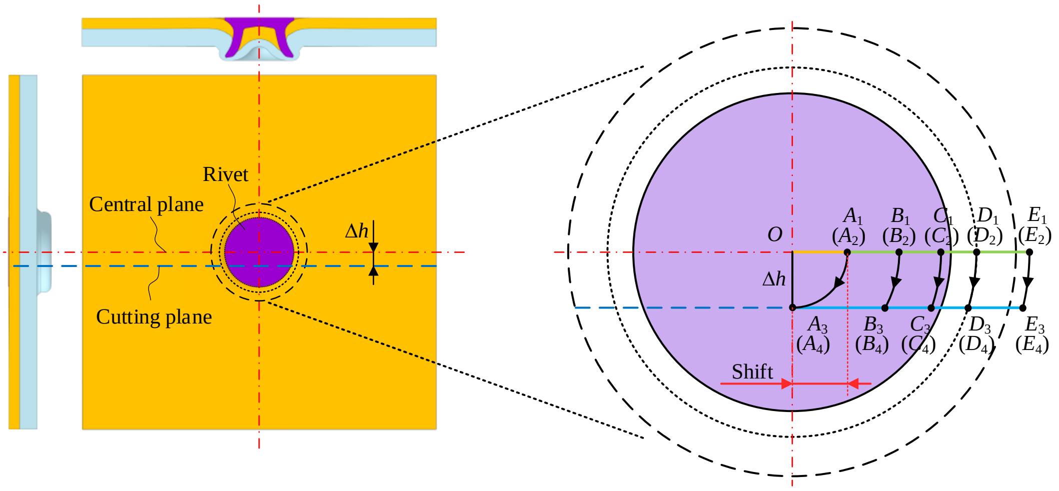

Figure 3.21: Projection trajectories of the boundary points from the joint central plane to the cutting plane with an offset distance (Δh)

Taking the SPR joint with the 1.2mm+2.0mm AA5754 sheets and the 6.0mm long boron steel rivet as an example, the virtually captured bottom sheet profiles with offset distances 0.0mm, 0.5mm, 1.0mm and 1.5mm are compared in **Figure 3.22**. It can be seen that the Δh showed very limited influences on the bottom sheet profile when the Δh had a small value (e.g., 0.5mm), as shown in **Figure 3.22** (a). The captured bottom sheet profile with Δh=0.5mm was still very close to that from the joint central plane (Δh=0.0mm). So the measurement error of bottom sheet thickness would maintain at a very low level. However, when the Δh increased to larger values (e.g., 1.0mm and 1.5mm), as shown in **Figure 3.22** (b), the inspected bottom sheet profiles became quite different from that on the joint central plane, especially around joint central area. Because of the high-level measurement error, the real quality of the deformed bottom sheet could not be reflected by the measured bottom sheet thickness on the cutting plane. Therefore, it is necessary to control the Δh within a small range in order to accurately evaluate the quality of the deformed bottom sheet.

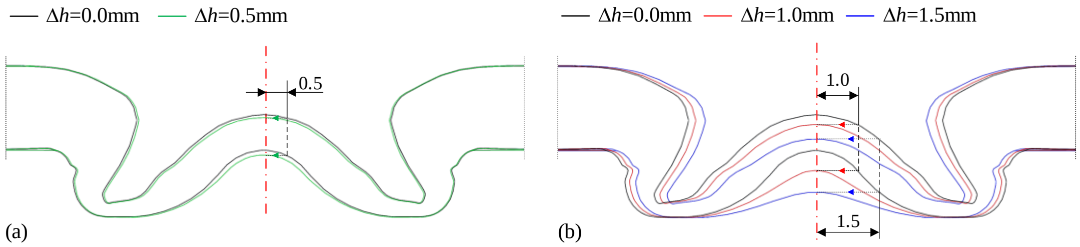

Figure 3.22: Virtually captured bottom sheet profiles on the cutting plane with different offset distances (Δh): (a) 0.0mm and 0.5mm, and (b) 0.0mm, 1.0mm and 1.5mm

3.3.3.2. With only the rotation angle (θ_1)

Figure 3.23 shows the captured bottom sheet profiles on the joint central plane and on the cutting plane with the θ_1. Similar to the Δh, the θ_1 would also lead to thickness data missing of the bottom sheet as well as distorted bottom sheet profile on the cutting plane. As presented in **Figure 3.23** (b), the width of this thickness data missing region (Yellow region) is determined not only by the θ_1 but also the relative distance between the rivet head and the bottom sheet. Increments of the θ_1 or the relative distance could result in more missing data of the bottom sheet thickness. Only the green region in **Figure 3.23** (b) was projected to the blue region in **Figure 3.23** (c) on the cutting plane. **Figure 3.24** shows the projection trajectories of these boundary points from the green region to the blue region. Due to the existence of θ_1, the boundary points on the green region were projected to different planes paralleling to the joint central plane. Different from with only the Δh, it can be seen that the boundary points located on the same vertical line in the green region (e.g., points B_1 and B_2) were projected to different vertical lines (e.g., points B_3 and B_4). As a result, the measured bottom sheet thickness along the vertical direction on the cutting plane in **Figure 3.23** (c) would be slightly larger than the true value on the joint central plane shown in **Figure 3.23** (b). The measured bottom sheet thickness along the direction perpendicular to the bottom sheet surface would be more likely larger than the true value.

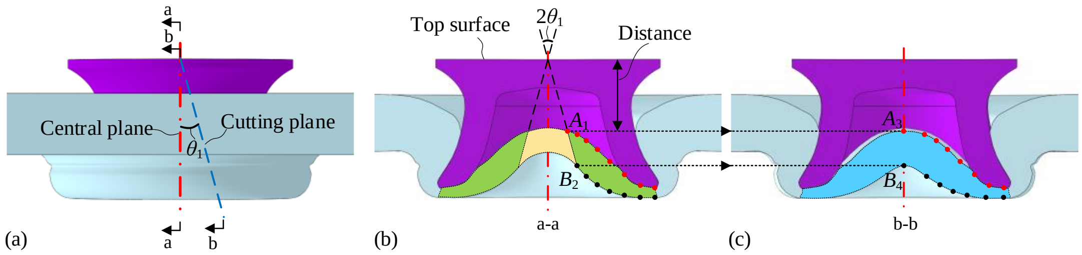
a
b
Central plane
Cutting plane
θ_1
(a)
a
b
Top surface
$2\theta_1$
Distance
A_1
B_2
a-a
(b)
A_3
B_4
b-b
(c)

Figure 3.23: Schematic of the (a) ideal and actual cutting positions, (b) the bottom sheet profile on the joint central plane and (c) the bottom sheet profile on the cutting plane with a rotation angle (θ_1)

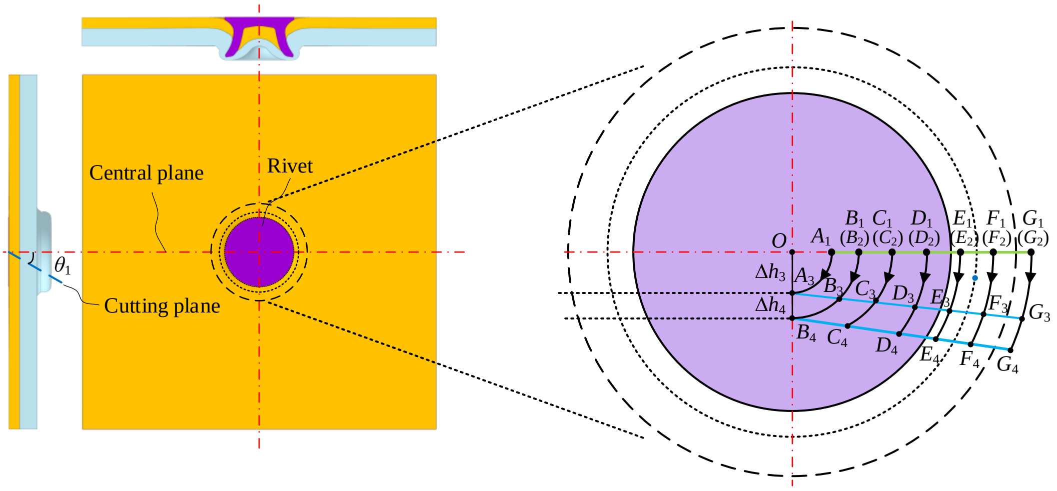
Central plane
Rivet
θ_1
Cutting plane
O
A_1
B_1 C_1 D_1 E_1 F_1 G_1
(B_2) (C_2) (D_2) (E_2) (F_2) (G_2)
Δh_3
Δh_4
A_3 B_3 C_3 D_3 E_3 F_3 G_3
B_4 C_4 D_4 E_4 F_4 G_4

Figure 3.24: Projection trajectories of the boundary points from the joint central plane to the cutting plane with a rotation angle (θ_1)

Taking the SPR joint with 1.2mm+2.0mm AA5754 sheets and 6.0mm long boron steel rivet as an example, the virtually captured bottom sheet profiles with rotation angles 0°, 5°, 10°, 15° and 20° are compared in **Figure 3.25**. As shown in **Figure 3.25** (a), the captured bottom sheet profile on the cutting plane with θ_1=5° was almost the same with that on the joint central plane (θ_1=0°). However, obviously different bottom sheet profiles were observed when the θ_1 increased to larger values (i.e., 10°, 15° and 20°) as shown in **Figure 3.25** (b). It can be seen that the θ_1 imposed a larger influence on the lower boundary (Zone1) than the upper boundary (Zone2) of the bottom sheet. Therefore, it is very important to control the θ_1 within a small range to accurately evaluate the quality of the deformed bottom sheet.

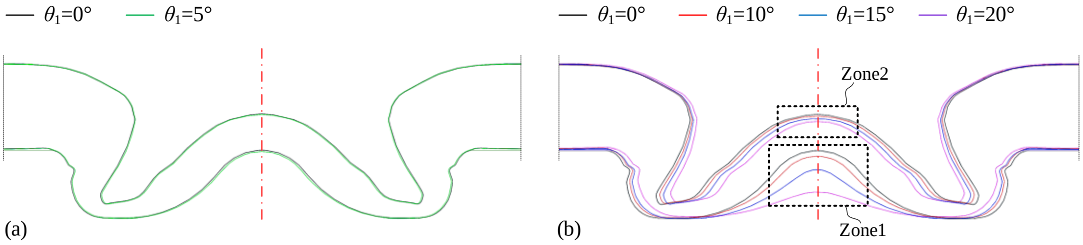

Figure 3.25: Virtually captured bottom sheet profiles on the cutting plane with different rotation angles (θ_1): (a) 0°, 5°, and (b) 0°, 10°, 15°, 20°

3.3.3.3. With the offset distance (Δ*h*) and rotation angle (θ_1)

When the cutting offset and the cutting rotation occurred at the same time, the effects of the Δ*h* and θ_1 would be superimposed to affect the bottom sheet profile. It is worth noting that the rotation direction of the cutting plane would impose different influences on the bottom sheet profile, as shown in **Figure 3.26**. When with a positive rotation angle ($\theta_1>0$), a larger part of the bottom sheet profile (yellow region) on the joint central plane cannot be projected onto the cutting plane as presented in **Figure 3.26** (a). This would lead to a larger measurement error of bottom sheet thickness than with only a Δ*h* or only a θ_1. In contrast, when with a negative rotation angle ($\theta_1<0$) as presented in **Figure 3.26** (b), the missing thickness data caused by the Δ*h* would reduce to a smaller amount (yellow region). This effectively reduces the distortion degree of the captured bottom sheet profile and improves the measurement accuracy of bottom sheet thickness.

Previously, the bottom sheet profiles of the SPR joint with AA5754 sheets and 6.0mm long rivet with varying Δ*h* and θ_1 have been compared in **Figure 3.22** and **Figure 3.25** respectively. With both of the Δ*h* and θ_1, the captured bottom sheet profile would be determined by the relative magnitudes of the Δ*h* and θ_1. Due to the plentiful combinations of the Δ*h* and θ_1, the bottom sheet profiles of this SPR joint at different cutting positions were not presented here.

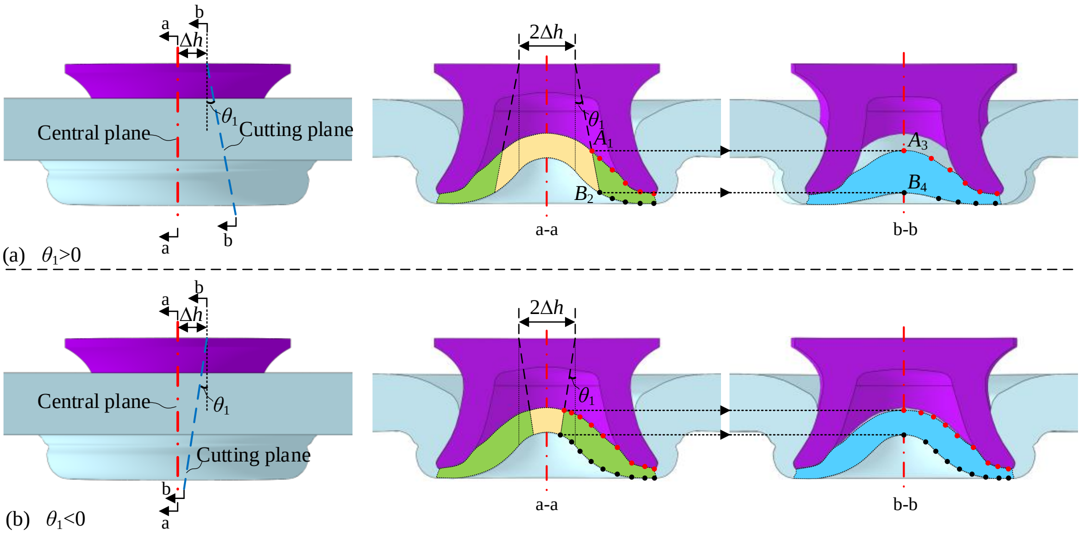

Figure 3.26: Schematic of the bottom sheet profiles on the joint central plane and on the cutting plane with an offset distance (Δ*h*) and a rotation angle (θ_1)

As discussed above, the appearances of the Δ*h* and θ_1 would affect the captured bottom sheet profile on the cutting plane. As a result, the measurement accuracy of the $T_{\min}$ would be inevitably influenced. Depending on the formation position, the measured $T_{\min}$ may have different error levels. If the $T_{\min}$ was formed around the joint central area, it may have a very large error because of the missing thickness data (yellow region in **Figure 3.26**) and the large bottom sheet profile distortion around the joint central area. In contrast, if the $T_{\min}$ was formed around the rivet tip, it more likely has a limited error due to the minor distortion of the bottom sheet profile around the rivet tip.

3.3.4. Correction of cutting position's effects on the joint quality indicators

Under the conditions when the SPR joints were not or could not be sectioned through the joint central plane (e.g., joints cut from the car BIW), it is important and necessary to correct/compensate the errors of joint quality indicators induced by the improper cutting position. As previously discussed, the rivet head height (*H*) is not affected by the cutting position and thus does not need any correction. In addition, because the bottom sheet profile is determined by an infinite number of points on the upper and lower surfaces of the deformed bottom sheet, it is very difficult to correct the error of the remaining bottom sheet thickness. First of all, the missing thickness data in the yellow region of the joint central plane (as shown in **Figure 3.26**) cannot be recovered from the captured joint profile on the cutting plane; Secondly, it is possible but requires a huge workload to eliminate the distortion of the captured bottom sheet profile from the cutting plane. Therefore, the correction of the bottom sheet thickness was not discussed in this study.

For the interlock, its value is only determined by the positions of the inner and outer interlock boundaries. Therefore, it is relatively easy to correct the interlock error induced by the improper cutting position. According to the geometrical relationships shown in **Figure 3.18**, the I_{true} can be expressed as a function of six dimensions measured on the sectioned joint specimen, as shown in Eq.(3.20). The R_{in} is the measured radius of the inner interlock boundary on the cutting plane. **Figure 3.27** shows the procedures to correct the interlock error in practical applications: First, the Δh and θ_1 were measured from the sectioned specimen; Then, the joint cross-sectional profile was captured, and the S_1, S_2, R_{in} and I_{m} were measured; Finally, all the six measured parameters were entered into the Eq.(3.20) to calculate the I_{true}.

$$I_{true} = \sqrt{\left(R_{in} + I_m\right)^2 + \left(\Delta h + S_1 \cdot \tan\theta_1 + S_2 \cdot \tan\theta_1\right)^2} - \sqrt{{R_{in}}^2 + \left(\Delta h + S_1 \cdot \tan\theta_1\right)^2} \tag{3.20}$$

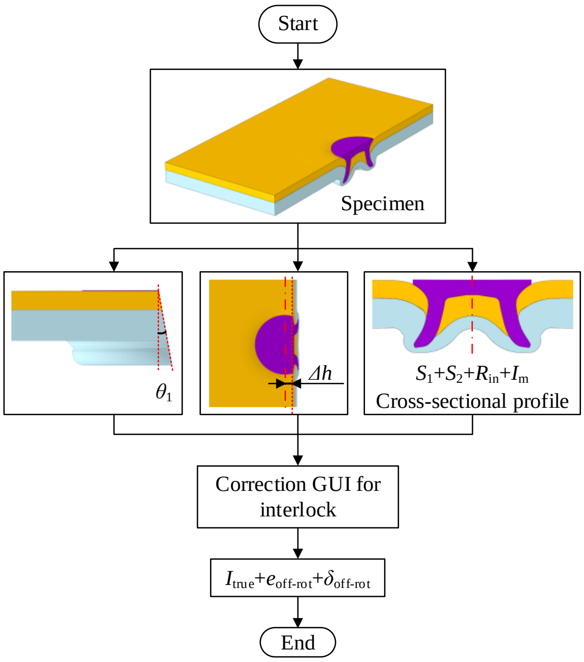
Start
Specimen
θ_1
Δh
$S_1+S_2+R_{in}+I_m$
Cross-sectional profile
Correction GUI for interlock
$I_{true}+e_{off\text{-}rot}+\delta_{off\text{-}rot}$
End

Figure 3.27: Flow chart for the interlock error correction in practical applications

In practical applications, measurement of the six parameters (i.e., Δh, θ_1, S_1, S_2, R_{in} and I_m) is very critical for the correction result of interlock. There are two ways to get the value of Δh: (1) Directly measure the diameter of the rivet head (D_h) and the remaining rivet head thickness perpendicular to the sectioned surface (l_1) on the specimen as shown in **Figure 3.28**(a), and then calculate the Δh using Eq.(3.21); (2) Measure the diameter of the rivet head (D_h) and the width of the rivet head (D_{h-m}) on the captured joint cross-sectional profile as presented in **Figure 3.28** (b), and then calculate the Δh using Eq.(3.22). Similarly, there are also two approaches to obtain the θ_1: (1) Directly measure the included angle (α) between the top surface of rivet head and the joint sectioned surface as shown in **Figure 3.28** (c), and then calculate the θ_1 using Eq.(3.23); (2) Measure the height of the captured joint cross-sectional profile from direction A (l_2) and the height of the captured joint cross-sectional profile from the direction B (l_3) as shown in **Figure 3.28** (d), and then calculate the θ_1 using Eq.(3.24).

$$\Delta h = l_1 - \frac{D_h}{2} \tag{3.21}$$

$$\Delta h = \frac{1}{2}\sqrt{{D_h}^2 + {D_{h-m}}^2} \tag{3.22}$$

$$\theta_1 = \alpha - \frac{\pi}{2} \tag{3.23}$$

$$\theta_1 = \arccos\left(\frac{l_2}{l_3}\right) \tag{3.24}$$

For the S_1, S_2, R_{in} and I_m, the observation directions (A or B) would not affect the measured values of the R_{in} and I_m but would influence the values of the S_1 and S_2. When observing the joint cross-sectional profile along the direction vertical to the joint central plane (Direction A), the positions of interlock boundaries along the vertical direction would not be affected by the Δh and θ_1. In other word, the measured S_1 and S_2 will be exactly equal to the values on the joint central plane. In contrast, when observing the joint cross-sectional profile along the direction vertical to the cutting plane (Direction B), the positions of interlock boundaries would be affected by the Δh and θ_1. As a result, the measured S_1 and S_2 became slightly larger than the values on the joint central plane. Therefore, it is suggested to measure these four parameters on the joint cross-sectional profile captured along the direction A. Moreover, it is also worth noticing that, compared with the joint profile captured from the direction A, the joint profile captured from the direction B was slightly stretched along the vertical direction, as shown in **Figure 3.28** (d). This leads to a larger distortion of the captured joint cross-sectional profile, and would affect the quality evaluation of the deformed bottom sheet. Therefore, it is recommended to inspect the joint cross-sectional profile along the direction A and then evaluate the joint quality.

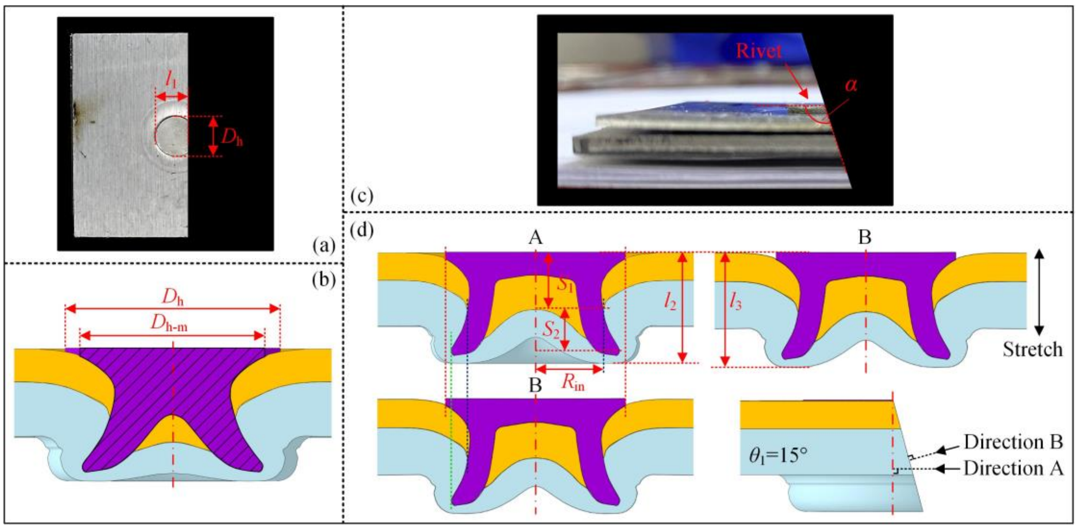

Figure 3.28: Strategies to obtain the six parameters (Δh, θ_1, S_1, S_2, R_{in} and I_m) for the interlock error correction

3.4. Assessment of the Proposed Estimation and Correction Methods

Using the proposed approach, the cutting position's influences on the measurement accuracy of interlock in physical SPR joints were estimated. The effectiveness of the developed interlock error correction method was also verified.

3.4.1. Development of graphical user interface (GUI)

For an easier use in practical applications, two graphical user interfaces for the interlock error estimation and correction were developed using the App Designer in MATLAB R2018a, as shown in **Figure 3.29**. In the GUI for interlock error correction, the initial interlock errors of the sectioned SPR joint were also calculated. The two GUIs were used in the following sections.

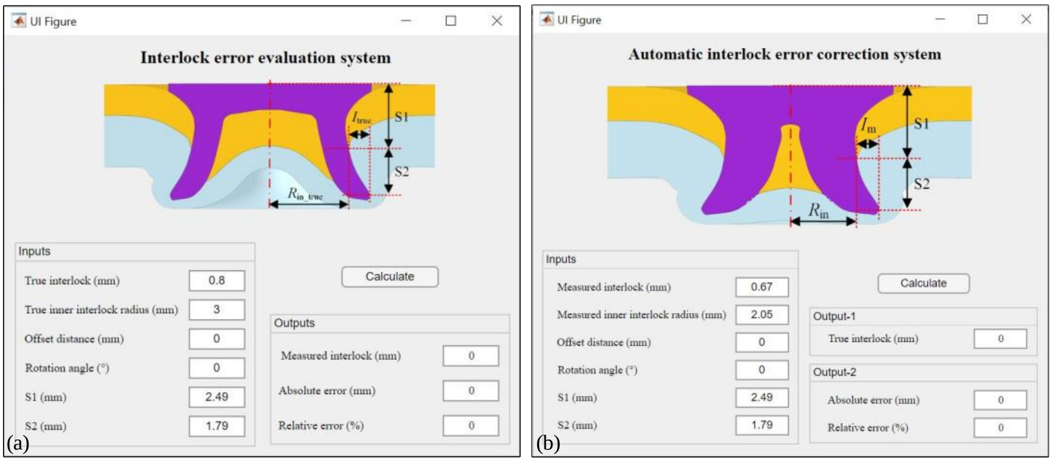

Inputs
True interlock (mm) 0.8
True inner interlock radius (mm) 3
Offset distance (mm) 0
Rotation angle (°) 0
S1 (mm) 2.49
S2 (mm) 1.79

Outputs
Measured interlock (mm) 0
Absolute error (mm) 0
Relative error (%) 0

Inputs
Measured interlock (mm) 0.67
Measured inner interlock radius (mm) 2.05
Offset distance (mm) 0
Rotation angle (°) 0
S1 (mm) 2.49
S2 (mm) 1.79

Output-1
True interlock (mm) 0

Output-2
Absolute error (mm) 0
Relative error (%) 0

Figure 3.29: Developed graphical user interfaces (GUI) for (a) interlock error estimation and (b) interlock error correction

3.4.2. Experiment design

Ø5.3mm boron steel rivets (Hardness: 280±30HV10) and aluminium alloy AA5754 sheets were used throughout the experiment. Fifteen SPR joints with different configurations were made as listed in **Table 3.1**. The top sheet thickness (T_t), bottom sheet thickness (T_b), rivet length (L_1) and die type varied from joint to joint. The specimen size is 40mm×40mm as presented in **Figure 3.30**. **Figure 3.31** illustrates the dimensions of the rivets and dies used in the experimental SPR tests. The intrinsic variability of the SPR process inevitably brings many variations into the joining process and thus affects the final laboratory test results. To minimise such effects, repeated trials were usually performed when evaluating the SPR joint quality. However, this chapter focused on the measurement error for the individual joint, and thus only one sample was made for each joint configuration. All the fifteen joints were manufactured using a servo SPR system manufactured by Tucker GmbH, as shown in **Figure 3.32**. This riveting system is displacement controlled rather than pressure controlled, and therefore the rivet head heigh (H) was set to 0.0mm for all the joints. The riveting speed is 300mm/s, and the clamping force of the blank-holder is approximately 5.0~6.0kN.

All the specimens were sectioned using an abrasive-wheel cutting machine. To ensure the cutting plane is as close as possible to the joint centre plane, the specially designed fixtures for the 40mm×40mm specimen were used during the riveting and the cutting processes. The cross-sectional profile for each joint was captured using an optical microscope after the surface polishing. The experimentally captured fifteen joint cross-sectional profiles are shown in **Figure 3.33**, and all of them were assumed to be the true joint profiles on the joint central plane. The necessary dimensions, including the S_1, S_2, $R_{\text{in-true}}$ and I_{true}, were measured and recorded in **Table 3.1**. Then, the interlock errors for each SPR joint were estimated if these joints were improperly sectioned at different cutting positions.

Table 3.1: Joint configurations and experiment results

Joint no.	Thickness (mm)		Rivet (Boron steel)	Die	Experiment results			
	Top sheet/T_t (AA5754)	Bottom sheet/T_b (AA5754)			S_1 (mm)	S_2 (mm)	$R_{\text{in-true}}$ (mm)	I_{true} (mm)
3-1	1.2	1.0	C5.3*5.0 (280±30HV10)	Pip die-A	2.60	0.71	3.47	0.45
3-2	1.2	1.2			2.60	0.87	3.18	0.50
3-3	1.2	1.5			2.72	0.97	3.11	0.54
3-4	1.2	2.0			2.54	1.24	2.86	0.66
3-5	1.0	1.5			2.34	1.16	2.99	0.61
3-6	1.5	1.5			2.95	0.86	3.19	0.42
3-7	1.5	1.2	C5.3*6.0 (280±30HV10)	Pip die-A	2.76	1.06	3.16	0.74
3-8	1.5	1.5			2.52	0.98	3.37	0.84
3-9	1.5	2.0			2.57	1.10	3.18	0.92
3-10	1.2	2.0			2.44	1.66	3.06	0.97
3-11	1.8	2.0			2.92	0.98	3.23	0.68
3-12	2.5	2.0			3.45	0.56	3.60	0.38
3-13	1.2	2.0	C5.3*6.0 (280±30HV10)	Flat die-A	2.68	2.11	2.84	0.93
3-14	1.8	2.0			3.16	1.61	2.94	0.78
3-15	2.5	2.0			3.65	0.74	3.28	0.49

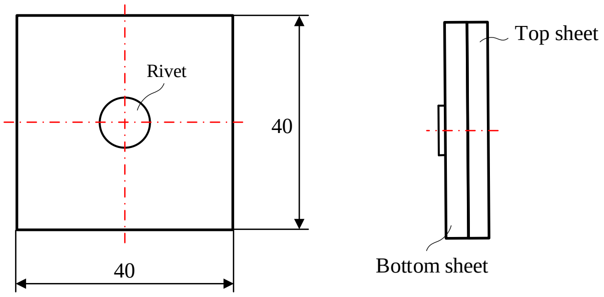

Figure 3.30: Specimen dimensions of the SPR joint (in mm)

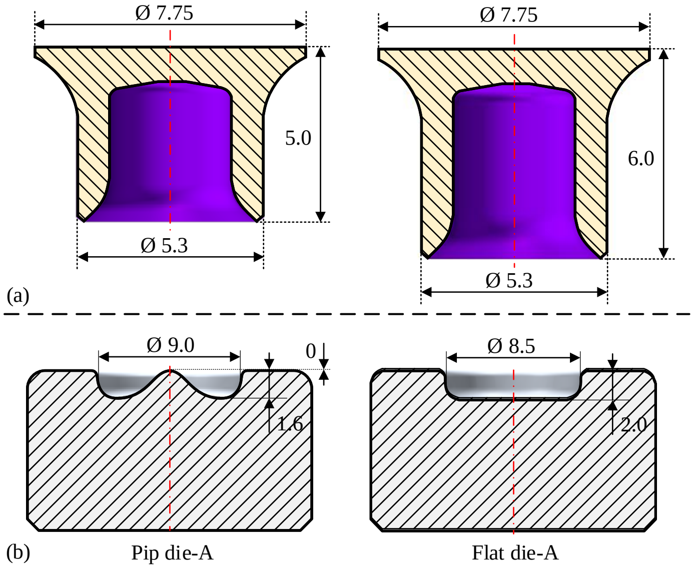
Ø 7.75
5.0
Ø 5.3
Ø 7.75
6.0
Ø 5.3
(a)
Ø 9.0
0
1.6
Ø 8.5
2.0
(b)
Pip die-A
Flat die-A

Figure 3.31: Dimensions of the (a) semi-tubular rivets and (b) dies (in mm)

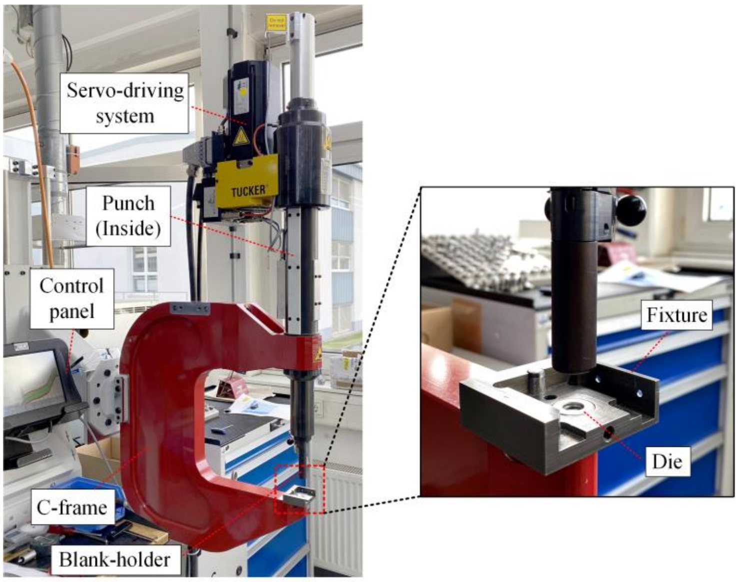
Servo-driving system
Punch (Inside)
Control panel
C-frame
Blank-holder
TUCKER
Fixture
Die

Figure 3.32: Structure of the Tucker SPR system

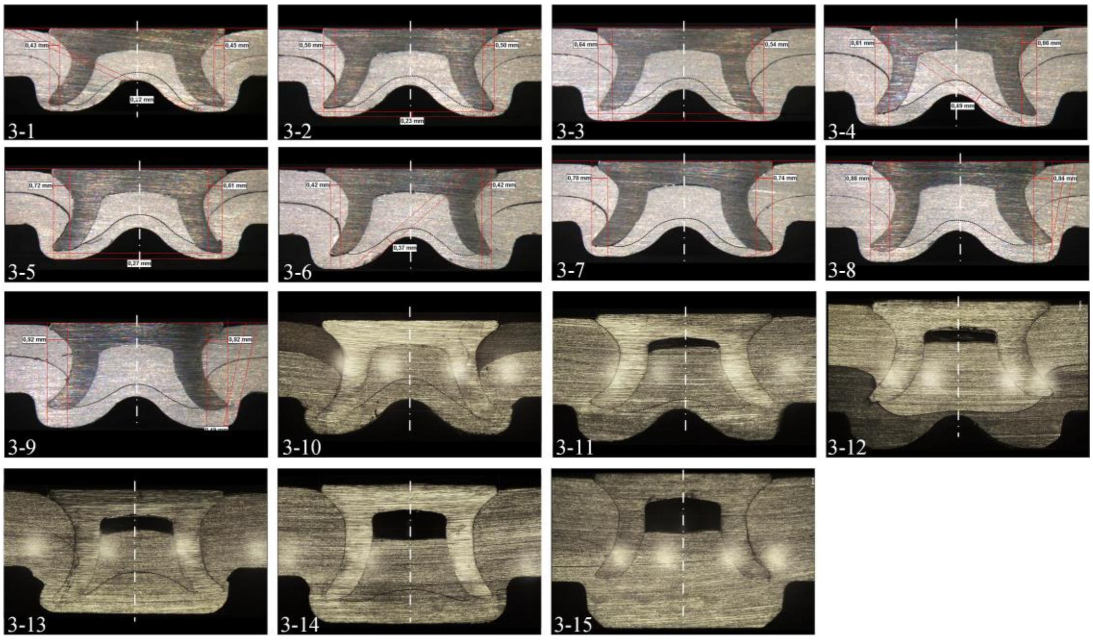

Figure 3.33: Joint cross-sectional profiles from experimental SPR tests

To verify the performance of the proposed interlock correction method, each SPR joint should be sectioned at different cutting positions. However, because every experimentally manufactured SPR joint is unique, it is very difficult to experimentally cut one SPR joint at different cutting positions (e.g., Ten positions) and observe the cross-sectional profiles. In order to overcome this difficulty, an alternative approach was proposed as shown in **Figure 3.34**. Firstly, a 2D geometry of the experimentally captured joint cross-sectional profile was extracted and used to establish a 3D dummy SPR joint in SolidWorks 2018. Then, this dummy joint was sectioned at different cutting positions, and the corresponding joint cross-sectional profiles were recorded. Finally, the interlock error at each cutting position was accessed and compensated using the proposed error correction method. The developed dummy model may be not exactly the same to the experimentally tested one, whilst this would not affect the performance assessment of the proposed interlock error correction method. In this research, taking the joint 3-10 as an example, the performance of the proposed interlock correction method was evaluated. The dummy joint 3-10 was sectioned at ten different cutting positions as listed in **Table 3.2** and the necessary data (i.e., S_1, S_2, I_m and R_{in}) was collected from the captured joint cross-sectional profiles. The P0 is the referenced cutting position (Δh=0mm, θ_1=0). Finally, the measured interlock from the remaining nine positions was corrected and compared with the interlock at the position P0.

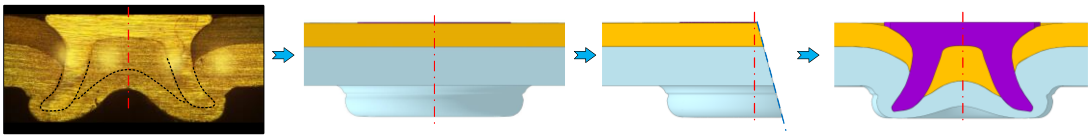
Joint cross-sectional profile
Dummy Joint model
Virtal Cutting at different positions
Joint cross-sectional profile

Figure 3.34: Procedures to virtually cut the SPR joint at different cutting positions and capture the corresponding cross-sectional profiles

Table 3.2: Ten cutting positions of the dummy joint 3-10

Position no.	Offset distance Δh (mm)	Rotation angle θ_1 (°)
P0	0.0	0.0
P1	0.5	5.0
P2	0.5	10.0
P3	0.5	15
P4	1.0	5.0
P5	1.0	10
P6	1.0	15
P7	1.5	5.0
P8	1.5	10
P9	1.5	15

3.4.3. Results and discussion

3.4.3.1. Interlock error with only the offset distance (Δ*h*)

Based on the proposed approach, as shown in **Figure 3.35**(a), the $R_{\text{in-true}}$ and I_{true} from the joint central plane should be used to evaluate the influences of the Δh on the measurement errors of the interlock. Under this ideal condition, a Δh was introduced into the $R_{\text{in-true}}$ and I_{true} to calculate the I_{m} by the Eq.(3.1). Then, the δ_{offset} and e_{offset} were estimated with the I_{true} and the I_{m}. However, in practice, the $R_{\text{in-true}}$ and I_{true} cannot be experimentally measured even with the assistance of specially designed fixtures. To verify the effectiveness of the proposed assessment method under practical conditions, as shown in **Figure 3.35** (b), an initial error was considered by introducing an initial offset distance (Δh_0). The calculated initially measured radius of inner interlock boundary (R_{in0}) and the initially measured interlock (I_{m0}) were regarded as the experimentally measured values. R_{in0} can be obtained by the Eq.(3.25) according to the geometrical relationships shown in **Figure 3.18**. Then, a Δh was introduced into the R_{in0} and I_{m0}, and the corresponding δ_{offset} and e_{offset} were evaluated using the calculated I_{m0} and the I_{m}.

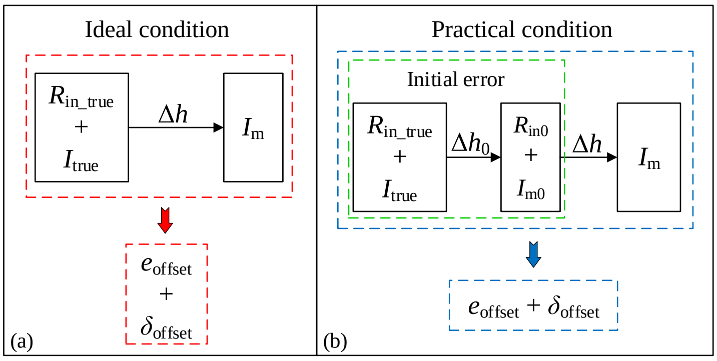

Figure 3.35: Estimation of the interlock errors caused by the offset distance (Δ*h*) under the (a) ideal condition and (b) practical condition

$$R_{in0} = \sqrt{R_{in-true}^2 - \left(\Delta h + S_1 \cdot \tan\theta_1\right)^2} \tag{3.25}$$

Figure 3.36 shows the calculated δ_{offset} and e_{offset} under the ideal condition (solid lines) and the practical condition (dash lines) for the 15 SPR joints in **Table 3.1**. For simplicity, the Δh_0 and Δh were set to same values in this study. It can be seen that, when the Δh equalled to 0.5mm and 1.0mm, the δ_{offset} and e_{offset} under the two conditions were almost the same (black and red lines). The calculated δ_{offset} and e_{offset} under the practical condition were still very close to that under the ideal condition with the Δh increasing to 1.5mm (blue lines). However, when the Δh further increased to 2.0mm, the δ_{offset} and e_{offset} under the practical condition became much larger than that under the ideal condition (green lines). Therefore, it is reasonable to believe that the error level of interlock can be estimated directly using the experimentally measured R_{in} and I_{m} as long as the Δh was smaller than 1.5mm. The e_{offset} fluctuated around 0.01mm, 0.025mm and 0.07mm for the Δh=0.5mm, 1.0mm and 1.5mm respectively. This means the measured interlock was always larger than the true interlock when only with the Δh. The δ_{offset} fluctuated around 1%, 5% and 10% for the Δh=0.5mm, 1.0mm and 1.5mm respectively. This indicated that the measured interlock can still maintain a very high accuracy if the Δh is smaller than 1.0mm.

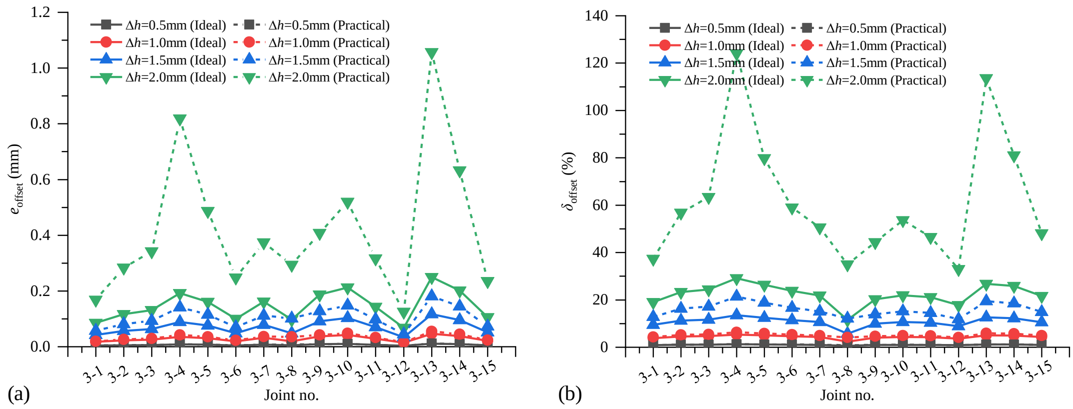

Figure 3.36: Estimated (a) absolute error e_{offset} and (b) relative error δ_{offset} of the tested SPR joints with different offset distances (Δ*h*)

3.4.3.2. Interlock error with only the rotation angle (θ_1)

When only with the θ_1, the measurement errors of interlock under the ideal and practical conditions for the 15 SPR joints were also calculated and compared. As shown in **Figure 3.37**(a), under the ideal condition, a θ_1 was introduced to calculate the I_{m}. Then, the I_{true} and the I_{m} were used to evaluate the $\delta_{rotation}$ and $e_{rotation}$. While under the practical condition, the $R_{\text{in\_true}}$ and I_{true} cannot be experimentally measured. As shown in **Figure 3.37**(b), an initial error was considered by introducing an initial rotation angle (θ_0). Then, the calculated R_{in0} and I_{m0}

were used to calculate the I_{m}. Finally, the $I_{\mathrm{m}0}$ and the I_{m} were used to calculate the $\delta_{rotation}$ and $e_{rotation}$ under the practical condition.

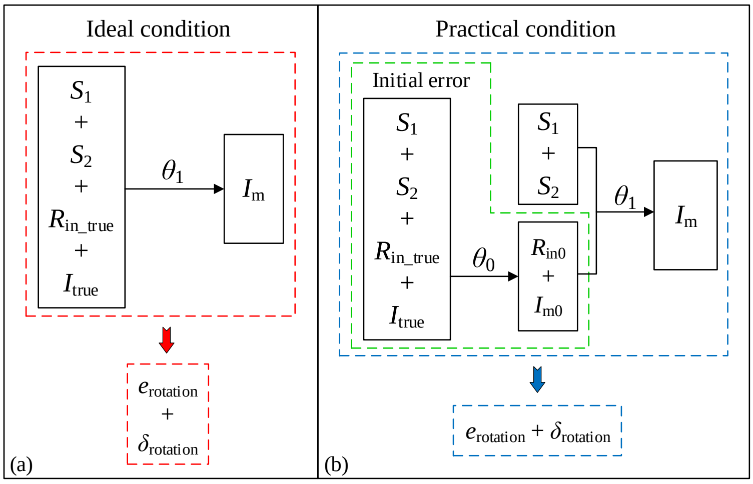
Ideal condition
S_1 + S_2 + $R_{\mathrm{in\_true}}$ + I_{true}
θ_1
I_{m}
e_{rotation} + $\delta_{\mathrm{rotation}}$
(a)
Practical condition
Initial error
S_1 + S_2 + $R_{\mathrm{in\_true}}$ + I_{true}
θ_0
S_1 + S_2
$R_{\mathrm{in}0}$ + $I_{\mathrm{m}0}$
θ_1
I_{m}
e_{rotation} + $\delta_{\mathrm{rotation}}$
(b)

Figure 3.37: Estimation of the interlock errors caused by the rotation angle (θ_1) under the (a) ideal condition and (b) practical condition

Figure 3.38 shows the evaluated $\delta_{rotation}$ and $e_{rotation}$ under the ideal condition (solid lines) and the practical condition (dash lines) for the 15 SPR joints. For simplicity, the θ_0 and θ_1 were set to the same values in this research. It is obvious that the calculated $\delta_{rotation}$ and $e_{rotation}$ under the two conditions were almost the same when the θ_1 equalled to 5°, 10° and 15° (black, red and blue lines). While when the θ_1 increased to 20°, the calculated $e_{rotation}$ and $\delta_{rotation}$ under the practical condition were still very close to that under the ideal condition in most SPR joints (green lines). Therefore, it is reasonable to believe that the error level of interlock can be estimated directly using the experimentally measured R_{in} and I_{m} as long as the θ_1 was smaller than 15°. The $e_{rotation}$ fluctuated around −0.01mm, −0.02mm and −0.05mm for θ_1=5°, 10° and 15° respectively. The $\delta_{rotation}$ fluctuated around −1%, −4% and −10% for θ_1=5°, 10° and 15° respectively. This suggested that the measured interlock with only the θ_1 was always smaller than the true interlock. Meanwhile, the interlock error could be maintained at a low level if the θ_1 is controlled smaller than 10° in practical applications.

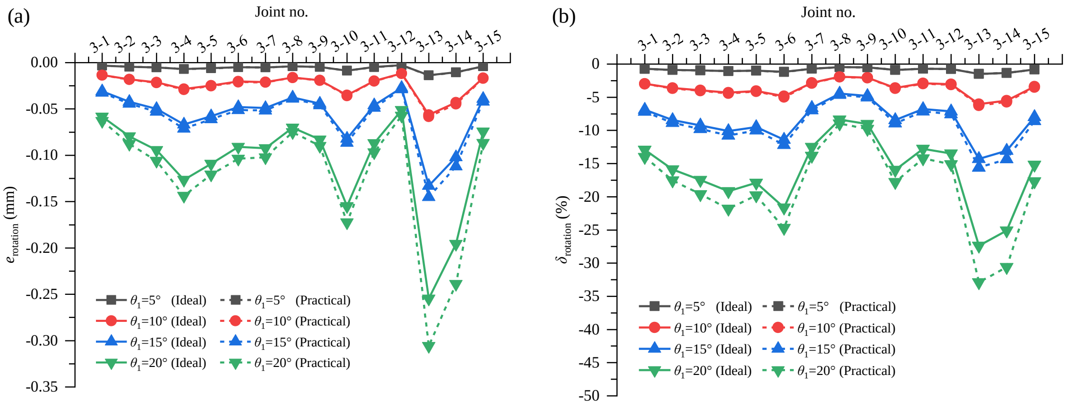

Figure 3.38: Estimated (a) absolute error $e_{rotation}$ and (b) relative error $\delta_{rotation}$ of the 15 SPR joints with different rotation angles (θ_1)

3.4.3.3. Interlock error with the offset distance (Δh) and rotation angle (θ_1)

When the Δh and θ_1 vary within the ranges of 0.0mm~1.5mm and 0°~20°, the contour graphs of the relative error ($\delta_{off+rot}$) of interlock for the 15 tested SPR joints were calculated and recorded in **Figure 3.39**. By comparing the 15 contour graphs, similar changing patterns of the $\delta_{off+rot}$ were found. The Δh and θ_1 imposed opposite effects on the interlock within the studied ranges. The appearance of θ_1 compensated part of the interlock error caused by the Δh. As a result, the $\delta_{off+rot}$ still maintained at low levels when the effects of the Δh and θ_1 on the interlock were roughly counteracted.

However, in most instances, the influences of the Δh and θ_1 on the interlock were not at the same level. The θ_1 played a leading role on top left portion of the figures and the $\delta_{off+rot}$ always had a negative value. Gradient densities of this region in the 15 contour figures were slightly different: SPR joints with the interlock formation position far away from the rivet head (i.e., large S_1 and S_2) but close to the joint axis (i.e., small $R_{\text{in-true}}$) were more sensitive to the θ_1 and had a higher gradient density. In contrast, the Δh showed a dominant influence on the bottom right portion of these figures and the $\delta_{off+rot}$ always had a positive value. The gradient densities of this region were almost the same in all the 15 joints. This is because the impact of Δh on the interlock is only influenced by the $R_{\text{in-true}}$ and I_{true}. The $R_{\text{in-true}}$ and I_{true} in the 15 joints changed within relatively small ranges as listed in **Table 3.1**, and therefore resulted in similar gradient densities of $\delta_{off+rot}$.

It was also found that the accuracy of interlock was just slightly affected by the improper cutting position ($\delta_{off+rot} \approx -5\%$~5%.) if the Δh and θ_1 can be controlled smaller than 1.0mm and 10° respectively. Although a positive θ_1 could compensate the interlock error caused by the Δh, it would lead to more missing data of the bottom sheet profile and further worsen the measurement accuracy of the remaining bottom sheet thickness.

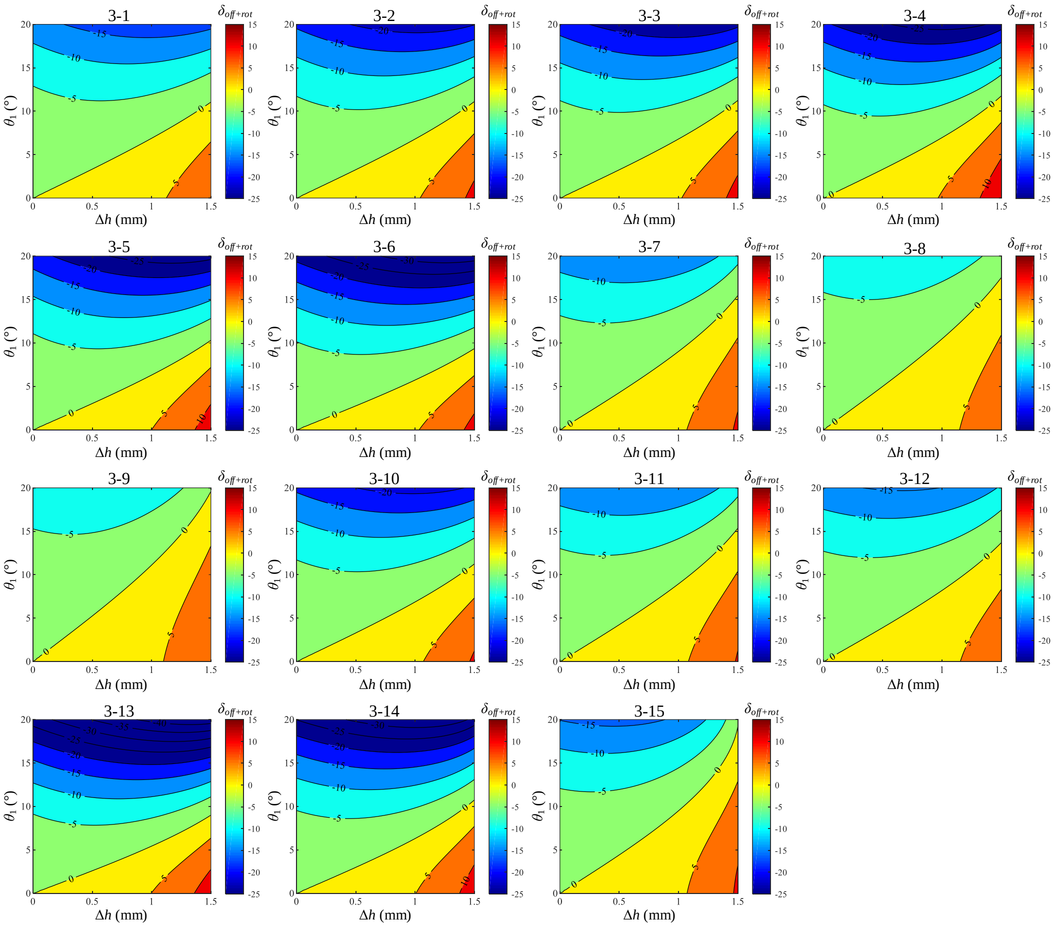

Figure 3.39: Relative error ($\delta_{off+rot}$) of the interlock in the 15 SPR joints with varying offset distances (Δh) and rotation angles (θ_1)

3.4.3.4. Correction of interlock error

Figure 3.40 shows the captured cross-sectional profiles of the dummy joint 3-10 at the ten different cutting positions in **Table 3.2**. When the Δh was greater than 1.0mm or the θ_1 was larger than 10°, it can be seen that the joint cross-sectional profiles (i.e., P3, P6~P9) already became very different from the referenced one (i.e., P0). **Figure 3.41**(a) compares the measured interlock values before and after correction. Before correction, the absolute error of the interlock was obvious in the positions P1~P9, and even reached to around −0.15mm at the positions P3, P6 and P9. In contrast, after correction using the proposed interlock error correction approach, the absolute error of interlock was effectively reduced to a very small value (less than 0.03mm). The interlock at all of the nine positions became almost the same to the referenced P0. It can be seen from **Figure 3.41**(b) that the relative error of interlock reduced to approximately 1%~3% at all of the nine improper cutting positions. The correction results indicated that no matter how large the interlock error induced by the improper cutting position is, the proposed correction method could always effectively compensate it to a very low level. Therefore, the developed interlock error correction method was proved effective and would be very helpful when the SPR joints were not properly sectioned in practical applications, such as SPR joints with irregular shapes extracted from the car BIW structures.

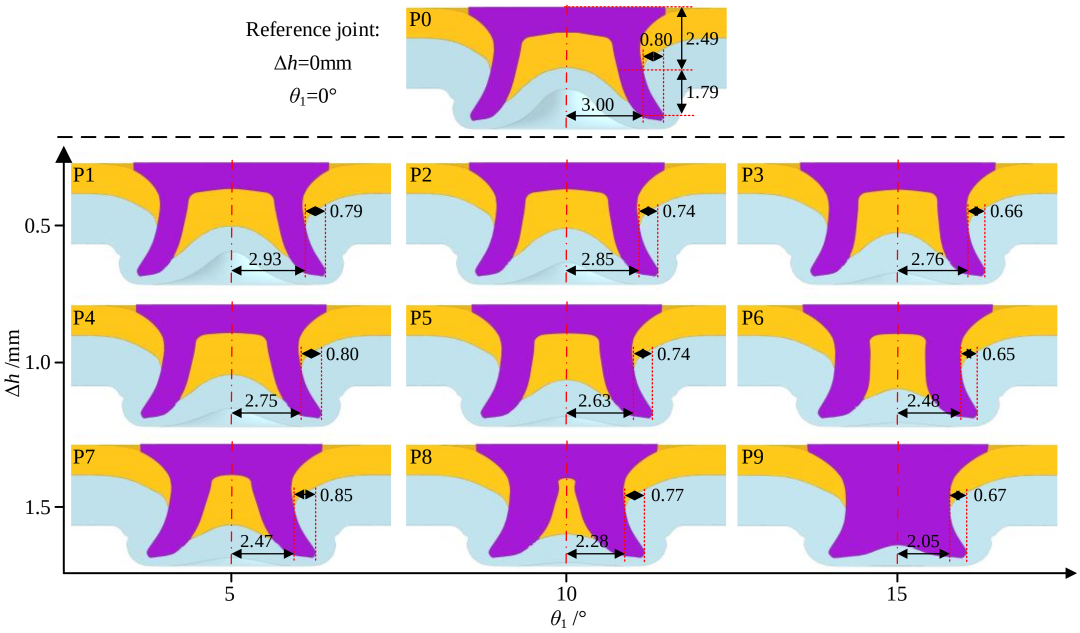
Reference joint:
Δh=0mm
θ1=0°
P0
0.80
2.49
1.79
3.00
P1
0.79
2.93
P2
0.74
2.85
P3
0.66
2.76
P4
0.80
2.75
P5
0.74
2.63
P6
0.65
2.48
P7
0.85
2.47
P8
0.77
2.28
P9
0.67
2.05
0.5
1.0
1.5
Δh /mm
5
10
15
θ1 /°

Figure 3.40: Cross-sectional profiles of the dummy joint 3-10 at the ten different cutting positions

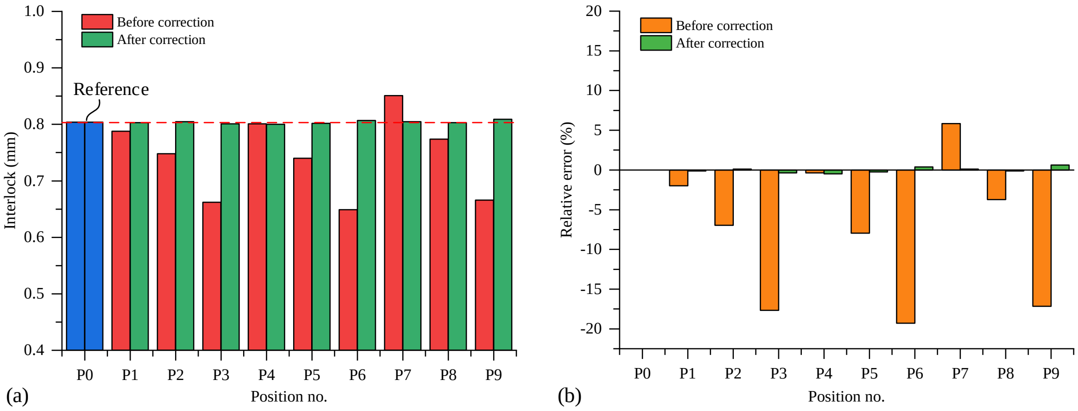

Figure 3.41: Comparison of the (a) interlock and (b) relative error at the ten cutting positions of the dummy joint 3-10

3.5. Conclusions

In this chapter, the influences of improper joint cutting positions on the measurement accuracy of SPR joint quality indicators were investigated and discussed. Error evaluation and correction methods for the joint interlock were proposed to minimise the impact of the improper cutting position on its measurement accuracy. Two GUIs were also developed to simplify the practical applications. The main conclusions from this chapter are summarised below:

(1) The offset distance (Δh) and rotation angle (θ_1) between the cutting plane and the joint central plane could significantly influence the measurement accuracy of the interlock (I) and the remaining bottom sheet thickness, but no impact on the measured rivet head height (H).

(2) The Δh and θ_1 imposed opposite influences on the interlock: the measured interlock (I_m) was always larger than the true interlock (I_true) with only the existence of Δh, while the I_m was always smaller than the I_true with only the existence of θ_1. The interlock error induced by the improper cutting position could still be very small when the effects of the Δh and θ_1 on the interlock were roughly counteracted.

(3) Under the studied joint configurations, the relative error of the interlock could be controlled to approximately −5%~5% if the Δh and θ_1 were smaller than 1.0mm and 10°. The proposed interlock error correction method showed a very good performance, and effectively reduced the relative error of interlock to around 1%~3%.

(4) The Δh and θ_1 could lead to missing data of the remaining bottom sheet thickness around the joint central area. Only part of the bottom sheet profile can be projected from the joint central plane to the cutting plane. The amount of missing data increased rapidly with the increment of the Δh and θ_1. Distortion occurred on the measured bottom sheet profile during the projection process, and resulted in a higher measurement error of the remaining bottom sheet thickness in the region close to the joint axis than in the region close to the rivet tip. It is difficult to quantitatively evaluate and correct the measurement error of the remaining bottom sheet thickness caused by the improper cutting position.

(5) The developed GUIs will facilitate the measurement error evaluation and correction of the interlock in practical applications.

4. Finite Element Modelling of Self-Piercing Riveting Process

During the last ten years, finite element (FE) modelling of SPR process has achieved a rapid development and become an effective approach for the study of SPR technique. In this chapter, a two-dimensional (2D) axisymmetric FE model of SPR process was successfully developed with the commercial software Simufact.Forming 15 and its prediction accuracy was validated by experimental SPR tests. Determination procedures of critical model input parameters, including the rivet and sheet material properties, the mesh sizes of deformable parts, the fracture model of top sheet and the friction coefficients at different interfaces, were discussed in detail. The FE model developed in this chapter was further employed in Chapter 5 to numerically observe and monitor the impact of different joining parameters on the formation process of SPR joints. In addition, this model also lays a foundation for the simulation model development of Riv-Bonding process in Chapter 6.

4.1. Introduction

The design process of new SPR joints relies heavily on experienced joining engineers and extensively trial-and-error experimental tests. It has been reported that more than one thousand SPR joints are used in a single vehicle, and about twenty thousand experimental SPR tests have to be conducted during the development of a new vehicle model [161]. To reduce the investments and shorten the design cycle of new SPR joints, it is urgent to find an effective way to reduce the number of experimental SPR tests required. Under such circumstances, the finite element modelling technique has been employed to develop simulation models that are capable of not only predicting the SPR joint quality but also directly inspecting the events happened during the riveting process.

To date, a large number of FE models of SPR process have been successfully developed. The FE software frequently employed for the modelling of SPR process include ABAQUS [3], LS-DYNA [4, 86, 143, 163, 164], DEFORM [74], ANSYS, MSC.Superform [165, 166], MSC Marc [54, 167], Forge2005 [167] and Simufact.Forming [2, 39]. Among the different types of software, the DEFORM and Simufact.Forming are mainly designed to simulate the metal forming process and therefore are relatively easier to use for industrial applications. Two methods based on different theories are widely used in most finite element software: (1) implicit method and (2) explicit method. The implicit method is more efficient for solving smooth nonlinear problems, while the explicit method is more suitable for a wave propagation analysis. The SPR process is a metal forming process, and thus can be regarded as a quasi-static problem. Both of the above two approaches are suitable for the development of SPR simulation model. In addition to the finite element method, some new simulation methods are also adopted to simulate the SPR process. For instance, Ishikawa and Aihara [168] simulated the SPR process using Arbitrary Lagrangian-Eulerian (ALE) approach, Coupled Eulerian-Lagrangian (CEL) approach and Smoothed Particle Hydrodynamic (SPH) method respectively in Abaqus/Explicit. It was found that the ALE method is not suitable because the top sheet blanking cannot be modelled. Although the fracture of top sheet could be modelled with the CEL approach, it required enormous CPU time and was not suitable for practical applications. In contrast, the simulation results showed a possibility to use SPH method to simulate the SPR process. Huang et al. [169] simulated the SPR process using Smoothed Particle Galerkin (SPG) method combined with finite element method (FEM) in LS-DYNA explicit with a 3D model. The material of the top sheet within the riveting zone was modelled using SPG particles, while other parts were modelled using the FEM. A reasonable agreement between the simulation and experimental results was achieved. Overall, the finite element method is still the most frequently used approach for the modelling of SPR process.

4.2. FE Model Development

4.2.1. Model simplification

It is important to point out that different SPR systems may produce different SPR joint quality and therefore correct modelling of the SPR system plays a critical role in prediction of the final joint quality. **Figure 4.1** shows the structure of the servo-driven SPR system manufactured by the Tucker GmbH. It consists of the servo-driving system, the control panel, the punch, the blank-holder, the C-frame and the die. To simplify the FE model and improve the simulation efficiency, only the components of SPR system close to the joining region (i.e., the punch, the blank-holder and the die) were involved in the simulation model. During the SPR process, the joining force (F) (i.e., riveting force F_r + clamping force $F_{clamping}$) can reach to a very high value (approximately 60kN~80kN). This will lead to C-frame deflection and result in a downward movement of the die, as shown in **Figure 4.2**. The deflection angle (α_1) of the C-frame can be roughly calculated using the die displacement along the vertical direction (L_2) and the length of the cantilever (L_3) in Eq.(4.1). According to the experimentally recorded force-displacement curve, the L_2 is only several millimetres and much smaller than the L_3 (approximately 250mm) in the Tucker SPR system. As a result, the α_1 will be a very small value. For instance, given that the L_2 and L_3 are 3.0mm and 250mm respectively, the calculated α_1 is just 0.69°. Hence, the die movement during the riveting process can be simplified to a pure vertical displacement. Assuming that the deformations of the rivet and sheets are axisymmetric, the SPR process can be further simplified as an axisymmetric process. Compared with the 3D model, the 2D simulation model has less requirements to the computer configuration and thus can effectively reduce the hardware investment. Meanwhile, the 2D model needs an apparently shorter simulation time for each case, and thus can give a much faster response. Therefore, to meet the fast response requirement for industrial applications, a 2D axisymmetric model of SPR process was developed in this research using the commercial software Simufact.Forming 15. This FE software was selected due to its simple model development procedures and good automatic re-meshing ability to deal with severe element distortions caused by large sheet deformations during the riveting process.

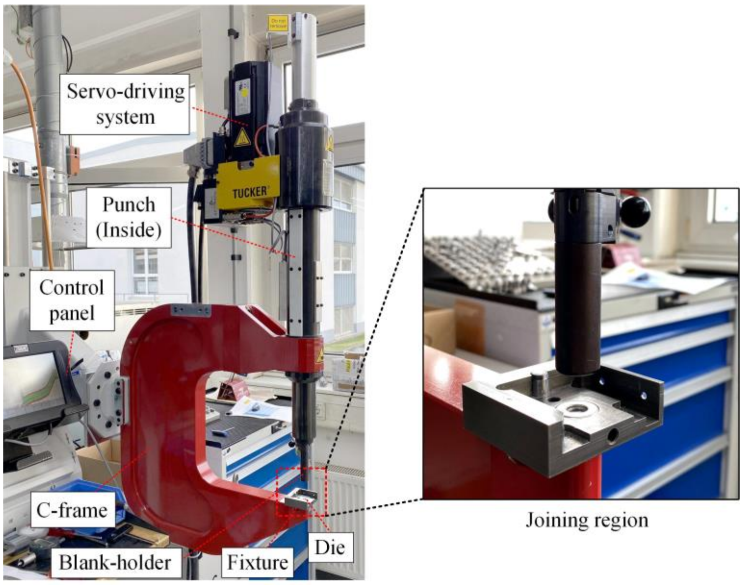
Servo-driving system
Punch (Inside)
Control panel
C-frame
Blank-holder
Fixture
Die
Joining region

Figure 4.1: Structure of the Tucker self-piercing riveting system

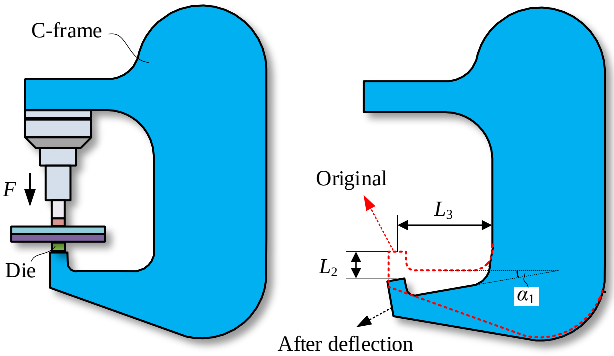
C-frame
F
Die
Original
L3
L2
α1
After deflection

Figure 4.2: Schematic of the C-frame deflection under a high joining force

$$\alpha_1 = \arctan\frac{L_2}{L_3}\cdot\frac{180^\circ}{\pi} \tag{4.1}$$

Figure 4.3 illustrates the structure of the developed SPR simulation model. Six components around the joining region were involved, including (1) the punch, (2) the blank-holder, (3) the die, (4) the rivet, (5) the top sheet and (6) the bottom sheet. The blank-holder, punch and die are made of high strength steels and usually undergo limited elastic deformations during the riveting process. To reduce the model size and shorten the simulation time, these three parts were modelled as rigid bodies. The rivet and sheets usually undergo large plastic deformations during the joining process, and thus were modelled as elastic-plastic bodies. For the downward movement of the die induced by C-frame deflection, the Simufact.Forming 15 provides a function to model this phenomenon by applying a high stiffness spring underneath the die. However, by comparing the simulation results with or without considering the die movement, it was found that the simulation results are not obviously different. Instead, when considering the die movement, a longer simulation time was required due to the greater rivet displacement. Therefore, the die movement during the riveting process was not considered in this model. In experimental SPR tests, the edges of sheets can move freely during the joining process. So the freedoms of sheet edges were not constrained in the simulation model. The punch moves downward at a constant speed (v_1) and the clamping force (F_{clamping}) on the blank-holder was modelled by a low stiffness spring with an initial force.

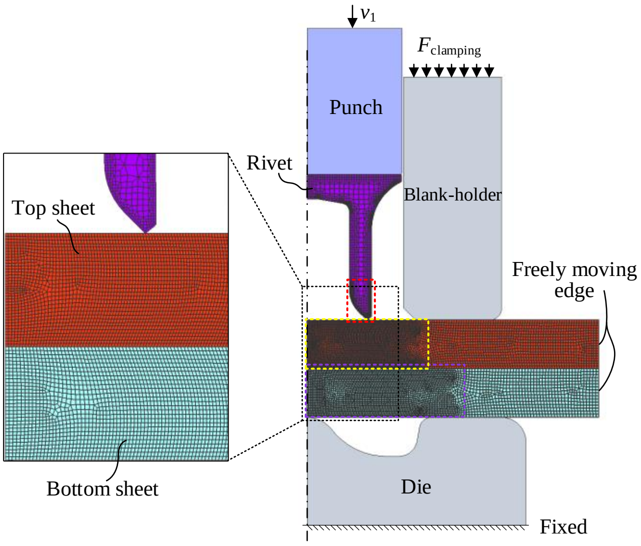

Figure 4.3: Schematic of the 2D axisymmetric simulation model of SPR process

4.2.2. Material properties of rivet and sheets

The materials of sheets and rivet are aluminium alloy AA5754 and boron steel respectively. **Table 4.1** lists the basic mechanical properties of the two materials. Plastic stress-strain curves were utilized to model the deformations of the rivet and sheets during the riveting process. The stress-strain curves of AA5754 aluminium alloy were provided by Jaguar Land Rover (JLR) and described in detail by Carandente et al. [170], in which the thermal softening effect and strain rate hardening effect were considered. However, due to the high punch velocity (v_1=300 mm/s), the sheet material deformed under very large strain rates (above 100 s^{-1}) during the riveting process. The stress-strain curves obtained under low level strain rates (e.g., 0.01 s^{-1}, 0.1 s^{-1} and 1.0 s^{-1}) are incapable of modelling the strain rate hardening effect on the material strength. Therefore, the strain rate hardening effect on the sheet material was not considered, and only the stress-strain curves under the highest strain rate (i.e., 1.0 s^{-1}) were employed as shown in **Figure 4.4**. Meanwhile, the thermal softening effect has a significant influence on the sheet material properties and was considered in this model. The stress-strain curve (strain rate=0.01 s^{-1}) of boron steel provided by JLR was used to describe the deformation of the rivet as shown in **Figure 4.5**. During the SPR process, the maximum temperature within the joining region is lower than 250℃ [2], which has very limited influence on the mechanical properties of the boron steel. Thus, the thermal effect on the rivet material properties was not considered.

Table 4.1: Material properties of the rivet and sheets

Material	Young's Modules (GPa)	Poisson's ratio
AA5754	70	0.3
Boron steel	200	0.3

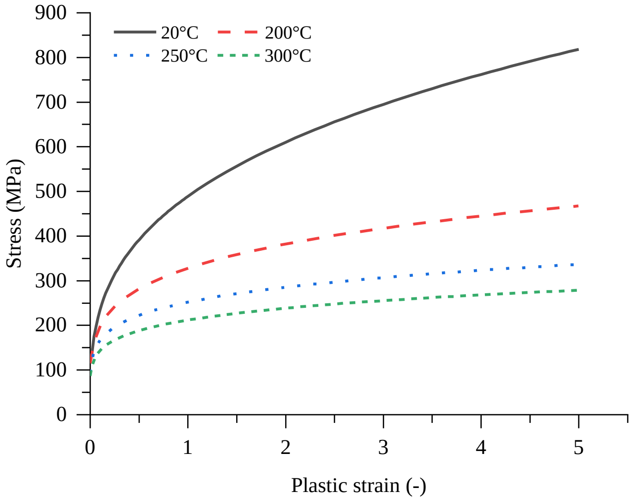

Figure 4.4: Plastic stress-strain curves of the AA5754 at different temperatures (strain rate=1.0 s^{-1}) [170]

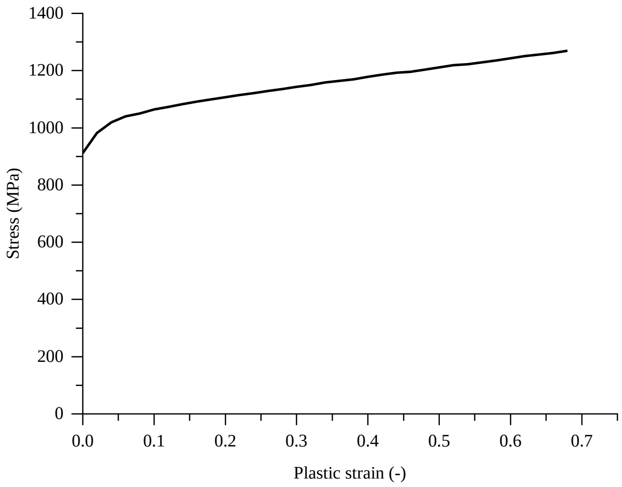

Figure 4.5: Plastic stress-strain curve of the boron steel (strain rate=0.01 s^{-1})

4.2.3. Fracture of the sheets and rivet

During the SPR process, the top sheet will be penetrated by the rivet shank. Two approaches are usually employed to model this phenomenon. The first one is called geometrical separation method. As shown in **Figure 4.6**, a threshold thickness value is predefined and the top sheet fracture/separation occurs if the remaining top sheet thickness becomes smaller than this critical thickness. This threshold thickness value can be conveniently identified by comparing the joint cross-sectional profiles obtained from experimental SPR tests and FE simulations [2]. This approach is proved effective for materials with a sufficient ductility, but is incapable for sheets made of brittle materials. Until now, it has been widely adopted in many FE models of SPR process due to the good performances [2, 6, 56].

The second method for modelling of the top sheet separation/fracture is using material damage criteria. The most commonly employed material damage models include the Cockcroft and Latham damage model (1968), the Johnson and Cook damage model (1985), the maximum shear strain failure criterion and the Lemaitre damage model [172]. The material damage model should be selected based on the failure modes of the sheet material. Once the predefined failure criterion is satisfied, the top sheet fracture/separation occurs and the failed elements are deleted from the simulation model [173]. To avoid too large volume loss, a fine mesh size is required around the region where the material failure may happen. Different from the geometrical criterion, this approach works well for not only ductile materials but also brittle materials as long as a suitable material damage criterion is chosen. However, extra experimental tests are usually required in order to identify the unknown coefficients in the damage model. During the riveting process, the fractures of rivet and bottom sheet may also happen, especially the bottom sheet made of materials with a low ductility. This can only be modelled with the second approach (i.e., material damage criteria).

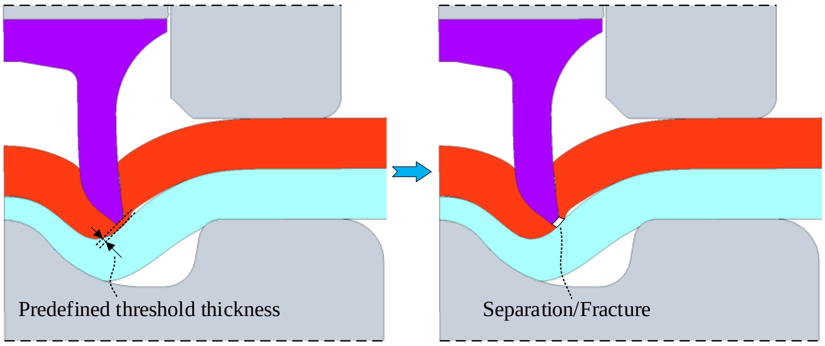

Figure 4.6: The critical thickness for the separation of the top sheet

In this research, due to the high ductility of aluminium alloy AA5754, the geometrical separation method was implemented to model the top sheet fracture/separation. The suitable threshold thickness for the AA5754 top sheet was determined through sensitivity analysis. By analysing all the experiment data of SPR joints provided by JLR, it was found that the rivet and bottom sheet fractures were only observed in SPR joints involving high strength steels or other brittle materials as the bottom sheet. The AA5754 bottom sheet rarely fractures during the riveting process unless the rivet length is much greater than the total sheet thickness. Therefore, to simplify the simulation model, fractures of the rivet and bottom sheet were not considered.

4.2.4. Element meshing of the sheets and rivet

Different element meshers integrated in the Simufact.Forming 15 can be chosen according to the selected model type (2D or 3D) and the deformation behaviour of the deformable parts. For the 2D axisymmetric model, two meshers with different meshing strategies are available: (a) ‘Quadtree mesher’ and ‘Advancing Front Quad mesher’. 4-nodes quad elements with four gauss points are used in the two meshers. The ‘Quadtree mesher’ can mesh the inside of the deformable part with regular quad elements and allocate finer quad elements around the part surface. During the SPR process, the boron steel rivet has a much higher strength than the AA5754 sheets, and usually undergoes limited deformation. So the ‘Quadtree mesher’ was adopted to mesh the rivet. The ‘Advancing Front Quad mesher’ can mesh the whole deformable part with regular quad elements, and thus was adopted to mesh the top and bottom sheets. Together with the geometrical criterion, it also has the ability to model the top sheet separation/fracture by splitting the elements during the simulation. As shown in **Figure 4.3**, three mesh refinement boxes were applied on the rivet tip (red box) and the central areas of the two sheets (yellow and green boxes). This can distribute fine elements around the joining region in the initial mesh, and improve the prediction accuracy without increasing too much simulation time. During the SPR process, the top and bottom sheets undergo severe plastic deformations, which can cause serious mesh distortion and convergence problems during the simulation [174]. To deal with this issue, the automatic re-meshing technique based on different re-meshing criteria was adopted for the top and bottom sheets. The re-meshing criteria for the top sheet are element distortion criterion, strain change criterion and minimum thickness criterion. While the re-meshing criteria for the bottom sheet are only element distortion criterion and strain change criterion. As for the rivet, the material deformation is not very large, and the initial rivet mesh is fine enough to avoid severe element distortion as well as the convergence problems. Thus, the re-meshing technique was not used for the rivet.

4.2.5. Friction coefficients

The Coulomb friction model was chosen to describe the interactions between the contact surfaces. It is reported in [175] that the friction coefficients between different surfaces have significant influences on the deformation behaviours of the rivet and sheets. For instance, the friction coefficient between the bottom sheet and the die could directly affect the final thickness distribution of the bottom sheet, while the friction coefficient between the top sheet and the rivet could directly influence the rivet shank flaring distance [19-20]. Therefore, the inverse method, by comparing the final shapes of the rivet and sheets from the simulations and experiments, was used to determine the friction coefficients at different interfaces. In this model, it was found that the suitable friction coefficient between the bottom sheet and the die was 0.22, while the suitable friction coefficient between other parts was 0.10.

4.3. Sensitivity Studies

During the FE modelling, the element mesh sizes for the deformable parts directly affect the model size and therefore impose significant influences on the efficiency of the simulation model. In theory, smaller mesh sizes can provide a higher prediction accuracy but requires more computational resource and time. For industrial applications, it is necessary to make a balance between the simulation accuracy and simulation efficiency. The threshold thickness of the geometrical criterion has significant influences on the predicted SPR joint quality, especially on the magnitude of interlock. A too large threshold thickness will lead to premature fracture of the top sheet, while a too small one might cause an unrealistic deformation of the top sheet material around the fracture location. Therefore, a mesh size sensitivity study was carried out to find out the suitable mesh sizes for different deformable parts. A sensitivity study was also conducted to identify the suitable threshold thickness for the AA5754 top sheet.

The SPR joint with the 1.5mm+1.5mm AA5754 sheets and the Φ5.3×5.0 H0 (280±30HV10) boron steel rivet was used in the sensitivity studies. A pip die (Pip die-A) was used, and its dimensions are shown in **Figure 4.7**. **Table 4.2** shows the simulation designs and twenty-seven simulations in total were performed. Seven levels for the mesh sizes of top sheet, bottom sheet and rivet were selected, whilst six levels for the threshold thickness of top sheet fracture/separation were chosen. For consistency, the rivet head height was set to 0.0mm in all joints. The influences of the element mesh sizes of deformable parts and the threshold thickness of the top sheet separation on the prediction accuracy and efficiency were evaluated. As shown in **Figure 4.8**, four indicators were measured on the simulated joint cross-sectional profile, including the interlock (I), the deformed rivet shank radius (R_2), the remaining bottom sheet thickness at the joint centre (t_c) and under the rivet tip (t_{tip}). The total element number for each simulation model and the corresponding simulation time were recorded.

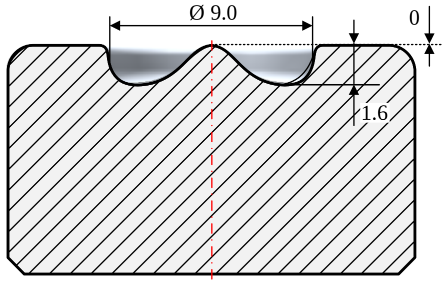

Figure 4.7: Dimensions of the employed pip die (Pip die-A) in the sensitivity studies

Table 4.2: Simulation design for the sensitivity studies

Joint no.	Sheet thickness (mm)		Rivet (Boron steel)	Die	Mesh size (mm)			Threshold thickness
	Top sheet/T_t (AA5754)	Bottom sheet/T_b (AA5754)			Top sheet	Bottom sheet	Rivet	
4-1	1.5	1.5	Φ5.3×5.0 H0 (280±30HV10)	Pip die-A	0.06	0.06	1.0	0.04
4-2						0.08		
4-3						0.10		
4-4						0.12		
4-5						0.15		
4-6						0.20		
4-7						0.25		
4-8	1.5	1.5	Φ5.3×5.0 H0 (280±30HV10)	Pip die-A	0.06	0.1	0.1	0.04
4-9					0.08			
4-10					0.10			
4-11					0.12			
4-12					0.15			
4-13					0.20			
4-14					0.25			
4-15	1.5	1.5	Φ5.3×5.0 H0 (280±30HV10)	Pip die-A	0.10	0.12	0.04	0.04
4-16							0.06	
4-17							0.08	
4-18							0.10	
4-19							0.12	
4-20							0.15	
4-21							0.20	
4-22	1.5	1.5	Φ5.3×5.0 H0 (280±30HV10)	Pip die-A	0.10	0.12	0.10	0.02
4-23								0.04
4-24								0.08
4-25								0.12
4-26								0.15
4-27								0.20

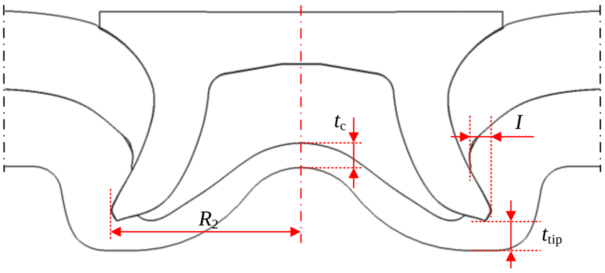

Figure 4.8: Four indicators measured on the joint cross-sectional profile

4.3.1. Mesh size of the bottom sheet

The predicted joint cross-sectional profiles with different bottom sheet mesh sizes are shown in **Figure 4.9**. It can be seen that the joint profile slightly changed with the increment of the bottom sheet mesh size. To evaluate the mesh size effect, the variation curves of the four indicators are presented in **Figure 4.10**. As shown in **Figure 4.10**(a)(b), the predicted values of the interlock (I) and the deformed rivet shank radius (R_2) fluctuated within very small ranges when the bottom sheet mesh size was no more than 0.15mm. However, the two indicators were apparently underestimated when the mesh size became greater than 0.15mm. This is because the interlock was formed between the rivet shank and the bottom sheet. Too large mesh size of the bottom sheet cannot effectively model the deformation of the bottom sheet material around the rivet tip. Meanwhile, the changed deformation of the bottom sheet further affects the rivet shank deformation behaviour. As shown in **Figure 4.10**(c), a similar variation trend of the remaining bottom sheet thickness under the rivet tip (t_{tip}) was observed. This can be explained by the changes of the predicted deformed rivet shank radius (R_2). The bottom sheet thickness under the rivet tip (t_{tip}) was directly determined by the final position of the rivet shank, and positively correlated with the deformed rivet shank radius (R_2). In contrast, as shown in **Figure 4.10**(d), the bottom sheet mesh size showed limited influences on the remaining bottom sheet thickness around the joint centre (t_c). Therefore, from the analysis above, it can be concluded that the suitable bottom sheet mesh size should be no more than 0.15mm to ensure the prediction accuracy of the FE model.

In addition to the simulation accuracy, the efficiency of the SPR simulation model is also very important. The mesh size can directly affect the total element number of the whole model, and thus influences the simulation time. As shown in **Figure 4.11**(a), the element number of the bottom sheet increased at a low rate when the mesh size was greater than 0.15mm, but a high rate when the mesh size was less than 0.15mm. As shown in **Figure 4.11**(b), a proportional relationship between the total element number of the whole model and the simulation time was observed. For the industry application, the bottom sheet mesh size can be set to 0.12mm to shorten the simulation time without compromising too much accuracy.

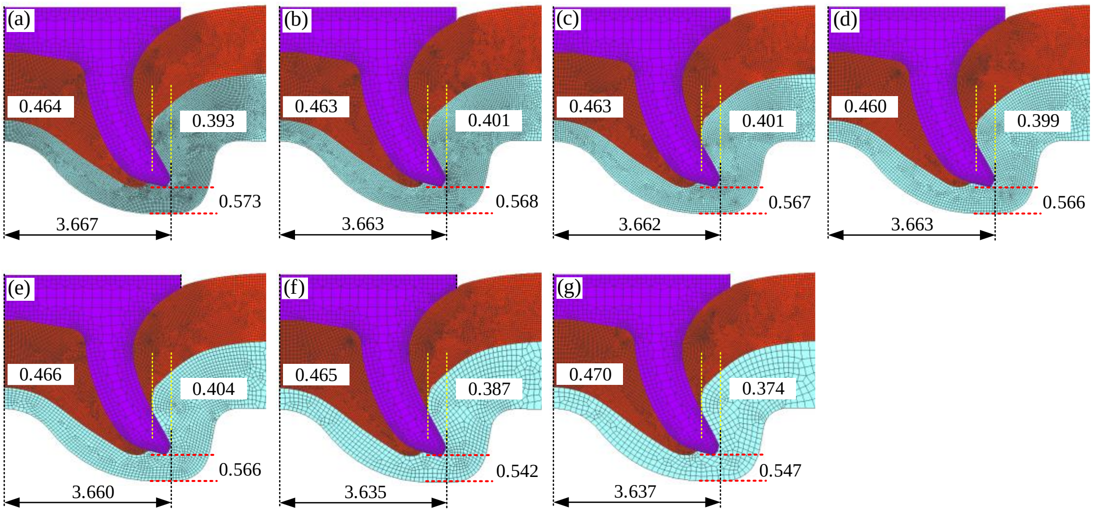
(a)
0.464
0.393
0.573
3.667
(b)
0.463
0.401
0.568
3.663
(c)
0.463
0.401
0.567
3.662
(d)
0.460
0.399
0.566
3.663
(e)
0.466
0.404
0.566
3.660
(f)
0.465
0.387
0.542
3.635
(g)
0.470
0.374
0.547
3.637

Figure 4.9: Simulated joint cross-sectional profiles with different bottom sheet mesh sizes: (a) 0.06mm, (b) 0.08mm, (c) 0.10mm, (d) 0.12mm, (e) 0.15mm, (f) 0.20mm and (g) 0.25mm

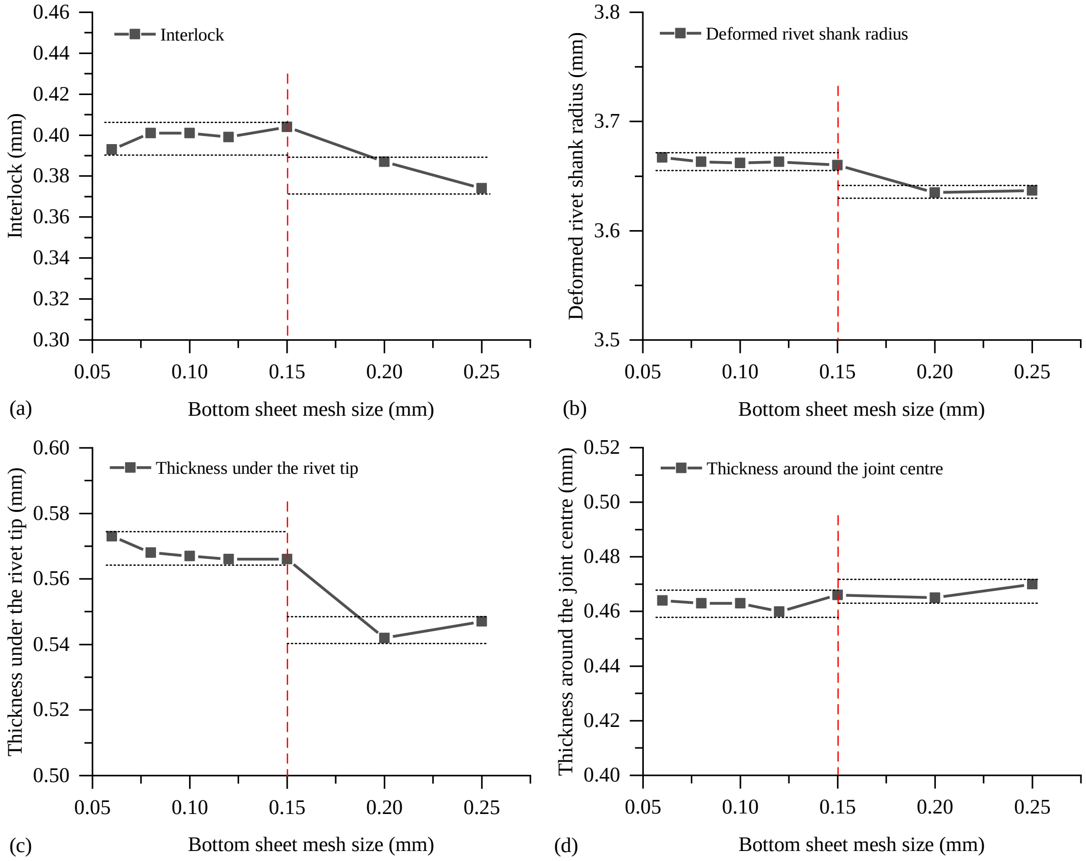

Figure 4.10: The predicted four indicators with varying bottom sheet mesh sizes: (a) interlock *I*, (b) deformed rivet shank radius R_2, (c) remaining bottom sheet thickness under the rivet tip t_{tip} and (d) remaining bottom sheet thickness around the joint centre t_c

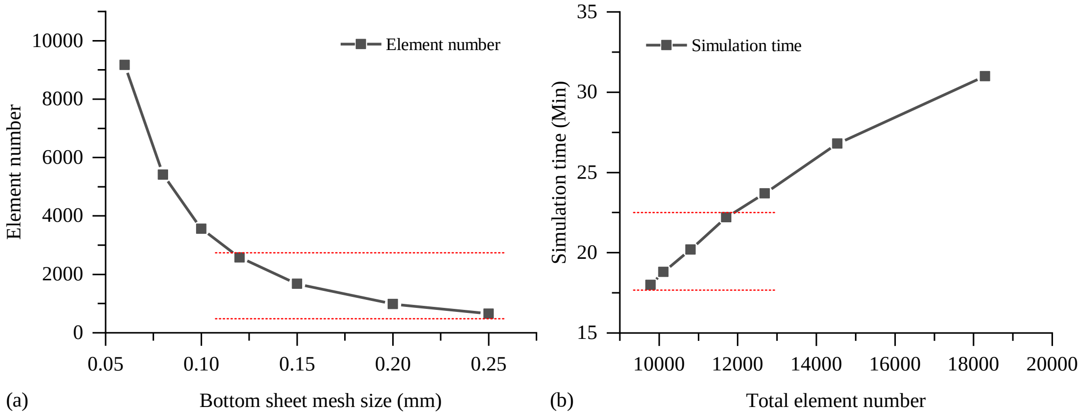

Figure 4.11: Influences of the bottom sheet mesh size on (a) the bottom sheet element number and (b) the simulation time

4.3.2. Mesh size of the top sheet

The predicted joint cross-sectional profiles with different top sheet mesh sizes are shown in **Figure 4.12**. It can be found that the prediction accuracy of the simulation model showed an obvious decreasing trend with the increment of the top sheet mesh size. **Figure 4.13** illustrates the variation trends of the four indicators. The predicted values of the interlock (I), the deformed rivet shank radius (R_2) and the remaining bottom sheet thickness under the rivet tip (t_{tip}) fluctuated within small ranges when the top sheet mesh size was no more than 0.10mm as shown in **Figure 4.13**(a)(b)(c). While the three indicators were all underestimated when the top sheet mesh size became greater than 0.10mm. This is mainly because too coarse top sheet mesh cannot accurately capture the deformation behaviour of the top sheet and the separation of the top sheet as shown in **Figure 4.14**(f)(g). Similar to the bottom sheet mesh size, the top sheet mesh size also showed limited influences on the remaining bottom sheet thickness around the joint centre (t_c): the t_c was only slightly underestimated when the top sheet mesh size was greater than 0.10mm. Therefore, to ensure the simulation accuracy, the top sheet mesh size should be no more than 0.10mm. Compared with the bottom sheet mesh size, the top sheet mesh size demonstrated a greater influence on the simulation result.

Figure 4.15 shows the effects of the top sheet mesh size on the element number of the top sheet and the simulation time. It can be seen that the top sheet element number increased rapidly when the top sheet mesh size was smaller than 0.10mm, as shown in **Figure 4.15**(a). Consequently, the simulation time increased almost linearly to the total element number as presented in **Figure 4.15**(b). Therefore, for industrial applications, the suitable top sheet mesh size could be set to 0.10mm.

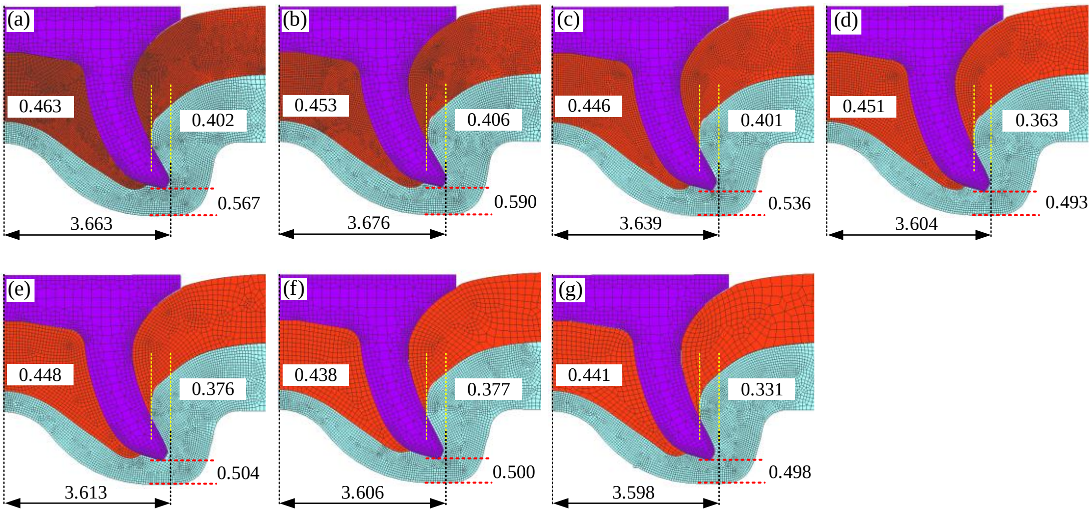
(a)
0.463
0.402
0.567
3.663
(b)
0.453
0.406
0.590
3.676
(c)
0.446
0.401
0.536
3.639
(d)
0.451
0.363
0.493
3.604
(e)
0.448
0.376
0.504
3.613
(f)
0.438
0.377
0.500
3.606
(g)
0.441
0.331
0.498
3.598

Figure 4.12: The simulated joint cross-sectional profiles with different top sheet mesh sizes: (a) 0.06mm, (b) 0.08mm, (c) 0.10mm, (d) 0.12mm, (e) 0.15mm, (f) 0.20mm and (g) 0.25mm

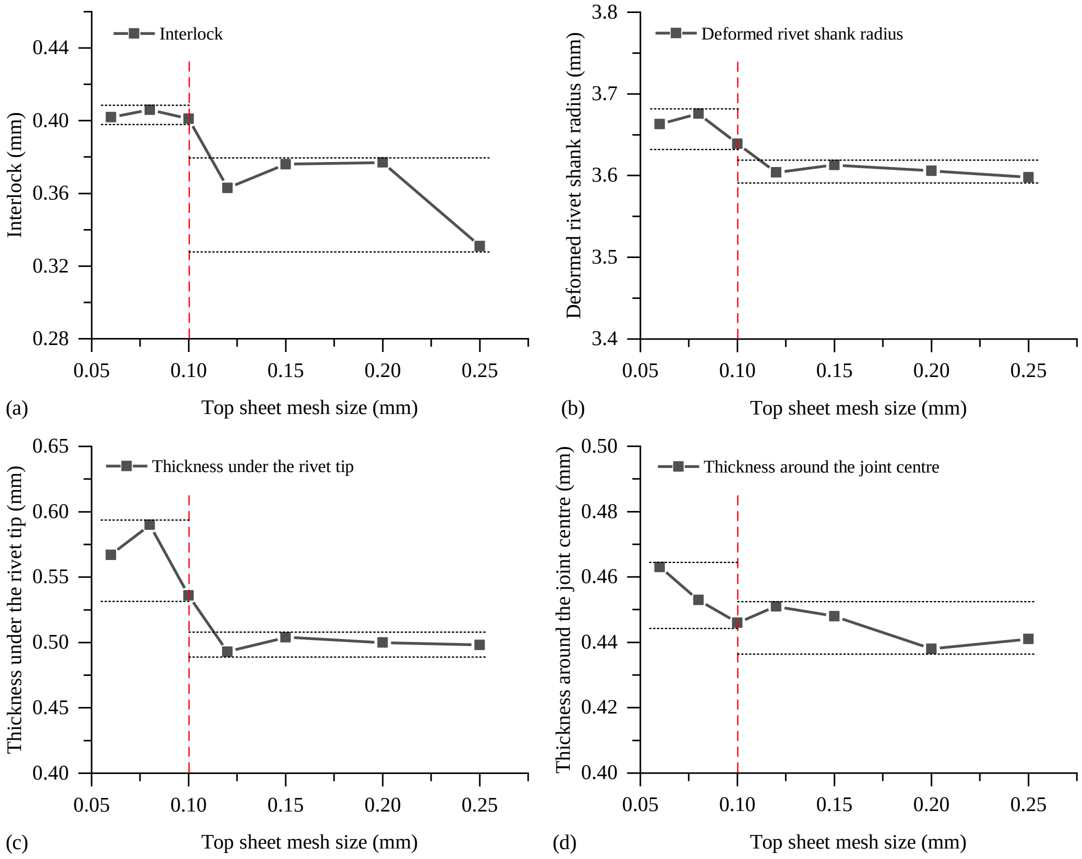

Figure 4.13: The predicted four indicators with different top sheet mesh sizes: (a) interlock *I*, (b) deformed rivet shank radius R_2, (c) remaining bottom sheet thickness under the rivet tip t_{tip} and (d) remaining bottom sheet thickness around the joint centre t_c

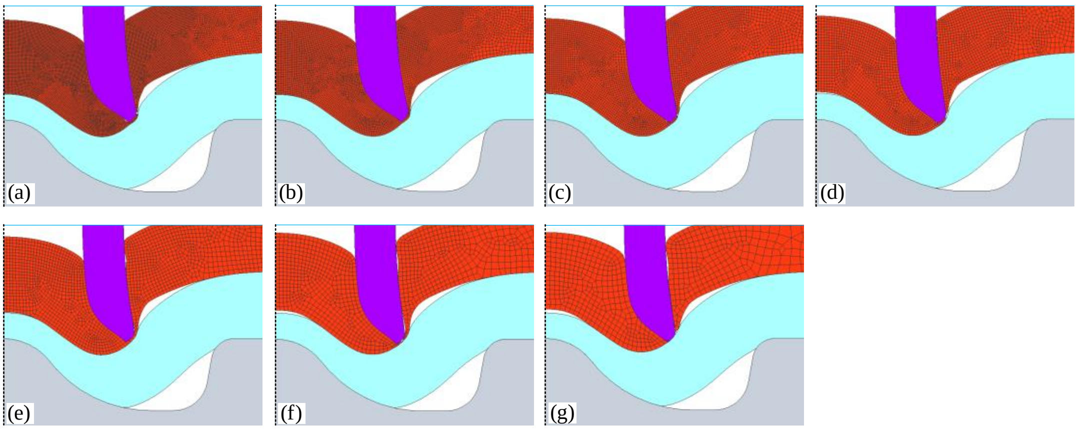

Figure 4.14: The simulated joint cross-sectional profiles when the rivet penetrated the top sheet (rivet displacement=3.29mm) with different top sheet mesh sizes: (a) 0.06mm, (b) 0.08mm, (c) 0.10mm, (d) 0.12mm, (e) 0.15mm, (f) 0.20mm and (g) 0.25mm

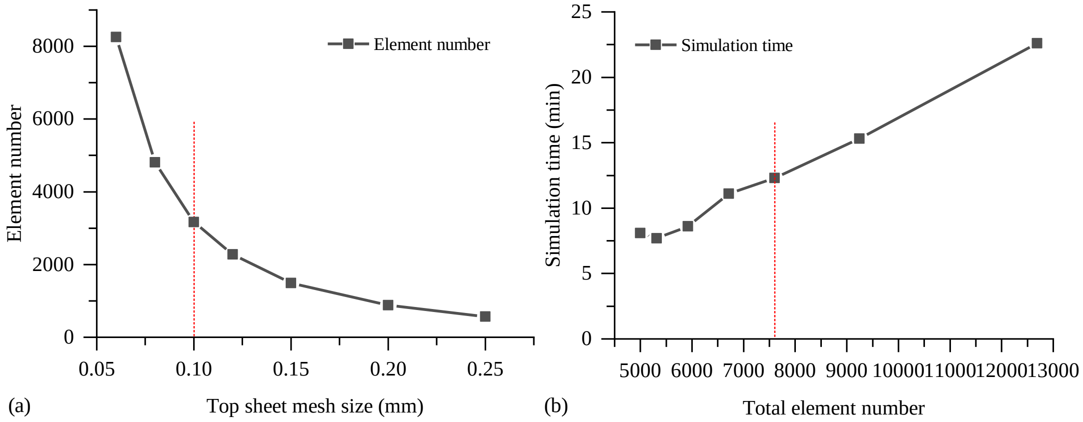

Figure 4.15: Influences of the top sheet mesh size on (a) the top sheet element number and (b) the simulation time

4.3.3. Mesh size of the rivet

The predicted joint cross-sectional profiles with different rivet mesh sizes are shown in **Figure 4.16**. It can be seen that the rivet mesh size also had influences on the simulation result, especially the interlock (I) and the deformed rivet shank radius (R_2). As shown in **Figure 4.17**(a)(b), the magnitudes of the I and R_2 varied within small ranges when the rivet mesh size was no more than 0.10mm, but were underestimated with coarse rivet element meshes (>0.10mm). The predicted remaining bottom sheet thickness under the rivet tip (t_{tip}) fluctuated with different rivet mesh sizes, as shown in **Figure 4.17**(c). The bottom sheet thickness around the joint centre (t_{c}) was not sensitive to the rivet mesh size, and kept almost the same with varying rivet mesh sizes. Therefore, it can be concluded that the rivet mesh size should be not greater than 0.10mm. **Figure 4.18** illustrates the influences of the rivet mesh size on the rivet element number and the simulation time. Different from the top sheet mesh size and bottom sheet mesh size, the rivet element number increased slowly with the decrease of the rivet mesh size, and the simulation time was not significantly affected within the studied range of rivet mesh size. Thus, for the industrial applications, the suitable rivet mesh size could be set to 0.10mm.

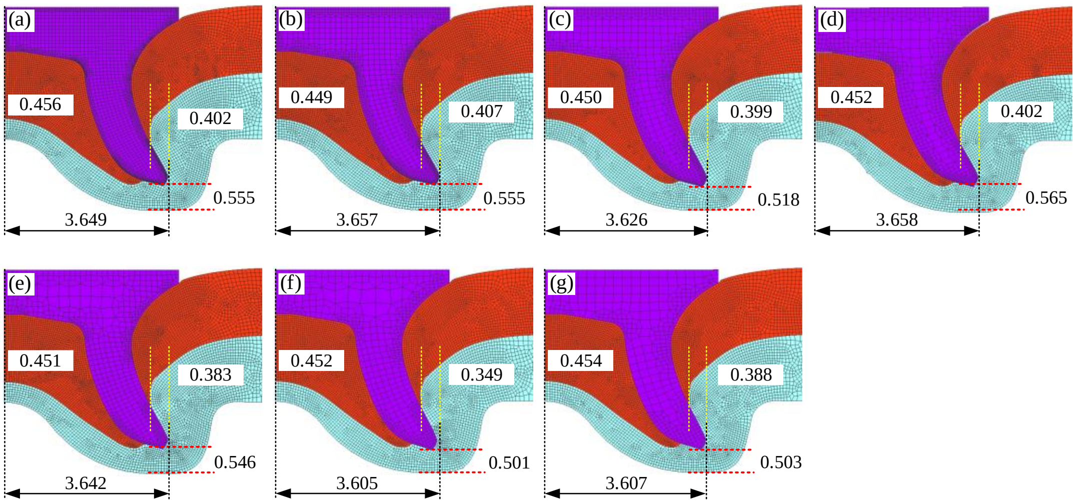
(a)
0.456
0.402
0.555
3.649
(b)
0.449
0.407
0.555
3.657
(c)
0.450
0.399
0.518
3.626
(d)
0.452
0.402
0.565
3.658
(e)
0.451
0.383
0.546
3.642
(f)
0.452
0.349
0.501
3.605
(g)
0.454
0.388
0.503
3.607

Figure 4.16: The simulated joint cross-sectional profiles with different rivet mesh sizes: (a) 0.04mm, (b) 0.06mm, (c) 0.08mm, (d) 0.10mm, (e) 0.12mm, (f) 0.15mm and (g) 0.20mm

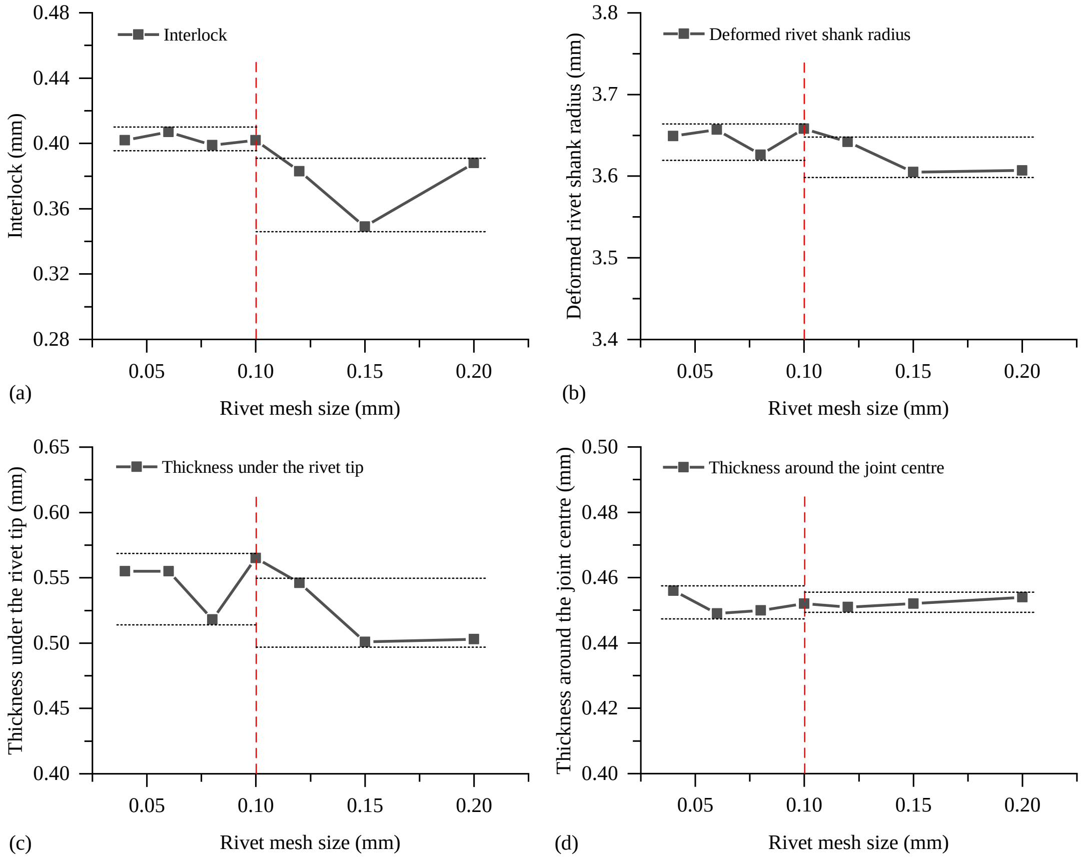

Figure 4.17: The predicted four indicators with different rivet mesh sizes: (a) interlock I, (b) deformed rivet shank radius R_2, (c) remaining bottom sheet thickness under the rivet tip t_{tip} and (d) remaining bottom sheet thickness around the joint centre t_c

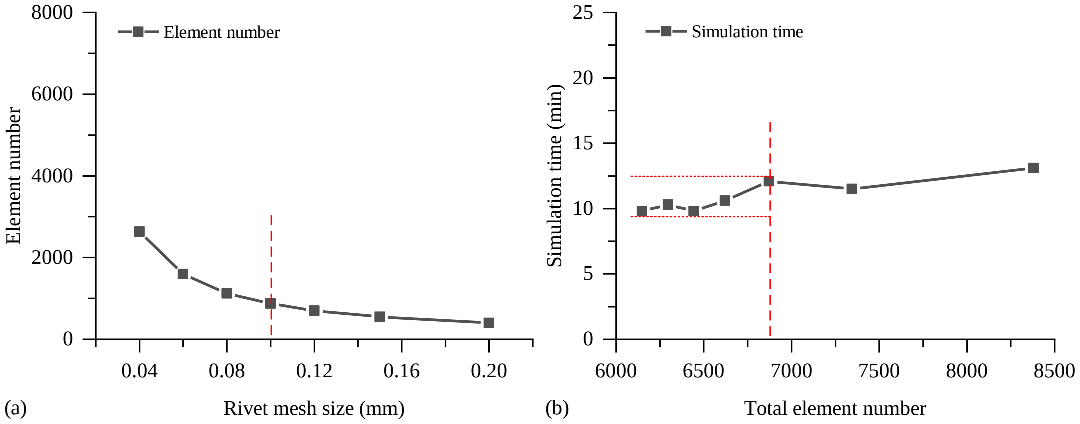

Figure 4.18: Influences of the rivet mesh size on (a) the rivet element number and (b) the simulation time

4.3.4. Threshold thickness for the top sheet separation

The predicted joint cross-sectional profiles with different threshold thicknesses for the top sheet fracture/separation are shown in **Figure 4.19**. It can be seen that the threshold thickness imposed significant influences on the simulated joint quality. This is mainly because the magnitude of the threshold thickness can directly affect the occurrence of the top sheet fracture/separation. As shown in **Figure 4.20**, with the increment of the threshold thickness, the fracture of the top sheet occurred at an earlier time and a larger part of the top sheet material was deleted from the simulation model. As a result, the rivet shank easily penetrates the top sheet and the interlock (I) was overestimated with a threshold thickness greater than 0.08mm, as shown in **Figure 4.21**(a). The threshold thickness demonstrated limited influences on the deformed rivet shank radius (R_2) as shown in **Figure 4.21**(b). Both of the remaining bottom sheet thicknesses under the rivet tip (t_{tip}) and around the joint centre (t_c) were underestimated with a too large threshold thickness. Different from the mesh size, the threshold thickness had no influence on the total element number and thus had limited influences on the simulation time. Therefore, considering that a too small threshold thickness may lead to unrealistic deformation of the top sheet material around the fracture position, the threshold thickness for the AA5754 top sheet was set to 0.04mm for industrial applications.

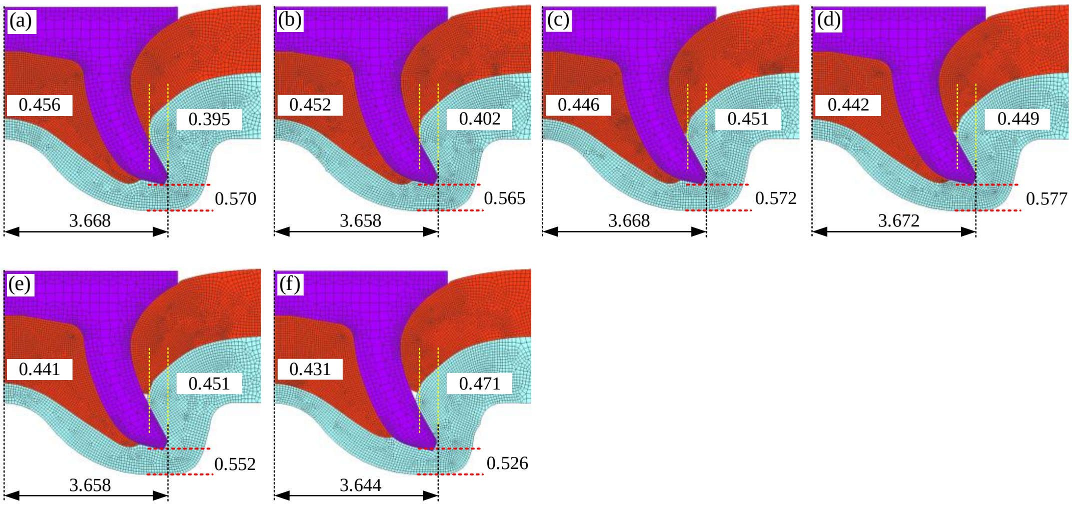
(a)
0.456
0.395
0.570
3.668
(b)
0.452
0.402
0.565
3.658
(c)
0.446
0.451
0.572
3.668
(d)
0.442
0.449
0.577
3.672
(e)
0.441
0.451
0.552
3.658
(f)
0.431
0.471
0.526
3.644

Figure 4.19: The simulated joint cross-sectional profiles with different threshold thicknesses: (a) 0.02mm, (b) 0.04mm, (c) 0.08mm, (d) 0.12mm, (e) 0.15mm and (f) 0.20mm

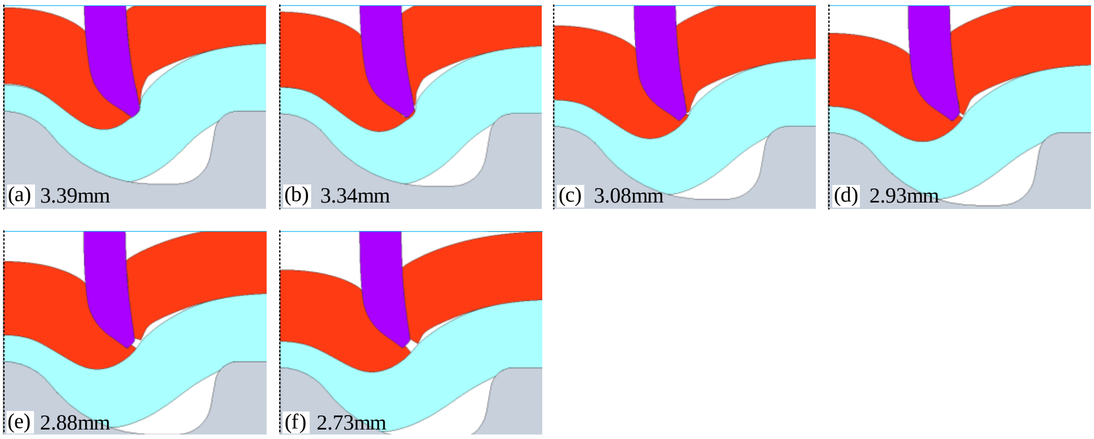
(a) 3.39mm
(b) 3.34mm
(c) 3.08mm
(d) 2.93mm
(e) 2.88mm
(f) 2.73mm

Figure 4.20: Fracture/separation of the top sheet with different threshold thicknesses: (a) 0.02mm, (b) 0.04mm, (c) 0.08mm, (d) 0.12mm, (e) 0.15mm and (f) 0.20mm

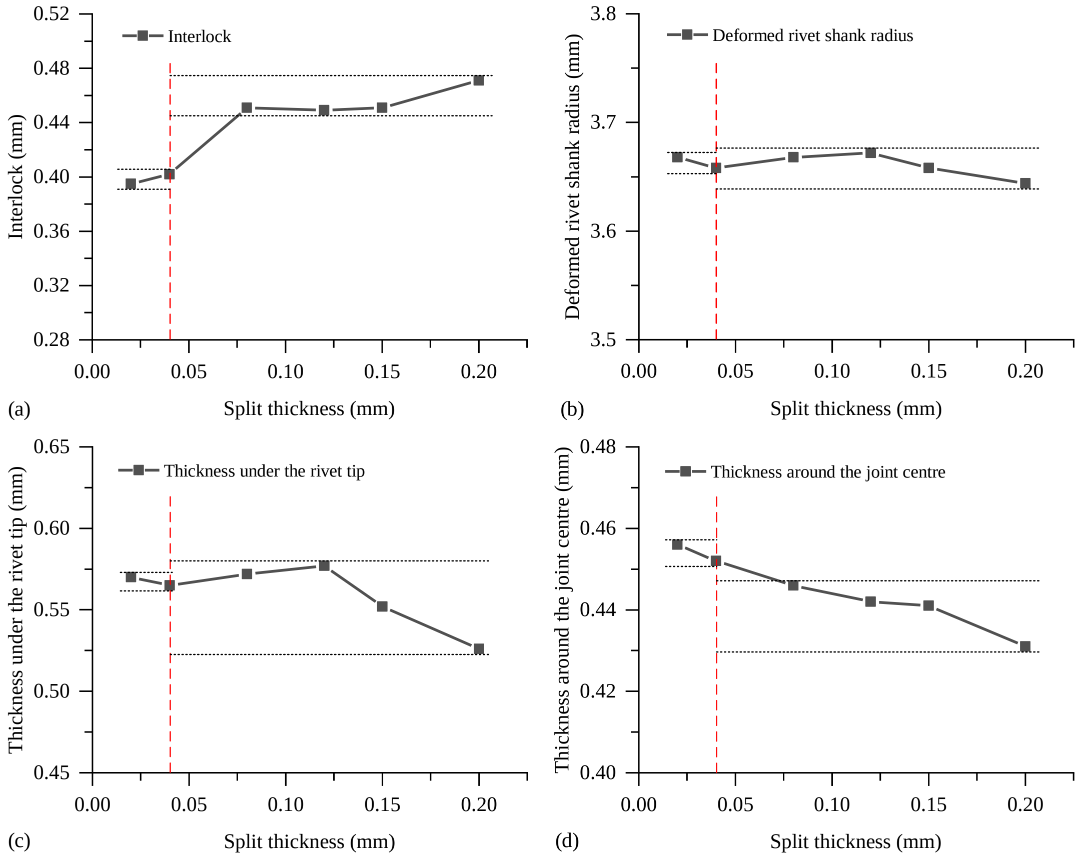

Figure 4.21: The predicted four indicators with different threshold thicknesses: (a) interlock I, (b) deformed rivet shank radius R_2, (c) remaining bottom sheet thickness under the rivet tip t_{tip} and (d) remaining bottom sheet thickness around the joint centre t_c

Overall, based on the analysis results from the sensitivity studies, the suitable mesh sizes for the rivet, top sheet and bottom sheet were set to 0.10 mm, 0.10 mm and 0.12 mm respectively. The suitable threshold thickness for the AA5754 top sheet fracture was set to 0.04mm.

4.4. Validation of the FE Model

4.4.1. Experiment design

To verify the prediction accuracy of the developed SPR simulation model, SPR joints with different top sheet thicknesses (T_t), bottom sheet thicknesses (T_b) and rivet lengths (L_1) were experimentally manufactured. Boron steel rivets with hardness 280±30HV10 (H0) and aluminium alloy AA5754 sheets were used throughout the experiment. The pip die-A shown in **Figure 4.7** was also utilized. A uniform specimen size 40mm×40mm was used for all joints as shown in **Figure 4.22**. As presented in **Table 4.3**, interrupted experimental tests of the SPR joint with 1.2mm+2.0mm sheets and C5.3*6.0 H0 rivet were carried out. The whole joining process was stopped at five positions by controlling the rivet head height (H). This was designed to assess the prediction performance of the SPR model on the rivet and sheets deformations. As shown in **Table 4.4**, another ten SPR joints with varying sheet thicknesses and rivet lengths were also experimentally manufactured. This was designed to evaluate the prediction accuracy of the SPR model on the final joint quality. All the SPR joints were made using the Tucker servo-driven SPR system shown in **Figure 4.1**, and only one specimen for each joint configuration was manufactured.

The manufactured SPR joints were sectioned along the joint central plane, and polished using a polishing machine. Then, the cross-sectional profile of each joint was captured with an optical microscope. The magnitudes of joint quality indicators were measured from the joint cross-sectional profiles, including the interlock (*I*) and the minimum remaining bottom sheet thickness (T_{min}). The force-displacement curve of each SPR joint was also recorded. All the SPR joints in **Table 4.3** and **Table 4.4** were also simulated using the developed SPR simulation model. The predicted joint cross-sectional profiles, the joint quality indicators and the force-displacement curves were recorded for further comparisons.

Table 4.3: Design of the interrupted experimental SPR tests

Joint no.	Thickness (mm) Top sheet/T_t (AA5754)	Thickness (mm) Bottom sheet/T_b (AA5754)	Rivet head height/*H* (mm)	Rivet (Boron steel)	Die
4-28	1.2	2.0	4.0	C5.3*6.0 (280±30HV10)	Pip die-A
4-29			3.0		
4-30			2.0		
4-31			1.0		
4-32			0.0		

Table 4.4: Design of the SPR joints with varing sheet thickness and rivet length

Joint no.	Thickness (mm) Top sheet/T_t (AA5754)	Thickness (mm) Bottom sheet/T_b (AA5754)	Rivet (Boron steel)	Die
4-33	1.2	1.0	C5.3*5.0 (280±30HV10)	Pip die-A
4-34		1.2		
4-35		1.5		
4-36		2.0		
4-37	1.0	1.5	C5.3*5.0 (280±30HV10)	Pip die-A
4-38	1.2			
4-39	1.5			
4-40	1.5	1.2	C5.3*6.0 (280±30HV10)	Pip die-A
4-41		1.5		
4-42		2.0		

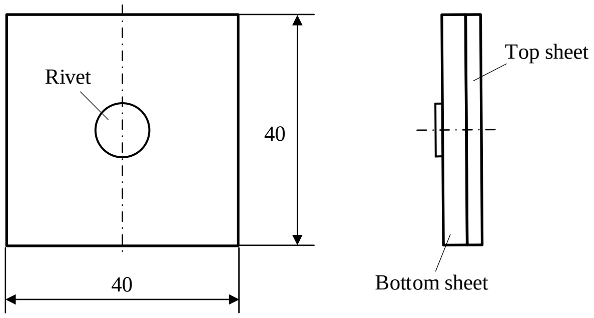

Figure 4.22: Specimen dimensions of the SPR joint (in mm)

During the experimental SPR test, the SPR system cannot record the riveting force at the moment when the rivet shank starts contacting with the top sheet. Instead, it needs to firstly detect the contact between the rivet shank and the top sheet by assessing the force applied on the punch. The contact is confirmed by the joining system once this force reaches a certain threshold value (e.g., approximately 5.0kN for the Tucker SPR system used in this study), and then the SPR system starts recording the force-displacement curve. This will lead to a riveting force offset and a displacement offset between the recorded starting point and the true starting point of the force-displacement curves. In addition, the C-frame deflection of the SPR system will lead to a backward movement of the die and therefore a longer rivet displacement. Because the die movement is not considered in the developed SPR simulation model, the predicted force-displacement curve will be the true force-displacement curve. To properly compare the simulated and the tested force-displacement curves, the influences of the above-mentioned two factors on the experimentally recorded force-displacement curve should be removed.

Figure 4.23 shows the experimentally recorded original force-displacement curve of a SPR joint (black line) and the corresponding modified true force-displacement curves (red, blue and green lines) after removing the influences of C-frame deflection (varying C-frame stiffnesses, kN/mm). It can be seen that the C-frame deflection shows a minor influence on the curve shape when the riveting force is relatively small (Zone 1), but a significant impact when the riveting force reaches to a high level (Zone2). Therefore, as shown in **Figure 4.24**(a), the experimentally recorded force-displacement curve can be firstly overlapped with the simulated one (Zone 3) to roughly determine the offsets of riveting force and rivet displacement (relative positions of the true starting point A_1 and the recorded starting point A_2). Then, the stiffness of the C-frame (K) could be roughly calculated using the Eq.(4.2) with the displacement difference between the two curves (ΔS) and the experimentally recorded maximum riveting force (F_{max}). Finally, as shown in **Figure 4.24**(b), the experimentally measured true force-displacement curve (blue line) is obtained, and used to evaluate the prediction performance of the simulation model.

$$K = \frac{F_{\max}}{\Delta S} \tag{4.2}$$

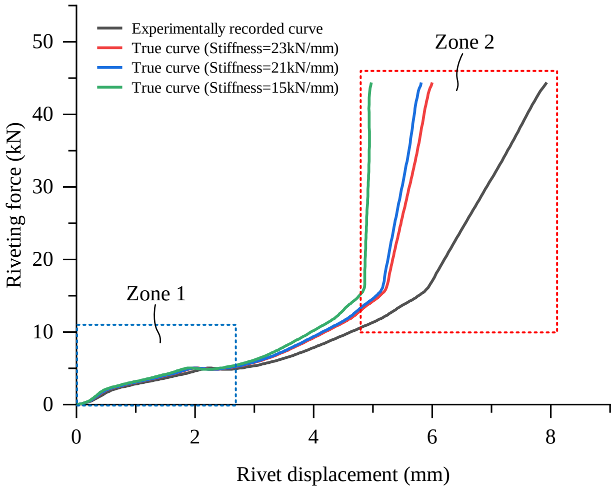

Figure 4.23 The experimentally recorded force-displacement curve and the corresponding true curves with different C-frame stiffnesses

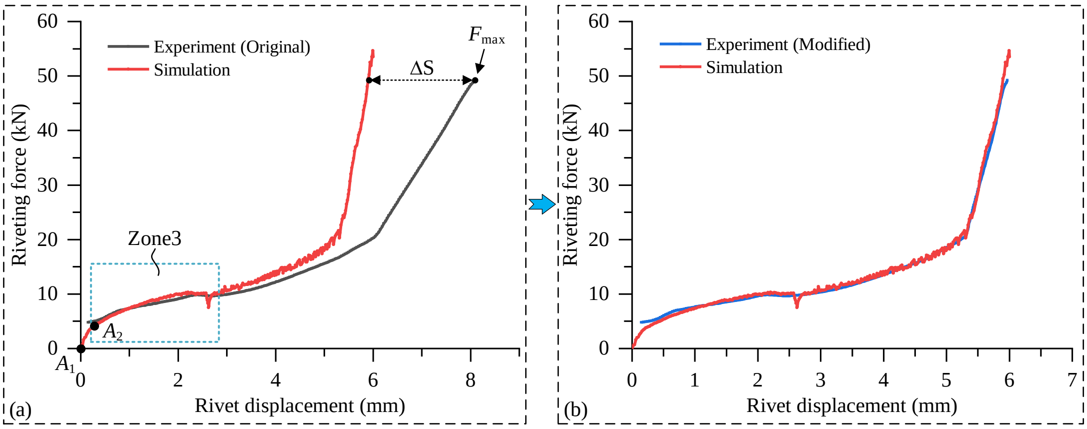

Figure 4.24 Comparisons of force-displacement curves: (a) between the experimentally recorded and simulated and (b) between the modified experimentally measured and simulated

4.4.2. Results and discussion

The experimentally captured and numerically simulated joint cross-sectional profiles at five positions during the SPR process are compared in **Figure 4.25**. It is apparent that the deformation behaviours of the sheets and the rivet at each position were accurately predicted by the simulation model. The separation of top sheet was also accurately captured using the geometrical criterion with the threshold thickness 0.04mm (Zone 1 and Zone 2). The gap formed between the two sheets (Zone 3 and Zone 4) and even the material folds on the bottom sheet (Zone 5 and Zone 6) were also captured by the simulation model. **Figure 4.26** shows the experimentally tested and simulated cross-sectional profiles of the SPR joints with varying T_t, T_b and L_1. It can be seen that the predicted joint profiles showed reasonable agreements with that from the experimental SPR tests. Comparisons between the tested and the predicted values of the I and T_{min} are given in **Figure 4.27** and **Figure 4.28** respectively. The Pearson's correlation coefficient (r) was adopted to evaluate the prediction accuracy of the simulation model. The calculated values of the r for the I and $T_{\min}$ are 0.97 and 0.90 respectively. This indicates that both of the I and $T_{\min}$ were predicted by the developed simulation model with a reasonable accuracy.

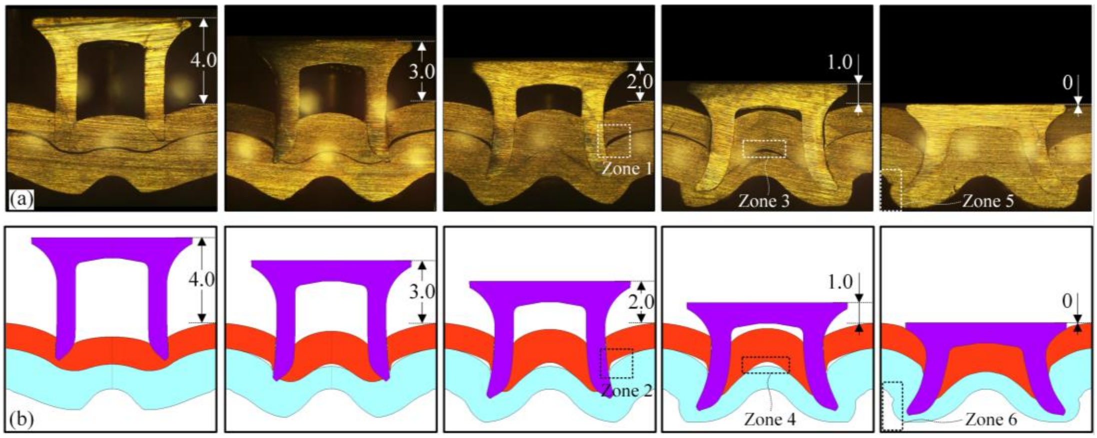
(a)
4.0
3.0
2.0
Zone 1
1.0
Zone 3
0
Zone 5
(b)
4.0
3.0
2.0
Zone 2
1.0
Zone 4
0
Zone 6

Figure 4.25: Comparison between joint cross-sectional profiles during the SPR process from (a) interrupted laboratory tests and (b) simulations

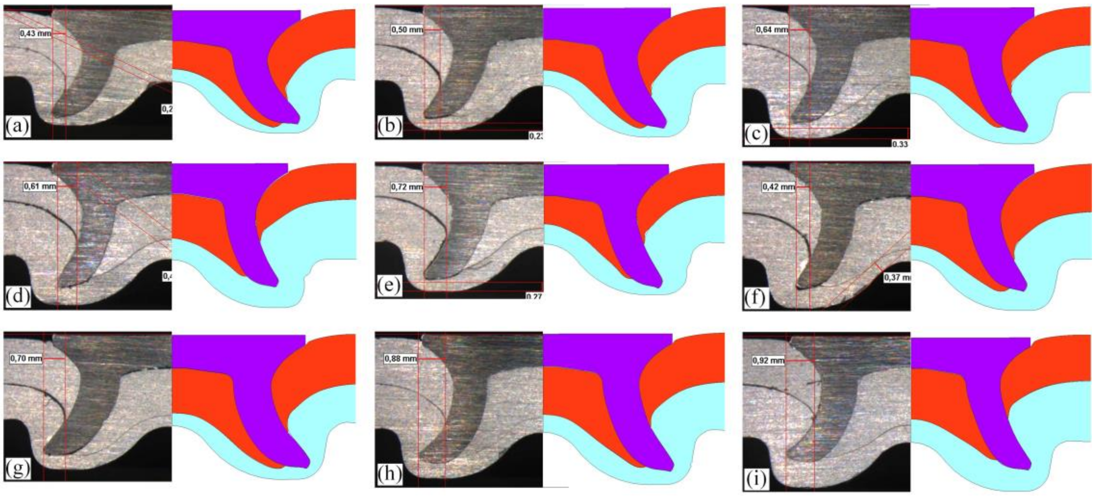
(a)
0,43 mm
(b)
0,50 mm
(c)
0,64 mm
0.33
(d)
0,61 mm
(e)
0,72 mm
(f)
0,42 mm
0,37 mm
(g)
0,70 mm
(h)
0,88 mm
(i)
0,92 mm

Figure 4.26:Comparison of the joint cross-sectional profiles from the simulations and experimental tests: (a) joint 4-33, (b) joint 4-34, (c) joint 4-35, (d) joint 4-36, (e) joint 4-37, (f) joint 4-39, (g) joint 4-40, (h) joint 4-41 and (i) joint 4-42

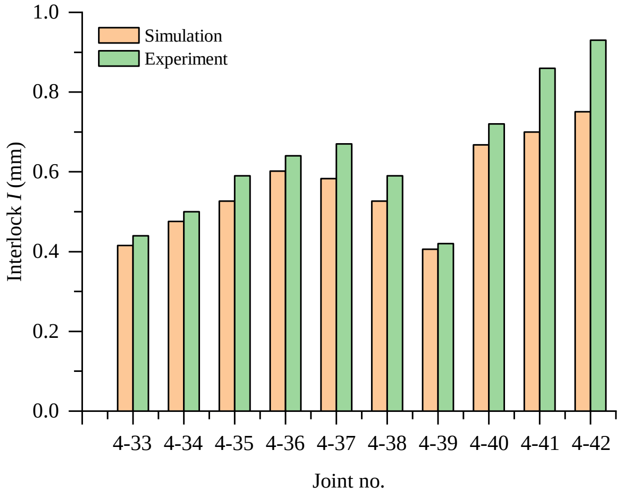

Figure 4.27: Comparisons between the experimentally tested and numerically predicted interlock (I) in SPR joints with varying configurations

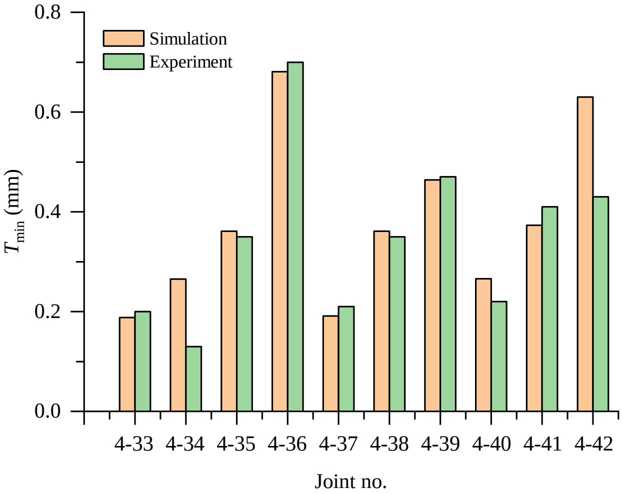

Figure 4.28: Comparisons between the experimentally tested and numerically predicted minimum remaining thickness on the bottom sheet (T_{min}) in SPR joints with varying configurations

As shown in **Figure 4.29**, the true force-displacement curves during the riveting process of the SPR joint 4-32 were extracted from both the laboratory interrupted experimental SPR test and the FE simulation. The calibrated C-frame stiffness (K) of the Tucker SPR system used in this study is approximately 21kN/mm. Therefore, the effect of C-frame deflection on the tested load-displacement curve was removed using Eq.(4.3). The s_t is the true rivet displacement relative to the die, and the s_a is the absolute rivet displacement. The F_r is the riveting force during the SPR process. It can be seen that the simulated force-displacement curve (black line) matched well with the tested true curve (red line). The tested curve started around 5.0kN rather than 0.0kN (Zone 1) due to the aforementioned contact detection between the rivet shank and the top sheet of the SPR joining system. The slightly decline of the riveting force (Zone 2) and the sudden growth rate change of the riveting force (Zone 3) were accurately predicted by the developed simulation model. Comparisons between the experimentally tested and FE simulated true force-displacement curves of the SPR joints in **Table 4.4** are given in **Figure**

4.30. It can be seen that not only similar increasing trends but also almost same magnitudes of the riveting force were observed on the simulated and tested curves. Therefore, it is reasonable to conclude that the developed SPR simulation model is capable of predicting the deformations of rivet and sheets during joining process and the final joint quality. So the developed FE model of SPR process was directly utilized in the following chapters.

$$s_t = s_a - \frac{F_r}{K} \tag{4.3}$$

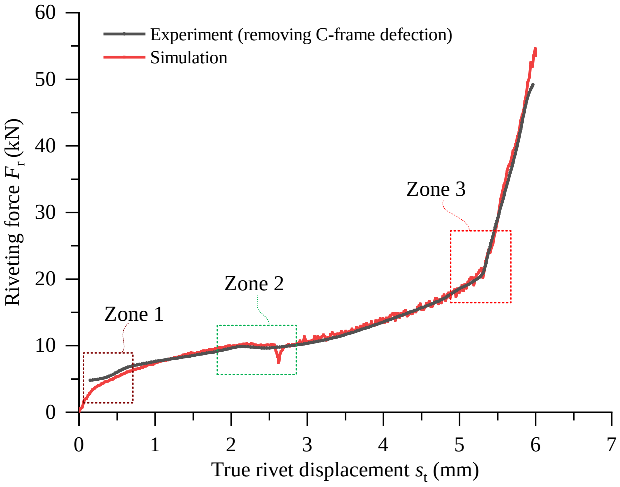

Figure 4.29: Comparisons between the simulated and experimentally tested true force-displacement curves of the SPR joint 4-32

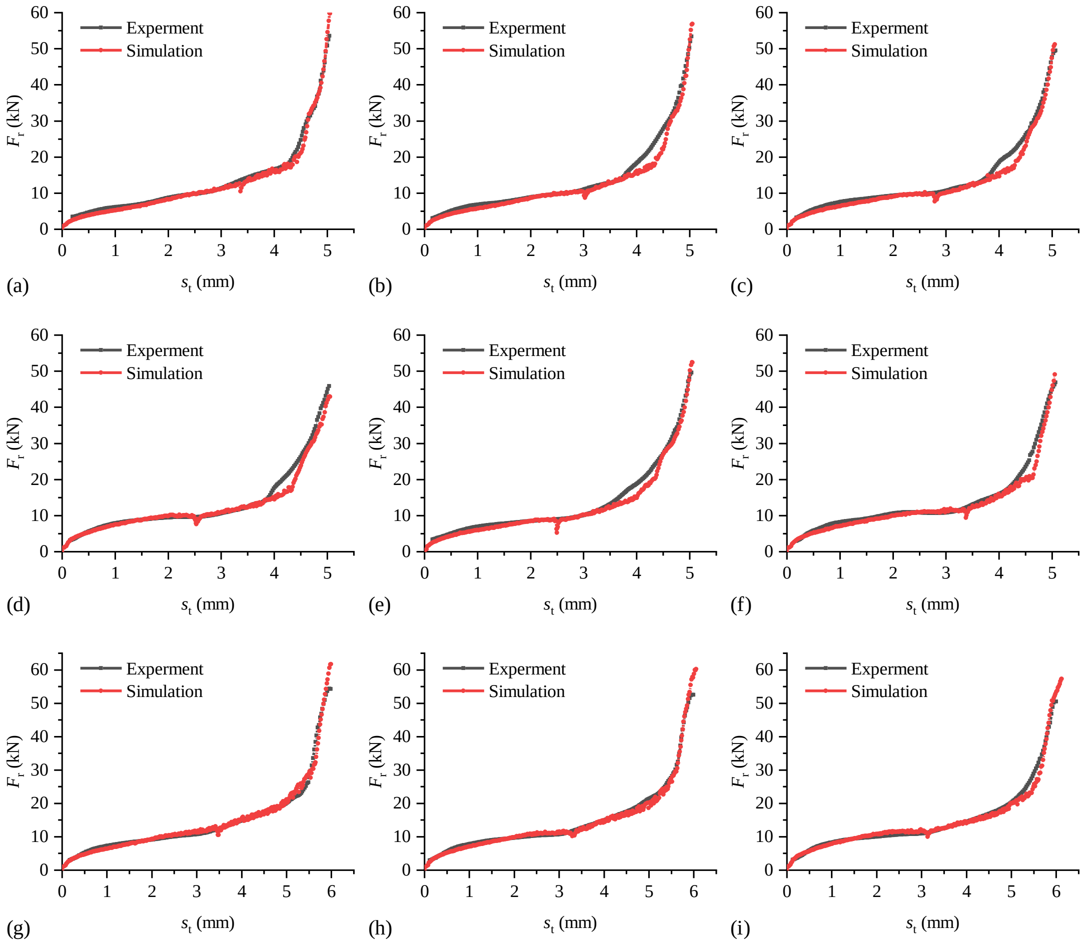

Figure 4.30: Comparisons of the true force-displacement curves from experimental SPR tests and simulations: (a) joint 4-33, (b) joint 4-34, (c) joint 4-35, (d) joint 4-36, (e) joint 4-37, (f) joint 4-39, (g) joint 4-40, (h) joint 4-41 and (i) joint 4-42

4.5. Conclusions

In this chapter, a 2D axisymmetric model of SPR process was successfully developed using the software Simufact.Forming 15. Sensitivity studies were carried out to determine the suitable element mesh sizes of deformable parts and the threshold thickness for the AA5754 top sheet separation. Interrupted experimental SPR tests and experimental tests of SPR joints with varying configurations were conducted to validate the prediction accuracy of the developed FE model. The main conclusions from this chapter are summarised below:

(1) The SPR process can be simplified to an axisymmetric process, and modelled with a 2D axisymmetric FE model using the software Simufac.Forming 15. The die movement induced by C-frame deflection can be simplified into a pure movement along the vertical direction.

(2) The results of sensitivity studies indicated that, for the industrial applications, the suitable mesh sizes for the rivet, top sheet and bottom sheet could be set to 0.10mm, 0.10mm and 0.12mm respectively. The geometrical criterion demonstrated a good performance for the

fracture/separation of AA5754 top sheet, and the suitable threshold thickness could be set to 0.04mm.

(3) The developed FE model of SPR process was successfully validated with the interrupted experimental tests and experimental SPR tests with varying joint configurations. The FE model demonstrated a reasonable prediction accuracy on the deformation behaviours of rivet and sheets, the final SPR joint quality and the riveting force during the riveting process.

(4) To properly compare the experimentally tested force-displacement curve with the simulated one, the influences of C-frame deflection on the force-displacement curve should be removed. The proposed method showed a good performance to transfer the experimentally recorded curve to the true force-displacement curve.

5. Influences of Different Die Parameters on the SPR Process

The die profile plays a very important role in the quality of SPR joints because it directly influences the events happened during the SPR process, especially the deformations of rivet and sheets. In order to improve the joint quality by optimizing the die profile, it is necessary to find out how different die geometrical parameters affect the joint formation process. In this chapter, the FE model of SPR process developed in Chapter 4 was employed to numerically study the events happened during the riveting process. The influences of die type, die diameter (D_1), die depth (H_1) and die pip height on the deformation behaviours of rivet and sheets were systematically studied. The variation trends of the flared rivet shank radius (R_1) and remaining bottom sheet thickness at the joint centre (t_c) during the SPR process were also numerically monitored. Moreover, the relationships between the material deformations and the final SPR joint quality were also discussed. Compared with the experimental SPR test, the FE model of SPR process demonstrates a huge advantage in efficiency to extend understanding of the SPR technique.

5.1. Introduction

To form a sufficient mechanical connection, the rivet and sheets always undergo very large plastic deformations during the SPR process. The main function of the die is to guide the deformations of rivet and sheets, and thus it has critical influences on the riveting process [24]. Any change of the die parameters (e.g., die diameter (D_1), die depth (H_1) and die pip height) will alter the material deformations of rivet and sheets, and inevitably affect the final joint quality, in terms of the interlock (I), the minimum remaining bottom sheet thickness ($T_{\min}$) and the rivet head height (H).

A large number of experimental and numerical studies have been carried out to explore the impact of different die parameters on the SPR process and on the final joint quality. For instance, Li et al. [176] experimentally studied the influences of die profile on the joint quality, mechanical strengths and failure behaviour. Ma et al. [24] experimentally investigated the effects of the die diameter and pip height on the rivetability of the AA6061-T6 and mild steel CR4 sheets. It was discovered that changes of the die diameter and die pip height influenced the joint quality by mainly altering the deformation behaviours of the top and bottom sheets. Mori et al. [73] numerically optimized the die profile for the SPR joints with high strength steel and aluminium alloy sheets. It was found that the severe compression of the rivet leg when piercing the top high strength steel sheet could be eliminated by optimizing the die diameter and depth. Abe et al. [51] numerically optimized the die profile and discovered that the die with larger depth and diameter could effectively extend the joining range of three layer joints with different high strength steels. Mathias et al. [74] numerically studied the effects of the die geometric parameters on the SPR joint quality with a 2D FE model, and found that the die depth was the most significant die parameter. To compensate the changes of the boundary conditions, a novel die geometry with a moveable bottom was proposed in their study to ensure a consistent joint quality. Similarly, a die with a force-controlled moveable bottom was proposed and numerically studied by Drossel and Jackel [75] to improve the joinability of materials with a limited ductility using SPR. Landgrebe et al. [76] experimentally studied the damages of the carbon fibre reinforced plastic (CFRP) sheet during the SPR process, and compared the effects of the traditional die and the new die with a moveable bottom proposed by Drossel and Jackel [75]. Less delamination but more fibre or matrix fractures in the CFRP sheet were captured with the new moveable die compared with that with the conventional die. Hoang et al. [27] numerically and experimentally studied the effects of the die type (flat die and pip die) on the SPR joint with aluminium sheets and aluminium rivet.

Although the influences of different die parameters on the SPR joint have been widely investigated, most of these studies paid more attention to the joint quality rather than the SPR process. Meanwhile, most conclusions in these studies were made by analysing the final joint cross-sectional profiles. However, the deformation behaviours of the rivet and sheets during the joining process directly affect the formations of the quality indicators (i.e., I, $T_{\min}$ and H). Therefore, it is necessary to find out how different die parameters affect the deformations of the rivet and sheets, and how the changes of material deformation affect the formation of critical joint quality indicators. Deeper understanding of the SPR processes with different dies will be helpful to form guidelines on how to select a suitable die for a given sheet combination, and how to develop new types of dies.

5.2. Simulation Design

To study the influences of die type, die diameter (D_1), die depth (H_1) and die pip height on the deformation behaviours of the rivet and sheets, ten SPR joints with different configurations were designed as listed in **Table 5.1**. The rivet and sheets were kept the same in all these joints. The materials of sheets and rivet are aluminium alloy AA5754 and boron steel respectively. The joints 5-1 and 5-2 were used to investigate the influences of the die type (i.e., flat die and pip die). The joints 5-3, 5-4 and 5-5 made by flat dies with different diameters ranged from

7.5mm to 14.0mm were designed to study the effects of the D_1. The joints 5-6 and 5-7 made by flat dies with different die depths were used to investigate the effects of the H_1. The joints 5-8, 5-9 and 5-10 made by pip dies with different pip heights were designed to discover the influences of the die pip height. **Figure 5.1** shows the cross-sectional profiles of the flat die-A and pip die-A. All other dies were modified based on these two referenced dies. The cross-sectional profiles of pip dies with varying pip heights are illustrated in **Figure 5.2**. All these SPR joints were numerically manufactured with the developed FE model, and the joining parameters were the same as that used in Chapter 4. Once all the simulations were completed, the simulation results were extracted and analysed in detail.

Table 5.1: Joint configurations with different die geometric parameters

Joint no.	Thickness (mm)		Rivet (Boron steel)	Die parameters (mm)			
	Top sheet/T_t (AA5754)	Bottom sheet/T_b (AA5754)		Die no.	Depth /H_1	Diameter /D_1	Pip height
5-1	1.2	2.0	C5.3*5.0 (280±30HV10)	Pip die-A	1.6	9.0	0.0
5-2				Flat die-A	2.0	8.5	--
5-3				Flat die-B	2.0	7.5	--
5-4				Flat die-C	2.0	10.0	--
5-5				Flat die-D	2.0	14.0	--
5-6				Flat die-E	1.8	8.5	--
5-7				Flat die-F	2.4	8.5	--
5-8				Pip die-A	1.6	9.0	0.0
5-9				Pip die-B	1.6	9.0	-0.4
5-10				Pip die-C	1.6	9.0	-0.8

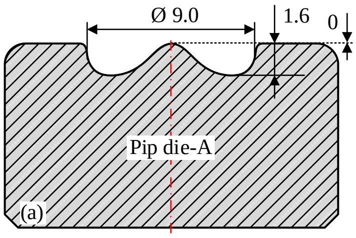

Figure 5.1: Cross-sectional profiles of the referenced dies: (a) pip die-A and (b) flat die-A

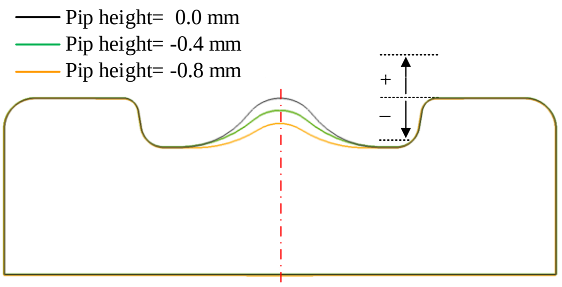

Figure 5.2: Cross-sectional profiles of the pip dies with different pip heights

5.3. Results and Discussion

As shown in **Figure 5.3**, for easy explanation, three spaces in the SPR joint were defined as: the cavity 1 (i.e., rivet cavity), cavity 2 (i.e., die cavity) and cavity 3 (part of the die cavity underneath the rivet cavity). The relationships between the filling conditions of these cavities and the deformation behaviours of the rivet and sheets were discussed in the following sections. Two indicators, including the remaining bottom sheet thickness at the joint centre (t_c) and the flared rivet shank radius (R_1), were also defined as shown in **Figure 5.4** to quantitatively analyse the deformation behaviours of the bottom sheet and the rivet shank.

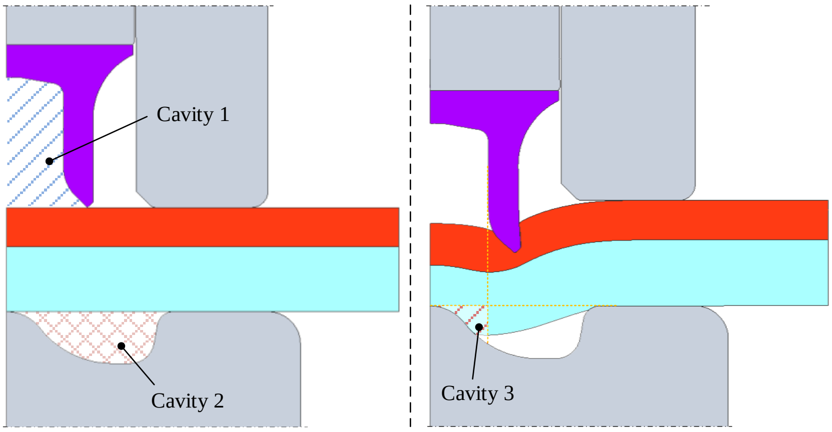

Figure 5.3: Schematic of the three critical rivet and die cavities

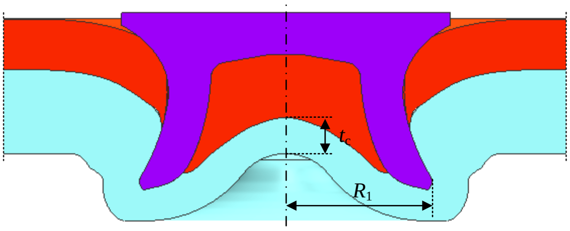

Figure 5.4: Schematic of the remaining bottom sheet thickness at the joint centre (t_c) and the flared rivet shank radius (R_1) measured on the joint cross-sectional profile

5.3.1. Effect of the die type

The deformation behaviours of the rivet and sheets are closely related to the riveting force. Therefore, as shown in **Figure 5.5**, the force-displacement curves in the joint 5-1 with the pip die-A and joint 5-2 with the flat die-A were recorded to assist the study of the SPR process. By comparing the magnitudes on the two curves, it can be found that the riveting force with the pip die is always greater than that with the flat die throughout the SPR process. The maximum riveting force was around 10kN larger with the pip die. To understand the influences of riveting force on the rivet and sheets deformations, the cross-sectional profiles of the joint 5-1 and joint 5-2 at different rivet displacements are presented in **Figure 5.6**(a) and **Figure**

5.6(b) respectively. For easy explanation, the top and bottom sheets were divided into left and right parts as shown in **Figure 5.6**(a-1).

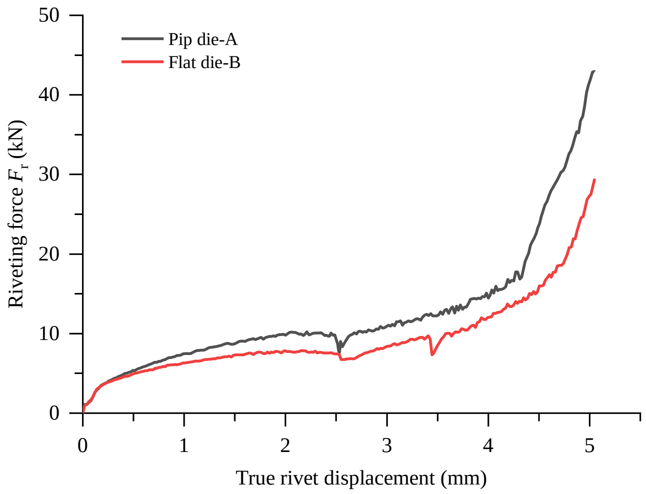

Figure 5.5: Force-displacement curves in the joint 5-1 with pip die-A and the joint 5-2 with flat die-A

Different deformation behaviours of the bottom sheet with the flat die and pip die were observed. Due to the existed die pip in the joint 5-1, a resistance force was applied on the bottom of the stack from the beginning of the riveting process. A larger riveting force, as shown in **Figure 5.5**, was needed for the rivet to press the sheet material downward into the die cavity. As a result, the bottom sheet thickness above the die pip decreased rapidly as shown in **Figure 5.6**(a-2) to (a-5), and large equivalent stresses were observed on the bottom sheet above the die pip as shown in **Figure 5.7**(a). In addition, a large portion of the bottom sheet material on the left part gradually accumulated in the region where the interlock was formed. This had positive effects on the formation of interlock and a larger remaining bottom sheet thickness around the rivet tip.

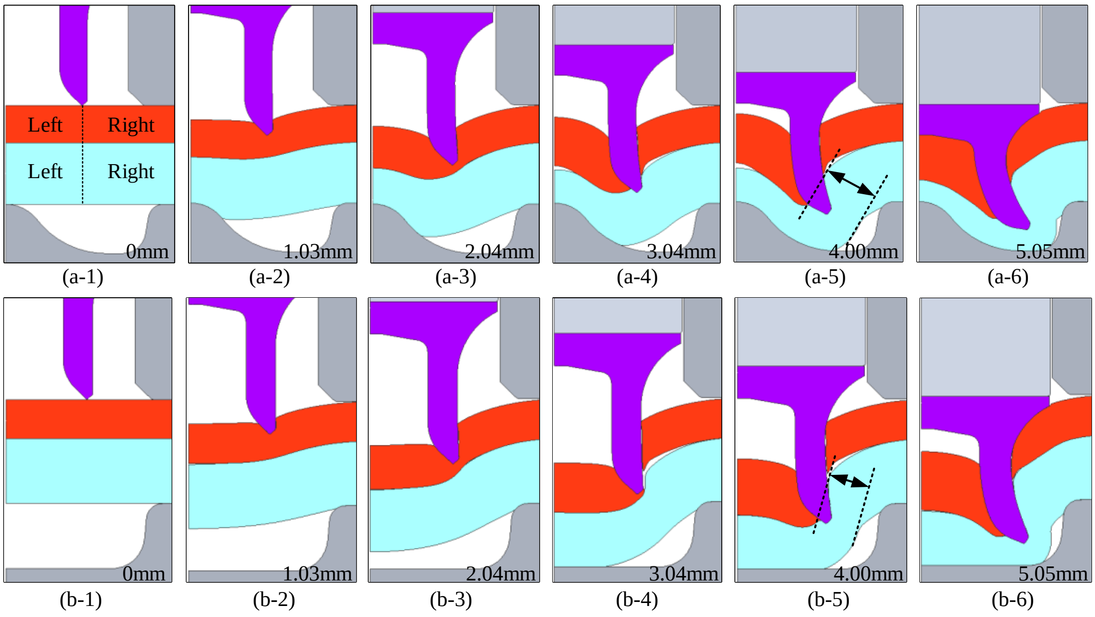

(a-1) (a-2) (a-3) (a-4) (a-5) (a-6)

(b-1) (b-2) (b-3) (b-4) (b-5) (b-6)

Figure 5.6: Joint cross-sectional profiles at different rivet displacements during the riveting processes of the (a) joint 5-1 with pip die-A and (b) joint 5-2 with flat die-A

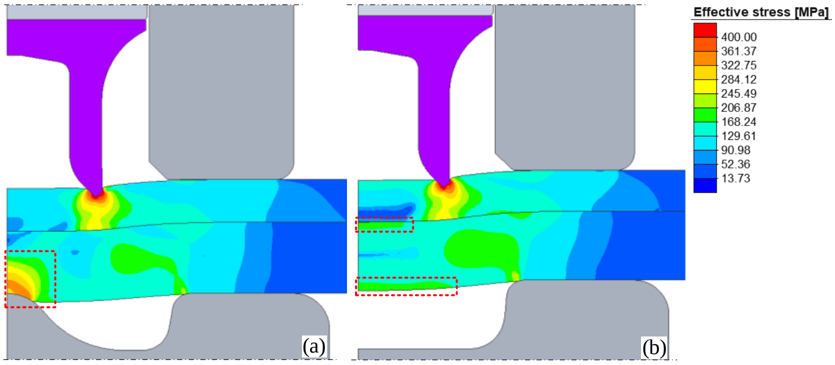

Figure 5.7: Equivalent stress distributions on the top and bottom sheets in (a) the joint 5-1 with pip die-A and (b) the joint 5-2 with flat die-A (rivet displacement=0.52mm)

In contrast, as presented in **Figure 5.6**(b-1), no resistance force was applied on the bottom of the stack with the flat die at the beginning of the SPR process. As a result, the left part of the bottom sheet was rapidly pressed into the die cavity without large plastic deformations as shown in **Figure 5.6**(b-2)(b-3). Relatively small equivalent stresses were observed on the left part of the bottom sheet as shown in **Figure 5.7**(b), and the bottom sheet thickness around the joint centre reduced a very small value. Furthermore, as shown in **Figure 5.6**(b-6), the majority of the left part material on the bottom sheet stayed underneath the rivet rather than being pressed into the region where the interlock was formed. This may have negative effects on the interlock formation and the final remaining bottom sheet thickness around the rivet tip. In addition, by comparing the **Figure 5.6**(a-6) and **Figure 5.6**(b-6), it can be seen that an almost uniform bottom sheet thickness was obtained with the pip die, while a large variation of the bottom sheet thickness was observed with the flat die. This indicated that the pip die could prevent too small bottom sheet thickness in local areas, especially around the rivet tip.

For the top sheet, as presented in **Figure 5.6**(a-5) and **Figure 5.6**(b-5), the left part of top sheet with the pip die underwent a larger plastic deformation than that with the flat die. Whilst similar deformations of the right parts of the top sheets were observed in the two joints. Therefore, the die type showed a greater influence on the bottom sheet deformation than that of the top sheet.

In order to evaluate the influences of the die type on the deformation behaviour of the rivet shank, the flared rivet shank radius (R_1) during the riveting process was recorded. **Figure 5.8** and **Figure 5.9** illustrate the variation curves of the R_1 with the pip die-A and the flat die-A respectively. According to the increasing trend, the variation curve of the R_1 with the pip die was divided into two phases (i.e., I and III), whilst the variation curve of the R_1 with the flat die was divided into three phases (i.e., I, II and III). During the phase I, similar increasing patterns of the R_1 were observed as the rivet displacement increased: the increasing speed of the R_1 firstly increased and then decreased to almost zero when the top sheets were penetrated at the points A_1 and A_2. This can be explained by the variation of the riveting force during this period as shown in **Figure 5.5**. After the fracture/separation of the top sheet, for the pip die, the R_1 continued increasing from point A_1 to the end of the SPR process (phase III). For the flat die, as shown in **Figure 5.9**, the R_1 kept almost constant from the point A_2 to B_2 (phase II), and then started increasing again at the point B_2 until the end of the SPR process (phase III).

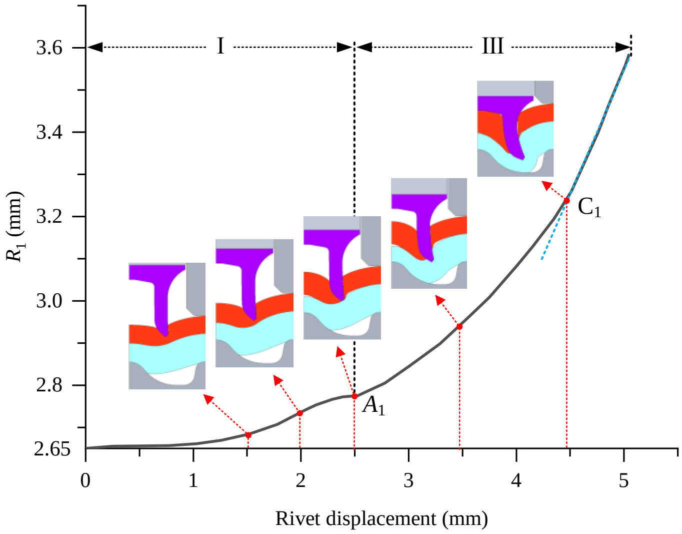

Figure 5.8: Variation curve of the flared rivet shank radius (R_1) in the joint 5-1 with pip die-A

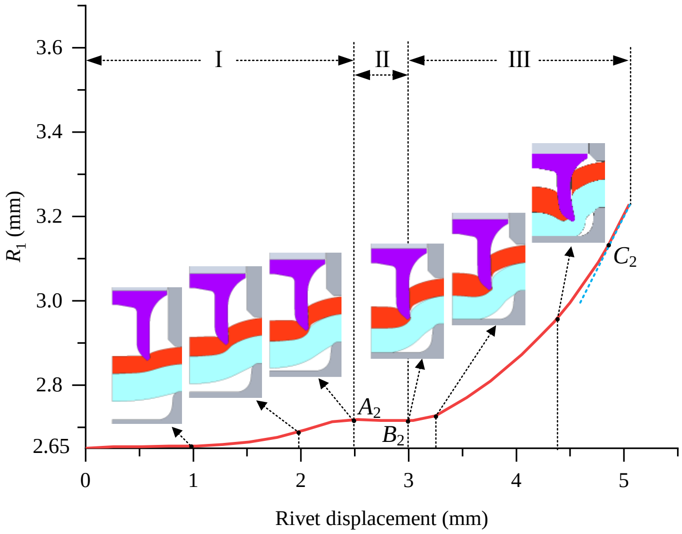

Figure 5.9: Variation curve of the flared rivet shank radius (R_1) in the joint 5-2 with flat die-A

The major difference between the two curves is the absence of the phase II for the pip die. By observing the cross-sectional profiles of the two joints in **Figure 5.8** and **Figure 5.9**, it was found that the phase II depended heavily on the filling condition of the cavity 3. There was no phase II in the joint 5-1 because the cavity 3 was fully filled before the top sheet was penetrated. Whilst the phase II appeared in the joint 5-2 after the top sheet was penetrated, and ended when the cavity 3 was fully filled at the point B_2. Once the cavity 3 was fully filled, the R_1 started increasing rapidly (phase III).

The necessity of the fully filled cavity 3 for the rapid increase of the R_1 in the phase III can be explained from different point of views. Take the joint 5-2 as an example, from the point view of material flow: Before the cavity 3 was fully filled as shown in **Figure 5.10**(a), the bottom sheet material was pushed into the die cavity (the space in Zone 1), which made more space for the top sheet material underneath the rivet shank to move downward rapidly (the material flow in Zone 2). As a result, the rivet shank also moved downward rather than flaring. Therefore, the R_1 kept almost constant during this period. In contrast, when the cavity 3 was fully filled as shown in **Figure 5.10**(b), the bottom sheet material kept being pushed into the die cavity (the space in Zone 3). However, the Zone 3 is not under the rivet shank, which led to a smaller downward moving speed of the top sheet material in Zone 4. Therefore, the rivet shank flared rather than moving downward, and a rapid increase of the R_1 was observed. From the point view of force: As presented in **Figure 5.11**, for the flat die, relatively small equivalent stresses on the rivet shank were observed after the fracture/separation of the top sheet and before the cavity 3 was fully filled. Thus, the rivet shank moved downward and the R_1 kept almost constant. After the cavity 3 was fully filled, large equivalent stresses on the rivet shank were observed and the rivet shank started flaring again. So the R_1 increased again with the increment of the rivet displacement.

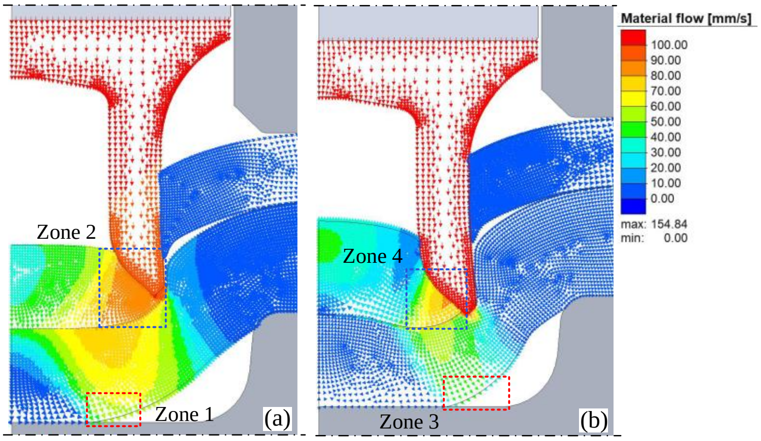

Figure 5.10: Materials flowing behaviour of the rivet and sheets in the joint 5-2: (a) before and (b) after the cavity 3 was fully filled

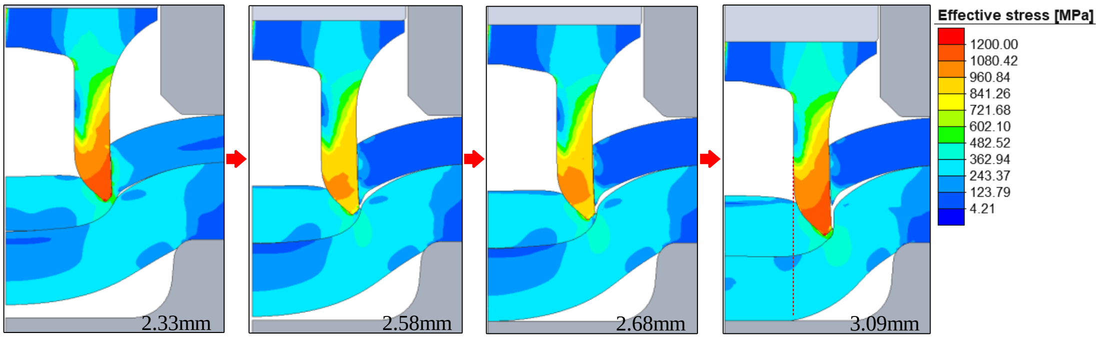

Figure 5.11: Equivalent stress distributions before and after the point *B* in the joint 5-2 with flat die-A

As shown in **Figure 5.8** and **Figure 5.9**, the almost linear increase of the R_1 started earlier at the point C_1 with pip die-A compared with the flat die-A at the point C_2 during the phase III. This phenomenon may be related to the filling condition of the rivet cavity. In the joint 5-1, the rivet cavity was gradually filled up from the point B_1 to C_1. Once the rivet cavity was fully filled at the point C_1, the material within the rivet cavity showed an almost constant guidance effect on the flaring of the rivet shank. In contrast, in the joint 5-2, the rivet cavity was not fully filled even at the end of the SPR process. The almost constant guidance effect appeared at point C_2 when the shape of the materials underneath the rivet cavity kept almost constant.

5.3.2. Effect of the die diameter

The force-displacement curves of the joints 5-3, 5-4 and 5-5 with different die diameters 7.5mm, 10.0mm and 14.0mm are presented in **Figure 5.12**. With the increment of the D_1, the riveting force at the beginning and at the end of the SPR process showed a decreasing trend, whilst it was almost the same in the middle of the SPR process. Meanwhile, the maximum riveting force dropped from around 40kN to only 20kN when the D_1 changed from 7.5mm to 14mm.

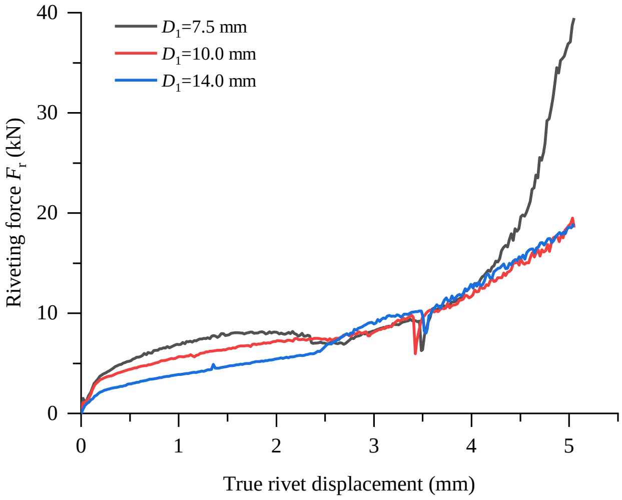

Figure 5.12: Force-displacement curves in the SPR joints with different die diameters

Figure 5.13 illustrates the cross-sectional profiles of the joints 5-3 and 5-4 at different rivet displacements. Comparing the **Figure 5.13**(a-2)(a-3) and (b-2)(b-3), smaller distances between the bottoms of the stack and the die cavity were observed in the joint 5-4. This is because the increment of the die diameter enlarged the area of sheets above the die cavity, which made it easier for the top and bottom sheets to be bent into the die cavity and led to a slightly smaller riveting force. However, at the same rivet displacements, the depth that the rivet shank pierced into the top sheet was smaller in the joint 5-4 than that in the joint 5-3. This phenomenon could be explained by the relatively larger downward bending rate of the top sheet and the smaller riveting force during this period in the joint 5-4 as shown in **Figure 5.12**. So a larger rivet displacement was required for the rivet to penetrate the top sheet in SPR joints with a larger die diameter. Furthermore, large gaps between the rivet and the right part of the top sheet (Gap 1 and Gap 2) were observed in the joint 5-4 as shown in **Figure 5.13**(b-6), while no apparent gap was found in the joint 5-3 as shown in **Figure 5.13**(a-6). This was mainly attributed to the bended distance of the right part on the top sheet when the fracture/separation of the top sheet occurred as shown in **Figure 5.13**(a-4) and (b-4). The increment of the die diameter caused a larger bended distance of the right part on the top sheet. However, the total rivet displacement was not large enough to make the rivet head to press the top sheet. So the Gap 1 and Gap 2 was not eliminated in the joint 5-4 at the end of the SPR process. The appearance of these gaps may have a negative effect on the mechanical strength of the SPR joint, and they could be eliminated by using a larger rivet displacement or a smaller die diameter.

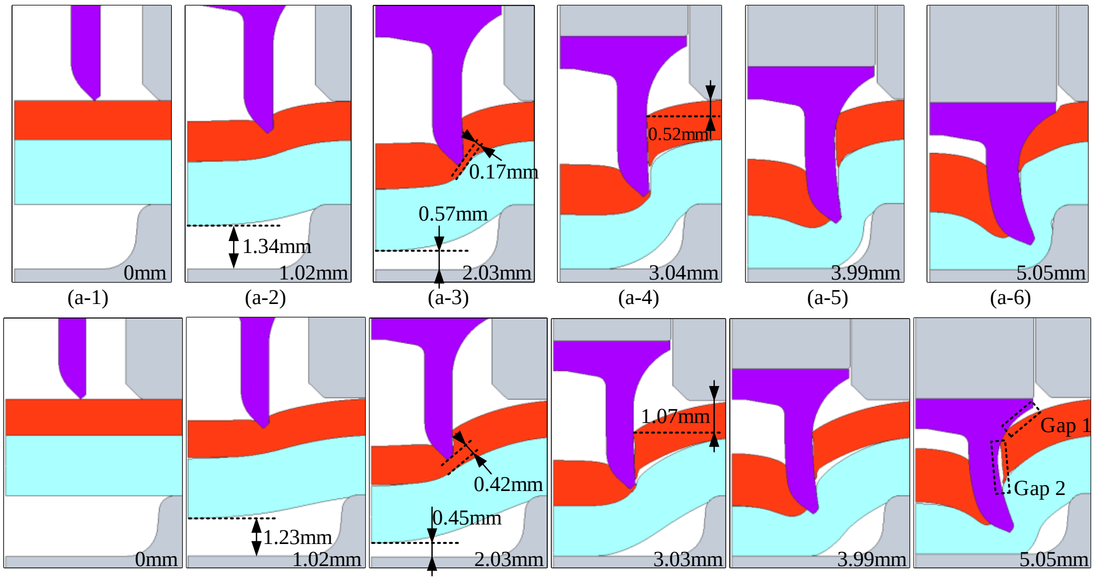

Figure 5.13: Joint cross-sectional profiles during SPR processes with different die diameters (D_1): (a) 7.5 mm (flat die-B) and (b) 10.0 mm (flat die-C)

To study the influence of the die diameter on the variation of the remaining bottom sheet thickness, the remaining bottom sheet thickness at the joint centre (t_c) in the joints with different die diameters was recorded as shown in **Figure 5.14**. For easy explanation, these curves were roughly divided into four phases according to the changing trend. A similar decreasing tendency of the t_c was observed among the three curves, except for the slight difference on the far right of these curves.

During the phase I, the left part of the bottom sheet was stretched along the radial direction and large equivalent stresses were observed only on the local region around the centre of the bottom sheet as shown in **Figure 5.15**(a). This caused the slow decline of the t_c. Once the bottom sheet contacted with the bottom of the die cavity, large equivalent stresses were observed on a larger region around the centre of the bottom sheet as presented in **Figure 5.15**(b). Thus, the t_c started decreasing at a higher rate during the phase II. The phase III started when the cavity 3 was fully filled. As illustrated in **Figure 5.15**(c), the high stress concentration area on the bottom sheet transferred to the region around the rivet tip. The low-level equivalent stress around the centre of the bottom sheet was not large enough to cause further reduction of the t_c. Therefore, the t_c kept almost constant during this period. During the phase IV, the increment value of the t_c was heavily influenced by the filling condition of the die cavity. Take the joint 5-3 as an example, the die cavity was fully filled before the end of the SPR process. With further increment of the rivet displacement, there was no space in the die cavity to accommodate extra sheet material. So the top and bottom sheets material was pressed towards the unfilled space of the rivet cavity, which caused the rapid increase of the t_c.

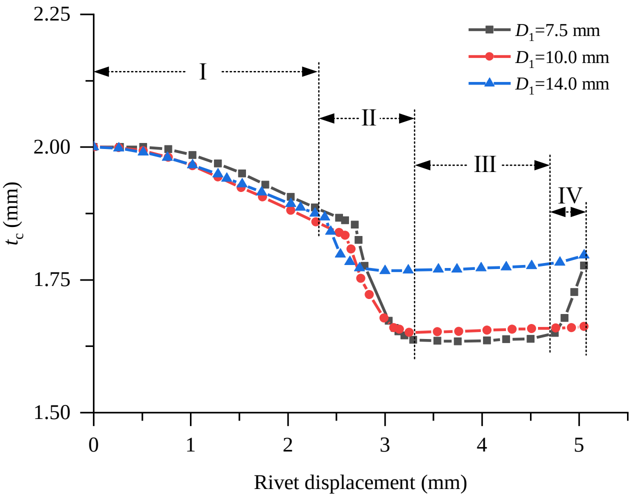

Figure 5.14: Variation curves of the remaining bottom sheet thickness at the joint centre (t_c) in SPR processes with different die diameters (D_1)

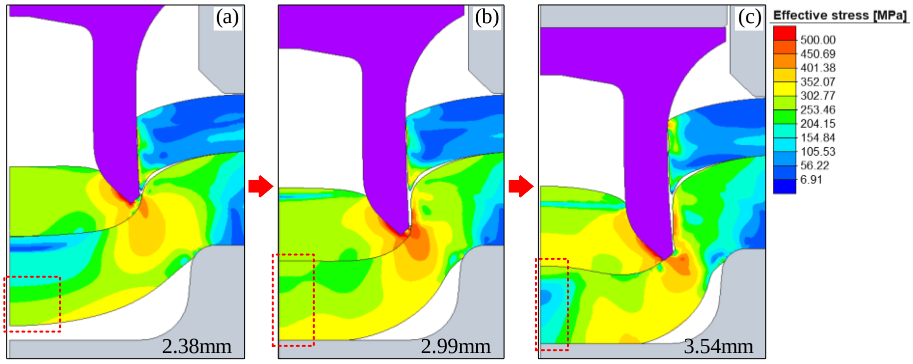

Figure 5.15: Equivalent stress distribution in the joint 5-3 at different phases (D_1=7.5 mm): (a) phase I, (b) phase II and (c) phase III

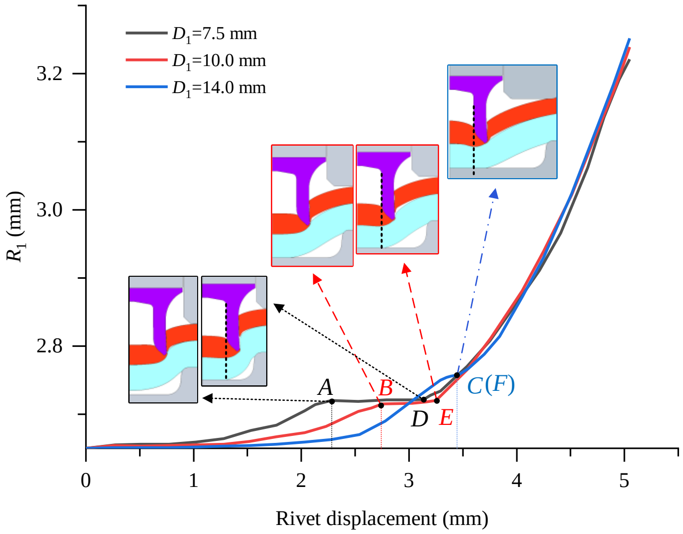

Figure 5.16: The flared rivet shank radius (R_1) in SPR processes with different die diameters (D_1)

The variation curves of the R_1 with different die diameters are illustrated in **Figure 5.16**. Before the fracture/separation of the top sheet at the points *A*, *B* and *C* in different joints, a smaller increment of the R_1 was observed with a larger die diameter. With the increment of the die diameter, the rivet shank encountered a smaller resistance force from the sheets as illustrated in **Figure 5.12**, which caused this smaller incremental value of the R_1. After the top sheet was penetrated, the R_1 kept almost constant for a period. The length of this period varied with the die diameter: the larger die diameter, the shorter this period. This is because, with a larger die diameter, the fracture of the top sheet delayed a larger time than the delayed time that the cavity 3 was fully filled. After the cavity 3 was fully filled at the points *D*, *E* and *F* in different joints, a rapid increase of R_1 was observed. However, very limited influences of the die diameter on the increasing speed of the R_1 was observed during this period. In addition, at the end of SPR process, a little bit larger R_1 was observed in the joints with a larger die diameter.

From the analysis above, it can be concluded that the die diameter had significant influences on the rivet shank flaring behaviour. With a larger die diameter, due to the reduction of the riveting force when the rivet pierced the top sheet, it is potential to reduce the possibility of the premature rivet shank compression. Similar conclusions were also made in [73]. Although the increment of the die diameter can lead to a larger R_1, the influence of this larger R_1 on the interlock formation needs to be further investigated.

5.3.3. Effect of the die depth

The force-displacement curves of the joints 5-6 and 5-7 with different die depths 1.8mm and 2.4mm are presented in **Figure 5.17**. The riveting forces are the same on the two curves when the rivet displacement changed from 0.0mm to around 2.5mm. With further increment of the rivet displacement, a smaller riveting force was observed in the joint 5-7 than in the joint 5-6.

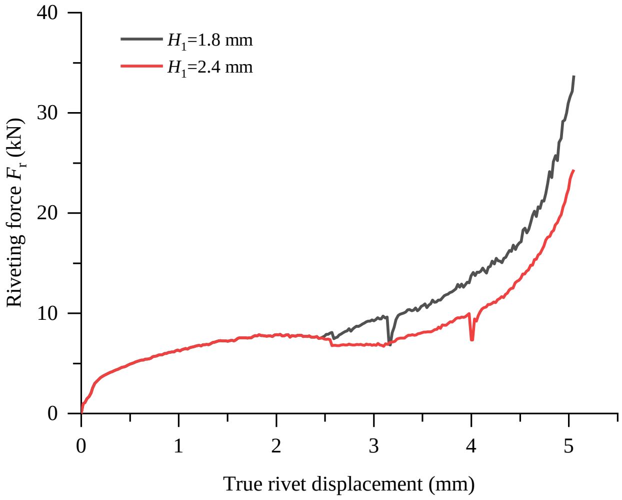

Figure 5.17: Force-displacement curves in the SPR joints with different die depths

Figure 5.18 shows the cross-sectional profiles of the joints 5-6 and 5-7 at different rivet displacements. Comparing the **Figure 5.18**(a-1)(a-2)(a-3) and (b-1)(b-2)(b-3), identical deformation behaviours of the rivet and sheets in the two joints were observed before the bottom sheet contacted with the bottom of the die cavity in the joint 5-6. With a larger die depth, the bottom sheet contacted with the bottom of the die cavity at a later time in the joint 5-7 than that in joint 5-6. Therefore, the bottom sheet material around the rivet tip in the joint 5-7 was stretched for a longer time, which resulted in a thinner bottom sheet thickness around the rivet tip (0.79 mm) as presented in **Figure 5.18**(b-5). Meanwhile, it was also noticed that the rivet shank did not flare into the bottom sheet when the bottom sheet thickness around the rivet tip had already become very thin. This is because the cavity 3 in the joint 5-7 was not fully filled for a longer period after the fracture/separation of the top sheet. The delayed filling of the cavity 3 and the relatively smaller rivet shank flaring distance caused the smaller riveting force in the joint 5-7 as shown in **Figure 5.17**. This phenomenon indicated that a too large die depth may have negative effects on the interlock formation and the T_{min}.

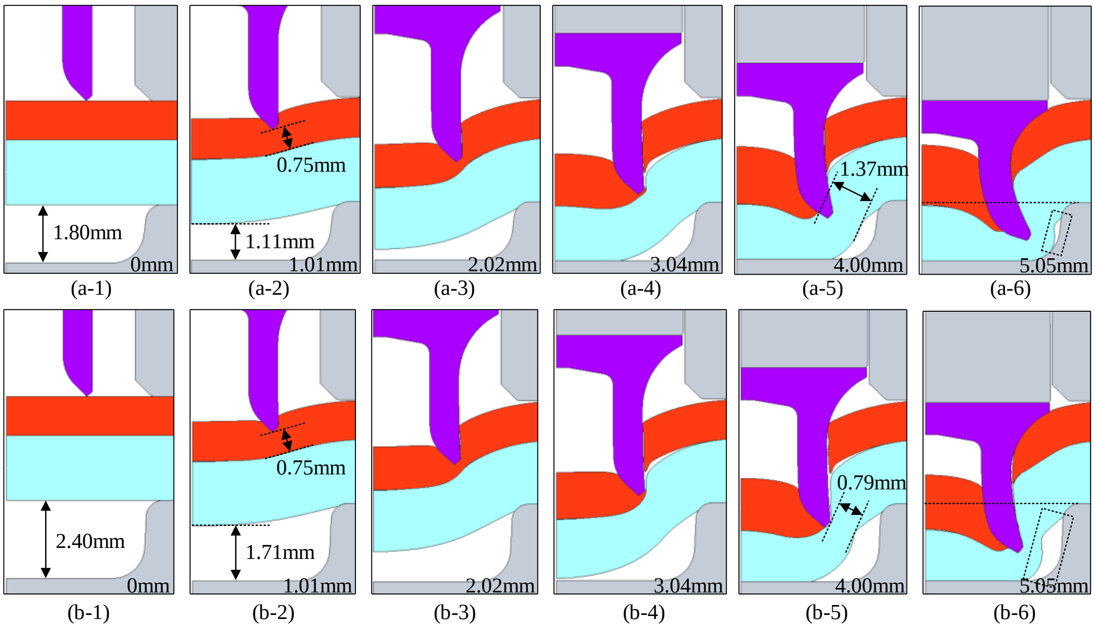
1.80mm
0mm
0.75mm
1.11mm
1.01mm
2.02mm
3.04mm
1.37mm
4.00mm
5.05mm
2.40mm
0mm
0.75mm
1.71mm
1.01mm
2.02mm
3.04mm
0.79mm
4.00mm
5.05mm

(a-1) (a-2) (a-3) (a-4) (a-5) (a-6)

(b-1) (b-2) (b-3) (b-4) (b-5) (b-6)

Figure 5.18: Joint cross-sectional profiles during SPR processes with different die depths: (a) H_1=1.8 mm (flat die-E) and (b) H_1=2.4 mm (flat die-F)

The variation curves of the t_c with different die depths are illustrated in **Figure 5.19**. A similar changing pattern of the t_c was observed on the two curves. The values of the t_c were the same on the two curves before the point *A*. While the rapid decline of the t_c in the joint 5-7 appeared at a later time compared with that in the joint 5-6. This is caused by the delayed contact between the bottom sheet and the bottom of the die cavity in the joint 5-7 at point *B*. Meanwhile, a little bit larger decreasing rate of the t_c in the joint 5-7 was observed. This can be explained by the slightly larger equivalent stresses distributed on the bottom sheet of the joint 5-7 as shown in **Figure 5.20**. Moreover, a smaller t_c was observed at the end of the SPR process in the joint 5-7. So the increment of the die depth could lead to a smaller remaining bottom sheet thickness around the joint centre.

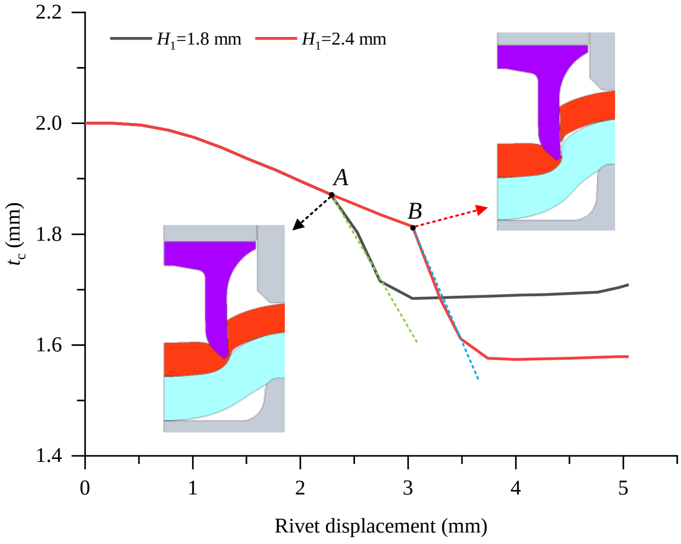

Figure 5.19: Variation curves of the remaining bottom sheet thickness at the joint centre (t_c) during the SPR processes with different die depths (H_1)

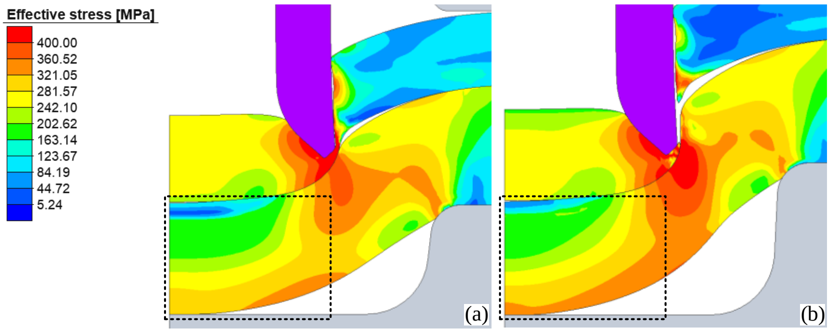

Figure 5.20: Equivalent stress distribution on the sheets after the bottom sheet contacted with the bottom of the die cavity: (a) H_1=1.8 mm (flat die-E) and (b) H_1=2.4 mm (flat die-F)

The changing curves of the R_1 with different die depths are presented in **Figure 5.21**. Similarly, same increasing values of the R_1 on the two curves were observed before the fracture/separation of the top sheet at the point *A*. However, the rapid increment of the R_1 appeared at a later time and lasted a shorter period in the joint 5-7. An almost same increasing speed of the R_1 during this rapidly increasing stage was captured. As a result, a smaller R_1 was achieved in the joint 5-7 at the end of the joining process. Therefore, it can be concluded that the die depth (H_1) could significantly influence the flaring behaviour of the rivet shank. A too large die depth might have negative effects on the interlock formation.

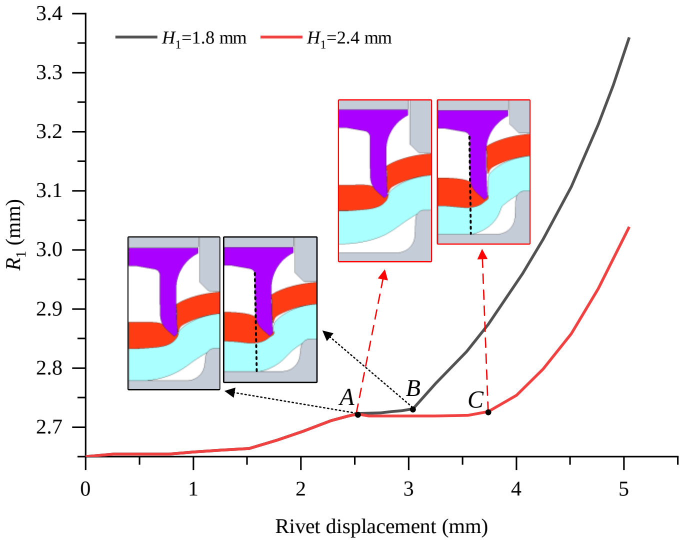

Figure 5.21: The flared rivet shank radius during SPR processes with different die depths (H_1)

5.3.4. Effect of the die pip height

The force-displacement curves of the joints 5-8, 5-9 and 5-10 with different die pip heights 0.0mm, −0.4mm and −0.8mm are presented in **Figure 5.22**. With the increment of the die pip height, the riveting force at the beginning and at the end of the SPR process showed an increasing trend, whilst it was almost the same in the middle of the SPR process. However, differing from other die parameters, no large changes of the maximum riveting force were observed.

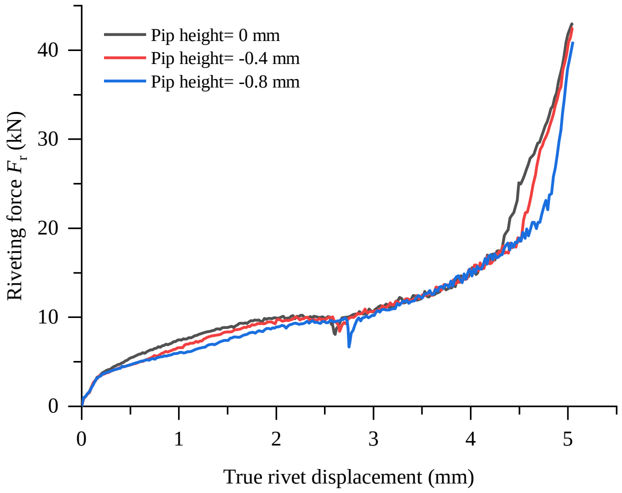

Figure 5.22: Force-displacement curves in the SPR joints with different die pip heights

The cross-sectional profiles of the joint 5-8, joint 5-9 and joint 5-10 at different rivet displacements are illustrated in **Figure 5.23**. Similar to the die depth, the die pip height could directly determine the time when the die pip contacted with the bottom sheet and applied a resistance force on the bottom of the stack. As a result, the deformed bottom sheet thickness was changed as shown in **Figure 5.23**(a-6), (b-6) and (c-6): the smaller the pip height, the thicker the remaining bottom sheet thickness above the die pip. This means that the thickness of the deformed bottom sheet can be controlled by adjusting the die pip height. Moreover, no apparent difference of the top sheet deformation was observed.

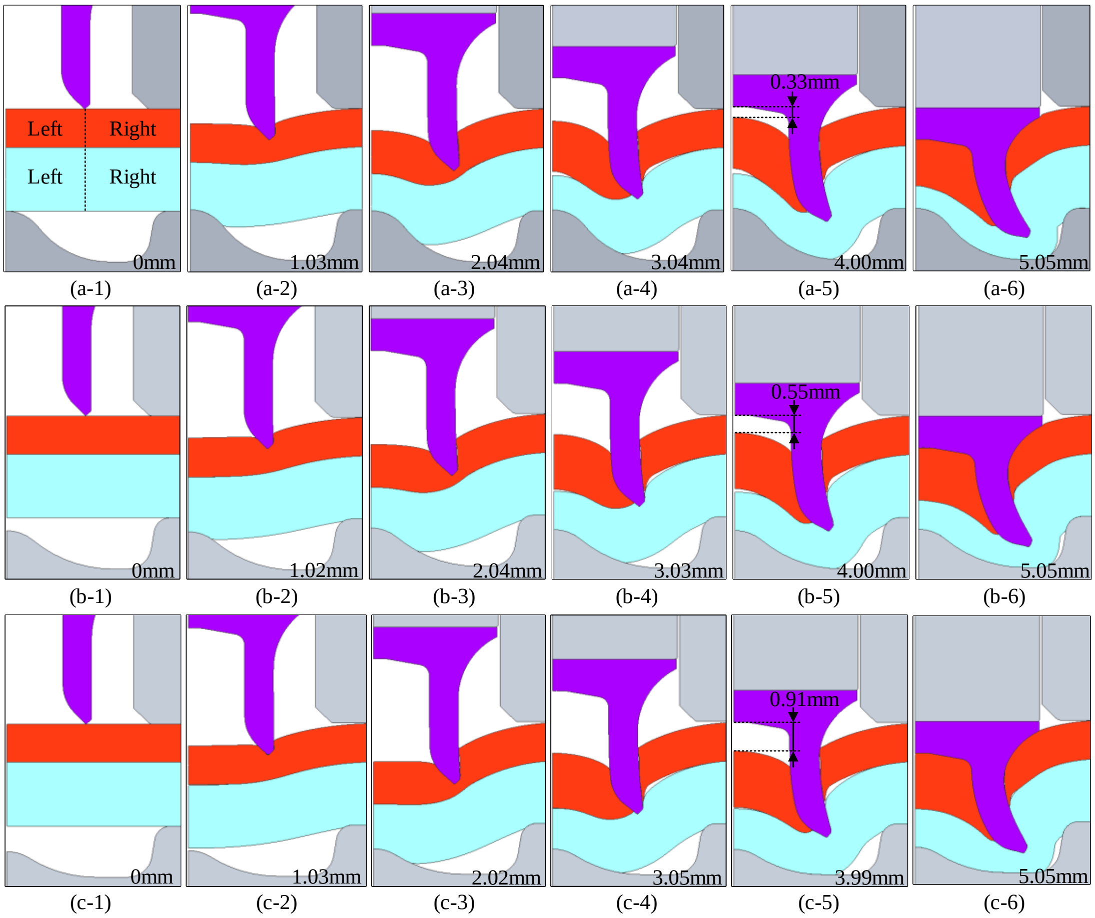

Left
Right
Left
Right
0mm
1.03mm
2.04mm
3.04mm
0.33mm
4.00mm
5.05mm
(a-1)
(a-2)
(a-3)
(a-4)
(a-5)
(a-6)
0mm
1.02mm
2.04mm
3.03mm
0.55mm
4.00mm
5.05mm
(b-1)
(b-2)
(b-3)
(b-4)
(b-5)
(b-6)
0mm
1.03mm
2.02mm
3.05mm
0.91mm
3.99mm
5.05mm
(c-1)
(c-2)
(c-3)
(c-4)
(c-5)
(c-6)

Figure 5.23: Joint cross-sectional profiles during SPR processes with different die pip heights: (a) 0.0mm (pip die-A), (b) −0.4mm (pip die-B) and (c) −0.8mm (pip die-C)

Figure 5.24 demonstrates the variation curves of the t_c with different die pip heights. When the pip height was 0.0mm, the die pip contacted with the bottom of the stack at the beginning of SPR process. So the t_c decreased rapidly with the increment of the rivet displacement at the beginning of SPR process. However, when the pip height was smaller than 0.0mm, the die pip did not contact with the bottom of the stack at the beginning of the SPR process. So the t_c first decreased slowly, and then decreased rapidly once the die pip contacted with the bottom of the stack. Moreover, the decreasing speed of the t_c at the end of the SPR process was almost identical among the three SPR joints, and this may be attributed to the same filling condition of the rivet cavity. This sharp decline of the t_c appeared at an earlier time and lasted a longer period with a larger die pip height. Because the rivet cavity was fully filled at an earlier time in the joints with a higher die pip. In addition, it was also found that the t_c reduced a larger value not only at the beginning but also at the end of SPR process with a larger die pip height. Therefore, it can be concluded that the die pip height had significant influences on the reduction of the t_c. The increment of the die pip height could lead to a smaller t_c at the end of the SPR process.

The variation curves of the R_1 with different die pip heights are illustrated in **Figure 5.25**. A similar increasing trend of the R_1 was observed on the three curves. It is worth noting that the rivet shank flared a little bit larger distance at the end of SPR process with a higher die pip, and this difference was mainly formed in Zone 1.

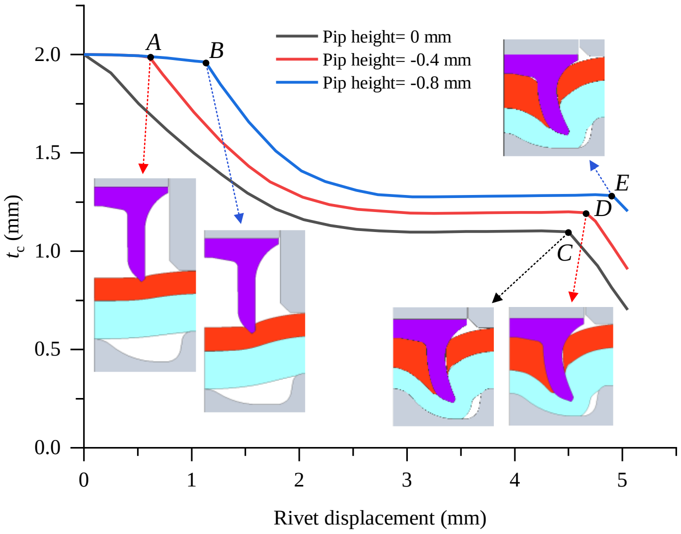

Figure 5.24: Variation curves of the remaining bottom sheet thickness at the joint centre (t_c) in SPR processes with different die pip heights

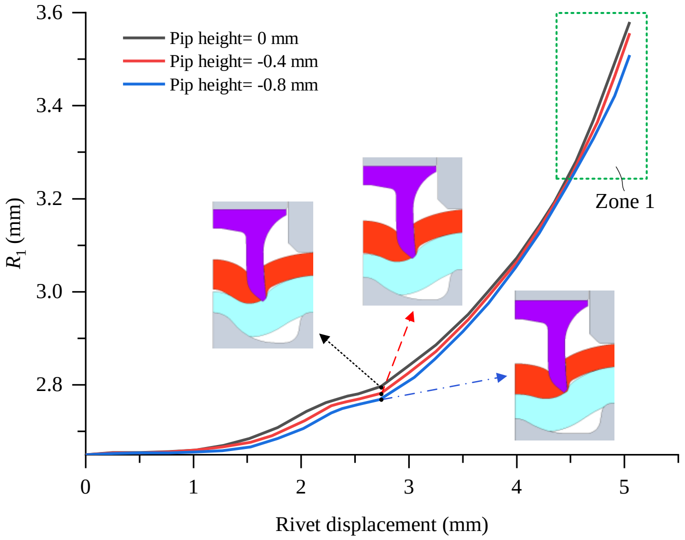

Figure 5.25: The flared rivet shank radius (R_1) during SPR processes with different die pip heights

5.3.5. Interaction effects among different die parameters

In practice, the die profile is usually optimized for new joint configurations by changing the different parameters together. It is necessary to understand how these die parameters work together to affect the SPR process. Therefore, based on the aforementioned single die factor effects on the SPR process, the interaction effects between different die parameters were also discussed.

For the flat die, the diameter and depth are the two most important parameters. The changes of the two factors would directly affect the deformations of the rivet and sheets, and the interaction effects of them on the SPR process as well as the joint quality could be roughly estimated by the single factor effects. Roughly speaking, the single factor effects of these two parameters would be superimposed together to affect the riveting process. According to the results above, it can be concluded that the die depth had a larger influence on the SPR process and would dominate the interaction effects of these two factors. For instance, a larger die diameter (die 1) could lead to a slight increase of the R_1 and t_c. For the joint quality, the interlock would decrease but the T_{min} would show an increasing trend. In contrast, a larger die depth (die 2) could lead to an obvious decrease of the R_1 and t_c. For the joint quality, both of the interlock and T_{min} would show a decreasing tendency. If the die with a larger diameter and a larger depth (die 3), the R_1 and the t_c would be more possible to reduce to a smaller value due to the dominated effect of the die depth. However, the reduction value of the R_1 and t_c would be smaller than that with the die 2. For the joint quality, the interlock would reduce to a smaller value than both of the die 1 and die 2, while it is difficult to predict the T_{min} because of the opposite changing trends caused by the larger die diameter and larger die depth.

For the pip die, except for the diameter and depth, the pip height is also a very important parameter. Although the single effects of the diameter and depth of the pip die on the SPR process were not discussed above, both of them should have similar influences on the SPR process like that in the flat die. The interaction effects between the diameter and depth of the pip die on the SPR process would be also similar like that of the flat die. So this is not repeated again. The die with a higher pip could lead to an obvious decrease of the t_c but a slight increase of the R_1. For the joint quality, the interlock would increase with a higher die pip, but the changing trend of the T_{min} is uncertain because of the location change. If the die with a larger diameter and a higher die pip, the t_c might lightly decrease because the die pip had a stronger effect on the t_c than the diameter, while the R_1 would show an increasing trend. For the joint quality, the interlock might show a slight increase rather than decrease, while the changing trend of the T_{min} is uncertain. If the die with a larger depth and a higher die pip, the t_c would decrease and the R_1 might be also decrease because the die depth may have a larger influence than the pip height. For the joint quality, it is hard to predict the interlock and T_{min} because of the lack of experiment or simulation data. More efforts are required to discover the interaction effects among different die parameters on the SPR process and the joint quality.

5.4. Conclusions

In this chapter, the influences of different die geometric parameters, including the die type, the diameter of flat die, the depth of flat die and the pip height of pip die, on the deformation behaviours of the rivet and sheets were numerically investigated. The major conclusions from this chapter are summarised below:

(1) For the studied joint configurations, an almost uniformly distributed bottom sheet thickness was obtained with the pip die, whilst a large variation of the bottom sheet thickness was observed with the flat die. Compared with the flat die, the pip die showed a stronger guidance effect on the rivet shank flare.

(2) Increment of the die diameter (D_1) could cause a delay of the top sheet separation/fracture, and facilitate the rivet shank flare. The remaining bottom sheet thickness at the joint centre (t_c) first decreased and then increased with the increment of the die diameter. For a larger diameter die, a slightly larger rivet displacement should be used to eliminate the gaps between the rivet and the right part of the top sheet. This would be benefit for the improvement of the joint mechanical strength.

(3) Increment of the die depth (H_1) caused a reduction of the flared rivet shank radius (R_1), which had a negative effect on the joint quality, especially the interlock. It also led to a reduction of the t_c, and a smaller bottom sheet thickness around the rivet tip.

(4) Increment of the die pip height resulted in a smaller t_c but a larger R_1. By adjusting the magnitude of the die pip height, the thickness distribution on deformed bottom sheet can be optimized to improve the joint quality.

(5) The flaring behaviour of the rivet shank depended heavily on the filling condition of the die cavity underneath the rivet cavity (cavity 3). Rapid rivet shank flare occurred after the cavity 3 was fully filled.

6. Finite Element Modelling of Riv-Bonding Process

To improve the mechanical strengths and water resistance performance of riveted structures, SPR technique is usually utilized together with adhesive bonding technique in the automotive industry. In this chapter, based on the developed simulation model of SPR process in Chapter 4, a 2D axisymmetric FE model of Riv-Bonding process was successfully developed for industrial applications. The Ostwald-de Waele power law was adopted to approximately represent properties of the adhesive SikaPower 498. Interrupted laboratory tests of the Riv-Bonding process, and experimental tests of the Riv-Bonding joints with varying configurations were carried out to validate the prediction accuracy of the developed FE model. The simulation model in this chapter lays a foundation for further quality prediction and mechanical strengths modelling of Riv-Bonding joints.

6.1. Introduction

The Riv-Bonding technique simply combines adhesive bonding and self-pierce riveting together to achieve a more reliable and efficient connection. **Figure 6.1** shows the major steps during the Riv-Bonding process. The adhesive is applied on the centre of the bottom sheet and distributed between the two sheets after the clamping process. Then, the normal SPR process is carried out to form the Riv-Bonding connection.

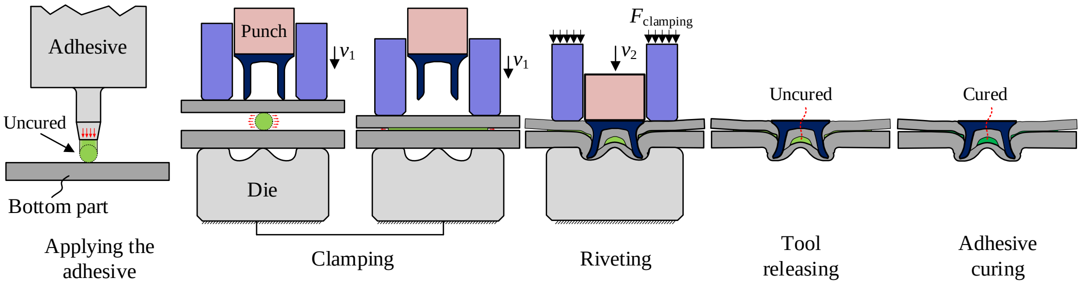

Figure 6.1: Schematic of the Riv-Bonding process

So far, only a limited number of studies relevant to the Riv-Bonding can be found and most of them focused on the joint mechanical performance evaluation. For instance, Baurova et al. [138] experimentally studied the shear strength of the Riv-Bonding joints with a hot-melt adhesive. He et al. [142] investigated the shear strength and energy absorption of the Riv-Bonding joints made with AA5754 sheets and a 0.10mm adhesive layer. Liu and Zhuang [143] experimentally studied the shear strength and failure modes of the Riv-Bonding joints with the top sheet of carbon fibre reinforced polymer (CFRP) and AA5754-H22 as the bottom sheet.

Miyashita et al. [144] investigated the shear strength and fatigue strength of the Riv-Bonding joints with AM50 magnesium alloy sheets. Sun et al. [6] found that the involved adhesive layer (Dow Betamate 4601) apparently improved the fatigue performance of the SPR joints under the lap-shear loading condition. The above studies have undoubtedly facilitated the applications of the Riv-Bonding technique in the industrial field. In addition, efforts have also been made by researchers to develop simulation models of the Riv-Bonding process, but the progress is not desirable because of the difficulties to describe the fluid-structure interaction (FSI) between the uncured adhesive and other solid parts. So far, the only accessible simulation model of the Riv-Bonding process was reported by Fricke and Vallée [131]. Two types of simulation software were used in their study: one for the modelling of solid parts using structural finite element method (FEM), and another for the modelling of the uncured adhesive (a high viscosity fluid) using computational fluid dynamic (CFD) method. In addition, a coupling software was also used to exchange information at the fluid-structure interfaces between the two software. The reason for using different types of software was triggered by the different natures between the solid and fluid. The results indicated a reasonable agreement between the simulation and the experimental results. However, despite the long time to set up the simulation model, this co-simulation method is also computationally expensive and requires a wide knowledge on three different software. In the automotive industry, an easy-to-use and fast response simulation model of the Riv-Bonding process is urgently needed. To deal with the FSI between the uncured adhesive and solid parts, a promising solution is the Ostwald–de Waele power law, which approximately describes the fluid flow behaviour by establishing a relationship between the shear stress and shear rate of the fluid. Due to the simplicity, it has already been adopted in many studies to model the fluid flow behaviour [178, 179]. Recently, based on the simulation method proposed by Ardakan [179], Gerstmann and Awiszus [180] successfully developed a fast response simulation model of the Clinch-Bonding process. The Ostwald-de Waele power law was used to model the uncured adhesive and showed a very good performance. Therefore, to better understand the Riv-Bonding technique, a fast response and easy-to-use FE model of the Riv-Bonding process was developed in this chapter.

6.2. Experiment Tests

6.2.1. Sample preparation

Before establishing the simulation model of the Riv-Bonding process, experimental tests were performed to collect necessary data for the model calibration and verification. Boron steel rivets with the hardness 280±30HV10 and aluminium alloy AA5754 sheets were used throughout the experiment. The structural adhesive SikaPower 498 was selected, and its basic properties are listed in **Table 6.1**. This is a one-component epoxy resin-based adhesive and can achieve a high mechanical strength once cured. This adhesive can be applied on oiled or coated surfaces, and suitable for connections with other joining methods (e.g., resistance spot welding, SPR and clinching) [181].

To calibrate the simulation model, interrupted laboratory tests of the SPR process and the Riv-Bonding process were carried out. **Table 6.2** lists the joint configurations of the interrupted test. The joining process was stopped at five positions by controlling the rivet head height (*H*). The size of the specimen dimensions is 40mm×40mm, and the thicknesses of the top and bottom sheets are 1.2mm and 2.0mm respectively. The rivet selected for this stack is 6.0mm long with a shank diameter of Ø5.3mm. To verify the prediction accuracy of the simulation model, as shown in **Table 6.3**, another four types of SPR joints and four types of Riv-Bonding joints with varying top sheet thicknesses and dies were also made experimentally. As for any mechanical fastening process, the intrinsic variability of the SPR and the Riv-Bonding processes inevitably brings many variations into the process and affect the final laboratory test results. To minimise such effects, the same equipment and the same dies as well as the same batch of materials were used throughout the experiment. In addition, at least two repeats for each position were made in the interrupted laboratory tests and three repeats for each joint in **Table 6.3** were performed when evaluating the performance of the simulation model. The nominal dimensions of the semi-tubular rivet and the die used in the laboratory tests are illustrated **Figure 6.2**. All the joints were made using the servo SPR system provided by Tucker GmbH, as shown in **Figure 3.32**. The riveting speed is set to 300mm/s, and the clamping force is approximately 6.0kN controlled by a compressed spring.

Due to the high viscosity (approximately 3000Pa·s) of the adhesive SikaPower 498 at the ambient temperature (shown in **Figure 6.3**), the adhesive was preheated to about 55℃ to reduce its viscosity before manually applied on the bottom sheet. To keep consistent with the real application in the automotive industry, as shown in **Figure 6.4**, the adhesive was applied along the centre line of the bottom sheet with a cartridge gun. The amount of the adhesive was controlled by the diameter of the gun nozzle (3.0mm in this research). After the adhesive was applied on the bottom sheet, the top sheet was rapidly placed on the top of the adhesive followed by the riveting process. All the Riv-Bonding joints were placed in a preheated oven at 175℃ for 20 minutes to cure the adhesive layer.

Table 6.1: Properties of the adhesive SikaPower 498 [181]

Name	Dynamic viscosity (Pa·s)		Application temperature (℃)	Curing time (min)	Elongation (After curing)
	(20℃)	(55℃)			
SikaPower 498	Approximately 3000	Approximately 1300	50~60	20 (175℃)	5.0%

Table 6.2: Experiment design of the interrupted laboratory tests for the SPR and the Riv-Bonding processes

Joint no.	Thickness (mm)		Adhesive SikaPower 498	Rivet head height/H (mm)	Rivet (Boron steel)	Die
	Top sheet/T_t (AA5754)	Bottom sheet/T_b (AA5754)				
6-1	1.2	2.0	--	4.0	C5.3*6.0 (280±30HV10)	Pip die-A
6-2				3.0		
6-3				2.0		
6-4				1.0		
6-5				0.0		
6-6	1.2	2.0	Yes (Ø3.0mm nozzle)	4.0		
6-7				3.0		
6-8				2.0		
6-9				1.0		
6-10				0.0		

Table 6.3: Experiment design of the SPR and Riv-Bonding joints for FE model verification

Joint no.	Thickness (mm)		Adhesive SikaPower 498	Rivet (Boron steel)	Die
	Top sheet/T_t (AA5754)	Bottom sheet/T_b (AA5754)			
6-11	1.8	2.0	--	C5.3*6.0 (280±30HV10)	Pip die-A
6-12	2.5				
6-13	1.8				Flat die-A
6-14	2.5				
6-15	1.8	2.0	Yes (Ø3.0mm nozzle)	C5.3*6.0 (280±30HV10)	Pip die-A
6-16	2.5				
6-17	1.8				Flat die-A
6-18	2.5				

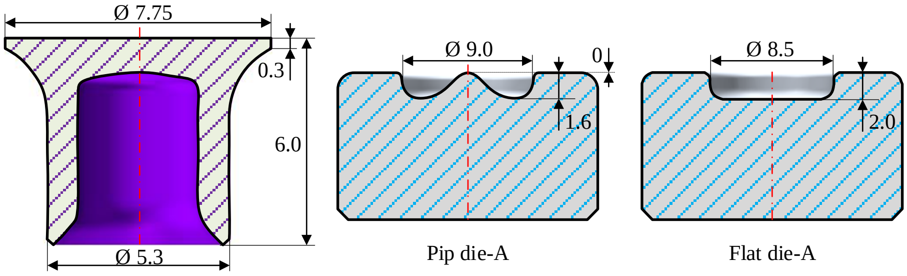

Pip die-A

Flat die-A

Figure 6.2: Schematic of the semi-tubular rivet and dies (in mm)

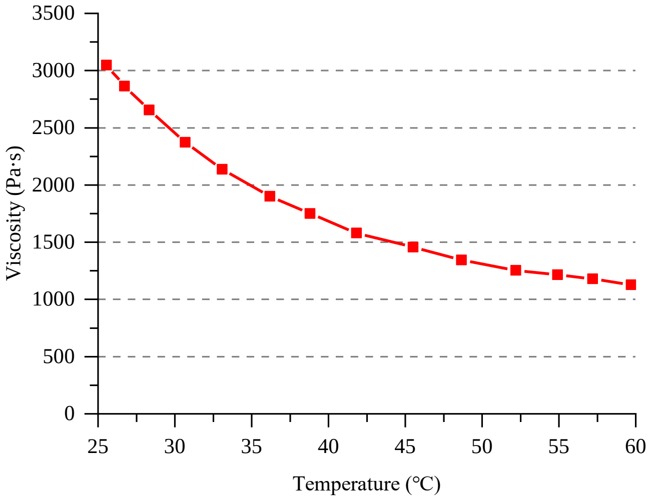

Figure 6.3: Dynamic viscosity-temperature curve of the adhesive SikaPower 498 [181]

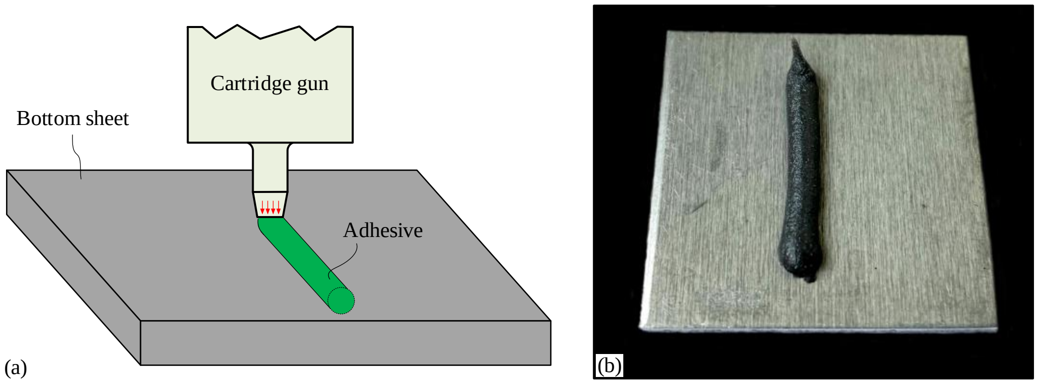

Figure 6.4: Schematic of applying the uncured adhesive on the bottom sheet

6.2.2. Geometrical characterization of the Riv-Bonding joints

To observe the adhesive distribution within the Riv-Bonding joints and to evaluate the joint quality, all the joints were sectioned using an abrasive-wheel cutting machine. To ensure the cross-sectional profile on the joint centre plane was captured, as shown in **Figure 6.5**, the joints were sectioned at a position slight offset the joint centre line to reserve enough distance for the subsequent surface polishing. Then, the cross-sectional profile of each joint was inspected and recorded using an optical microscope. To evaluate the prediction performance of the FE model on the joint quality, six dimensions were measured on the cross-sectional profiles of the Riv-bonding joints as shown in **Figure 6.6**. The interlock (I), the rivet head height (H), the remaining bottom sheet thickness at the joint centre (t_c) and under the rivet tip (t_{tip}) are the key joint quality indicators. The diameters of inner interlock boundary (D_{in}) and outer interlock boundary (D_{out}) are used to evaluate the rivet shank deformation and the formation of interlock.

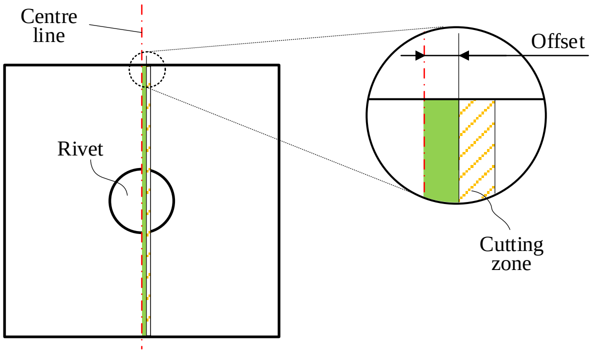

Figure 6.5: Schematic of the cutting position on the specimen

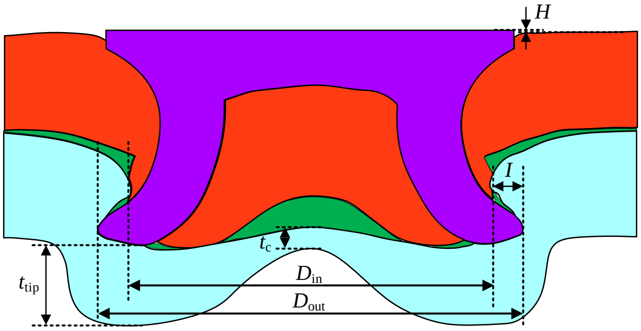

Figure 6.6: Geometrical dimensions measured on the cross-sectional profile of the Riv-Bonding joint

6.3. FE Model Development

6.3.1. Model description

Similar to the FE model of SPR process, a 2D axisymmetric FE model of the Riv-bonding process was also developed using the software Simufact.Forming 15 to meet the fast response requirement in the industrial applications. **Figure 6.7** shows the seven components involved in the simulation model: (1) punch; (2) blank-holder; (3) rivet; (4) top sheet; (5) adhesive layer, (6) bottom sheet and (7) die. Simulation parameters for the solid parts are the same as that used in the SPR simulation model, and therefore not described in detail here. The adhesive layer was modelled as a superplastic body. Quadrangle element with four gauss points (type 10) was chosen, and the ‘advancing front quad mesher’ was used to mesh the adhesive layer. The mesh size was set to 0.05mm to allocate enough elements along the adhesive thickness direction. During the riveting process, the adhesive flows rapidly within the gap between the top and bottom sheets. This will lead to severe element distortion of the adhesive layer and convergence difficulty during the simulation. Thus, the automatic element re-meshing was implemented for the adhesive layer. During the joining process, the adhesive layer will be penetrated by the rivet. To model this phenomenon, the geometrical criterion was also implemented for the adhesive layer. A too large threshold thickness value may cause unrealistic adhesive separation and large adhesive volume loss due to the element deletion.

Thus, in this model, the threshold thickness for the adhesive layer was set to 0.03mm. For the interaction between the adhesive and other solid parts, the two sheets and the adhesive layer were glued together using the contact type 'Glued'. The contact interface between the adhesive and the rivet was modelled as a friction free condition by setting the friction coefficient to zero.

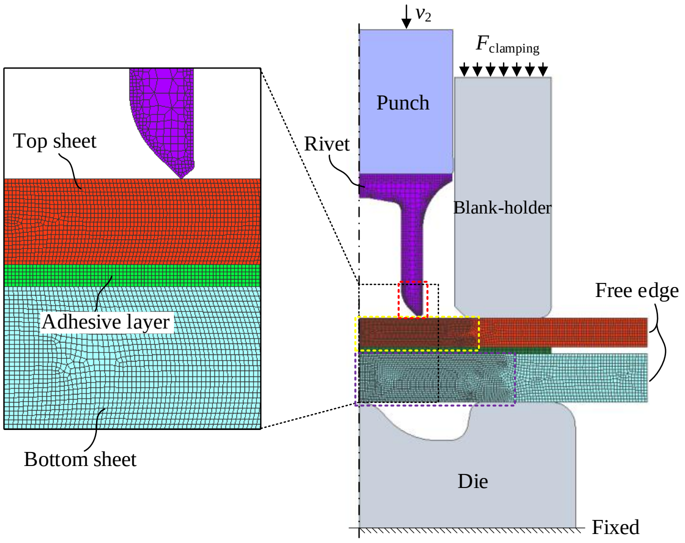

Figure 6.7: 2D axisymmetric simulation model of the Riv-Bonding process

During the Riv-Bonding process, the blank-holder moved downward with an initial speed, and struck on the top sheet. Then, a clamping force was applied on the blank-holder by a compressed spring. This clamping procedure had significant effects not only on the adhesive distribution, but also on the deformation of the top sheet. **Figure 6.8** shows the cross-sectional profiles of the SPR joint 6-1 and the Riv-bonding joint 6-6 (H = 4.0mm). It can be found that the top sheet outside the rivet bent downward during the SPR process (Zone 1), but kept almost flat during the Riv-Bonding process (Zone 2). This difference indicated that the top sheet in the Riv-Bonding process first bent upward due to the hydraulic force introduced by the accumulated adhesive beneath its central area, but then became almost flat as the riveting process proceeded as shown in **Figure 6.8**(b). Therefore, according to the adhesive distribution, the clamping process during the Riv-Bonding process could be divided into two stages as presented in **Figure 6.9**. At the stage 1, the gap between the two sheets is quite large and the adhesive could easily flow towards the outside of the interface. The sheets undergo very limited elastic deformation due to the low-level pressure from the adhesive layer. An almost uniform adhesive distribution can be observed during this stage. However, with further downward movement of the blank-holder, the gap between the two sheets becomes narrower and the outward flow of the adhesive becomes more and more restricted. At the stage 2, the adhesive starts being trapped around the joint centre and less adhesive remains under the circular edge of the blank-holder. Plastic deformations occur on the two sheets due to the hydraulic pressure from the trapped adhesive. During this stage, the adhesive unevenly distributes between the two sheets.

To properly simulate the blank-holder strike and to simplify the simulation model, in this study, the clamping process was simulated from the beginning of the stage 2. The initial adhesive layer thickness was determined using the inverse method and set to 0.3mm. The simulation procedures of the Riv-Bonding process are shown in **Figure 6.10**. When simulating the clamping process, the blank-holder first moves 0.3mm at a velocity v_1=100mm/s to model the blank-holder strike on the sheets. Then, the blank-holder velocity is set to zero and a 5.3kN clamping force (F_{clamping}) is applied to model the blank-holder clamping effect. Subsequently, the riveting process is simulated.

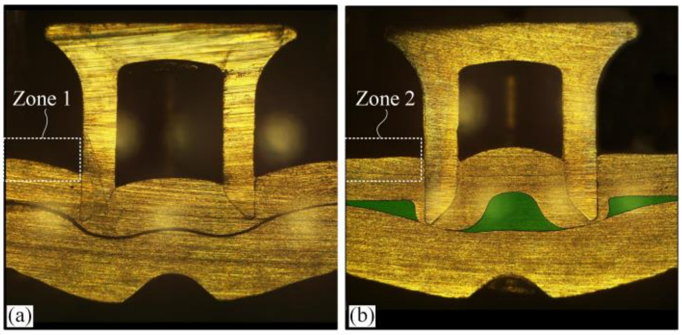

Figure 6.8: Deformed top sheets at the rivet head height H=4.0mm: (a) the SPR joint 6-1 and (b) the Riv-Bonding joint 6-6

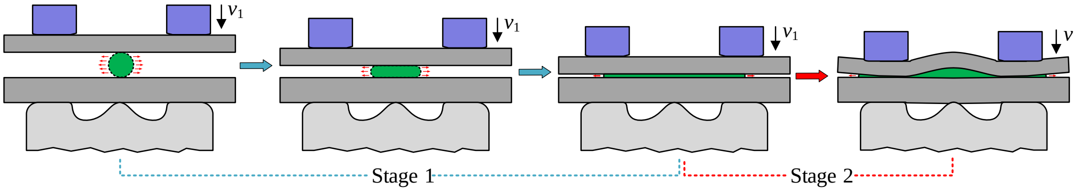

Figure 6.9: Two stages of the adhesive flow during the clamping process

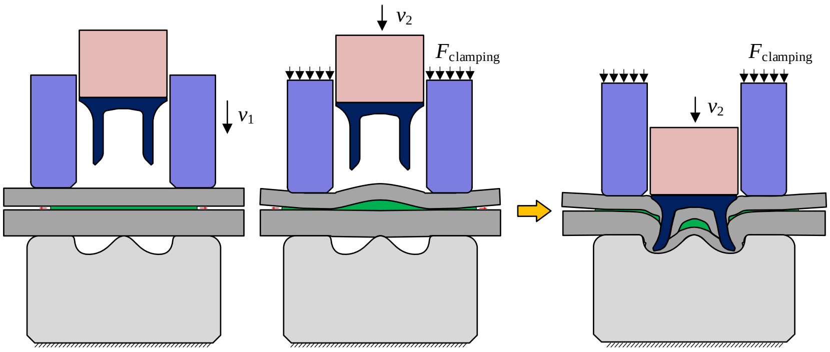

(a) (b)

Figure 6.10: Simulation procedures of the Riv-Bonding process: (a) clamping process and (b) riveting process

6.3.2. Material properties

The properties of the rivet and sheets were the same as that used in the FE model of SPR process. The uncured adhesive is a kind of high viscosity liquid and its behaviour is quite different from the solid materials. Therefore, the biggest challenge is to find out a suitable material constitutive model to represent the adhesive flow of the uncured adhesive during the riveting process. The uncured adhesive (SikaPower 498) demonstrates a viscoelastic behaviour depending heavily on the dynamic viscosity. This adhesive is a non-Newtonian fluid, and its viscosity shows a decreasing trend with the increment of the strain rate (i.e., pseudoplastic fluid). The adhesive flow between the two sheets is quite simple, and regarded as a laminar flow in this research. The Ostward and de Waele power law, which was proved capable for the modelling of power law fluids by Jabbari et al. [178], was adopted to describe the relationships between the shear stress (τ) and the shear strain rate ($\dot{\gamma}$) of the adhesive layer, as shown in Eq.(7.1). The coefficients k and n could be easily identified using rheological experiments. The dynamic viscosity (η) of adhesive depends heavily on the shear strain rate, and can be expressed as a function of the shear stress (τ) and shear strain rate ($\dot{\gamma}$) in Eq.(7.2). Substituting Eq.(7.1) into Eq.(7.2) yields the dynamic viscosity (η) as a function of the shear strain rate ($\dot{\gamma}$) in Eq.(7.3).

$$\tau = k\dot{\gamma}^{n} \tag{7.1}$$

$$\eta = \frac{\tau}{\dot{\gamma}} \tag{7.2}$$

$$\eta = k\dot{\gamma}^{n-1} \tag{7.3}$$

In this research, the experimental viscosity data of the adhesive SikaPower 498 was extracted from the paper of Weber et al. [182]. **Figure 6.11** shows the shear stress-viscosity curves at different temperatures. Using the Eq.(7.2), the adhesive viscosity under varying shear strain rates was derived and presented in **Figure 6.12**. In this model, only the shear strain rate-viscosity curve at 50°C was implemented. By employing the least squares technique, the unknown coefficients in Eq.(7.3) were identified. Values of the k and n are 1582.04 and 0.23 respectively. However, this fitted shear rate-viscosity curve has very small viscosity values (less than 2.0Pa·s) at very high strain rates (greater than 5000 s^{-1}), which is not coincident with the reality and also causes simulation stability problems in software Simufact.Forming 15. Thus, the index n was adjusted to a larger value 0.48 by using the inverse method. The viscosity of SikaPower 498 at 50°C under different shear strain rates was defined in Eq.(7.4).

$$\eta = 1582.04 \cdot \dot{\gamma}^{-0.52} \tag{7.4}$$

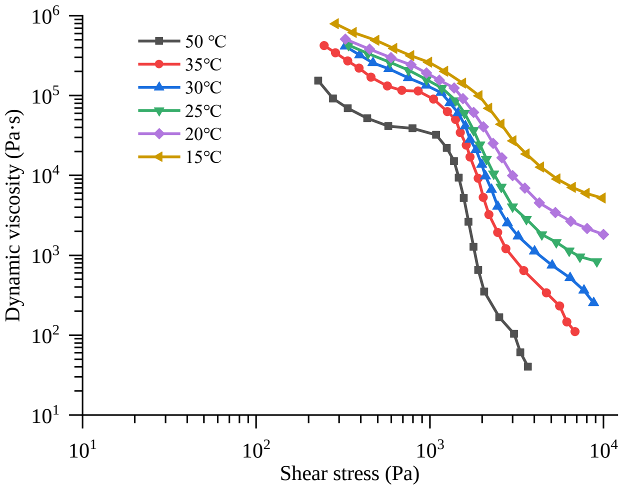

Figure 6.11: Shear stress-viscosity curves of the adhesive SikaPower 498 at different temperatures [182]

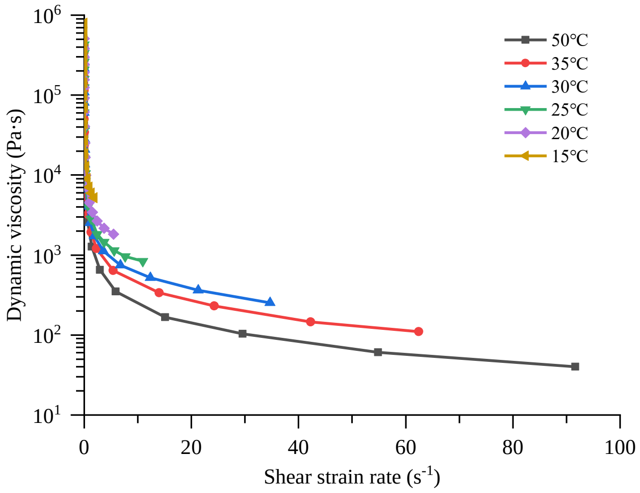

Figure 6.12: Shear strain rate-viscosity curves of the adhesive SikaPower 498 at different temperatures

The adhesive was modelled as a superplastic material using the rate-power law constitutive model shown in Eq.(7.5) (Hot forging material form 1 in Simufact.Forming 15). By setting the coefficient N to zero, the effect of equivalent strain ($\bar{\varepsilon}$) on the equivalent stress (σ_f) was inactive and the Eq.(7.5) is simplified to Eq.(7.6). The shear stress (τ) and the shear strain rate ($\dot{\gamma}$) could be expressed as a function of equivalent stress (σ_f) and equivalent strain rate ($\dot{\bar{\varepsilon}}$) individually in Eq.(7.7) and Eq. (7.8) according to the study of Gerstmann and Awiszus [180].

$$\sigma_f = C\dot{\bar{\varepsilon}}^M \bar{\varepsilon}^N \tag{7.5}$$

$$\sigma_f = C\dot{\bar{\varepsilon}}^M \tag{7.6}$$

$$\tau = \frac{\sigma_f}{\sqrt{3}} \tag{7.7}$$

$$\dot{\gamma} = \sqrt{3} \cdot \dot{\bar{\varepsilon}} \tag{7.8}$$

Substituting the Eq.(7.7) and Eq.(7.8) into Eq.(7.1) yields Eq.(7.9). Comparing the Eq.(7.6) and Eq.(7.9), the coefficients *C* and *M* could be expressed as a function of *k* and *n* shown in Eq.(7.10). Substituting the identified *k* and *n* into Eq.(7.10), the equivalent stress-strain rate curve of the adhesive SikaPower 498 could be deduced into Eq.(7.11) and illustrated in **Figure 6.13**.

$$\sigma_f = \sqrt{3}^{n+1} \cdot k \cdot \dot{\bar{\varepsilon}}^{n} \tag{7.9}$$

$$\begin{cases} C = \sqrt{3}^{n+1} \cdot k \\ N = n \end{cases} \tag{7.10}$$

$$\sigma_f = 3143.53 \cdot \dot{\bar{\varepsilon}}^{0.48} \tag{7.11}$$

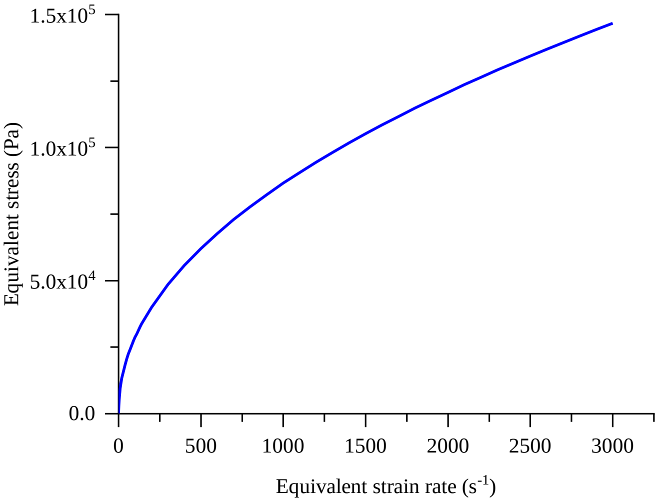

Figure 6.13: Equivalent stress-strain rate curve of the adhesive SikaPower 498 (50°C)

6.3.3. Validation of the FE model

To evaluate the performance of the developed simulation model, the SPR and Riv-Bonding joints in **Table 6.2** and **Table 6.3** were numerically made and compared with the experimental test results, including the joint cross-sectional profiles at different joining stages, the values of joint quality indicators and the load-displacement curves. All the simulations were executed on a PC with a 4-core Intel Core i7 3.4GHz CPU and RAM 16.0G.

Figure 6.14 presented the experimentally tested and numerically simulated joint cross-sectional profiles at five positions during the Riv-Bonding process. To highlight the effect of the blank-holder strike on the simulation result of the Riv-Bonding process, the simulated joint cross-sectional profiles considering (model 1) and without considering (model 2) the blank-holder strike are compared with that from the laboratory tests. It is obvious that the simulation result considering the blank-holder strike (**Figure 6.14**(b)) showed a much better agreement with the laboratory result (**Figure 6.14**(a)) than that without considering the blank-holder strike (**Figure 6.14**(c)). When the rivet penetrated the top sheet, the deformation of the top sheet material around the rivet tip (Zone 1) and the adhesive distribution under the top sheet (Zone 4) were accurately predicted by the simulation model 1 (Zones 2 and 5). The flat top sheet (Zone 7) and the final adhesive distribution (Zone 10) were also captured by the simulation model 1 (Zones 8 and 11). In contrast, although the model 2 captured the adhesive distribution around the joint centre, the deformation of the top sheet and the adhesive distribution outside the joining region were not properly simulated. As shown in **Figure 6.15**, the top sheet deflection caused by the adhesive layer was also accurately captured when considering the blank-holder strike in the simulation model (model 1). Therefore, in this research, the blank-holder strike was considered when developing the simulation model of the Riv-Bonding process.

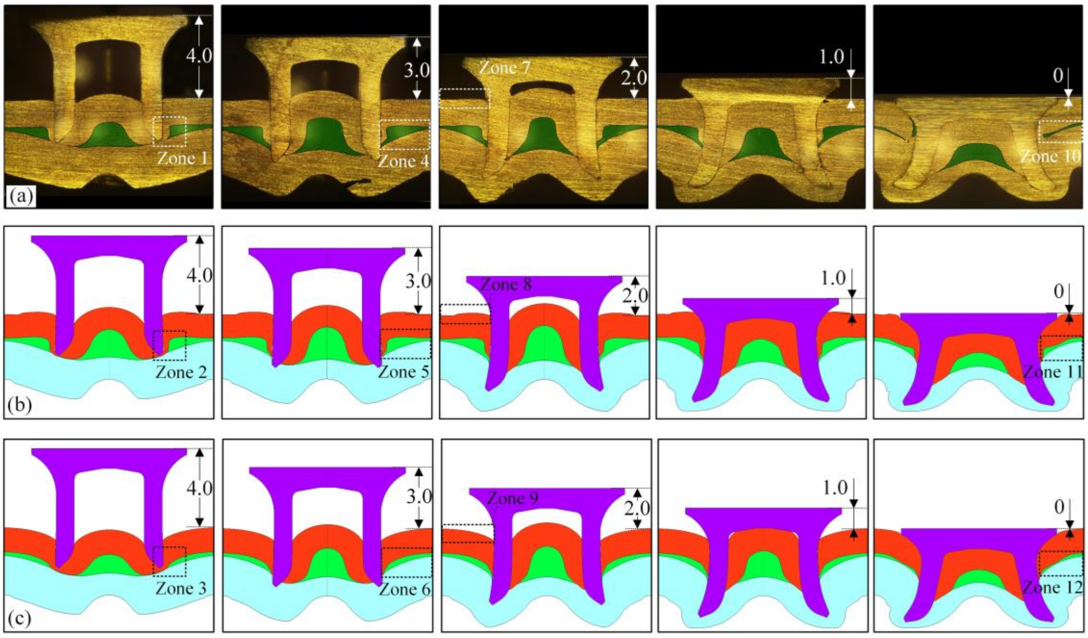

Figure 6.14: Comparison between the joint cross-sectional profiles during the Riv-Bonding process from (a) the interrupted laboratory tests and simulations, (b) considering or (c) without considering the blank-holder strike

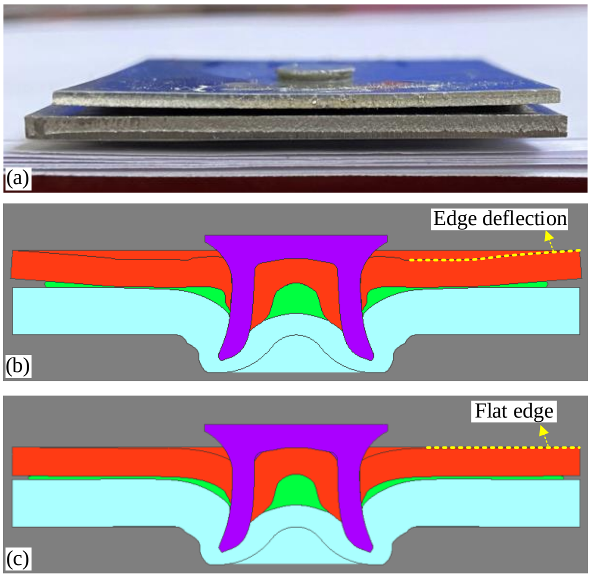

Figure 6.15: Shapes of the Riv-Bonding joint 6-9 (H=1.0mm): (a) tested, (b) simulated with or (c) without considering the blank-holder strike

To assess the accuracy of quality prediction of the developed FE model for the Riv-Bonding joint, the dimensions of the quality indicators measured from the laboratory tested and the simulated cross-sectional profiles of the Riv-Bonding joint 6-10 are compared as shown in **Figure 6.16**. For easier comparison, the predicted value of each indicator was normalized to the percentage of the correspondingly tested value. It can be seen that there is a reasonable agreement between the simulated and the tested values. The simulated interlock is 80% of the tested value, and the simulated diameters of the two interlock boundaries (D_{in} and D_{out}) are approximately 98% and 95% of the tested values. The simulated rivet head height is about 94% of the tested value. The bottom sheet thickness around the joint centre (t_c) was around 15% overestimated, and the remaining bottom sheet thickness under the rivet tip (t_{tip}) was around 30% underestimated by the developed simulation model. The tested and simulated cross-sectional profiles of the Riv-Bonding joint 6-10 are shown in **Figure 6.17**. Apart from the bottom sheet thickness under the rivet tip, the simulated adhesive distribution and the sheet deformation agreed well with the laboratory tested results. **Figure 6.18** compares the true load-displacement curves extracted from the simulated and tested Riv-Bonding joint 6-10. The C-frame deflection effect on the tested curve was removed. It can be found that, except for the slight difference in Zone 3, the predicted load-displacement curve (black line) matched well with the tested curve (red line). The slight decline (Zone 1) and the rapid increase (Zone 2) of the riveting force were accurately captured by the simulation model. The above results and analyses indicate that the developed simulation model considering the blank-holder strike is capable of predicting the Riv-Bonding process.

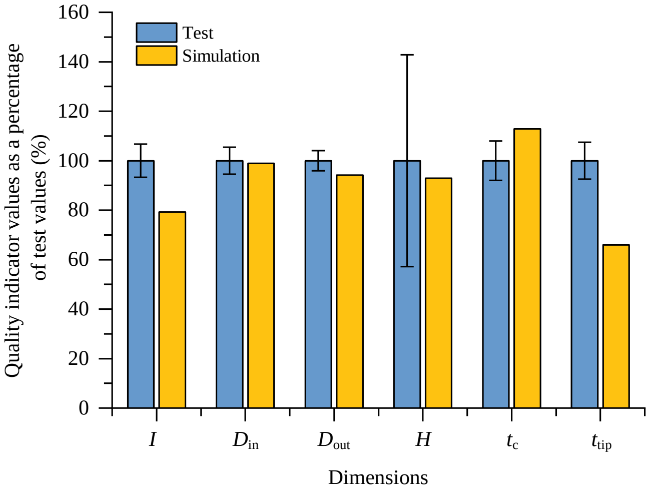

Figure 6.16: Comparison of the Riv-Bonding joint 6-10 quality indicators between the laboratory tests and the simulation

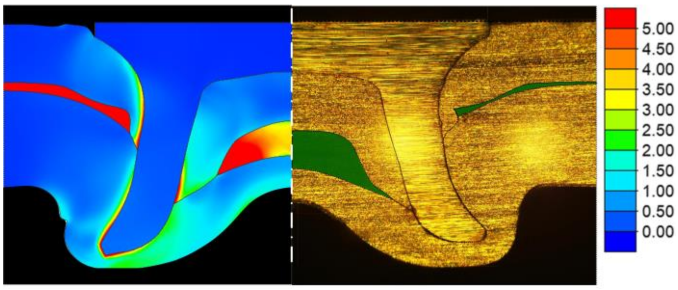

Figure 6.17: Simulated and tested cross-sectional profiles of the Riv-Bonding joint 6-10 (Effective plastic strain)

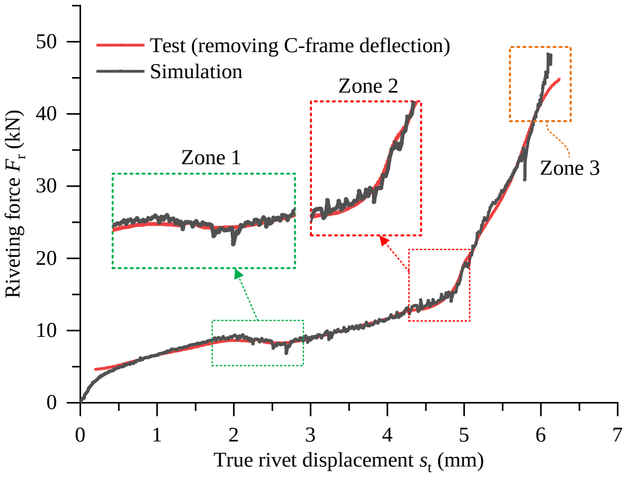

Figure 6.18: Simulated and tested true load-displacement curves of the Riv-Bonding joint 6-10

To further verify the performance of the developed simulation model for different joint configurations, the simulated and experimentally tested cross-sectional profiles of the eight types of joints in **Table 6.3** are compared in **Figure 6.19**. It can be seen that the simulated rivet and sheets deformations matched well with that from the experimental tests. Meanwhile, the predicted adhesive distributions in the Riv-Bonding joints also showed reasonable agreements with that in the tested Riv-Bonding joints. **Figure 6.20** compared the simulated and tested joint quality indicators, including the interlock (*I*), the remaining bottom sheet thickness at the joint centre (t_c) and under the rivet tip (t_{tip}), the diameter of outer interlock boundary (D_{out}). With varying top sheet thicknesses and die types, the changing trends of these indicators were accurately predicted by the simulation model. The predicted magnitudes of these indicators also showed reasonable agreements with that from the experimental tests. **Figure 6.21** shows the simulated and tested true load-displacement curves. It can be noticed that no matter with or without the adhesive layer, the changing trend and the magnitude of the riveting force were accurately predicted by the developed simulation model. Therefore, the developed simulation model is also capable of predicting the quality of SPR joints and Riv-Bonding joints with varying joint configurations.

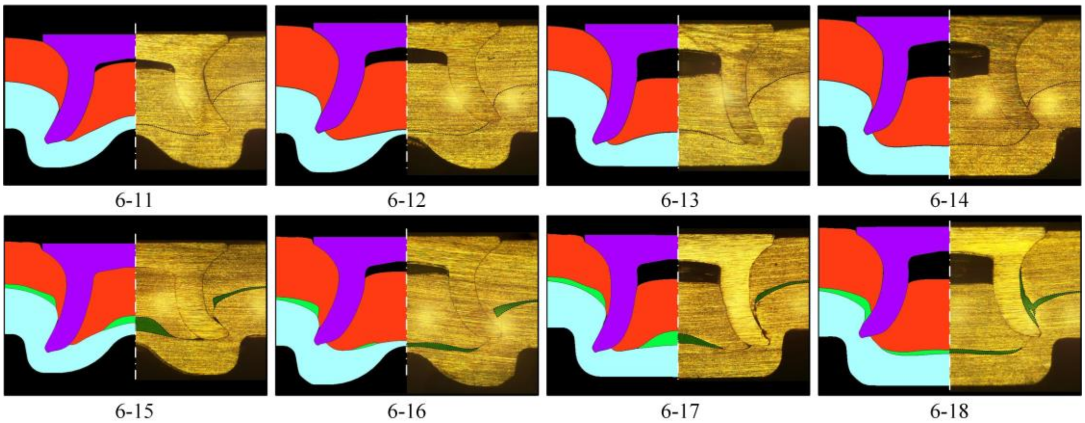

Figure 6.19: Simulated and tested joint cross-sectional profiles for model validation

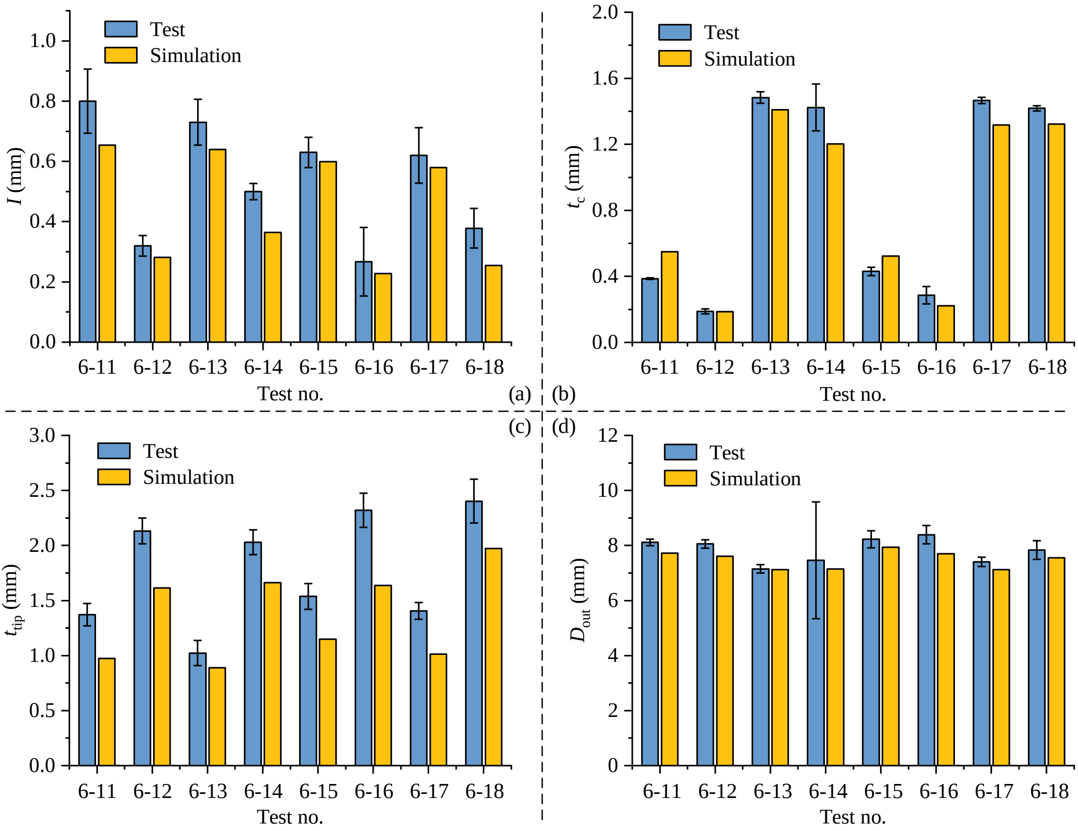

Figure 6.20: Comparison of the critical quality indicators between the experimentally tested and simulated joints

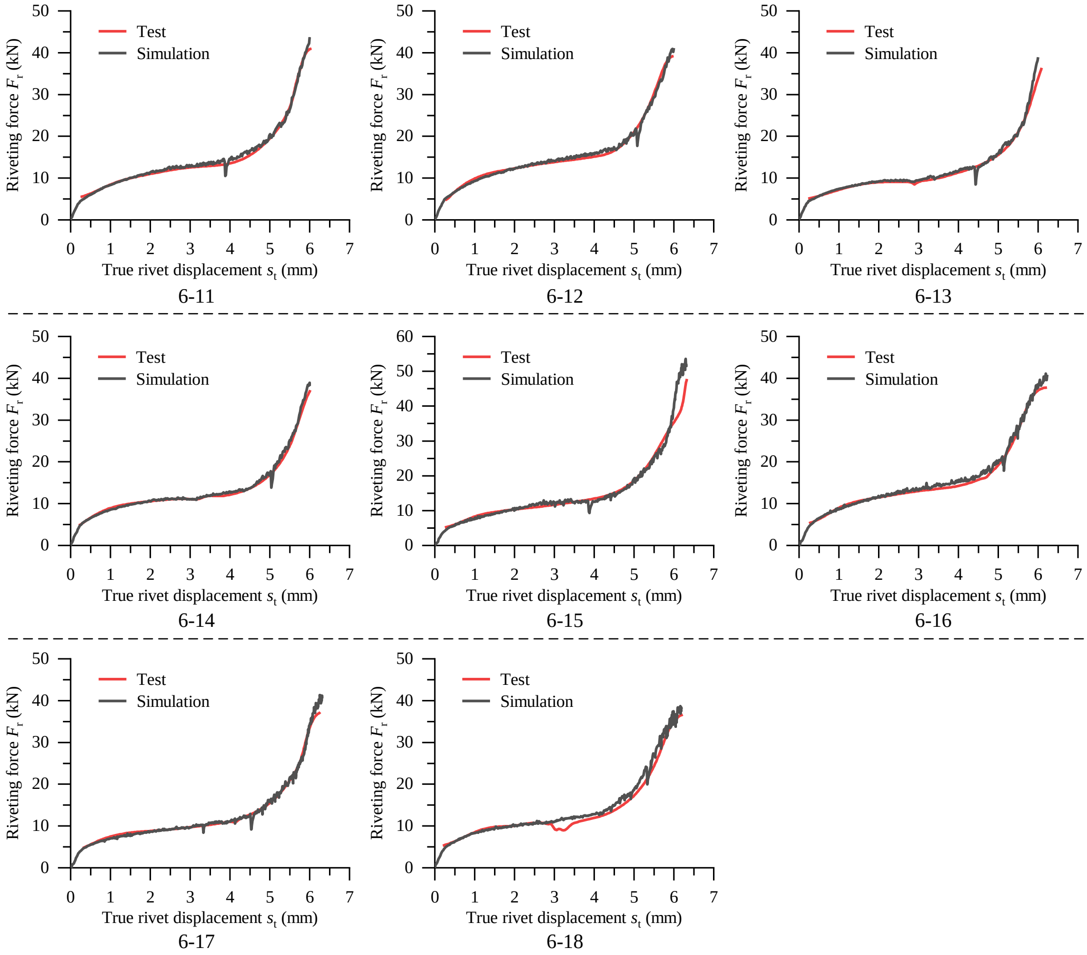

6-11 6-12 6-13

6-14 6-15 6-16

6-17 6-18

Figure 6.21: Simulated and experimentally tested true load-displacement curves for FE model validation

6.4. Conclusions

In this chapter, a 2D simulation model of the Riv-Bonding process, suitable for industry applications, was developed using the software Simufact.Forming 15. Interrupted laboratory tests of the Riv-Bonding process, and experimental tests of the Riv-Bonding joints with varying configurations were carried out to validate the prediction accuracy of the proposed simulation model. The main conclusions are summarised below:

(1) The developed FE model is capable of capturing the events happened during the Riv-Bonding process, and predicting the quality of the Riv-Bonding joints.

(2) The blank-holder strike has significant influences on the Riv-Bonding process, and should be modelled properly in the simulation model.

(3) The Ostwald-de Waele power law was proved effective as the material constitutive of adhesives, and could be used to approximately predict the adhesive flow during the Riv-Bonding process.

(4) The adhesive layer imposed significant influences on the riveting process by affecting the load-displacement curve and the deformation behaviours of the rivet and the sheets.

(5) The FE simulation model offers a new approach to investigate the Riv-Bonding process and provides a foundation for future simulation model development, in terms of the quality prediction and mechanical strength prediction under different joint configurations.

7. Influences of the Adhesive Layer on the Riv-Bonding Process and Joint Quality

This chapter explores the impacts of the adhesive layer on the joining process, including the deformation behaviours of the rivet and sheets, variation trend of the riveting force and distribution of the adhesive. Interrupted experimental tests were carried out to visually observe and compare the joint formation during the SPR process and Riv-Bonding process. Two types of die (i.e., flat die and pip die) were utilized to investigate the effects of die type on the Riv-Bonding processes. The potential defects and benefits induced by the adhesive layer on the riveted connection with different dies were also identified and analysed. The influences of the adhesive layer on the quality of the riveted connection were also evaluated. In addition, single factor experiments were carried out to investigate the influences of top sheet thickness on the final quality of the riveted connection and the adhesive distribution.

7.1. Introduction

Riv(et)-Bonding is developed from the SPR technique by simply adding a thin adhesive layer between the connected sheets. Comparisons between the major steps during a SPR process and during a Riv-Bonding process are given in **Figure 7.1**. The only difference between the two processes is whether a thin adhesive layer is involved or not. It has been widely reported that this additional bonded connection effectively improves the joint mechanical strengths and advances the NVH performance of the connected structures. To date, the Riv-Bonding technique has been widely applied to assemble the car Body-in-White (BIW) structures in the automotive industry.

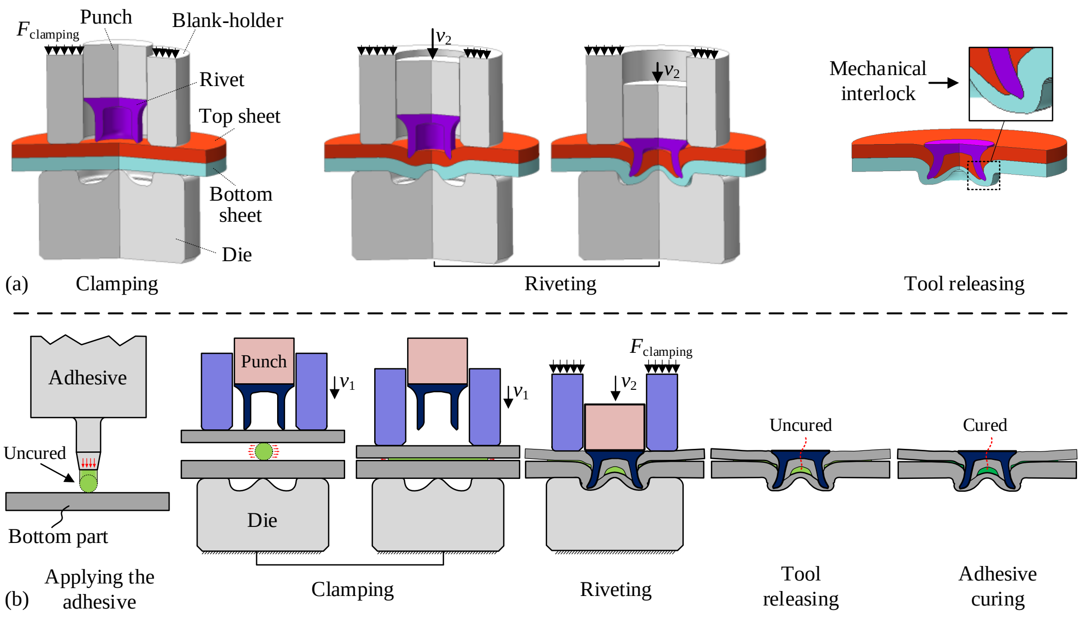
F_{clamping}
Punch
Blank-holder
Rivet
Top sheet
Bottom sheet
Die
(a)
Clamping
v_2
v_2
Riveting
Mechanical interlock
Tool releasing
Adhesive
Uncured
Bottom part
Punch
v_1
v_1
Die
F_{clamping}
v_2
Uncured
Cured
(b)
Applying the adhesive
Clamping
Riveting
Tool releasing
Adhesive curing

Figure 7.1: Schematic of the (a) self-piercing riveting process and (b) Riv-Bonding process

There are already some studies relevant to this joining technique in the public domain, and most of them investigated the performance improvement of Riv-Bonding joints compared with the original SPR joints. Baurova et al. [138] concluded that the Riv-Bonding joints had an apparently higher shear strength compared to the SPR joints. He et al. [142] found that the maximum shearing load of the Riv-Bonding joint is 14% higher, whereas the energy absorption is much lower than that of the solo SPR joint. Liu and Zhuang [143] reported that the ply angle of the CFRP and the sheet thickness had significant impacts on the shear strength and failure modes of the Riv-Bonding joints. Sun et al. [6] found that the application of the adhesive Dow Betamate 4601 significantly enhanced the fatigue strength of the SPR joints under the lap-shear loading condition, but a smaller improvement was observed under the cross-tension loading condition. Miyashita et al. [144] reported that the adhesive layer could not eliminate the cracks on the bottom sheet, but effectively improve the joint shear strength and fatigue strength. It was also found that the adhesive properties had significant influence on the shear strength of the Riv-Bonding joints. Presse et al. [152] developed a simulation model of Riv-Bonding joints with aluminium EN AW-6016 and high strength steel CR330Y590T-DP sheets, and successfully predicted the joint fatigue life by superposing the contributions of the riveted connection and the bonded connection. Wu et al. [153] experimentally found that the failure location within the SPR joint was altered after adding the adhesive layer. A mechanism-based fatigue life evaluation method was also proposed for the Riv-Bonding joints.

Actually, the performance of the Riv-Bonding joint depends on both the bonded connection and the riveted connection. The existing studies emphasize the benefits of the adhesive layer on the overall joint performance, but rarely mention the effects of the adhesive layer on the riveted connection. Few reports relevant to the impact of adhesive layer on the joining process and the joint quality can be found in the public domain. For a specific joint configuration, the viscosity and the application amount of the adhesive may significantly influence the rivet and sheet deformations, and thus alter the quality of the riveted connection. With the same type of adhesive and application amount, changes of the joint configurations (e.g., the sheet thickness, sheet material and the die type) may also alter the effects of the adhesive layer on the riveted connection. Fricke and Vallée [131] found that a larger amount of adhesive was trapped around the joining region in Riv-Bonding joints with the steel HC340LA sheets. Hahn and Wibbeke [140] mentioned that the adhesive layer would impose limited influences on the quality of the riveted connection when the total sheet thickness was greater than 2.0mm, but obvious influences when the sheet thickness was smaller than 1.6mm. Test results from the study of Franco [141] strongly supported this view: no adhesive was found around the joining region of the Riv-Bonding joints with 2.0mm/2.0mm AA5754-H32 sheets. In addition, the flow behaviour of the uncured adhesive is very sensitive to the strain rate [131], and therefore the riveting speed may also affect the quality of the Riv-Bonding joints. There is still a lot of work to do in order to have comprehensive understanding of the Riv-Bonding technique.

7.2. Experimental Procedures

7.2.1. Experiment plan

The boron steel semi-tubular rivet with the hardness 280±30HV10 was adopted throughout the experiment, and its nominal dimensions are shown in **Figure 7.2**. The material for both top and bottom sheets is aluminium alloy AA5754. The structure adhesive SikaPower 498, which is widely used in the automotive industry, was selected for the Riv-Bonding joints. To study the influences of the adhesive layer on the riveting process, as listed in **Table 7.1**, interrupted experimental tests of the SPR process and the Riv-Bonding process were carried out. The top sheet thickness (T_t) and the bottom sheet thickness (T_b) are fixed at 1.2mm and 2.0mm respectively. Two types of dies (i.e., pip die-A and flat die-A) presented in **Figure 7.3** were adopted to explore the impact of the die type on the joining process. Each riveting process was interrupted at five positions by controlling the rivet head height (H). In addition, as listed in **Table 7.2**, the influences of the T_t on the Riv-Bonding joint quality and the adhesive distribution were also investigated experimentally. Twelve joint configurations with or without the adhesive layer were made using two different dies, and three levels of the T_t were chosen.

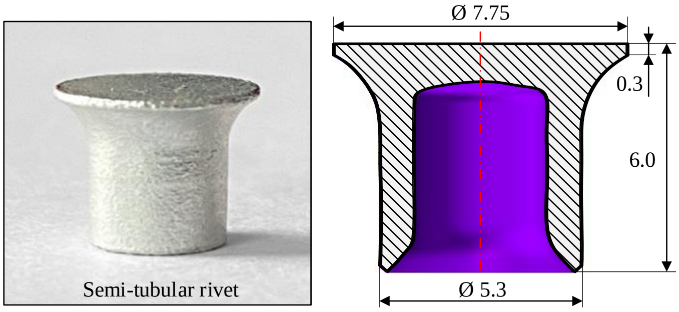
Semi-tubular rivet
Ø 7.75
0.3
6.0
Ø 5.3

Figure 7.2: Schematic of the semi-tubular rivet (in mm)

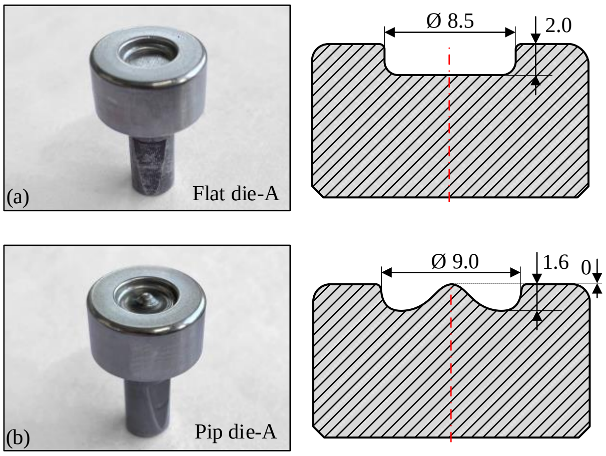
Ø 8.5
2.0
(a)
Flat die-A
Ø 9.0
1.6
0
(b)
Pip die-A

Figure 7.3: Schematic of the (a) flat die-A and (b) pip die-A (in mm)

Table 7.1: Interruption tests of SPR process and Riv-Bonding process with different types of dies

Joint no.	Thickness (mm)		Adhesive SikaPower 498	Rivet head height/H (mm)	Rivet (Boron steel)	Die type
	Top sheet/T_t (AA5754)	Bottom sheet/T_b (AA5754)				
7-P1	1.2	2.0	--	4.0	C5.3*6.0 (280±30HV10)	Pip die-A
7-P2				3.0		
7-P3				2.0		
7-P4				1.0		
7-P5				0.0		
7-P6	1.2	2.0	Yes (Ø3.0mm nozzle)	4.0		
7-P7				3.0		
7-P8				2.0		
7-P9				1.0		
7-P10				0.0		
7-F1	1.2	2.0	--	4.0	C5.3*6.0 (280±30HV10)	Flat die-A
7-F2				3.0		
7-F3				2.0		
7-F4				1.0		
7-F5				0.0		
7-F6	1.2	2.0	Yes (Ø3.0mm nozzle)	4.0		
7-F7				3.0		
7-F8				2.0		
7-F9				1.0		
7-F10				0.0		

Table 7.2: SPR and Riv-Bonding joints with different top sheet thicknesses (T_t)

Joint no.	Thickness (mm)		Adhesive SikaPower 498	Rivet (Boron steel)	Die type
	Top sheet/T_t (AA5754)	Bottom sheet/T_b (AA5754)			
7-P11	1.2	2.0	--	C5.3*6.0 (280±30HV10)	Pip die-A
7-P12	1.8				
7-P13	2.5				
7-P14	1.2		Yes (Ø3.0mm nozzle)		
7-P15	1.8				
7-P16	2.5				
7-F11	1.2	2.0	--	C5.3*6.0 (280±30HV10)	Flat die-A
7-F12	1.8				
7-F13	2.5				
7-F14	1.2		Yes (Ø3.0mm nozzle)		
7-F15	1.8				
7-F16	2.5				

7.2.2. Sample preparation

The specimen size of the SPR and Riv-Bonding joints is 40mm×40mm. All the rivets, dies and adhesive were provided by the Tucker GmbH, whilst the AA5754 sheets were provided by Jaguar Land Rover (JLR). To keep consistent with the practical application conditions in the automotive industry, the rivet and sheets were directly used without any surface treatment (e.g., degreasing). The adhesive was preheated to about 55℃ to reduce its viscosity, and then applied on the bottom sheet along the centre line with a cartridge gun, as shown in **Figure 7.4**. This is because the adhesive SikaPower 498 has a poor fluidity at the ambient temperature due to the high viscosity (approximately 3000Pa.s at 25℃ in **Figure 7.5**). The amount of the adhesive was controlled by the diameter of the gun nozzle (3.0mm). Once the adhesive was applied on the bottom sheet, the top sheet was placed on the top of the adhesive. Then, the riveting process was carried out within a very short time to eliminate the temperature effect on the adhesive flow behaviour.

All the joints were made using the servo SPR system manufactured by Tucker GmbH, as shown in **Figure 3.32**. The riveting speed was set to 300mm/s and the clamping force on the blank-holder was around 5.0kN~6.0kN controlled by a compressed spring. To ensure the effectiveness of the experiment results, three repeats for each joint configuration were performed. The Riv-Bonding joints were placed in a preheated oven at 175℃ for 20mins to cure the adhesive layer. To eliminate the influences of the heat treatment on the joint quality, the corresponding SPR joints were also heat-treated under the same conditions.

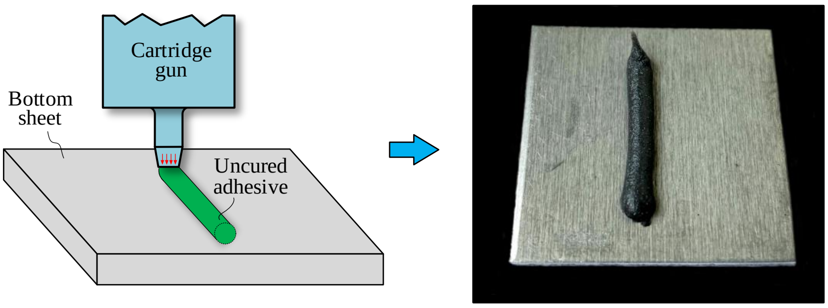

Figure 7.4: Schematic of applying the uncured adhesive on the bottom sheet

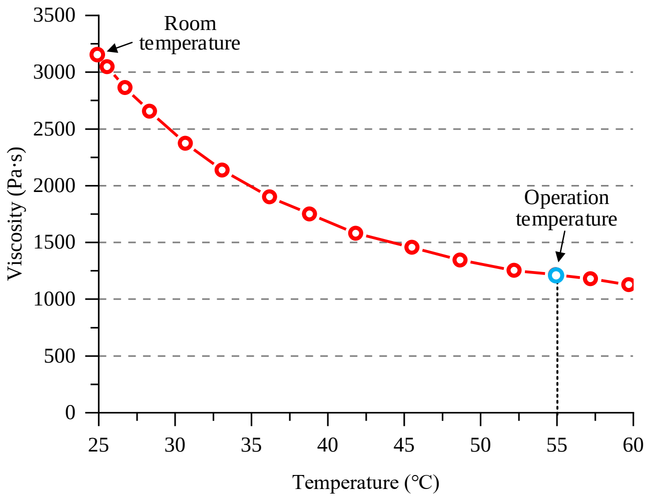

Figure 7.5: Dynamic viscosity-temperature curve of the adhesive SikaPower 498 [181]

7.2.3. Geometrical characterization of the SPR and Riv-Bonding joints

All the joints were sectioned using an abrasive-wheel cutting machine. According to the results in Chapter 3, any improper cutting position will impose apparent influences on the observed joint cross-sectional profile, and the measured magnitudes of joint quality indicators. Therefore, to ensure the cross-sectional profile on the joint central plane was captured, the joint was cut at a position slightly offsetting the joint central plane as shown in **Figure 6.5** with a specially designed fixture. This preserved enough space for the subsequent surface polishing work. The joint cross-sectional profile was inspected with an optical microscope after polishing. As shown in **Figure 7.6**, the rivet head height (H), the interlock (I), the remaining bottom sheet thickness under the rivet tip (t_{tip}) and at the joint centre (t_c) were measured to evaluate the quality of the riveted connection for the SPR and Riv-Bonding joints. The radius of the interlock inner boundary (R_{in}) and outer boundary (R_{out}) were measured to analyse the interlock formation as well as the rivet shank flare behaviour. Meanwhile, the adhesive distribution within the Riv-Bonding joints was also inspected visually.

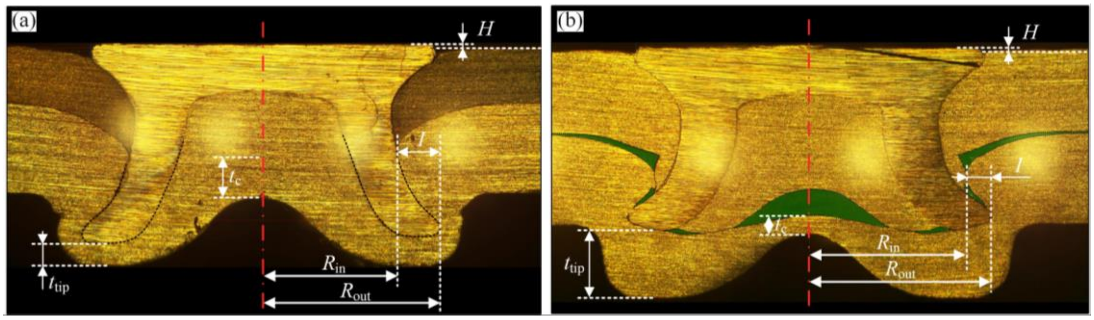
(a)
H
I
tc
ttip
Rin
Rout
(b)
H
I
tc
ttip
Rin
Rout

Figure 7.6: Dimensions measured on the cross-sectional profiles of the (a) SPR joint and (b) Riv-Bonding joint

7.3. Results and Discussion

7.3.1. Influence of the adhesive layer on the joining process

Using the interrupted experimental tests, the joint cross-sectional profiles at five positions during the SPR process and the Riv-Bonding process with two types of dies were extracted and compared in **Figure 7.7** and **Figure 7.8** respectively. From the **Figure 7.7**(b) and **Figure 7.8**(b), it can be seen that a large amount of adhesive was trapped between the top and bottom sheets regardless of the die type. The preheated adhesive (approximately 55°C) had a high flowability and thus applied a uniform hydraulic pressure on the top and bottom sheets. This changed the initial interactive forces between the two sheets in the SPR joints. As a result, the deformation behaviours of the rivet and sheets were affected.

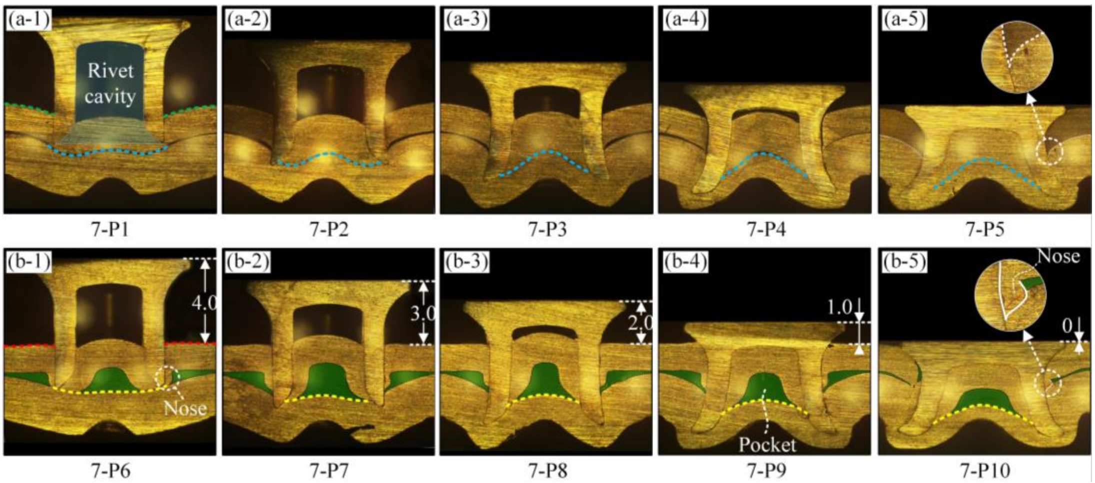
(a-1)
Rivet cavity
(a-2)
(a-3)
(a-4)
(a-5)
7-P1
7-P2
7-P3
7-P4
7-P5
(b-1)
4.0
Nose
(b-2)
3.0
(b-3)
2.0
(b-4)
1.0
Pocket
(b-5)
Nose
0
7-P6
7-P7
7-P8
7-P9
7-P10

Figure 7.7: Comparison of the joint cross-sectional profiles during the (a) SPR process and (b) Riv-Bonding process with the pip die-A

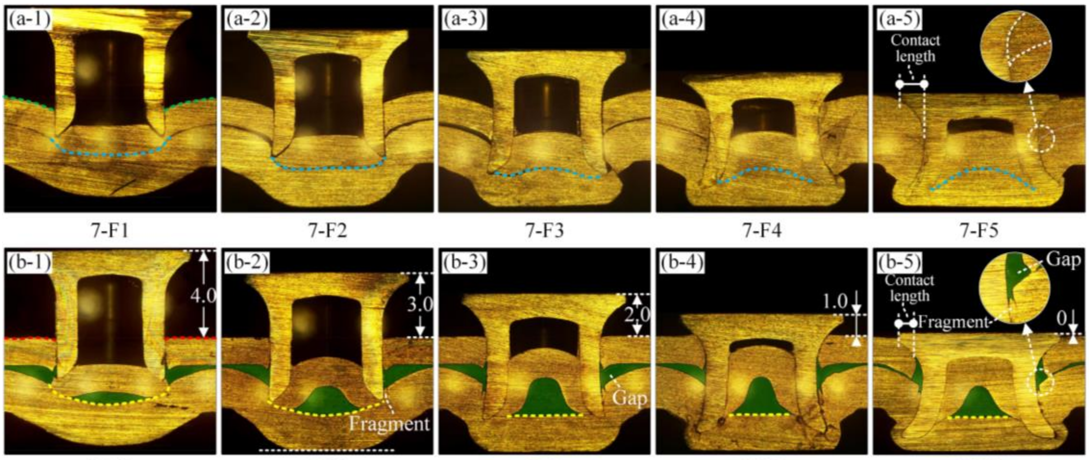

7-F1 7-F2 7-F3 7-F4 7-F5

7-F6 7-F7 7-F8 7-F9 7-F10

Figure 7.8: Comparison of the joint cross-sectional profiles during the (a) SPR process and (b) Riv-Bonding process with the flat die-A

7.3.1.1. Flow behaviour of the adhesive layer

As shown in **Figure 7.7**(b-1), after the top sheet was penetrated by the rivet, the remaining adhesive in the joining region was divided into two parts. A large part of the adhesive was trapped into the rivet cavity and the amount kept unchanged as the riveting process continued from **Figure 7.7**(b-1) to **Figure 7.7**(b-5). Another part of the adhesive was squeezed outside the rivet shank, and its total amount apparently reduced at the end of the joining process as shown in **Figure 7.7**(b-5). Only a thin adhesive layer was left between the two sheets. This is because some adhesive was pressed out of the joining region due to the high pressure from the rivet head. With the flat die, a similar adhesive distribution was observed during the joining process in **Figure 7.8**(b), and the only difference is that more adhesive was left outside the rivet shank at the end of the riveting process. This is because a gap was formed between the rivet shank and the top sheet as shown in **Figure 7.8**(b-5). The main reason for this difference is that the top sheets underwent different separation/fracture behaviours with the pip die and the flat die. Detailed explanations about the different top sheet fracture behaviours were given in the following sections.

During the Riv-Bonding process, the movement of the blank-holder may impose a significant influence on the initial amount of adhesive trapped in the joining region. Compared with the aluminium alloy AA5754 sheets, the uncured adhesive is much easier to be deformed. As shown in **Figure 7.9**(a), the uncured adhesive more likely distributes evenly between the two sheets with a low blank-holder speed. Because there is enough time for the adhesive around the joint centre to flow outward. In contrast, with a high blank-holder speed, the uncured adhesive more likely distributes unevenly at the interface of the two sheets as shown in **Figure 7.9**(b). This is because the adhesive around the joint central area does not have enough time to escape through the narrow gap under the blank-holder. The high sensitivity of the adhesive flow behaviour to the strain rate [180] might also contribute to these different initial adhesive distributions. In this research, the blank-holder first moved rapidly downward at a speed of 100mm/s and struck on the two sheets. The strong impact mainly applied on the circle region underneath the blank-holder. As a result, the adhesive around this region was squeezed partially towards the joint centre and partially outside the joining region. **Figure 7.10** shows the adhesive distribution in the Riv-Bonding joint 7-F6. It can be seen that only a very thin adhesive layer was left around the clamping region, but a large amount adhesive was trapped in the joining region. A constant clamping force (Approximately 6.0kN) was then applied on the blank-holder to clamp the sheets together. This restricted the relative movement of the two sheets, and also limited the outward flow of the adhesive trapped in the joining region. Therefore, the blank-holder speed and the magnitude of clamping force should be selected carefully when manufacturing the Riv-Bonding joints.

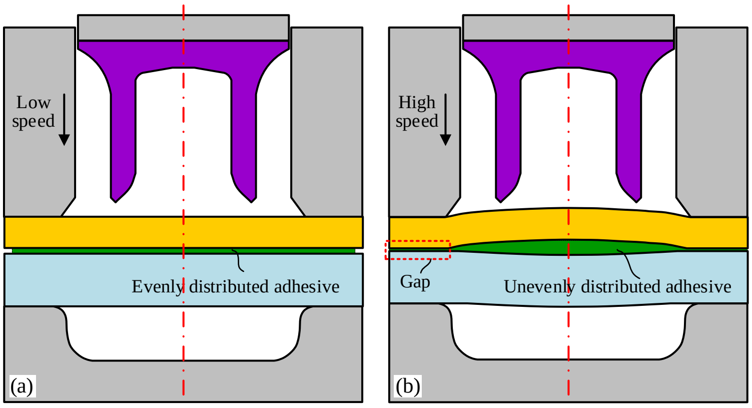

Figure 7.9: Schematics of the adhesive distribution after the clamping process with (a) a low blank-holder speed and (b) a high blank-holder speed

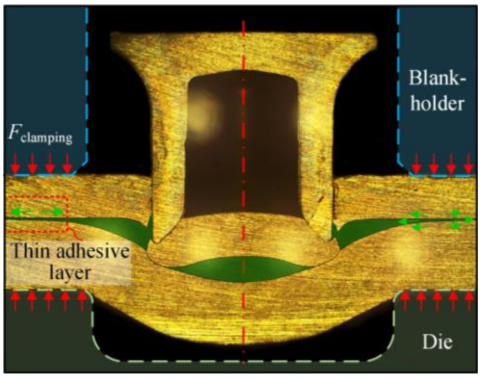

Figure 7.10: Remaining adhesive around the clamping region between the blank-holder and the die (joint 7-F6)

7.3.1.2. Deformations of the top and bottom sheets

By comparing the cross-sectional profiles of SPR joints and Riv-Bonding joints in **Figure 7.7** and **Figure 7.8**, it can be found that the deformation behaviours of the top and bottom sheets were significantly affected by the adhesive layer. As shown in **Figure 7.7**(a-1) and **Figure 7.8**(a-1), the top sheet outside the rivet was bent downward (green lines) when pierced by the rivet shank in the SPR joints. In contrast, as shown in **Figure 7.7**(b-1) and **Figure 7.8**(b-1), it still remained almost flat (red lines) after the top sheet was penetrated in the Riv-bonding joints. Such different top sheet deformations were highly linked with the resistance force that the adhesive applied on the bottom surface of the top sheet outside the rivet. Due to the increasing forces imposed on the two sheets by the rivet and die, the hydraulic pressure in the trapped adhesive reached to a very high level. This effectively prevented the large downward movement of the top sheet in the Riv-Bonding joint. In practical applications, the top and bottom sheets sometimes cannot be tightly connected with the SPR technique if the top sheet undergoes a too large downward movement. For example, **Figure 7.11** illustrates a SPR joint with a large gap formed between the rivet head and the top sheet. By adding an adhesive layer, the less downward movement of the top sheet outside the rivet may have a great possibility to avoid the formation of such gaps, and therefore effectively eliminate this kind of defect in the initial SPR joints.

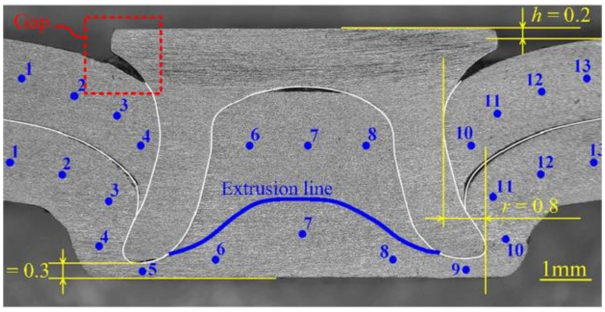

Figure 7.11: A loosely connected SPR joint with a gap formed between the rivet head and the top sheet [183]

In addition to the deformation behaviour, the fracture behaviours of top sheets with the flat die and pip die were also affected by the added adhesive layer. To facilitate the explanation, **Figure 7.12** schematically plots the top sheet penetration processes of the Riv-Bonding joints with the flat die and pip die. As shown in **Figure 7.12**(a-1) and (b-1), the trapped adhesive at the joint centre flowed outward (yellow arrows) with the increment of the rivet displacement. The top sheet outside the rivet underwent less downward movement, but the top sheet underneath the rivet was pressed downward rapidly, as shown in **Figure 7.12**(a-2) and (b-2). This induced an obvious displacement difference between the two parts of top sheet. With the pip die, the die pip applied an increasing resistance force on the bottom sheet, and thus the downward movements of the two sheets were effectively restricted as shown in **Figure 7.12**(a). Due to the different displacements of the two parts of top sheet, the top sheet material around the rivet tip was stretched and experienced a large plastic deformation as shown in **Figure 7.12**(a-3). With further increment of the rivet displacement, the top sheet was gradually penetrated by the rivet shank and a ductile fracture was observed as shown in **Figure 7.12**(a-4). A long nose was formed because of the severely localized top sheet deformation. However, due to the lack of die pip, the flat die could not provide a sufficient resistance force at the central area of the bottom sheet during the early stage of the joining process, as shown in **Figure 7.12**(b-1). So the adhesive pocket, the top sheet underneath the rivet and the bottom sheet around the joining region were pressed downward rapidly by the rivet as shown in **Figure 7.12**(b-2). With the increment of the rivet displacement, the riveting force gradually increased but the remaining top sheet thickness around the rivet tip decreased rapidly. After the top sheet thickness reduced to a threshold value, the stresses within the thinnest region surpassed the ultimate tensile strength of the top sheet material. As a result, initial formation of cracks started on the top sheet, and a premature fracture of the top sheet occurred as the cracks propagated in **Figure 7.12**(b-3). The insufficient resistance from the bottom sheet, which allowed the rapid downward movement of the top sheet underneath the rivet, significantly contributed to this early top sheet separation. This type of fracture behaviour was also reported in [19] with a very deep flat die as shown in **Figure 7.13**(a). Due to the premature failure of top sheet, fragments were formed with further increment of the rivet displacement as shown in **Figure 7.12**(b-4). This type of fragments was also reported in [184] with a low ductile top sheet as shown in **Figure 7.13**(b). Furthermore, because of the premature top sheet fracture with the flat die, a gap was formed between the top sheet and the rivet shank as shown in **Figure 7.8**(b-5). On the one hand, this may weaken the riveted connection due to the smaller contact length between the rivet head and the top sheet in **Figure 7.8**(b-5) than in **Figure 7.8**(a-5). On the other hand, the adhesive accumulated in this gap could bond the rivet and the top sheet together once cured. This might enhance the total connection strength of the Riv-Bonding joint to some degree.

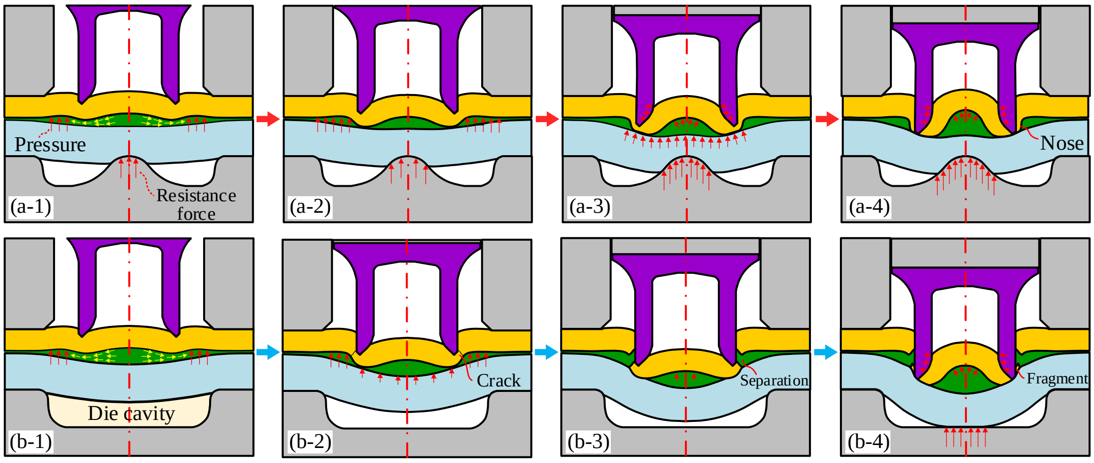

Figure 7.12: Schematic of the top sheet penetration processes in Riv-Bonding joints with (a) the pip die and (b) the flat die

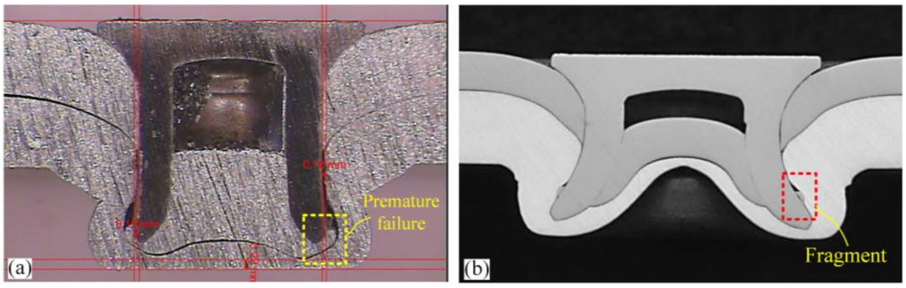

Figure 7.13: Joint cross-sectional profiles with (a) premature failure of top sheet [19] and (b) top sheet fragment [184]

The changes of the top sheet fracture behaviour after adding the adhesive layer also bring some influences on the interlock formation. With the pip die, the long nose formed on the top sheet was partially pressed into the interface between the rivet shank and the bottom sheet, as shown in **Figure 7.7**(b-5). While with the flat die, the top sheet fragments were pressed downward and trapped into the interface between the rivet shank and the bottom sheet in **Figure 7.8**(b-5). From the definition of interlock, both of the inserted nose and the trapped fragments will impose negative effects on the formation of interlock, and therefore may weaken the mechanical strengths of the riveted connection.

From the **Figure 7.7** and **Figure 7.8**, it can also be seen that, regardless of the die types, the top sheet underneath the rivet underwent a larger plastic deformation in the Riv-Bonding joints than in the corresponding SPR joints. However, slightly different deformation behaviours of this part of top sheet were observed during the Riv-Bonding process with different types of dies. With the pip die, as shown in **Figure 7.7**(b-1), the top sheet underneath the rivet was already deformed to a n-shape at the moment when the top sheet was penetrated. In contrast, with the flat die, this part of top sheet only slightly bended upward as shown in **Figure 7.8**(b-1). This is because the die pip prevented the rapid downward movement of the sheets, and the hydraulic pressure within the trapped adhesive increased with the increment of the rivet displacement. A large hydraulic force was applied at the central area of the top sheet, and led to the rapid deformation of the top sheet underneath the rivet. For Riv-Bonding joints with the flat die, rapid deformation of this part of top sheet occurred after the bottom sheet contacted the bottom of the die cavity in **Figure 7.8**(b-2). This is because the hydraulic pressure in the adhesive pocket could increase only after the bottom sheet stopped the rapid downward movement by reaching the bottom of the die cavity. Therefore, the rapid deformation of the top sheet underneath the rivet happened apparently later in the Riv-Bonding joints with the flat die than with the pip die. The following deformation behaviour of this top sheet part was quite similar in the Riv-Bonding processes with the pip die and the flat die. It is also worth mentioning that, due to the trapped adhesive pocket, the rivet cavity was filled at a faster speed in the Riv-Bonding joints than in the corresponding SPR joints. According to [185], this change may affect the riveting force and the bottom sheet thickness distribution. These influences will be discussed in the following sections.

The deformation behaviour of the bottom sheet was also affected by the involved adhesive layer. With the pip die, at the same rivet head height (H), the curvature of the top surface on the bottom sheet was always smaller in the Riv-Bonding joints than in the SPR joints as shown in **Figure 7.7**. In contrast, with the flat die, the trapped adhesive pocket led to a larger curvature of the bottom sheet before the bottom sheet contacted the bottom of the die cavity, as shown in **Figure 7.8**(a-1) and **Figure 7.8**(b-1). While the bottom sheet around the joint centre gradually became flat again in **Figure 7.8**(b-2)~(b-5) after the bottom sheet contacted the bottom of the die cavity. This is mainly attributed to the rapid deformation of the top sheet underneath the rivet and the uniform hydraulic pressure applied on the bottom sheet.

7.3.1.3. Flare behaviour of the rivet shank

Due to the changes of the top and bottom sheet deformations, the rivet shank flare behaviour in the Riv-Bonding joints also became slightly different from that in the corresponding SPR joints. **Figure 7.14** shows the variation curves of the deformed rivet shank diameter (D_r=2R_{out}) during the joining processes with or without the adhesive layer. A similar increasing pattern of the D_r was found on the four curves: it firstly increased slowly at the early stage of the joining processes and then sharply increased. Close to the end of the joining processes, the D_r increased almost linearly with the decline of the rivet head height (H), which agreed well with the results reported by Haque et al. [186]. According to the different increasing speeds, each variation curve of the D_r can be roughly divided into a slow increment phase and a rapid increment phase.

By comparing the changing curves with or without the adhesive layer, it was found that the starting point of the rapid increment phase was altered after adding the adhesive layer. As shown in Zone 1 of **Figure 7.14**(a), the rapid increment of the D_r with the pip die was delayed from the Point A in the SPR joint 7-P5 to the Point B in the Riv-Bonding joint 7-P10. Similarly, as shown in Zone 2 of **Figure 7.14**(b), the rapid rivet shank flare with the flat die was also slightly delayed in the Riv-Bonding joint 7-F10 compared with that in the SPR joint 7-F5. According to the results reported in [185], the rapid rivet shank flare started after the die cavity space underneath the rivet was fully filled. Therefore, the changes of rivet shank flare behaviour before and after adding the adhesive layer can be explained from the view of die cavity filling conditions. The threshold filling conditions of the pip die (Region 1) and the flat die (Region 2) for the rapid rivet shank flare are shown in **Figure 7.15**(a) and **Figure 7.15**(b) respectively. It can be seen that, due to the existence of die pip, the volume of the Region 1 in the pip die is obvious smaller than that of the Region 2 in the flat die. So the Region 1 is much easier to be filled up than the Region 2. As a result, the rapid increment of the D_r started earlier with the pip die than with the flat die as shown in **Figure 7.14**. This phenomenon also indicated the contribution of the die pip to the rivet shank flare. As shown in **Figure 7.15**(c), with the pip die, the Region 1 in the SPR joint was nearly filled up at H=4.0mm, but was just fully filled at H=3.0mm in the corresponding Riv-Bonding joint. This is because the large hydraulic pressure within the trapped adhesive pocket caused a larger deformation of the top sheet underneath the rivet, and thus delayed the filling of the Region 1 in the Riv-Bonding joint. Similarly, with the flat die, the Region 2 was completely filled up in the SPR joint and was nearly filled up in the Riv-Bonding joint at H=3.0mm as shown in **Figure 7.15**(d). The trapped adhesive pocket with the flat die also caused a larger deformation of the top sheet underneath the rivet, but imposed limited influences on the filling of the Region 2 in the Riv-Bonding joint. The filling condition changes of the Region1 and Region 2 in **Figure 7.15** clearly explained the delay of the rapid increment phase after adding the adhesive layer in **Figure 7.14**.

During the rapid increment phase, with either the pip die or the flat die, the increment speeds of the D_r before and after adding the adhesive layer were nearly constant and very close to each other as shown in **Figure 7.14**. At the end of the joining processes, the maximum values of the D_r were a little bit smaller in the Riv-Bonding joints 7-P10 and 7-F10 compared with that in the SPR joints 7-P5 and 7-F5.

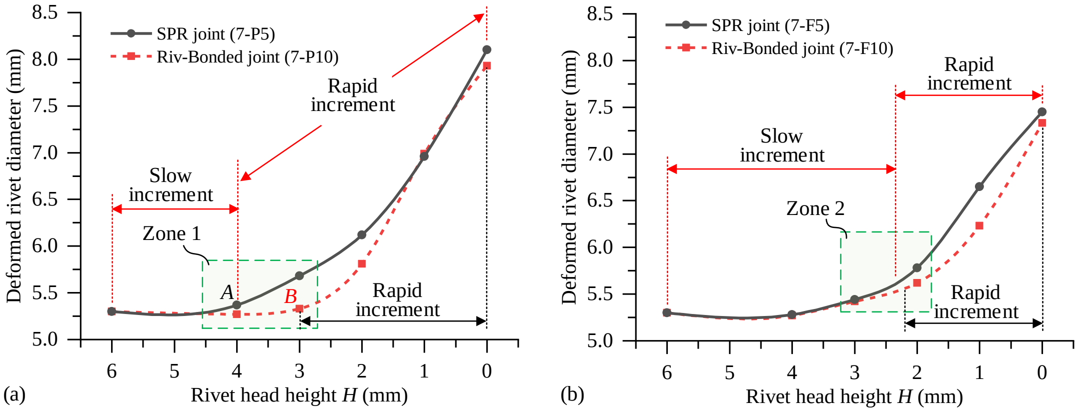

Figure 7.14: Variation curves of the deformed rivet shank diameter (D_r) with or without the adhesive layer: (a) pip die-A and (b) flat die-A

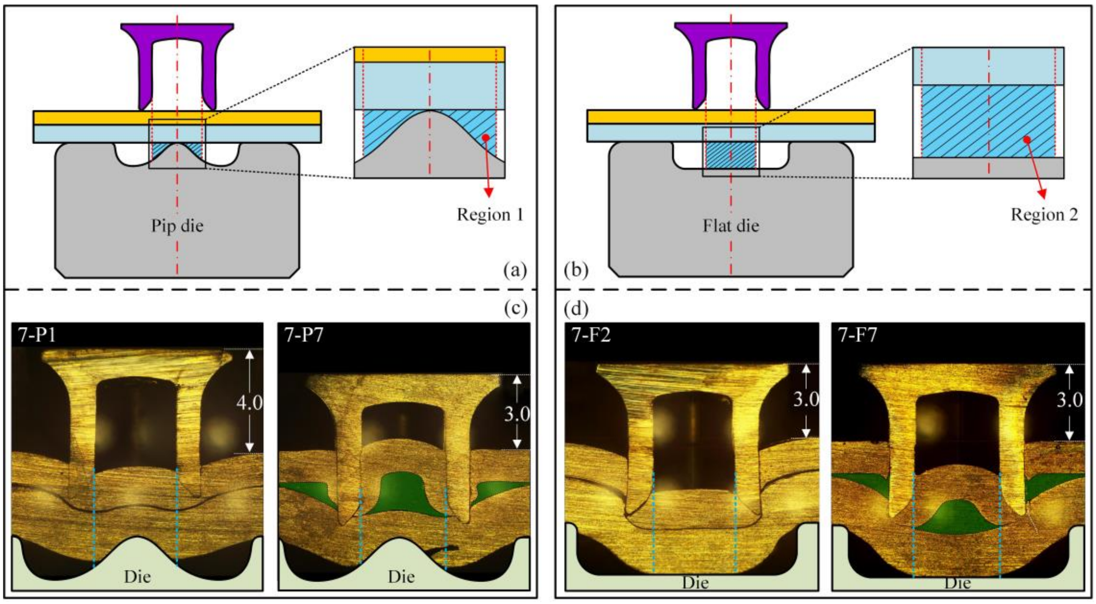

Figure 7.15: Threshold filling conditions of the die cavity for rapid rivet shank flare with the pip die and flat die

7.3.1.4. Riveting forces

The force-displacement curves during the joining processes of the SPR joints 7-P5, 7-F5 and the Riv-Bonding joints 7-P10 and 7-F10 are given in **Figure 7.16**. A similar changing trend of the riveting force was observed on the four curves: it first increased slowly at the early stage of the joining process and then increased rapidly at the end of the joining process. During the slow increment phase, the riveting force was slightly smaller in the Riv-Bonding joints 7-P10 and 7-F10 than that in the corresponding SPR joints 7-P5 and 7-F5. As shown in **Figure 7.16**(a), the turning point between the slow increment and the rapid increment of riveting force was very clear, and appeared earlier in the Riv-Bonding joint 7-P10 (point B) than in the SPR joint 7-P5 (point A) with the pip die. This is because the rapid increment of the riveting force was directly caused by the fully filled rivet cavity. The trapped adhesive pocket speeded up the filling of the rivet cavity, and therefore led to the shift of the turning point from A to B. In contrast, as shown in **Figure 7.16**(b), the turning point in the SPR joint 7-F5 with the flat die (point C) was not obvious. This is because the rivet cavity in this joint was not fully filled as shown in **Figure 7.8**(a-5). After adding the adhesive layer, the rivet cavity in the Riv-Bonding joint 7-F10 was filled up almost at the end of the joining process as shown in **Figure 7.8**(b-4)(b-5). So the trapped adhesive did not impose obvious influences on the turning point (point D) in the Riv-Bonding joint 7-F10. During the rapid increment phase, the increasing speed of riveting force reduced to a smaller value in the Riv-Bonding joint 7-P10 than in the SPR joint 7-P5. This is because the rivet cavity in the Riv-Bonding joint 7-P10 was partially filled with the uncured adhesive, which was much easier to be deformed than the sheet material and thus imposed less resistance on the rivet. Whilst the rapid increment speed of the riveting force was almost the same in the SPR joint 7-F5 and the Riv-Bonding joint 7-F10. Finally, the maximum riveting force in the Riv-Bonding joint 7-P10 was approximately 4kN smaller than that in the SPR joint 7-P5. The maximum riveting force in the Riv-Bonding joint 7-F10 was approximately 3kN greater than that in the SPR joint 7-F5. Therefore, the adhesive layer would not significantly affect the maximum riveting force required.

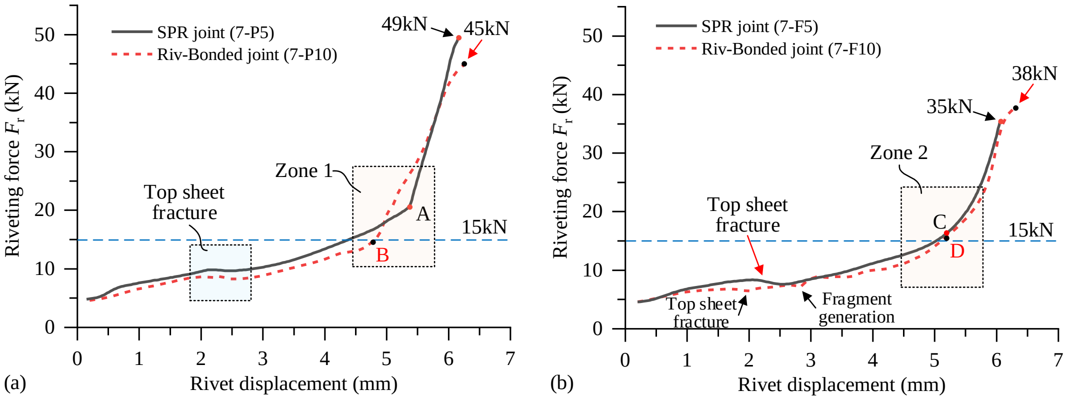

Figure 7.16: Force-displacement curves during the joining processes with or without the adhesive layer: (a) pip die and (b) flat die

7.3.2. Effects of the top sheet thickness on the Riv-Bonding joints

According to [56], the flexural rigidity of the sheet (D) depends heavily on the sheet thickness (h) as shown in Eq.(8.1). The E and v denote the Young's modulus and the Poisson's ratio of the sheet material. Increment of the h would significantly increase the sheet flexural rigidity and thus makes the sheet more difficult to be deformed. **Figure 7.17** and **Figure 7.18** shows the joint cross-sectional profiles of the SPR and Riv-Bonding joints with 1.2mm, 1.8mm and 2.5mm top sheets. It can be seen that the top sheet thickness (T_t) not only influenced the flexural rigidity of the top sheet, but also directly affected the length of rivet shank inserted into the bottom sheet. As a result, the deformed shapes of the rivet and the sheets, the distribution of the trapped adhesive, and the magnitudes of joint quality indicators (i.e., interlock and the remaining bottom sheet thickness) were significantly influenced. These changes were analysed and discussed individually in the following sections.

$$D = \frac{Eh^3}{12\left(1-v^2\right)} \tag{8.1}$$

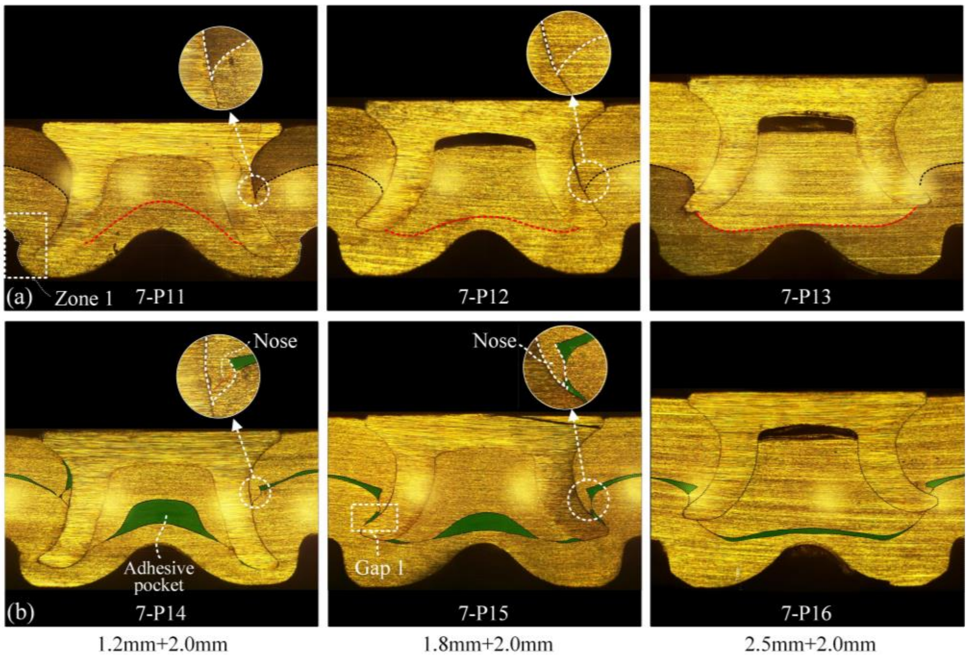
(a)
Zone 1
7-P11
7-P12
7-P13
Nose
Nose
Adhesive pocket
Gap 1
(b)
7-P14
7-P15
7-P16
1.2mm+2.0mm
1.8mm+2.0mm
2.5mm+2.0mm

Figure 7.17: Cross-sectional profiles of (a) the SPR joints 7-P11~7-P13 and (b) the Riv-Bonding joints 7-P14~7-P16 with different top sheet thicknesses T_t (pip die)

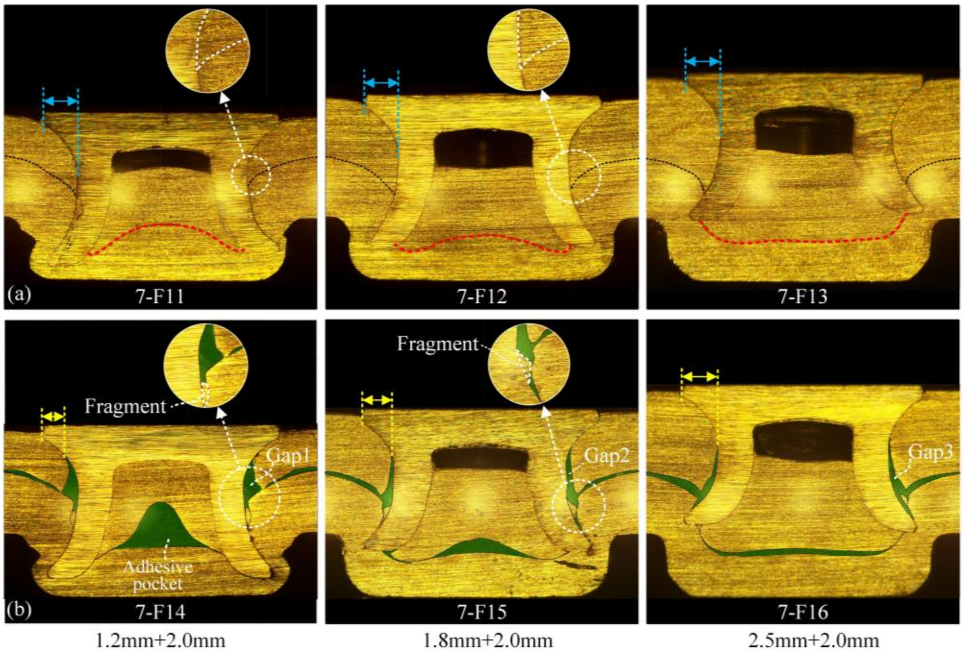
(a)
7-F11
7-F12
7-F13
Fragment
Fragment
Gap1
Gap2
Gap3
Adhesive pocket
(b)
7-F14
7-F15
7-F16
1.2mm+2.0mm
1.8mm+2.0mm
2.5mm+2.0mm

Figure 7.18: Cross-sectional profiles of (a) the SPR joints 7-F11~7-F13 and (b) the Riv-Bonding joints 7-F14~7-F16 with different top sheet thicknesses T_t (flat die)

7.3.2.1. Distribution of the trapped adhesive

As shown in **Figure 7.16**(b), with the pip die, the T_t demonstrated a remarkable influence on the shape of the trapped adhesive pocket underneath the rivet. The 1.2mm top sheet in the joint 7-P14 had a relatively low rigidity and was easy to be deformed. As a result, a large amount of adhesive was accumulated around the joint central area. The 1.8mm top sheet in the joint 7-P15 had a higher rigidity and became hard to be deformed. So more adhesive around the joint central area was pressed outward and a smaller amount of adhesive was trapped around the central area compared with that in the joint 7-P14. With the T_t further increasing to 2.5mm in the joint 7-P16, the top sheet became much more difficult to be deformed. The bottom surface of the top sheet underneath the rivet remained almost flat during the riveting process. As a result, the adhesive was not gathered around the joint central area, but almost uniformly distributed at the interface of the two sheets. In contrast, the T_t imposed limited impact on the distribution of adhesive outside the rivet. A similar distribution pattern of adhesive was found in the Riv-Bonding joints 7-P14~7-P16: only a thin adhesive layer was left between the two sheets.

As shown in **Figure 7.18**(b), with the flat die, the changing trend of the trapped adhesive pocket underneath the rivet with different T_t was very similar to that in **Figure 7.16**(b) with the pip die: first gathered around the joint centre with the 1.2mm top sheet in the joint 7-F14 and then almost uniformly distributed between the two sheets with the 2.5mm top sheet in the joint 7-F16. However, different from the Riv-Bonding joints with the pip die, the T_t also imposed a significant influence on the shape of remaining adhesive outside the rivet. Except for the thin adhesive layer left between the two sheets, there was a large amount of adhesive accumulated in the gaps (i.e., gap 1, gap 2 and gap 3) around the rivet shank. As mentioned above, these gaps were formed due to the premature fracture of the top sheet and the downward displacement of the top sheet outside the rivet. The final shape and forming position of this gap were apparently affected by the T_t. With the 1.2mm top sheet in the joint 7-F14, the gap 1 had a triangle shape and was very close to the rivet head. It can be seen that the contact length between the rivet head and the top sheet (yellow line with arrows) was obviously reduced compared with that in the joint 7-F11 (blue line with arrows). This may weaken the mechanical strengths of the riveted connection, and increase the probability of pull-out failure from the top sheet. Whilst with the 2.5mm top sheet in the joint 7-F16, the gap 3 had a strip shape and was farther away from the rivet head. Almost no influence was found on the contact length formed between the rivet head and the top sheet.

Meanwhile, it is also worth noting that, with the increment of the T_t, the reduction of the remaining adhesive in the Riv-Bonding joints might be also attributed to the changes of the initial adhesive trapped around the joining region after the clamping process. **Figure 7.19** schematically shows the initially trapped adhesive after the clamping process with a thin and a thick top sheet. The thin top sheet has a relatively low flexural rigidity and thus will undergo a large elastic-plastic deformation during the clamping process with a high blank-holder speed. Thus, a great amount of adhesive might be trapped around the joining region, as shown in **Figure 7.19**(a). While the thick top sheet is more difficult to be deformed due to its high rigidity. Thus, more adhesive might be squeezed outside the joining region during the clamping process, and less adhesive would be trapped between the two sheets as shown in **Figure 7.19**(b).

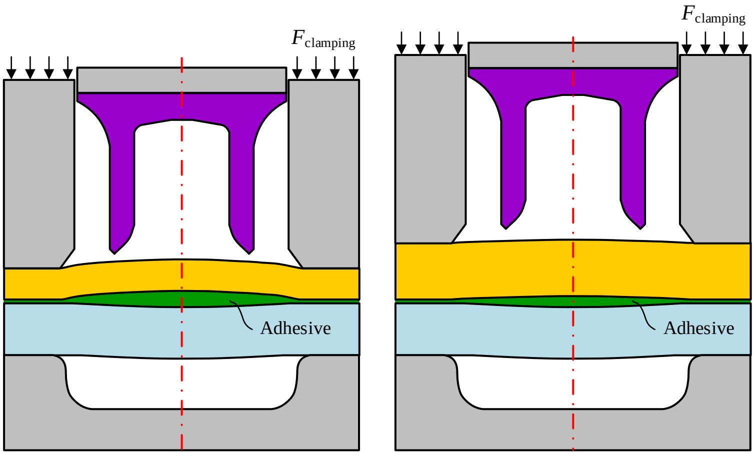

(a) Thin top sheet (b) Thick top sheet

Figure 7.19: Schematics of the initially trapped adhesive around the joining region after the clamping processes with (a) a thin top sheet and (b) a thick top sheet

7.3.2.2. Magnitude of the interlock

The magnitudes of interlock (I) in the SPR and the Riv-Bonding joints are shown in **Figure 7.20**(a) with the pip die and in **Figure 7.21**(a) with the flat die. It can be seen that, regardless of the die type, a smaller I was always observed in the Riv-Bonding joints than in the corresponding SPR joints. This indicates that the adhesive layer had negative effects on the interlock formation. According to the definition, the magnitude of the I is directly determined by the radius of the interlock inner boundary (R_{in}) and outer boundary (R_{out}) shown in **Figure 7.6**, and can be calculated using the Eq.(8.2). To better understand the influences of the T_t and the adhesive layer on the interlock formation, the R_{in} and R_{out} in all of the twelve joints with or without the adhesive layer were also recorded in **Figure 7.20**(b) with the pip die and in **Figure 7.21**(b) with the flat die. It can be found that the magnitudes of the R_{in} and R_{out} were apparently influenced by the trapped adhesive. Compared with the initial values in the SPR joints, the increment amount of the R_{in} was always greater than that of the R_{out} in the Riv-Bonding joints. This directly led to the smaller I in the Riv-Bonding joints than in the SPR joints.

$$I = R_{out} - R_{in} \tag{8.2}$$

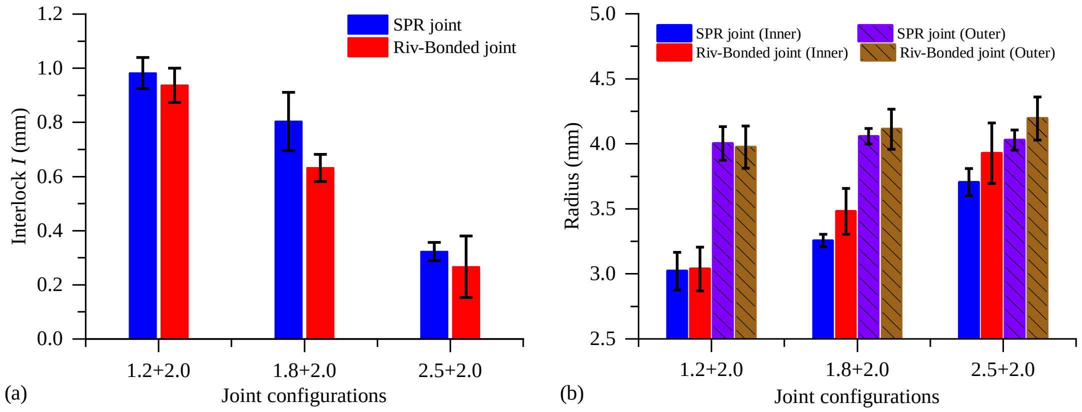

Figure 7.20: Changing trends of the (a) interlock and (b) radius of the interlock boundaries in the SPR and Riv-Bonding joints with the pip die

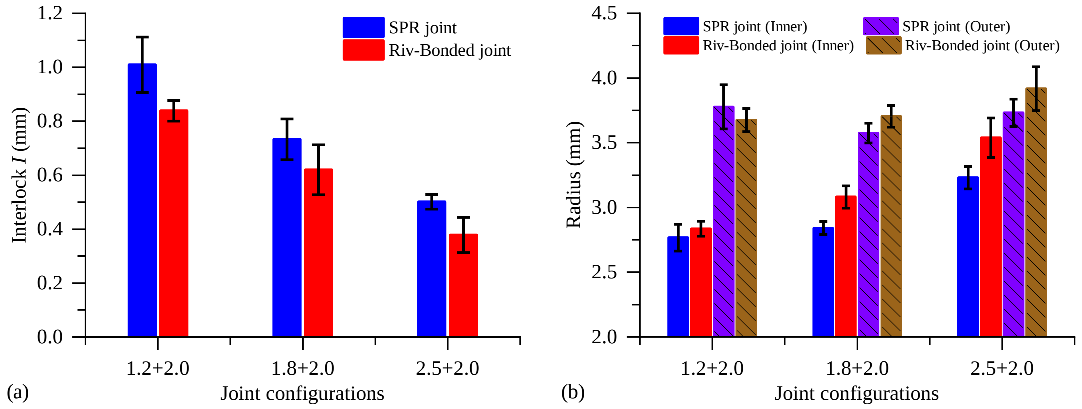

Figure 7.21: Changing trends of the (a) interlock and (b) radius of the interlock boundaries in the SPR and Riv-Bonding joints with the flat die

In the Riv-Bonding joints with the pip die, the increased value of the R_{in} was mainly attributed to the long nose formed on the top sheet as shown in **Figure 7.16**(b). A part of the nose was inserted into the interface between the rivet shank and the bottom sheet, which affected the position of the inner interlock boundary and resulted in a larger R_{in}. Similarly, in the Riv-Bonding joints with the flat die, the increment of the R_{in} was primarily caused by the top sheet fragments generated during the joining process as shown in **Figure 7.18**(b). These fragments were pressed downward by the rivet shank and finally trapped at the interface between the rivet shank and the bottom sheet. This affected the local material deformation of the bottom sheet and led to a greater R_{in}. With the different T_{t}, the adhesive layer showed almost the same influences on the R_{out} with the pip die and the flat die. Compared with the R_{out} in the SPR joints 7-P11 and 7-F11, a smaller R_{out} was found in the Riv-Bonding joints 7-P14 and 7-F14. This is because the trapped adhesive pocket led to a larger deformation of the 1.2mm top sheet, which delayed the rivet shank flare. In contrast, compared with the R_{out} in the SPR joints 7-P12, 7-P13, 7-F12 and 7-F13, a larger R_{out} was found in the corresponding Riv-Bonding joints 7-P15, 7-P16, 7-F15 and 7-F16. This is because the 1.8mm and 2.5mm top sheets were rigid enough to avoid large deformations. The trapped adhesive pocket enhanced the guidance effects of the top sheet underneath the rivet cavity on the rivet shank flare.

Except for the impact of the inserted nose on the interlock formation, it is also worth noting that gaps filled up with adhesive might be also formed between the rivet shank and the bottom sheet (e.g., gap 1 in the joint 7-P15 as shown in **Figure 7.16**(b)). This may also weaken the mechanical performance of the riveted connection in the Riv-Bonding joints.

7.3.2.3. Remaining bottom sheet thickness

The remaining bottom sheet thickness is very important for the corrosion performance and mechanical strengths of the SPR joints and the Riv-Bonding joints. Fatigue failure may occur on the bottom sheet if the remaining bottom sheet thickness is too small [41]. **Figure 7.22** shows the magnitudes of the remaining bottom sheet thickness at the joint centre (t_c) and under the rivet tip (t_{tip}) in the SPR and the Riv-Bonding joints with 1.2mm, 1.8mm and 2.5mm top sheets. It can be seen that, with the different T_t, the adhesive layer imposed apparently different influences on the remaining bottom sheet thickness.

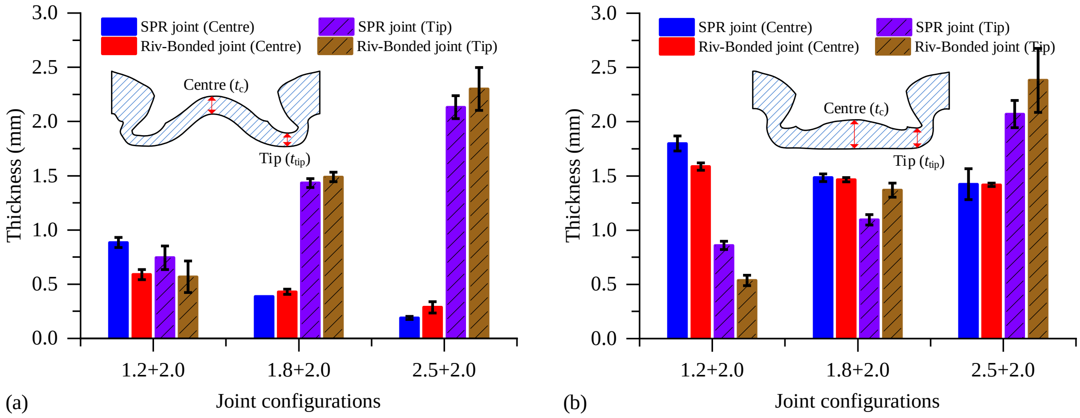

Figure 7.22: Influences of the top sheet thickness T_t on the remaining bottom sheet thickness in the SPR and Riv-Bonding joints with (a) the pip die and (b) the flat die

As shown in **Figure 7.22**(a), with the pip die, a smaller t_c was observed in the Riv-Bonding joint 7-P14 than that in the corresponding SPR joint 7-P11 with the 1.2mm top sheet. This was mainly attributed to the earlier fully filled rivet cavity in the joint 7-P14 because of the trapped adhesive pocket. The rapid decrease of the t_c started again after the rivet cavity was filled up [185], and lasted for a longer period in the joint 7-P14 than in the SPR joint 7-P11. In contrast, with the 1.8mm and 2.5mm top sheets, a slightly larger t_c was observed in the Riv-Bonding joints 7-P15 and 7-P16 than in the SPR joints 7-P12 and 7-P13. This was caused by the slightly larger deformation of the top sheet underneath the rivet, which reduced the pressure applied on the central area of the bottom sheet and thus slowed down the reduction of the t_c. As shown in **Figure 7.22**(b), with the flat die, the changing trend of the t_c became slightly different. When the T_t=1.2mm, the t_c in the Riv-Bonding joint 7-F14 was smaller than that in the SPR joint 7-F11. This was mainly caused by the uniform hydraulic pressure applied around the central area of the bottom sheet, which changed the curved bottom sheet around the joint centre in the SPR joint 7-F11 into the almost flat bottom sheet in the Riv-Bonding joint 7-F14, as shown in **Figure 7.18**. The trapped adhesive pocket also speeded up the filling of the rivet cavity in the joint 7-F14. However, this contributed very little to the smaller t_c because the rivet cavity was fully filled almost at the end of the joining process. When the T_t=1.8mm and 2.5mm, the t_c in the Riv-Bonding joints 7-F15 and 7-F16 were almost the same as that in the corresponding SPR joints 7-F12 and 7-F13. This might be explained by the already very flat bottom sheet around the centre area of the SPR joints, and the reduction of the adhesive pocket size. The uniform hydraulic pressure in the trapped adhesive pocket imposed little influence on the bottom sheet deformation.

Regardless of the die type, the adhesive layer imposed similar influences on the bottom sheet thickness under the rivet tip (t_{tip}) in all these joints. The t_{tip} reduced to a smaller value in the Riv-Bonding joints with the 1.2mm top sheet, but obviously increased the Riv-Bonding joints with the 1.8mm and 2.5mm top sheets. This phenomenon is highly associated with the impact of the adhesive layer on the rivet shank flare behaviour (or the R_{out}), as shown in **Figure 7.20**(b) and **Figure 7.21**(b). A larger R_{out} usually resulted in a larger t_{tip} while a smaller R_{out} more likely led to a smaller t_{tip}.

7.3.2.4. Influences on the mechanical strength

The mechanical performance of the riveted connection is highly associated to the magnitude of interlock. From the above experimental results, the reduction of the interlock value caused by the trapped adhesive pocket would unavoidably weaken the mechanical strengths of the riveted connection. On the other hand, the trapped adhesive in the Riv-Bonding joints may also provide some benefits for the riveted connection. For instance, under the lap-shear loading condition, the top sheet underneath the rivet in the SPR joint will not provide any resistance to prevent the rivet rotation because this part of top sheet can move freely with the rivet, as shown in **Figure 7.23**(a). In contrast, by adding an adhesive layer, after being cured, the adhesive accumulated around the joint centre can bond the top sheet underneath the rivet and the bottom sheet together, as shown in **Figure 7.23**(b). Therefore, the top sheet inside the rivet cavity may impose a resistance on the rivet shank under the lap-shear loading condition, which might delay the rivet rotation and therefore enhance the lap-shear strength of the riveted connection in some degrees. This phenomenon might be the reason why the riveted connection of the Riv-Bonding joint could endure a slightly greater shearing load after the failure of the bonded connection than the solo SPR joint [144].

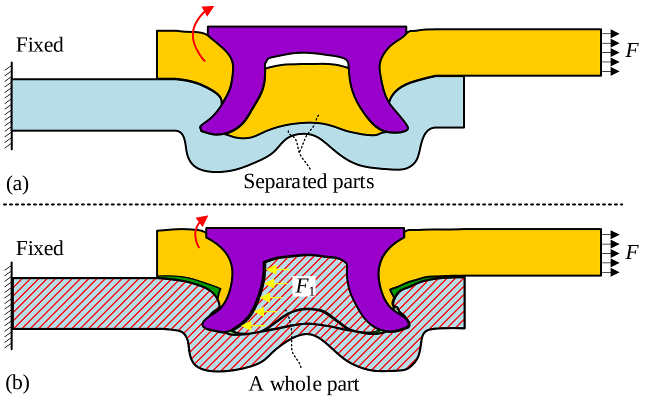

Figure 7.23: Schematic of the (a) the SPR joint and (b) the Riv-Bonding joint under the lap-shear loading condition

7.4. Conclusions

In this chapter, influences of the adhesive layer on the events that happen during the riveting process were experimentally investigated, including the adhesive distribution, the rivet and sheets deformation behaviours and the force-displacement curve. The impact of the trapped adhesive on the quality of joints with varying top sheet thicknesses (T_t) was analysed in detail. Two types of dies (i.e., pip die and flat die) were utilized in the experiments to assess the possible influences of die type on the joining process as well as on the joint quality. The main conclusions from this chapter are summarised below:

(1) The adhesive was distributed unevenly in the Riv-Bonding joints. A large adhesive pocket was formed around the joint centre. The shape and magnitude of this adhesive pocket were significantly affected by the T_t and the clamping process, but less influenced by the die type. A thin adhesive layer was observed between the two sheets outside the rivet. A large gap filled up with the adhesive was found around the rivet shank with the flat die.

(2) The adhesive layer imposed larger influences on the top sheet deformation than on the bottom sheet deformation. In the Riv-Bonding joints, the top sheet outside the rivet underwent a smaller downward movement, but the top sheet underneath the rivet experienced a greater plastic deformation due to the trapped adhesive pocket. A long nose was formed on the top sheet when it was penetrated by the rivet shank with the pip die, but small top sheet fragments were observed with the flat die due to the premature fracture of the top sheet.

(3) The adhesive layer showed different influences on the rivet shank flare behaviour with varying T_t. Compared with sole SPR joints, the rivet shank flared a smaller distance with a small T_t, but flared a greater distance with a large T_t. The load-displacement curves were also affected by the adhesive layer, but the maximum riveting force only changed within a small range (i.e., −5kN~5kN).

(4) Compared with the corresponding SPR joints, regardless of the die types, a smaller interlock was always found in the Riv-Bonding joints. The long noses formed with the pip die and the fragments formed with the flat die directly affected the position of the left interlock boundary, and thus negatively influenced the interlock formation.

(5) The influences of adhesive layer on the remaining bottom sheet thickness varied with different T_t and die types. Compared with the corresponding SPR joints, regardless of the die types, the bottom sheet thickness at the joint centre (t_c) and under the rivet tip (t_{tip}) reduced to a smaller value in the Riv-Bonding joints with the 1.2mm top sheet. However, in the Riv-Bonding joints with 1.8mm and 2.5mm top sheets, the t_c slightly increased with the pip die but kept almost constant with the flat die. The t_{tip} achieved a larger value with both of the pip die and flat die.

(6) All the conclusions above were made based on the employed high viscosity adhesive SikaPower 498 and the specific amount of adhesive applied in the joints. In fact, both the adhesive viscosity and the adhesive amount will affect the joining results. More experimental tests are required in order to get comprehensive understanding of the adhesive layer's impact on the joining process and on the quality of the riveted connection.

8. Conclusions and Future Work

This chapter summarises the main conclusions drawn from the experimental and numerical studies of this thesis. Potential research directions/ideas raised during the current research are also summarised as the future work.

8.1. Conclusions

In this thesis, experimental and numerical investigations were carried out to deepen the understanding of the SPR technique and the Riv-Bonding technique. The investigation of improper specimen cutting positions offers useful guidelines for the acquisition of joint cross-sectional profile, and also improves the reliability of the joint quality evaluation results. The development of SPR simulation model highlights the importance of element mesh size and the threshold separation thickness of top sheet, and lays a foundation for further development of Riv-Bonding simulation model. The numerical study of the die parameters' (i.e., die type, die diameter, die depth and die pip height) impact on the SPR process clearly demonstrates the flare behaviour of rivet shank, deformation behaviours of two sheets and the variation of riveting force under different joint conditions. The development of Riv-Bonding simulation model presents the detailed procedures to simulate the Riv-Bonding process using the Ostwald-de Waele power law to describe the flow behaviour of uncured adhesive. The experimental investigation of adhesive layer's effects on the riveting process and the final quality of riveted connection demonstrates the differences between the SPR process and the corresponding Riv-Bonding process. The main conclusions drawn from this thesis are summarised below:

(1) During experimental SPR tests, improper specimen cutting position will directly affect the captured joint cross-sectional profiles, and therefore influence the reliability of joint quality evaluation results. The offset distance (Δh) and rotation angle (θ_1) between the cutting plane and the joint central plane imposed opposite influences on the interlock: the measured interlock (I_m) was always larger than the true interlock (I_{true}) with only the existence of Δh, while the I_m was always smaller than the I_{true} with only the existence of θ_1. The Δh and θ_1 will lead to missing data of the remaining bottom sheet thickness around the joint central area. Due to the different distortion degrees of the captured bottom sheet profile, the measurement error of the remaining bottom sheet thickness shows a decline trend from the joint axis to the region around the rivet tip. The measurement accuracy of

rivet head height is not affected by the specimen cutting position. The measurement error of interlock can be evaluated and corrected with the proposed strategies, whilst it is very hard to quantitatively evaluate and correct the measurement error of the remaining bottom sheet thickness.

(2) The SPR process can be simplified and simulated with a 2D axisymmetric FE model. Sensitivity studies are important in order to determine the suitable element mesh sizes for different deformable parts. The geometrical criterion is proved effective for the modelling of AA5754 top sheet fracture, and the threshold thickness value should be selected carefully. By comparing with experimental results, it is validated that the developed FE model is capable of accurately predicting the deformation behaviours of rivet and sheets during the SPR process, and predicting the SPR joint quality as well as the riveting force. By deducing the C-frame stiffness of the SPR system, the experimentally recorded force-displacement curve can be successfully transferred into the true force-displacement curve.

(3) The FE model of SPR process is a very convenient tool to investigate the influences of different die parameters on the riveting process. Compared with the flat die, the pip die demonstrates a stronger guidance effect on the flaring of rivet shank but requires a larger riveting force. The die pip can effectively guide the bottom sheet material around the joint centre moving towards the formation region of interlock. Increment of the die diameter (D_1) will delay the top sheet fracture, and lead to a slightly larger deformed rivet shank radius. Meanwhile, it will also lead to defects and result in a loosely connected joint. Increment of the die depth (H_1) will reduce the maximum riveting force and negatively affect the flaring of rivet shank. It will also lead to a smaller remaining bottom sheet thickness at the joint centre and around the rivet tip. Increment of the die pip height will lead to a smaller remaining bottom sheet thickness at the joint centre but a greater deformed rivet shank radius. The remaining thickness distribution on the bottom sheet can be controlled conveniently by adjusting the die pip height. The filling condition of the die cavity directly affects the flaring behaviour of rivet shank during the SPR process.

(4) A two-dimensional FE model of Riv-Bonding process was successfully developed with the software Simufact.Forming 15. It is proved that the flow behaviour of uncured adhesive can be approximately described with the Ostwald-de Waele power law. The blank-holder strike has a critical impact on the adhesive distribution before the riveting process, and should be modelled properly. By comparing with the experimental results, it is validated that the developed FE model is capable of predicting the flow behaviour of uncured adhesive, and the deformation behaviours of rivet and sheets. Meanwhile, it can also give reasonable prediction results on the quality of Riv-Bonding joint and the riveting force. This FE model provides a new way to investigate the events happened during the

Riv-Bonding process, and also lays a foundation for the simulation model development of joint mechanical strengths.

(5) The uncured adhesive layer can impose significant influences on the riveting process and the final quality of riveted connection. A large adhesive pocket might be formed around the joint centre, and its size is apparently affected by the top sheet thickness (T_t) and the clamping process. The deformation behaviour of top sheet is highly influenced by the adhesive layer. When the top sheet is gradually penetrated by the rivet shank, a long nose is formed on the top sheet with the pip die while small top sheet fragments are generated due to the premature fracture of the top sheet with the flat die. The adhesive layer will also affect the flaring behaviour of rivet shank, but its influences vary in joints with different top sheet thicknesses. Regardless of the die type and top sheet thickness, a smaller interlock is always found in the Riv-Bonding joints. The influences of adhesive layer on the remaining bottom sheet thickness vary with different top sheet thicknesses and die types.

8.2. Future Work

Although the SPR and Riv-Bonding techniques have been widely used in the automotive industry, more work is still required to speed up their developments and to simplify their design process in practical applications. Based on the author's experience, some potential research directions are summarised below:

(1) The surface condition of die cavity can influence the deformation behaviour of bottom sheet. It might be possible to restrict the movement of bottom sheet material towards the radial direction by modifying the bottom surface texture of the flat die, as shown in **Figure 8.1**. This may be helpful for the rivet shank to flare into the bottom sheet more effectively, and form a greater mechanical interlock.

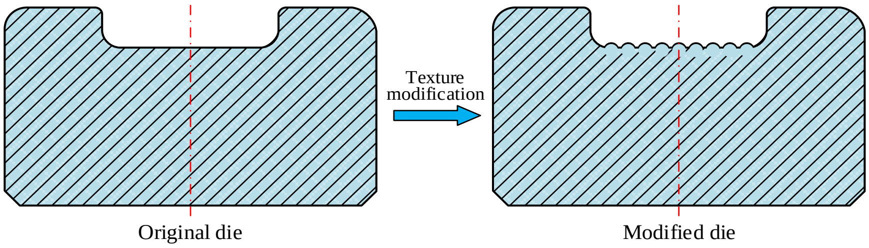

Figure 8.1: Texture modification of the die bottom surface

(2) During the SPR process, the rivet profile will not only affect the final joint quality, but also the maximum riveting force. However, there are only a few studies relevant to this issue. It is necessary to find out how different rivet geometric parameters, such as the

thickness of rivet head in **Figure 8.2**(a), position of the indentation on rivet shank in **Figure 8.2**(b) and the shape of rivet head in **Figure 8.2**(c), affect the joining results.

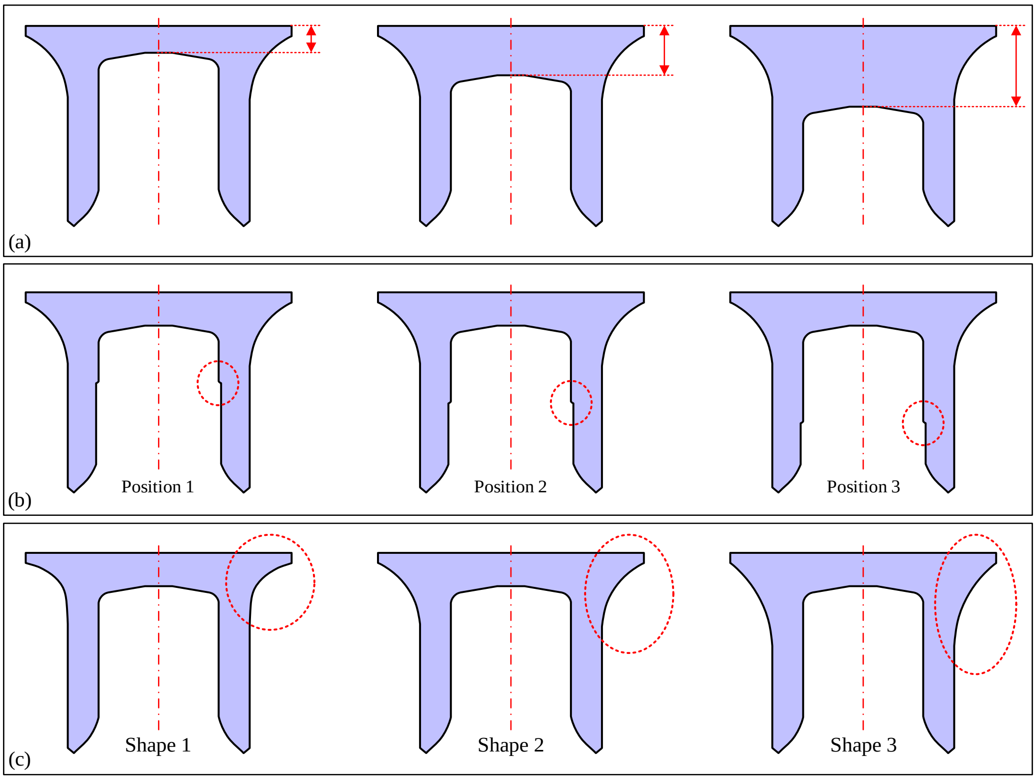

Figure 8.2: Schematic of the three rivet geometric parameters

(3) Although SPR/Riv-Bonding joints with three layers have been widely utilized in the industrial sector, there are only a few studies relevant to this topic in the public domain. It is necessary to find out the differences between the joining processes of two-layer joint and three-layer joint, as shown in **Figure 8.3**. The possibility to guide the design of three-layer joints with experimental results of two-layer joints is also worth investigating.

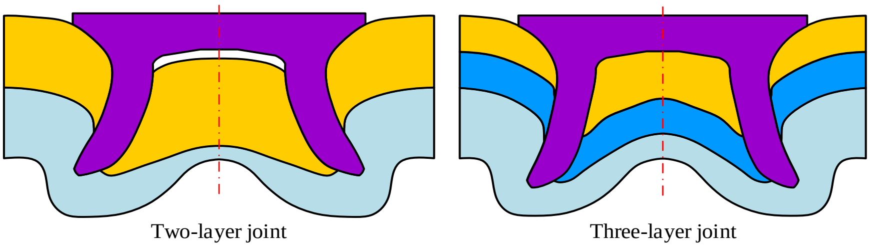

Figure 8.3: Cross-sectional profiles of the two-layer and three-layer SPR joints

(4) In addition to the die type and top sheet thickness, attentions should also be paid to other joining parameters that may affect the final quality of Riv-Bonding joints as shown in **Figure 8.4**, including the amount of adhesive, the clamping force, the blank-holder speed, the adhesive viscosity, the sheet material and the bottom sheet thickness.

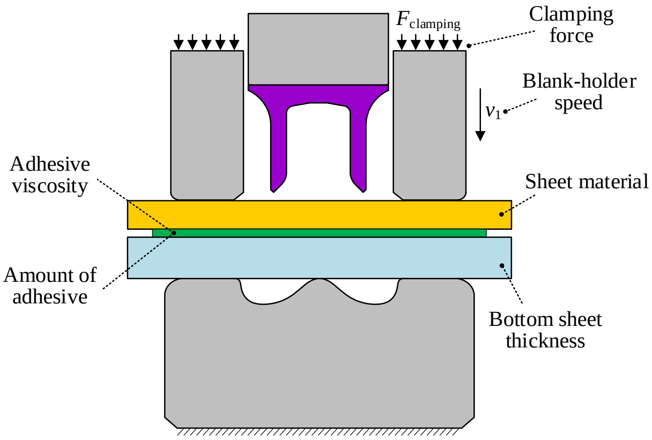
$F_{clamping}$
Clamping force
Blank-holder speed
v_1
Sheet material
Adhesive viscosity
Amount of adhesive
Bottom sheet thickness

Figure 8.4: Schematic of the joining parameters that may affect the final quality of Riv-Bonding joints

(5) Simulation model of Riv-Bonding joint for mechanical strength prediction is rarely reported in the public domain, but is important for further modelling of structures assembled with multiple Riv-Bonding joints.

(6) When using the Riv-Bonding technique to assemble structures, adhesive pockets might be formed between the multiple joints as shown in **Figure 8.5**(a). This will inevitably cause deformation of the connected structures [156]. Therefore, it is necessary to find out how the amount of adhesive, adhesive viscosity and joining parameters affect the connected structures. Meanwhile, structure deformation induced by the joining sequence of multiple joints as shown in **Figure 8.5**(b) is also worth studying [187]. The way of applying uncured adhesive as shown in **Figure 8.5**(c) is also worth investigating.

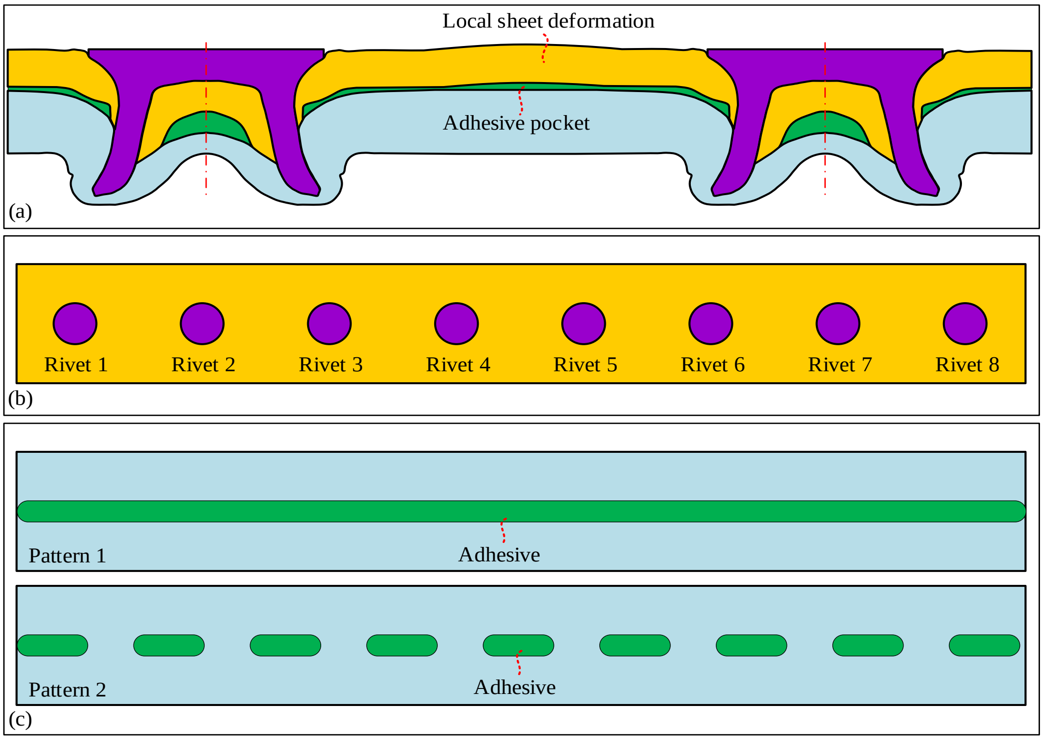
Local sheet deformation
Adhesive pocket
(a)
Rivet 1
Rivet 2
Rivet 3
Rivet 4
Rivet 5
Rivet 6
Rivet 7
Rivet 8
(b)
Pattern 1
Adhesive
Pattern 2
Adhesive
(c)

Figure 8.5: Schematics of the (a) local sheet deformation induced by the adhesive pocket, (b) joining sequence of multiple Riv-Bonding joints and (c) ways of applying uncured adhesive

References

[1] X. He, Application of finite element analysis in sheet material joining, Finite Elem. Anal. - From Biomed. Appl. to Ind. Dev. (2012) 343–368. https://doi.org/10.5772/37703.

[2] M. Carandente, R.J. Dashwood, I.G. Masters, L. Han, Improvements in numerical simulation of the SPR process using a thermo-mechanical finite element analysis, J. Mater. Process. Technol. 236 (2016) 148–161. https://doi.org/10.1016/j.jmatprotec.2016.05.001.

[3] E. Atzeni, R. Ippolito, L. Settineri, Experimental and numerical appraisal of self-piercing riveting, CIRP Ann. - Manuf. Technol. 58 (2009) 17–20. https://doi.org/10.1016/j.cirp.2009.03.081.

[4] K. Mori, T. Kato, Y. Abe, Y. Ravshanbek, Plastic joining of ultra high strength steel and aluminium alloy sheets by self piercing rivet, CIRP Ann. - Manuf. Technol. 55 (2006) 283–286. https://doi.org/10.1016/S0007-8506(07)60417-X.

[5] L. Han, M. Thornton, M. Shergold, A comparison of the mechanical behaviour of self-piercing riveted and resistance spot welded aluminium sheets for the automotive industry, Mater. Des. 31 (2010) 1457–1467. https://doi.org/10.1016/J.MATDES.2009.08.031.

[6] X. Sun, E. V. Stephens, M.A. Khaleel, Fatigue behaviors of self-piercing rivets joining similar and dissimilar sheet metals, Int. J. Fatigue. 29 (2007) 370–386. https://doi.org/10.1016/j.ijfatigue.2006.02.054.

[7] A. Kochan, Audi moves forward with all-aluminium cars, Assem. Autom. 20 (2000) 132–135. https://doi.org/10.1108/01445150010321751.

[8] R. Haque, J.H. Beynon, Y. Durandet, Characterisation of force-displacement curve in self-pierce riveting, Sci. Technol. Weld. Join. 17 (2012) 476–488. https://doi.org/10.1179/1362171812Y.0000000036.

[9] Z. Xie, W. Yan, C. Yu, T. Mu, L. Song, Improved shear strength design of cold-formed steel connection with single self-piercing rivet, Thin-Walled Struct. 131 (2018) 708–717. https://doi.org/10.1016/J.TWS.2018.03.025.

[10] L. Han, Y.K. Chen, A. Chrysanthou, J.M. O'Sullivan, Self-pierce riveting - A new way

for joining structures, Am. Soc. Mech. Eng. Press. Vessel. Pip. Div. PVP. 446 (2002) 123–127. https://doi.org/10.1115/PVP2002-1495.

[11] A. Ferjaoui, T. Yue, M. Abdel Wahab, R. Hojjati-Talemi, Prediction of fretting fatigue crack initiation in double lap bolted joint using Continuum Damage Mechanics, Int. J. Fatigue. 73 (2015) 66–76. https://doi.org/10.1016/J.IJFATIGUE.2014.11.012.

[12] H. Jiang, C. Zeng, G. Li, J. Cui, Effect of locking mode on mechanical properties and failure behavior of CFRP/Al electromagnetic riveted joint, Compos. Struct. 257 (2021) 113162. https://doi.org/10.1016/J.COMPSTRUCT.2020.113162.

[13] X. He, L. Zhao, C. Deng, B. Xing, F. Gu, A. Ball, Self-piercing riveting of similar and dissimilar metal sheets of aluminum alloy and copper alloy, Mater. Des. 65 (2015) 923–933. https://doi.org/10.1016/J.MATDES.2014.10.002.

[14] W. Cai, P.C. Wang, W. Yang, Assembly dimensional prediction for self-piercing riveted aluminum panels, Int. J. Mach. Tools Manuf. 45 (2005) 695–704. https://doi.org/10.1016/J.IJMACHTOOLS.2004.09.023.

[15] B. Wang, C. Hao, J. Zhang, H. Zhang, A new self-piercing riveting process and strength evaluation, J. Manuf. Sci. Eng. Trans. ASME. 128 (2006) 580–587. https://doi.org/10.1115/1.2137746.

[16] A. Luo, T.M. Lee, J.T. Carter, Self-Pierce Riveting of Magnesium to Aluminum Alloys, SAE Int. J. Mater. Manuf. 4 (2011) 158–165. https://doi.org/10.4271/2011-01-0074.

[17] H.R. Kotadia, A. Rahnama, I.R. Sohn, J. Kim, S. Sridhar, Performance of dissimilar metal Self-Piercing Riveting (SPR) joint and coating behaviour under corrosive environment, J. Manuf. Process. 39 (2019) 259–270. https://doi.org/10.1016/J.JMAPRO.2019.02.024.

[18] D. Li, L. Han, M. Thornton, M. Shergold, Influence of edge distance on quality and static behaviour of self-piercing riveted aluminium joints, Mater. Des. 34 (2012) 22–31. https://doi.org/10.1016/j.matdes.2011.07.046.

[19] D. Li, A. Chrysanthou, I. Patel, G. Williams, Self-piercing riveting-a review, Int. J. Adv. Manuf. Technol. 92 (2017) 1777–1824. https://doi.org/10.1007/s00170-017-0156-x.

[20] G. Di Franco, B. Zuccarello, Analysis and optimization of hybrid double lap aluminum-GFRP joints, Compos. Struct. 116 (2014) 682–693. https://doi.org/10.1016/J.COMPSTRUCT.2014.05.044.

[21] H.Q. Ang, An Overview of Self-piercing Riveting Process with Focus on Joint Failures, Corrosion Issues and Optimisation Techniques, Chinese J. Mech. Eng. 34 (2021) 1–25. https://doi.org/10.1186/s10033-020-00526-3.

[22] R. Haque, Quality of self-piercing riveting (SPR) joints from cross-sectional perspective: A review, Arch. Civ. Mech. Eng. 18 (2018) 83–93. https://doi.org/10.1016/j.acme.2017.06.003.

[23] X. He, F. Gu, A. Ball, Recent development in finite element analysis of self-piercing riveted joints, Int. J. Adv. Manuf. Technol. 58 (2012) 643–649. https://doi.org/10.1007/s00170-011-3414-3.

[24] Y. Ma, M. Lou, Y. Li, Z. Lin, Effect of rivet and die on self-piercing rivetability of AA6061-T6 and mild steel CR4 of different gauges, J. Mater. Process. Technol. 251 (2018) 282–294. https://doi.org/10.1016/J.JMATPROTEC.2017.08.020.

[25] H. Zhao, L. Han, Y. Liu, X. Liu, Modelling and interaction analysis of the self-pierce riveting process using regression analysis and FEA, Int. J. Adv. Manuf. Technol. 113 (2021) 159–176. https://doi.org/10.1007/s00170-020-06519-9.

[26] B. Uhe, C.-M. Kuball, M. Merklein, G. Meschut, Strength of self-piercing riveted Joints with conventional Rivets and Rivets made of High Nitrogen Steel, ESAFORM 2021. (2021) 1–8. https://doi.org/10.25518/esaform21.1911.

[27] N.-H. Hoang, R. Porcaro, M. Langseth, A.-G. Hanssen, Self-piercing riveting connections using aluminium rivets, Int. J. Solids Struct. 47 (2010) 427–439. https://doi.org/10.1016/j.ijsolstr.2009.10.009.

[28] H.M. Rao, J. Kang, G. Huff, K. Avery, Structural stress method to evaluate fatigue properties of similar and dissimilar self-piercing riveted joints, Metals (Basel). 9 (2019) 359. https://doi.org/10.3390/met9030359.

[29] M.A. Karim, T.E. Jeong, W. Noh, K.Y. Park, D.H. Kam, C. Kim, D.G. Nam, H. Jung, Y. Do Park, Joint quality of self-piercing riveting (SPR) and mechanical behavior under the frictional effect of various rivet coatings, J. Manuf. Process. 58 (2020) 466–477. https://doi.org/10.1016/j.jmapro.2020.08.038.

[30] L. Han, A. Chrysanthou, Evaluation of quality and behaviour of self-piercing riveted aluminium to high strength low alloy sheets with different surface coatings, Mater. Des. 29 (2008) 458–468. https://doi.org/10.1016/J.MATDES.2006.12.020.

[31] J. Liang, H. Jiang, J. Zhang, X. Wu, X. Zhang, G. Li, J. Cui, Investigations on

mechanical properties and microtopography of electromagnetic self-piercing riveted joints with carbon fiber reinforced plastics/aluminum alloy 5052, Arch. Civ. Mech. Eng. 19 (2019) 240–250. https://doi.org/10.1016/J.ACME.2018.11.001.

[32] M. Lou, Y. Li, Y. Li, G. Chen, Behavior and quality evaluation of electroplastic self-piercing riveting of aluminum alloy and advanced high strength steel, J. Manuf. Sci. Eng. Trans. ASME. 135 (2013). https://doi.org/10.1115/1.4023256.

[33] L. Deng, M. Lou, Y. Li, B.E. Carlson, Thermally assisted self-piercing riveting of AA6061-T6 to ultrahigh strength steel, J. Manuf. Sci. Eng. Trans. ASME. 141 (2019). https://doi.org/10.1115/1.4044255.

[34] Y. Durandet, R. Deam, A. Beer, W. Song, S. Blacket, Laser assisted self-pierce riveting of AZ31 magnesium alloy strips, Mater. Des. 31 (2010) S13–S16. https://doi.org/10.1016/j.matdes.2009.10.038.

[35] O. Hahn, R. Neugebauer, G. Leuschen, C. Kraus, R. Mauermann, Research in impulse joining of self pierce riveting, 3rd Int. Conf. High Speed Form. (2008) 173–180. https://d-nb.info/1103231278/34 (accessed October 1, 2019).

[36] L. Han, M. Thornton, D. Li, M. Shergold, Effect of setting velocity on self-piercing riveting process and joint behaviour for automotive applications, SAE Tech. Pap. (2010). https://doi.org/10.4271/2010-01-0966.

[37] T. Markowski, J. Mucha, W. Witkowski, FEM analysis of clinching joint machine’s C-frame rigidity, Eksploat. i Niezawodn. 15 (2013) 51–57.

[38] R. Haque, J.H. Beynon, Y. Durandet, Characterisation of force-displacement curve in self-pierce riveting, Sci. Technol. Weld. Join. 17 (2012) 476–488. https://doi.org/10.1179/1362171812Y.0000000036.

[39] F. Hönsch, J. Domitner, C. Sommitsch, B. Götzinger, M. Kölz, Numerical simulation and experimental validation of self-piercing riveting (SPR) of 6xxx aluminium alloys for automotive applications, J. Phys. Conf. Ser. 1063 (2018) 012081. https://doi.org/10.1088/1742-6596/1063/1/012081.

[40] D.H. Kam, T.E. Jeong, M.G. Kim, J. Shin, Self-piercing riveted joint of vibration-damping steel and aluminum alloy, Appl. Sci. 9 (2019) 4575. https://doi.org/10.3390/app9214575.

[41] X. Zhang, X. He, B. Xing, W. Wei, J. Lu, Quasi-static and fatigue characteristics of self-piercing riveted joints in dissimilar aluminium-lithium alloy and titanium sheets,

J. Mater. Res. Technol. 9 (2020) 5699–5711. https://doi.org/10.1016/j.jmrt.2020.03.095.

[42] N.-H. Hoang, O.S. Hopperstad, M. Langseth, I. Westermann, Failure of aluminium self-piercing rivets: An experimental and numerical study, Mater. Des. 49 (2013) 323–335. https://doi.org/10.1016/J.MATDES.2013.01.034.

[43] E. Atzeni, R. Ippolito, L. Settineri, FEM Modeling of Self-Piercing Riveted Joint, Key Eng. Mater. 344 (2007) 655–662. https://doi.org/10.4028/www.scientific.net/KEM.344.655.

[44] Y. Abe, T. Kato, K. Mori, Self-piercing riveting of high tensile strength steel and aluminium alloy sheets using conventional rivet and die, J. Mater. Process. Technol. 209 (2009) 3914–3922. https://doi.org/10.1016/j.jmatprotec.2008.09.007.

[45] J. Zhang, S. Yang, Self-piercing riveting of aluminum alloy and thermoplastic composites, J. Compos. Mater. 49 (2015) 1493–1502. https://doi.org/10.1177/0021998314535456.

[46] S.H. Kang, D.W. Han, H.K. Kim, Fatigue strength evaluation of self-piercing riveted joints of AZ31 Mg alloy and cold-rolled steel sheets, J. Magnes. Alloy. 8 (2020) 241–251. https://doi.org/10.1016/j.jma.2019.11.006.

[47] L. Fratini, V.F. Ruisi, Self-piercing riveting for aluminium alloys-composites hybrid joints, Int. J. Adv. Manuf. Technol. 43 (2009) 61–66. https://doi.org/10.1007/s00170-008-1690-3.

[48] L. Zhao, X. He, B. Xing, X. Zhang, C. Deng, Y. Liu, Fracture mechanism of titanium sheet self-piercing riveted joints, Thin-Walled Struct. 144 (2019) 106353. https://doi.org/10.1016/j.tws.2019.106353.

[49] X. He, Y. Wang, Y. Lu, K. Zeng, F. Gu, A. Ball, Self-piercing riveting of similar and dissimilar titanium sheet materials, Int. J. Adv. Manuf. Technol. 80 (2015) 2105–2115. https://doi.org/10.1007/s00170-015-7174-3.

[50] T. Kato, Y. Abe, K. Mori, Finite element simulation of self-piercing riveting of three aluminium alloy sheets, Key Eng. Mater. 340 (2007) 1461–1466. https://doi.org/10.4028/www.scientific.net/kem.340-341.1461.

[51] Y. Abe, T. Kato, K. Mori, Self-pierce riveting of three high strength steel and aluminium alloy sheets, Int. J. Mater. Form. 1 (2008) 1271–1274. https://doi.org/10.1007/s12289-008-0134-9.

[52] Y. Abe, T. Maeda, D. Yoshioka, K.I. Mori, Mechanical clinching and self-pierce riveting of thin three sheets of 5000 series aluminium alloy and 980 MPa grade cold rolled ultra-high strength steel, Materials (Basel). 13 (2020) 1–22. https://doi.org/10.3390/ma13214741.

[53] L. Han, A. Chrysanthou, K.W. Young, Mechanical behaviour of self-piercing riveted multi-layer joints under different specimen configurations, Mater. Des. 28 (2007) 2024–2033. https://doi.org/10.1016/j.matdes.2006.06.015.

[54] J. Mucha, A study of quality parameters and behaviour of self-piercing riveted aluminium sheets with different joining conditions, Stroj. Vestnik/Journal Mech. Eng. 57 (2011) 323–333. https://doi.org/10.5545/sv-jme.2009.043.

[55] W. Yan, T. Mu, Z. Xie, C. Yu, Experimental investigation of typical connections for fabricated cold-formed steel structures, Adv. Struct. Eng. 22 (2019) 141–155. https://doi.org/10.1177/1369433218781901.

[56] R. Asaro, V. Lubarda, R. Asaro, V. Lubarda, Deformation of plates, in: Mech. Solids Mater., 2010: pp. 280–292. https://doi.org/10.1017/cbo9780511755514.017.

[57] A. Porcaro, R., Hanssen, A.G., Langseth, M., Aalberg, Through process modelling of self-piercing riveting, Met. Form. 8th Int. LS-DYNA User Conf. (2004) 7–16.

[58] Y. Abe, T. Kato, K. Mori, Aluminium alloy self-pierce riveting for joining of aluminium alloy sheets, Key Eng. Mater. 410 (2009) 79–86. https://doi.org/10.4028/www.scientific.net/KEM.410-411.79.

[59] S.N. Van Hall, K.O. Findley, A.K. Freis, Improved self-pierce rivet performance through intentional decarburization, J. Mater. Process. Technol. 251 (2018) 350–359. https://doi.org/10.1016/j.jmatprotec.2017.08.018.

[60] H. Jiang, S. Gao, G. Li, J. Cui, Structural design of half hollow rivet for electromagnetic self-piercing riveting process of dissimilar materials, Mater. Des. 183 (2019) 108141. https://doi.org/10.1016/j.matdes.2019.108141.

[61] N. Karathanasopoulos, K.S. Pandya, D. Mohr, Self-piercing riveting process: Prediction of joint characteristics through finite element and neural network modeling, J. Adv. Join. Process. 3 (2021) 100040. https://doi.org/10.1016/j.jajp.2020.100040.

[62] B. Uhe, C.M. Kuball, M. Merklein, G. Meschut, Improvement of a rivet geometry for the self-piercing riveting of high-strength steel and multi-material joints, Prod. Eng. 14 (2020) 417–423. https://doi.org/10.1007/s11740-020-00973-w.

[63] D. Li, L. Han, M. Shergold, M. Thornton, G. Williams, Influence of rivet tip geometry on the joint quality and mechanical strengths of self-piercing riveted aluminium joints, Mater. Sci. Forum. 765 (2013) 746–750. https://doi.org/10.4028/www.scientific.net/MSF.765.746.

[64] M. Fu, P.K. Mallick, Effect of process variables on the static and fatigue properties of self-piercing riveted joints in aluminum alloy 5754, SAE Tech. Pap. (2001). https://doi.org/10.4271/2001-01-0825.

[65] D. Li, Influence of aluminium sheet surface modification on the self-piercing riveting process and the joint static lap shear strength, Int. J. Adv. Manuf. Technol. 93 (2017) 2685–2695. https://doi.org/10.1007/s00170-017-0710-6.

[66] D. Li, Influence of local surface texture by tool impression on the self-piercing riveting process and the static lap shear strength, J. Manuf. Process. 29 (2017) 298–309. https://doi.org/10.1016/j.jmapro.2017.08.003.

[67] M. Lovell, C.F. Higgs, P. Deshmukh, A. Mobley, Increasing formability in sheet metal stamping operations using environmentally friendly lubricants, J. Mater. Process. Technol. 177 (2006) 87–90. https://doi.org/10.1016/j.jmatprotec.2006.04.045.

[68] L. Ying, T. Gao, M. Dai, P. Hu, J. Dai, Towards joinability of thermal self-piercing riveting for AA7075-T6 aluminum alloy sheets under quasi-static loading conditions, Int. J. Mech. Sci. 189 (2021) 105978. https://doi.org/10.1016/j.ijmecsci.2020.105978.

[69] R. Haque, Y.C. Wong, A. Paradowska, S. Blacket, Y. Durandet, SPR characteristics curve and distribution of residual stress in self-piercing riveted joints of steel sheets, Adv. Mater. Sci. Eng. 2017 (2017). https://doi.org/10.1155/2017/5824171.

[70] Z. Du, L. Duan, L. Jing, A. Cheng, Z. He, Numerical simulation and parametric study on self-piercing riveting process of aluminium–steel hybrid sheets, Thin-Walled Struct. 164 (2021) 107872. https://doi.org/10.1016/J.TWS.2021.107872.

[71] Z.M. Su, P.C. Lin, W.J. Lai, J. Pan, Fatigue analyses of self-piercing rivets and clinch joints in lap-shear specimens of aluminum sheets, Int. J. Fatigue. 72 (2015) 53–65. https://doi.org/10.1016/j.ijfatigue.2014.09.022.

[72] X. Zhang, X. He, F. Gu, A. Ball, Self-piercing riveting of aluminium–lithium alloy sheet materials, J. Mater. Process. Technol. 268 (2019) 192–200. https://doi.org/10.1016/j.jmatprotec.2019.01.019.

[73] K. Mori, Y. Abe, T. Kato, Finite element simulation of plastic joining processes of steel

and aluminum alloy sheets, AIP Conf. Proc. 908 (2007) 197–202. https://doi.org/10.1063/1.2740811.

[74] M. Jäckel, T. Falk, D. Landgrebe, Concept for further development of self-pierce riveting by using cyber physical systems, Procedia CIRP. 44 (2016) 293–297. https://doi.org/10.1016/j.procir.2016.02.073.

[75] W.G. Drossel, M. Jäckel, New die concept for self-pierce riveting materials with limited ductility, Key Eng. Mater. 611 (2014) 1452–1459. https://doi.org/10.4028/www.scientific.net/KEM.611-612.1452.

[76] D. Landgrebe, M. Jäckel, R. Niegsch, Influence of process induced damages on joint strength when self-pierce riveting carbon fiber reinforced plastics with aluminum, Key Eng. Mater. 651 (2015) 1493–1498. https://doi.org/10.4028/www.scientific.net/KEM.651-653.1493.

[77] M. Lou, Y. Li, S. Huang, G. Chen, Influence of die-rivet volume ratio on forming performance of self-piercing riveting joints of dissimilar materials, China Mech. Eng. 20 (2009) 1873–1876.

[78] H. Zhao, L. Han, Y. Liu, X. Liu, Quality prediction and rivet/die selection for SPR joints with artificial neural network and genetic algorithm, J. Manuf. Process. 66 (2021) 574–594. https://doi.org/10.1016/j.jmapro.2021.04.033.

[79] R. Porcaro, A.G. Hanssen, A. Aalberg, M. Langseth, Joining of aluminium using self-piercing riveting: Testing, modelling and analysis, Int. J. Crashworthiness. 9 (2004) 141–154. https://doi.org/10.1533/ijcr.2004.0279.

[80] L. Zhao, X. He, B. Xing, X. Zhang, Q. Cheng, F. Gu, A. Ball, Fretting behavior of self-piercing riveted joints in titanium sheet materials, J. Mater. Process. Technol. 249 (2017) 246–254. https://doi.org/10.1016/j.jmatprotec.2017.06.016.

[81] D. Li, L. Han, A. Chrysanthou, M. Shergold, Influence of corrosion of self-piercing riveted high strength aluminium alloy joints with button cracks on the mechanical strength, J. Mater. Sci. Technol. Res. 5 (2018) 16–27. https://doi.org/10.15377/2410-4701.2018.05.4.

[82] X. He, B. Xing, Y. Ding, Y. Hu, K. Zeng, Strength and energy absorption of self-piercing riveted joints, Adv. Mater. Res. 616 (2013) 1783–1786. https://doi.org/10.4028/www.scientific.net/AMR.616-618.1783.

[83] L. Han, A. Chrysanthou, J.M. O’Sullivan, Fretting behaviour of self-piercing riveted

aluminium alloy joints under different interfacial conditions, Mater. Des. 27 (2006) 200–208. https://doi.org/10.1016/j.matdes.2004.10.014.

[84] N. Leconte, B. Bourel, F. Lauro, C. Badulescu, E. Markiewicz, Strength and failure of an aluminum/PA66 self-piercing riveted assembly at low and moderate loading rates: Experiments and modeling, Int. J. Impact Eng. 142 (2020) 103587. https://doi.org/10.1016/j.ijimpeng.2020.103587.

[85] F. Hönsch, J. Domitner, C. Sommitsch, B. Götzinger, Modeling the failure behavior of self-piercing riveting joints of 6xxx aluminum alloy, J. Mater. Eng. Perform. 29 (2020) 4888–4897. https://doi.org/10.1007/s11665-020-04894-8.

[86] N.-H. Hoang, M. Langseth, R. Porcaro, A.-G. Hanssen, The effect of the riveting process and aging on the mechanical behaviour of an aluminium self-piercing riveted connection, Eur. J. Mech. A/Solids. 30 (2011) 619–630. https://doi.org/10.1016/j.euromechsol.2011.02.006.

[87] M. Alfano, F. Furgiuele, G. Lubineau, G.H. Paulino, Simulation of debonding in Al/epoxy T-peel joints using a potential-based cohesive zone model, in: Procedia Eng., 2011: pp. 1760–1765. https://doi.org/10.1016/j.proeng.2011.04.293.

[88] Weidong Dang, Finite element modelling of hybrid (spot welded/bonded) joints under service conditions, 2016. https://tel.archives-ouvertes.fr/tel-01296998/.

[89] L.F.M. da Silva, T.N.S.S. Rodrigues, M.A.V. Figueiredo, M.F.S.F. de Moura, J.A.G. Chousal, Effect of adhesive type and thickness on the lap shear strength, J. Adhes. 82 (2006) 1091–1115. https://doi.org/10.1080/00218460600948511.

[90] V.K. Goyal, E.R. Johnson, V.K. Goyal, Predictive strength-fracture model for composite bonded joints, Compos. Struct. 82 (2008) 434–446. https://doi.org/10.1016/j.compstruct.2007.01.029.

[91] K.R. Ramakrishnan, E. Sarlin, M. Kanerva, M. Hokka, Experimental study of adhesively bonded natural fibre composite – steel hybrid laminates, Compos. Part C Open Access. 5 (2021) 100157. https://doi.org/10.1016/j.jcomc.2021.100157.

[92] R.D.S.G. Campilho, D.C. Moura, M.D. Banea, L.F.M. da Silva, Adhesive thickness effects of a ductile adhesive by optical measurement techniques, Int. J. Adhes. Adhes. 57 (2015) 125–132. https://doi.org/10.1016/J.IJADHADH.2014.12.004.

[93] D.M. Gleich, M.J. L Van Tooren, A. Beukers, Analysis and evaluation of bondline thickness effects on failure load in adhesively bonded structures, J. Adhes. Sci. Technol.

15 (2001) 1091–1101. https://doi.org/10.1163/156856101317035503.

[94] N.G.C. Barbosa, R.D.S.G. Campilho, F.J.G. Silva, R.D.F. Moreira, Comparison of different adhesively-bonded joint types for mechanical structures, Appl. Adhes. Sci. 6 (2018) 15. https://doi.org/10.1186/s40563-018-0116-1.

[95] F. Heidarpour, M. Farahani, P. Ghabezi, Experimental investigation of the effects of adhesive defects on the single lap joint strength, Int. J. Adhes. Adhes. 80 (2018) 128–132. https://doi.org/10.1016/J.IJADHADH.2017.08.005.

[96] M. Elhannani, K. Madani, Z. Chama, E. Legrand, S. Touzain, X. Feaugas, Influence of the presence of defects on the adhesive layer for the single-lap bonded joint—Part II: Probabilistic assessment of the critical state, Aerosp. Sci. Technol. 63 (2017) 372–386. https://doi.org/10.1016/J.AST.2016.12.020.

[97] A. Safari, M. Farahani, P. Ghabezi, Experimental study on the influences of different surface treatment processes and adhesive type on the aluminum adhesive-bonded joint strength, Mech. Based Des. Struct. Mach. (2020) 1–14. https://doi.org/10.1080/15397734.2020.1777876.

[98] M. Alfano, G. Ambrogio, F. Crea, L. Filice, F. Furgiuele, Influence of laser surface modification on bonding strength of Al/Mg adhesive joints, J. Adhes. Sci. Technol. 25 (2011) 1261–1276. https://doi.org/10.1163/016942410X533381.

[99] A.T. Lee, M. Michel, E. Ferrier, B. Benmokrane, Influence of curing conditions on mechanical behaviour of glued joints of carbon fibre-reinforced polymer composite/concrete, Constr. Build. Mater. 227 (2019) 116385. https://doi.org/10.1016/J.CONBUILDMAT.2019.07.111.

[100] K. Matsui, Effects of curing conditions and test temperatures on the strength of adhesive-bonded joints, Int. J. Adhes. Adhes. 10 (1990) 277–284. https://doi.org/10.1016/0143-7496(90)90046-Z.

[101] L.F.M. da Silva, R.D. Adams, Joint strength predictions for adhesive joints to be used over a wide temperature range, Int. J. Adhes. Adhes. 27 (2007) 362–379. https://doi.org/10.1016/J.IJADHADH.2006.09.007.

[102] X. Jiang, X. Qiang, M.H. Kolstein, F.S.K. Bijlaard, Experimental investigation on mechanical behaviour of FRP-to-steel adhesively-bonded joint under combined loading – Part 2: After hygrothermal ageing, Compos. Struct. 125 (2015) 687–697. https://doi.org/10.1016/J.COMPSTRUCT.2014.12.040.

[103] L. Liao, C. Huang, T. Sawa, Effect of adhesive thickness, adhesive type and scarf angle on the mechanical properties of scarf adhesive joints, Int. J. Solids Struct. 50 (2013) 4333–4340. https://doi.org/10.1016/J.IJSOLSTR.2013.09.005.

[104] U.A. Khashaba, I.M.R. Najjar, Adhesive layer analysis for scarf bonded joint in CFRE composites modified with MWCNTs under tensile and fatigue loads, Compos. Struct. 184 (2018) 411–427. https://doi.org/10.1016/j.compstruct.2017.09.095.

[105] A. Zeaiter, G. Challita, K. Khalil, Investigation of vibration modes of a double-lap bonded joint, SN Appl. Sci. 1 (2019) 1–15. https://doi.org/10.1007/s42452-019-0340-8.

[106] H. Rangaswamy, I. Sogalad, S. Basavarajappa, M.P.G. Chandrashekarappa, A comprehensive modelling, analysis and optimisation of adhesive bonded single lap glass fibre reinforced composite joints, Int. J. Mater. Eng. Innov. 10 (2019) 286–309. https://doi.org/10.1504/IJMATEI.2019.103609.

[107] T. Dai, Y. Yang, H.-L. Dai, Z. Hu, Interfacial stress analysis of a CFRR-metal adhesively bonded joint with/without defect under hygrothermal environment, Appl. Math. Model. 67 (2019) 357–377. https://doi.org/10.1016/J.APM.2018.10.032.

[108] M.D. Aydin, A. Özel, Ş. Temiz, The effect of adherend thickness on the failure of adhesively-bonded single-lap joints, J. Adhes. Sci. Technol. 19 (2005) 705–718. https://doi.org/10.1163/1568561054890499.

[109] X. Zhan, S. Chen, Y. Li, H. Wang, Y. Yang, Effect of surface cold ablation on shear strength of CFRP adhesively bonded joint after UV laser treatment, Int. J. Adhes. Adhes. 94 (2019) 13–23. https://doi.org/10.1016/J.IJADHADH.2019.05.006.

[110] J. Peng, M. Wang, B. Sadeghi, R. Wang, H. Liu, P. Cavaliere, Increasing shear strength of Au–Sn bonded joint through nano-grained interfacial reaction products, J. Mater. Sci. 56 (2021) 7050–7062. https://doi.org/10.1007/s10853-020-05623-1.

[111] K.R. Lyathakula, F.G. Yuan, A probabilistic fatigue life prediction for adhesively bonded joints via ANNs-based hybrid model, Int. J. Fatigue. 151 (2021) 106352. https://doi.org/10.1016/j.ijfatigue.2021.106352.

[112] M. Mariam, M. Afendi, M.S. Abdul Majid, M.J.M. Ridzuan, A.I. Azmi, M.T.H. Sultan, Influence of hydrothermal ageing on the mechanical properties of an adhesively bonded joint with different adherends, Compos. Part B Eng. 165 (2019) 572–585. https://doi.org/10.1016/J.COMPOSITESB.2019.02.032.

[113] S.Y. Park, W.J. Choi, B.C. Yoon, Analysis of effects of process factors on corrosion resistance of adhesive bonded joints for aluminum alloys, J. Mater. Process. Technol. 276 (2020) 116412. https://doi.org/10.1016/j.jmatprotec.2019.116412.

[114] H. Wan, J. Lin, J. Min, Effect of laser ablation treatment on corrosion resistance of adhesive-bonded Al alloy joints, Surf. Coatings Technol. 345 (2018) 13–21. https://doi.org/10.1016/j.surfcoat.2018.03.087.

[115] R.D.F. Moreira, R.D.S.G. Campilho, Strength improvement of adhesively-bonded scarf repairs in aluminium structures with external reinforcements, Eng. Struct. 101 (2015) 99–110. https://doi.org/10.1016/J.ENGSTRUCT.2015.07.001.

[116] R.D.S.G. Campilho, M.D. Banea, F.J.P. Chaves, L.F.M. da Silva, eXtended Finite Element Method for fracture characterization of adhesive joints in pure mode I, Comput. Mater. Sci. 50 (2011) 1543–1549. https://doi.org/10.1016/j.commatsci.2010.12.012.

[117] G. Kelly, Quasi-static strength and fatigue life of hybrid (bonded/bolted) composite single-lap joints, Compos. Struct. 72 (2006) 119–129. https://doi.org/10.1016/j.compstruct.2004.11.002.

[118] H. Özer, Ö. Öz, Three dimensional finite element analysis of bi-adhesively bonded double lap joint, Int. J. Adhes. Adhes. 37 (2012) 50–55. https://doi.org/10.1016/j.ijadhadh.2012.01.016.

[119] Y. Zhang, A.P. Vassilopoulos, T. Keller, Mode I and II fracture behavior of adhesively-bonded pultruded composite joints, Eng. Fract. Mech. 77 (2010) 128–143. https://doi.org/10.1016/j.engfracmech.2009.09.015.

[120] T. Vallée, J.R. Correia, T. Keller, Optimum thickness of joints made of GFPR pultruded adherends and polyurethane adhesive, Compos. Struct. 92 (2010) 2102–2108. https://doi.org/10.1016/j.compstruct.2009.09.056.

[121] Z.M. Yan, M. You, X.S. Yi, X.L. Zheng, Z. Li, A numerical study of parallel slot in adherend on the stress distribution in adhesively bonded aluminum single lap joint, Int. J. Adhes. Adhes. 27 (2007) 687–695. https://doi.org/10.1016/j.ijadhadh.2007.02.003.

[122] P. Papanikos, K.I. Tserpes, G. Labeas, S. Pantelakis, Progressive damage modelling of bonded composite repairs, Theor. Appl. Fract. Mech. 43 (2005) 189–198. https://doi.org/10.1016/j.tafmec.2005.01.004.

[123] R.A. Odi, C.M. Friend, An improved 2D model for bonded composite joints, Int. J.

Adhes. Adhes. 24 (2004) 389–405. https://doi.org/10.1016/j.ijadhadh.2001.06.001.

[124] M.J. van den Bosch, P.J.G. Schreurs, M.G.D. Geers, An improved description of the exponential Xu and Needleman cohesive zone law for mixed-mode decohesion, Eng. Fract. Mech. 73 (2006) 1220–1234. https://doi.org/10.1016/J.ENGFRACMECH.2005.12.006.

[125] Z. Chen, R.D. Adams, L.F.M. Da Silva, Prediction of crack initiation and propagation of adhesive lap joints using an energy failure criterion, Eng. Fract. Mech. 78 (2011) 990–1007. https://doi.org/10.1016/j.engfracmech.2010.12.004.

[126] K.N. Anyfantis, N.G. Tsouvalis, A novel traction–separation law for the prediction of the mixed mode response of ductile adhesive joints, Int. J. Solids Struct. 49 (2012) 213–226. https://doi.org/10.1016/J.IJSOLSTR.2011.10.001.

[127] S.K. Panigrahi, B. Pradhan, Three dimensional failure analysis and damage propagation behavior of adhesively bonded single lap joints in laminated FRP composites, J. Reinf. Plast. Compos. 26 (2007) 183–201. https://doi.org/10.1177/0731684407070026.

[128] G.P. Marques, R.D.S.G. Campilho, F.J.G. Da Silva, R.D.F. Moreira, Adhesive selection for hybrid spot-welded/bonded single-lap joints: Experimentation and numerical analysis, Compos. Part B Eng. 84 (2016) 248–257. https://doi.org/10.1016/j.compositesb.2015.09.002.

[129] T. Sadowski, P. Golewski, M. Kneć, Experimental investigation and numerical modelling of spot welding–adhesive joints response, Compos. Struct. 112 (2014) 66–77. https://doi.org/10.1016/J.COMPSTRUCT.2014.01.008.

[130] F. Esmaeili, M. Zehsaz, T.N. Chakherlou, S. Barzegar, Fatigue life estimation of double lap simple bolted and hybrid (bolted/bonded) joints using several multiaxial fatigue criteria, Mater. Des. 67 (2015) 583–595. https://doi.org/10.1016/J.MATDES.2014.11.003.

[131] H. Fricke, T. Vallée, Numerical modeling of hybrid-bonded joints, J. Adhes. 92 (2016) 652–664. https://doi.org/10.1080/00218464.2015.1100995.

[132] J. Cui, S. Gao, H. Jiang, X. Huang, G. Lu, G. Li, Adhesive bond-electromagnetic rivet hybrid joining technique for CFRP/Al structure: Process, design and property, Compos. Struct. 244 (2020) 112316. https://doi.org/10.1016/j.compstruct.2020.112316.

[133] G. Sun, X. Xia, X. Liu, Q. Luo, Q. Li, On quasi-static behaviors of different joint

methods for connecting carbon fiber reinforce plastic (CFRP) laminate and aluminum alloy, Thin-Walled Struct. 164 (2021) 107657. https://doi.org/10.1016/j.tws.2021.107657.

[134] T. Balawender, T. Sadowski, M. Kneć, Technological problems and experimental investigation of hybrid: Clinched - Adhesively bonded joint, Arch. Metall. Mater. 56 (2011) 439–446. https://doi.org/10.2478/V10172-O11-0047-3.

[135] K. Bodjona, L. Lessard, Load sharing in single-lap bonded/bolted composite joints. Part II: Global sensitivity analysis, Compos. Struct. 129 (2015) 276–283. https://doi.org/10.1016/J.COMPSTRUCT.2015.03.069.

[136] Y. Liu, L. Zhang, W. Liu, P.C.C. Wang, Single-sided piercing riveting for adhesive bonding in vehicle body assembly, J. Manuf. Syst. 32 (2013) 498–504. https://doi.org/10.1016/j.jmsy.2013.04.005.

[137] A. Zvorykina, O. Sherepenko, M. Neubauer, S. Jüttner, Dissimilar metal joining of aluminum to steel by hybrid process of adhesive bonding and projection welding using a novel insert element, J. Mater. Process. Technol. 282 (2020) 116680. https://doi.org/10.1016/j.jmatprotec.2020.116680.

[138] N. Baurova, A. Anoprienko, Y. Romanova, Providing dismountable rivet bonded joints through the use of hot-melt adhesives, MATEC Web Conf. 129 (2017) 01004. https://doi.org/10.1051/matecconf/201712901004.

[139] F. Moroni, A. Pirondi, Technology of rivet: Adhesive joints, Adv. Struct. Mater. 6 (2011) 79–108. https://doi.org/10.1007/8611_2010_37.

[140] O. Hahn, T.M. Wibbeke, Application of low-heat hybrid joining technologies for the joining of thin-walled sheet materials, Weld. Cut. 4 (2005) 208–214.

[141] F. Moroni, Fatigue behaviour of hybrid clinch-bonded and self-piercing rivet bonded joints, J. Adhes. 95 (2019) 577–594. https://doi.org/10.1080/00218464.2018.1552586.

[142] X. He, B. Xing, K. Zeng, F. Gu, A. Ball, Numerical and experimental investigations of self-piercing riveting, Int. J. Adv. Manuf. Technol. 69 (2013) 715–721. https://doi.org/10.1007/s00170-013-5072-0.

[143] Y. Liu, W. Zhuang, Self-piercing riveted-bonded hybrid joining of carbon fibre reinforced polymers and aluminium alloy sheets, Thin-Walled Struct. 144 (2019) 106340. https://doi.org/10.1016/j.tws.2019.106340.

[144] Y. Miyashita, Y.C. Jack Teow, T. Karasawa, N. Aoyagi, Y. Otsuka, Y. Mutoh, Strength

of adhesive aided SPR joint for AM50 magnesium alloy sheets, Procedia Eng. 10 (2011) 2532–2537. https://doi.org/10.1016/j.proeng.2011.04.417.

[145] G. Di Franco, L. Fratini, A. Pasta, Analysis of the mechanical performance of hybrid (SPR/bonded) single-lap joints between CFRP panels and aluminum blanks, Int. J. Adhes. Adhes. 41 (2013) 24–32. https://doi.org/10.1016/j.ijadhadh.2012.10.008.

[146] G. Di Franco, L. Fratini, A. Pasta, Influence of the distance between rivets in self-piercing riveting bonded joints made of carbon fiber panels and AA2024 blanks, Mater. Des. 35 (2012) 342–349. https://doi.org/10.1016/j.matdes.2011.09.036.

[147] W. Lee, I. Kim, H.M. Cho, Study on stress depending on HSS panel joint method in automobiles, Turkish J. Comput. Math. Educ. (2021) 7570–7579. https://www.turcomat.org/index.php/turkbilmat/article/view/5666 (accessed May 13, 2021).

[148] H. Jiang, Y. Liao, S. Gao, G. Li, J. Cui, Comparative study on joining quality of electromagnetic driven self-piecing riveting, adhesive and hybrid joints for Al/steel structure, Thin-Walled Struct. 164 (2021) 107903. https://doi.org/10.1016/j.tws.2021.107903.

[149] C. Song, X. He, W. Wei, J. Lu, K. Liu, Effect of adhesive on mechanical properties of composite/steel self-piercing joints, Nonferrous Met. Eng. 10 (2020) 13–17.

[150] M. Guo, G. El-Tawil, Experimental study on static and fatigue performance of self-piercing riveted joints and adhesively bonded self-piercing riveted joints connecting steel and aluminum components, SAE Tech. Pap. 2020 (2020). https://doi.org/10.4271/2020-01-0177.

[151] V. Fiore, F. Alagna, G. Galtieri, C. Borsellino, G. Di Bella, A. Valenza, Effect of curing time on the performances of hybrid/mixed joints, Compos. Part B Eng. 45 (2013) 911–918. https://doi.org/10.1016/J.COMPOSITESB.2012.05.016.

[152] J. Presse, K. Boris, M. Thorsten, Stress-based approach for fatigue life calculation of multi-material connections hybrid joined by self-piercing rivets and adhesive, Thin-Walled Struct. 159 (2021) 107192. https://doi.org/10.1016/j.prostr.2019.12.046.

[153] G. Wu, D. Li, W.J. Lai, Y. Shi, H. Kang, Y. Peng, X. Su, Fatigue behaviors and mechanism-based life evaluation on SPR-bonded aluminum joint, Int. J. Fatigue. 142 (2021) 105948. https://doi.org/10.1016/j.ijfatigue.2020.105948.

[154] H. Fricke, T. Vallee, B. Mayer, Modelling of industrial hybrid bonding processes

considering fluid-Structure-Interaction, in: Proc. 7th Int. Conf. Coupled Probl. Sci. Eng. COUPLED Probl., 2017: pp. 393–399. http://congress.cimne.com/coupled2017/admin/files/fileabstract/a7.pdf (accessed August 22, 2018).

[155] R. Neugebauer, M. Israel, B. Mayer, H. Fricke, Numerical and experimental studies on the clinch-bonding and riv-bonding process, Key Eng. Mater. 504 (2012) 771–776. https://doi.org/10.4028/www.scientific.net/KEM.504-506.771.

[156] D. Landgrebe, B. Mayer, S. Niese, H. Fricke, I. Neumann, M. Ahnert, T. Falk, Adhesive distribution and global deformation between hybrid joints, Key Eng. Mater. 651 (2015) 1465–1471. https://doi.org/10.4028/www.scientific.net/KEM.651-653.1465.

[157] L. Potgorschek, J. Domitner, F. Hönsch, C. Sommitsch, S. Kaufmann, Numerical simulation of hybrid joining processes: self-piercing riveting combined with adhesive bonding, Procedia Manuf. 47 (2020) 413–418. https://doi.org/10.1016/j.promfg.2020.04.322.

[158] L. Huang, J.F.C. Moraes, D.G. Sediako, J.B. Jordon, H. Guo, X. Su, Finite-element and residual stress analysis of self-pierce riveting in dissimilar metal sheets, J. Manuf. Sci. Eng. Trans. ASME. 139 (2017) 021007. https://doi.org/10.1115/1.4034437.

[159] F. Hirsch, S. Müller, M. Machens, R. Staschko, N. Fuchs, M. Kästner, Simulation of self-piercing rivetting processes in fibre reinforced polymers: Material modelling and parameter identification, J. Mater. Process. Technol. 241 (2017) 164–177. https://doi.org/10.1016/j.jmatprotec.2016.10.010.

[160] A. Rusia, S. Weihe, Development of an end-to-end simulation process chain for prediction of self-piercing riveting joint geometry and strength, J. Manuf. Process. 57 (2020) 519–532. https://doi.org/10.1016/j.jmapro.2020.07.004.

[161] M. Buckley, H. Gese, M. Reissner, G. Oberhofer, Simulation of the manufacturing process of self- piercing rivets with LS-DYNA with focus on failure prediction for sheets and rivet, in: 10th Eur. LS-DYNA Conf., 2015. https://www.dynalook.com/conferences/10th-european-ls-dyna-conference/3 Process V - Miscellaneous/02-Buckley-JaguarLandRover-Gese-Matfem-P.pdf (accessed December 2, 2019).

[162] H.H. Porcaro R, Langseth M, Weyer S, An experimental and numerical investigation on self-piercing riveting, Int. J. Mater. Form. 1 (2008) 1307–1310.

https://doi.org/10.1115/GT2013-94267.

[163] R. Porcaro, M. Langseth, A.G. Hanssen, H. Zhao, S. Weyer, H. Hooputra, Crashworthiness of self-piercing riveted connections, Int. J. Impact Eng. 35 (2008) 1251–1266. https://doi.org/10.1016/j.ijimpeng.2007.07.008.

[164] S.G. Qu, W.J. Deng, Finite element simulation of the self-piercing riveting process, in: ASME Int. Mech. Eng. Congr. Expo. Proc., 2008: pp. 243–249. https://doi.org/10.1115/IMECE2008-67017.

[165] P. Czyżewski, R. Cacko, Verification of numerical modelling of the SPR joint by experimentul stack-up, in: Comput. Methods Mater. Sci., 2007: pp. 124–129.

[166] G. Testa, N. Bonora, G. Iannitti, A. Ruggiero, D. Gentile, Numerical simulation of self-piercing riveting process (SRP) using continuum damage mechanics modelling, Frat. Ed Integrita Strutt. 12 (2018) 161–172. https://doi.org/10.3221/IGF-ESIS.44.13.

[167] P.O. Bouchard, T. Laurent, L. Tollier, Numerical modeling of self-pierce riveting-From riveting process modeling down to structural analysis, J. Mater. Process. Technol. 202 (2008) 290–300. https://doi.org/10.1016/j.jmatprotec.2007.08.077.

[168] S. Ishikawa, H. Aihara, Modelling of self-piercing riveting with ALE, CEL and SPH based on abaqus/explicit, in: Proc. 14th Int. Conf. Comput. Plast. - Fundam. Appl. COMPLAS, 2017: pp. 682–691.

[169] L. Huang, Y. Wu, G. Huff, S. Huang, A. Ilinich, A. Freis, G. Luckey, Simulation of self-piercing rivet insertion using smoothed particle galerkin method, in: 5th Int. LS-DYNA Users Conf., 2018: pp. 1–11. https://www.dynalook.com/15th-international-ls-dyna-conference/spg/simulation-of-self-piercing-rivet-insertion-using-smoothed-particle-galerkin-method (accessed November 22, 2018).

[170] M. Carandente, FE simulation of the SPR process to predict joint characteristics: innovation report, University of Warwick, 2016. https://ethos.bl.uk/OrderDetails.do?uin=uk.bl.ethos.731306 (accessed April 24, 2019).

[171] R. Cacko, Review of different material separation criteria in numerical modeling of the self-piercing riveting process - SPR, Arch. Civ. Mech. Eng. 8 (2008) 21–30. https://doi.org/10.1016/S1644-9665(12)60190-3.

[172] M. Otroshi, M. Rossel, G. Meschut, Stress state dependent damage modeling of self-pierce riveting process simulation using GISSMO damage model, J. Adv. Join. Process. 1 (2020) 100015. https://doi.org/10.1016/j.jajp.2020.100015.

[173] L. Huang, J. V. Lasecki, H. Guo, X. Su, Finite element modeling of dissimilar metal self-piercing riveting process, SAE Int. J. Mater. Manuf. 7 (2014) 2014-01–1982. https://doi.org/10.4271/2014-01-1982.

[174] R. Porcaro, A.G. Hanssen, M. Langseth, A. Aalberg, Self-piercing riveting process: An experimental and numerical investigation, J. Mater. Process. Technol. 171 (2006) 10–20. https://doi.org/10.1016/j.jmatprotec.2005.05.048.

[175] S.L. Han, X.D. Tang, Y. Gao, Q.L. Zeng, Effects of friction factors on flat bottom self-pierce riveting joints of AZ31 magnesium alloy, Mater. Res. Innov. 19 (2015) S10-235–238. https://doi.org/10.1179/1432891715Z.0000000002155.

[176] D. Li, L. Han, Z. Lu, M. Thornton, M. Shergold, Influence of die profiles and cracks on joint buttons on the joint quality and mechanical strengths of high strength aluminium alloy joint, Adv. Mater. Res. 548 (2012) 398–405. https://doi.org/10.4028/www.scientific.net/AMR.548.398.

[177] H.I. Andersson, J.B. Aarseth, N. Braud, B.S. Dandapat, Flow of a power-law fluid film on an unsteady stretching surface, J. Nonnewton. Fluid Mech. 62 (1996) 1–8. https://doi.org/10.1016/0377-0257(95)01392-X.

[178] M. Jabbari, R. Bulatova, J.H. Hattel, C.R.H. Bahl, Quasi-steady state power law model for flow of (La 0·85 Sr 0·15) 0·9 MnO 3 ceramic slurry in tape casting, Mater. Sci. Technol. 29 (2013) 1080–1087. https://doi.org/10.1179/1743284713Y.0000000255.

[179] S.E. Ardakani, Entwicklung einer praxisnahen Methodik für die Simulation des Clinchklebeprozesses, Universität Paderborn, 2012. https://www.shaker.de/de/content/catalogue/index.asp? lang=de&ID=8&ISBN=978-3-8440-1606-2.

[180] T. Gerstmann, B. Awiszus, Hybrid joining: Numerical process development of flat-clinch-bonding, J. Mater. Process. Technol. 277 (2020) 116421. https://doi.org/10.1016/j.jmatprotec.2019.116421.

[181] SikaPower ® -498, 2016. https://deu.sika.com/dms/getdocument.get/741b0a84-53dc-3677-981c-e19cb4c0b6a3/SikaPower-498 DE 04-16.pdf.

[182] G. Weber, H. Thommes, H. Gaul, O. Hahn, M. Rethmeier, Mechanical properties of weldbonded joints of advanced high strength steels, J. Adhes. Sci. Technol. 25 (2011) 2369–2407. https://doi.org/10.1163/016942411X580090.

[183] X. Zhang, X. He, W. Wei, J. Lu, K. Zeng, Fatigue characterization and crack

propagation mechanism of self-piercing riveted joints in titanium plates, Int. J. Fatigue. 134 (2020) 105465. https://doi.org/10.1016/J.IJFATIGUE.2019.105465.

[184] X. Sun, Optimization of the strength of self-piercing rivets (SPRs), in: Self-Piercing Riveting Prop. Process. Appl., Woodhead Publishing, 2014: pp. 149–170. https://doi.org/10.1533/9780857098849.2.149.

[185] Y. Liu, H. Li, H. Zhao, X. Liu, Effects of the die parameters on the self-piercing riveting process, Int. J. Adv. Manuf. Technol. 105 (2019) 3353–3368. https://doi.org/10.1007/s00170-019-04567-4.

[186] R. Haque, N.S. Williams, S.E. Blacket, Y. Durandet, A simple but effective model for characterizing SPR joints in steel sheet, J. Mater. Process. Technol. 223 (2015) 225–231. https://doi.org/10.1016/j.jmatprotec.2015.04.006.

[187] H. Zhang, Influence of riveting sequence/direction on distortion of steel and aluminum sheets, J. Manuf. Process. 53 (2020) 304–309. https://doi.org/10.1016/j.jmapro.2020.02.039.